Energy disposal in the reaction of fluorine atoms with iodine.

by

John Ross Wheeler

PhD

University of Edinburgh

1982

Declaration

I declare that this thesis is my own composition and that the work described herein is my own or where done in collaboration with others contains a substantial contribution from me. Where reported work was done mainly by others due credit is given and references are given to all other sources of information.

Abstract

The product internal energy distributions for the reaction $F + I_2 \rightarrow IF + I$ have been investigated. Laser induced fluorescence techniques in a crossed molecular beam environment were used to obtain the relative populations of the vibrational levels. The (6,0), (5,0), (3,0), (8,1), (6,2) and (8,3) bands of the IF (X) IF(B) spectrum were probed by a nitrogen pumped dye laser in the region 460 - 500nm. Relative populations for the v" = 0,1,2,3 levels are reported with the v" = 0 level strongly favoured. Boltzmann like distributions were observed for the rotational distribution of the v" = 0 level with a temperature of (230 $\pm$ 10)K.

A classical trajectory study of the reaction is also reported, using nine LEPS potential energy surfaces at near thermal energies. The results suggest that a mechanism which is intermediate between direct and complex reaction dynamics is involved. Good agreement with the measured reaction cross section is obtained.

In order to explain the discrepancies in the experimental data two reaction branches are proposed. One which gives highly vibrationally excited products occurring on the ground state surface gives good agreement with the trajectory results. It is proposed that the second branch forms $I(^2P_{\frac{1}{2}})$ products and accounts for the large v" = 0 population.

Contents

Chapter 1

Introduction

1 Introduction

Recent progress in molecular beam techniques has been reviewed by Grice (GRI81) and the theoretical tools for interpreting the resulting data is comprehensively covered in ref. BER79. In efforts to extend the scope of reactions studied in molecular beams much work since 1973 has gone into the construction of efficient non-metal atom beam sources. Vastly improved beam intensities over simple effusive sources have been achieved by supersonic nozzle sources working at high Mach numbers (GRI75). This increase in intensity is essential for the production of highly reactive atomic species such as oxygen or fluorine where a large proportion of the beam is a buffer gas. Another direction in recent years has been to explore the internal energy disposal of bimolecular reactions. Two techniques which stand out in this field are arrested relaxation chemiluminescence (ANL67) and laser induced fluorescence (SCH72). Reviews of these methods are given in references CAM78 and KIN77 respectively.

Interpretation of the results of molecular beam studies usually relies on comparison of the results with simple kinetic and dynamic models. Often reactions are split into direct or complex reaction dynamics according to the angular product distribution. If an intermediate is formed with a lifetime of the order of its rotational period or greater, then a symmetric distribution of products is expected (FIS67). RRKM-AM theory has been used to explain the energy distributions in such reactions (SAF72, HOL77). Some direct interactions

are explained in terms of simple reaction models with surprising success (POL74). Other systems require more sophisticated models, for example the DIPR (KUN70) and FOTO (PAT74) models, which require more detailed knowledge of the potential energy surface. However if the potential energy surface is known to a reasonable degree of accuracy it can best be probed by a classical trajectory study (MUC79).

As in other branches of chemistry, periodic trends exist and are looked for, molecular beam studies are no exception. Because of the relative ease of production of beams of halogen diatomics and hydrides systematic trends in such series have been observed, for example the series of reactions (CRU73)

$$Ba + HX \rightarrow BaX + H \quad ; \quad X = F, Cl, Br, I$$

Chlorine and bromine atom reactions with all the halogens and inter-halogens have been studied by angular distribution measurements. Most of these results were obtained with effusive beam sources (LEE69, BLA70), but velocity selection in the reaction $Cl + Br_2$ has shown little dependence of the cross section on the input energy (LEE77). In most cases the scattering is forward peaked with cross sections less than the hard sphere value. This suggested that the dominant process is short range attraction. Complex lifetimes determined from the angular distributions (FIS67) are consistent with the electronegativity ordering rule for triatomics (PEY68). Charge transfer from the central atom of the intermediate

stabilizes the orbitals of the complex. Thus the complex formed in the reaction Br + I_2 is longer lived than that of the similar reaction Cl + Br_2 (LEE68). In contrast the reaction

$$Br + ICl \rightarrow Br\,Cl + I$$

gives a smaller cross section and is backward peaked (LEE69) showing the instability of the Br....Cl....I intermediate.

Angular scattering measurements have also been carried out on the reaction (CAR73, WON73).

$$F + I_2 \rightarrow IF + I$$

Lee's results which exployed velocity selection of the reactants implied a complex mechanism which might be expected as I_2F has been observed to be stable by 12 KJ mol^{-1} (VAL77). The two reports agreed on the average translational energy of 15% of the available energy but disagreement on the angular distribution led Grice to conclude that an appreciable energy dependence existed. These results suggested that this reaction would continue the trend observed in the other halogen - inter-halogen reactions. However, the rate constant measured for this reaction and those for F + ICl/Br_2 (APP75) are significantly larger than their counterparts in the series and are close to the hard sphere bimolecular collision frequency. This indicates that long range attraction dominates in the potential contrary to the behaviour in the reactions of Cl and Br.

The spectroscopy of IF is known in great detail (CLY76, CLY78) and is well suited to the laser induced fluorescence technique. Preliminary studies of the reactions F + I_2 (DON80) and F + ICl (STE79) reported non statistical vibrational energy distributions with internal energies similar to those for Cl + Br_2/I_2 (70%: LOE71). If the lifetime is sufficiently long to produce a statistical angular distribution then statistical energy distributions are usually expected which is not what was observed.

In chapter two improvements to the apparatus used in the early study of the F + I_2 reaction are described. New relative populations for the v" = 0, 1, 2, 3 states of IF are reported along with the rotational energy distribution for the v" = 0 level.

In chapter three a classical trajectory study of the reaction is reported. It was hoped to show that the disparate results obtained to date could be explained by reactant energy variations in conjunction with the unusual mass combination.

The results of these two studies are discussed in detail in chapter four along with more detailed laser induced fluorescence data for the three reactions F + I_2/ICl/IBr which was obtained in a concurrent study by the Garching group (TRI80). In order to explain the energy disposal in these reactions the possibility of a spin orbit excited atomic product is proposed. Some of the consequences for the potential energy surface are also assessed.

Chapter 2

Laser induced fluorescence study of F + I_2 reactive scattering.

2.1 Vacuum system

The vacuum system consisted of a cylindrical stainless steel tank (fig.2.1) 1m across and 0.45m deep. It had eight ports sited radially around the walls and several in the base and the top. It was pumped by three 6 in oil diffusion pumps, Edwards E06 (1400 ls^{-1}) and one Leybold 501 pump (600ls^{-1}), backed by two separate roughing lines, 450ls^{-1} each. The main chamber was also pumped by five liquid nitrogen cryotraps (area approx. $1m^2$) with another smaller one operating as the iodine beam stop.

Two of the diffusion pumps evacuated the main chamber while another differentially pumped a chamber which housed the atom beam source. The central (Leybold) pump acted principally as the atom beam dump. A large conical skimmer captured the beam and carried it with as little resistance as possible to the pump (KAH80). The tank pressure was measured using an Edwards IG7 ion gauge with an Edwards IG5M gauge head. Pressures down to 4×10^{-7} Torr could be attained with rigorous cryotroapping.

The laser beam entered and left the tank through two windows attached to the tank by means of bellows which permitted some degree of alignment. The beam was then conducted to the reaction zone at the tank centre by baffle arms which reduced stray light and any scattered by the windows. The photo multiplier was mounted perpendicularly to the laser axis in a stainless steel arm which brought it close to the reaction zone. The vacuum seal was made between the face of

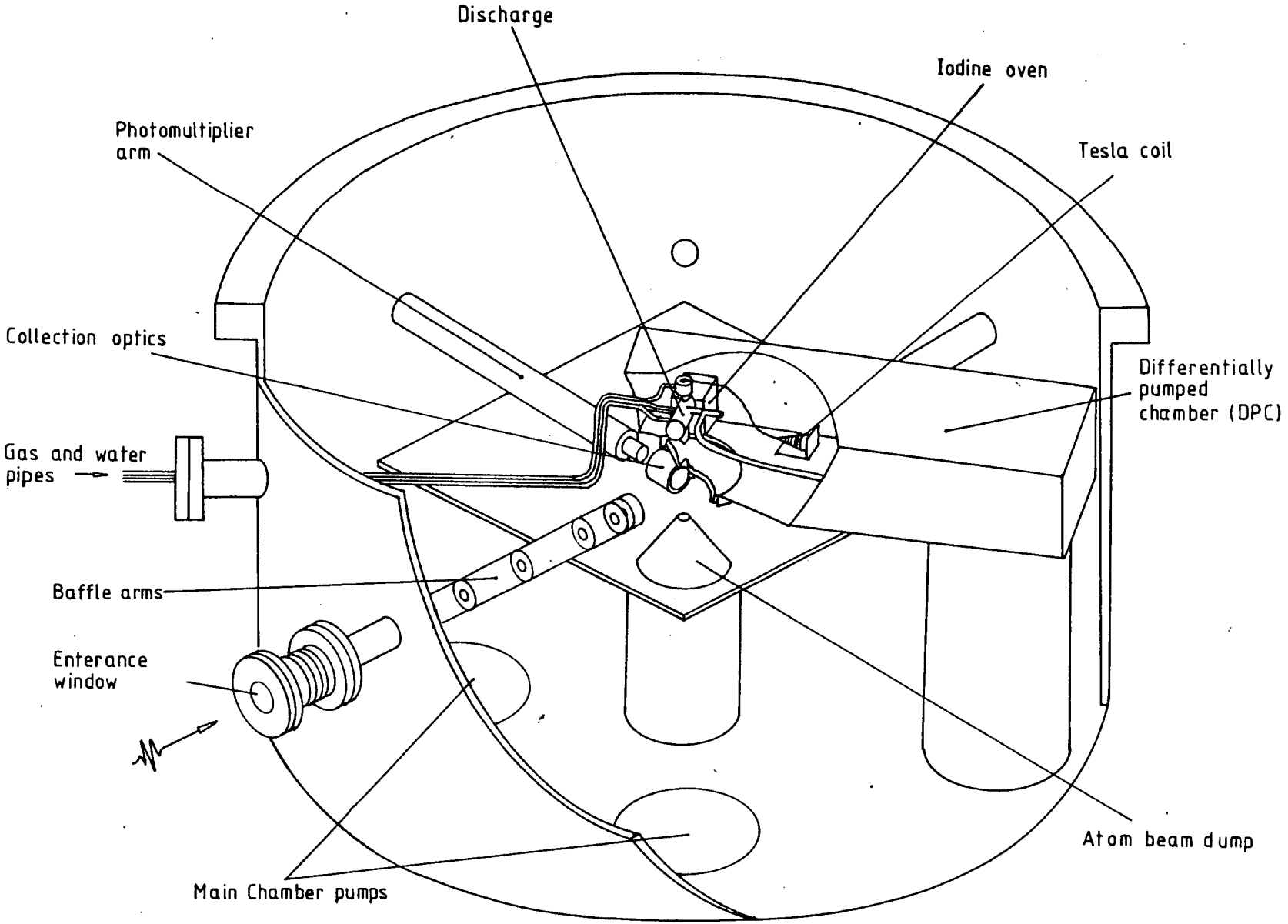

Figure 2.1 Vacuum system.

the photomultiplier and an 'O' ring.

To reduce reflection from the metallic walls, much of the inside of the tank was painted black.

The atom beam source, housed in the differentially pumped chamber, was aligned vertically, perpendicular to the laser and photomultiplier axes. The iodine beam was horizontal and made an angle of about 30° with the photomultiplier.

2.2 Laser system

2.2.1 Nitrogen laser.

The pump for the dye laser was a nitrogen laser built at Edinburgh. It was of the parallel plate Blumlein design and was that described by Fernie (FER80) with a few modifications. The discharge was formed in a cavity 1m long, 40mm gap width and 3mm electrode height. Gas pressures of 35 - 40 torr were used at the repetition rate of 100Hz. The peak power under optimum conditions was measured as 35kw with a pulse length of 6 ns fwhm.

Variations in the laser power are summarised for various operating conditions in figure 2.2.

2.2.2 Dye laser

The dye laser based on the Hansch design (HAN72) was built on an Oriel 600mm optical bench. The laser cavity was formed by a 50% transmitting, partially silvered concave mirror radius 37cm and a diffraction grating ruled at 1200 lines per mm and blazed for a wavelength of 450nm. The grating was mounted on a rotating table driven by a stepping motor, which changed the wavelength in 1.1Å steps.

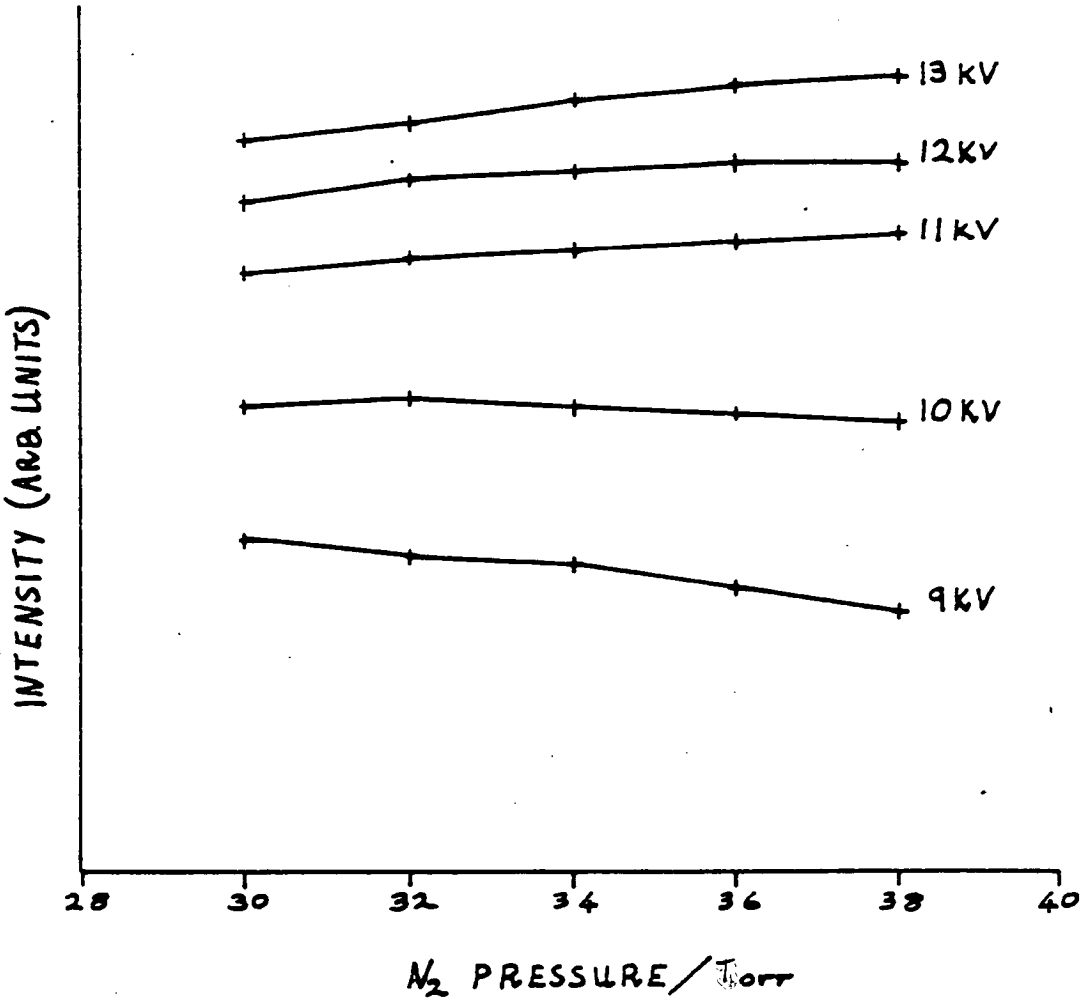

Figure 2.2 Nitrogen laser power variation with pressure at different operating voltages.

The beam was expanded by a telescope (x10 - Oriel) whose position was adjusted by four micrometer screws (fig. 2.3). The dye cell was positioned on a kinetic mount so that it could be placed exactly at the focus of the gas laser beam and its position in the cavity could be adjusted to optimise the dye laser output.

The dye cell (fig.2.4) consisted of a stainless steel block with a square slot machined in it and with two tubes which permitted the dye solution to circulate. The normal to the end windows made an angle of about 5° with the beam axis to prevent undesirable etalon effects. The windows

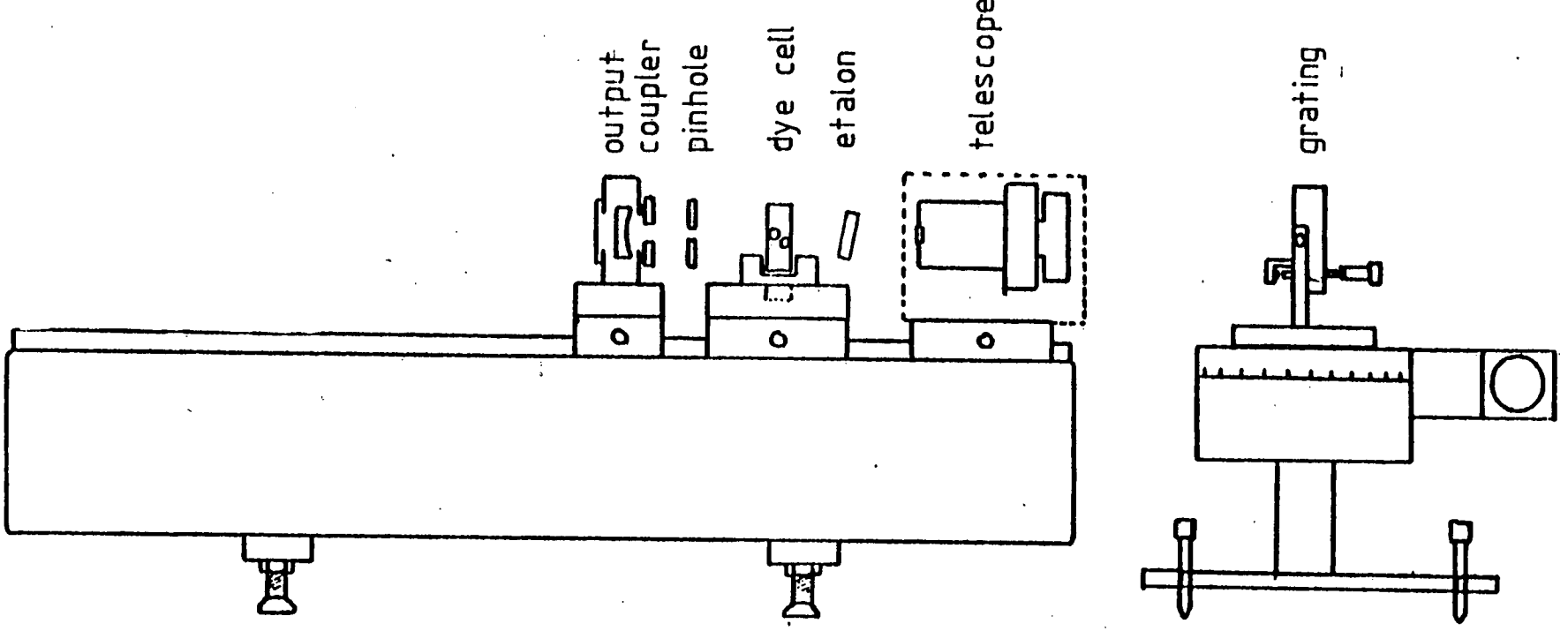

DYE LASER ASSEMBLY (scale 1:4)

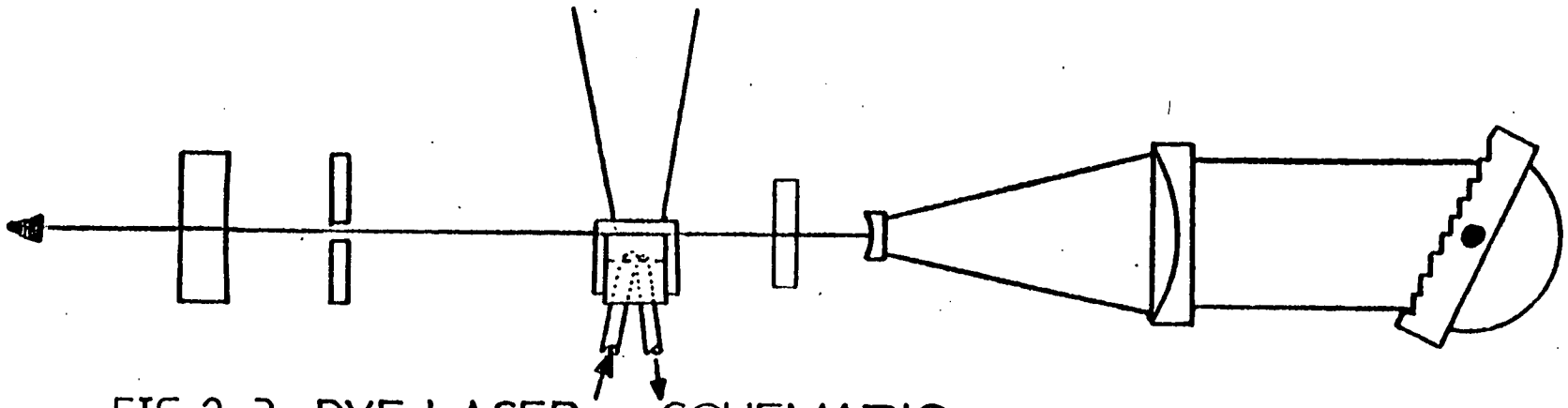

FIG 2·3 DYE LASER – SCHEMATIC

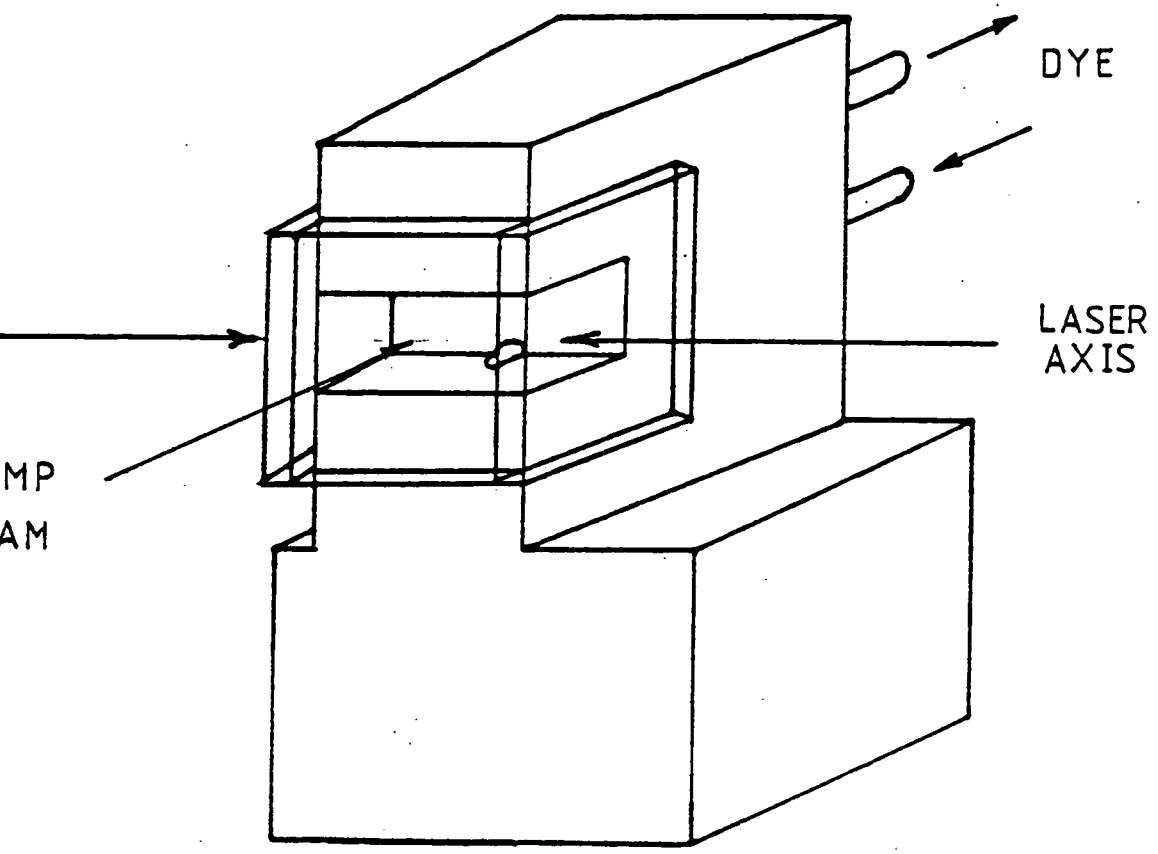

Figure 2.4 Dye cell

were 2mm fused quartz plate (Spectrosil) bonded to the cell body with IS 496 adhesive. A problem with this design was that the dye solvent dissolved the adhesive limiting the cell's lifetime. With ethanol as solvent the cell would last for up to 3 months but dioxin caused immediate collapse. This precluded the use of coumarin 152A dye whose peak gain occurs conveniently at 485 mm.

The length of the dye cell was found to be an important consideration. If the active region was too long (10mm) then it gave rise to a considerable degree of super-radiance. This occurred preferentially at the peak in the dye's gain curve. The effect was most noticeable for the dye coumarin 307 whose peak occurs at 500 nm. When this dye was used the super-radiance caused fluorescence of the I_2 beam giving typically a count of about 10Hz. With the dye lasing at 500nm the count rate was in excess of 10^6Hz. The ratio of these values, 10^5, explains why attempts to measure the intensity failed but also gives an indication of the sensitivity of the apparatus. Reduction of the cell length to 4mm and sharper focusing of the pump beam eliminated this signal almost completely while maintaining the laser power.

The dye laser beam profile was known to vary with the dye concentration (HAN72). Hansch managed to produce an almost circular beam cross section simply by adjustment of this concentration and varying the pump laser focusing system. Probably because of defects of the cell construction and very simple pump laser optics this procedure was not sufficient with our system. The addition of the pinhole (1mm) to the

dye laser configuration was necessary to improve the beam shape. This resulted in a slight loss of power but reduced the effective beam divergence.

A later improvement in the dye cell construction was to use anti-reflection coated windows. These were 2mm quartz plates coated on one side with two dielectric layers, 1.2um of MgF_2 over 0.1 um ZnS. This increased the output power and improved the beam profile by reducing spurious reflections.

Measurements carried out using a scanning Fabry-Perot etalon (HUT78) showed that the best line width attainable with the dye laser was 2.4Å. This was sufficient to resolve vibrational bands in many diatomics but would allow only the envelope of the rotational structure to be obtained. The introduction of an etalon (Spectra Physics 0411-6503 10GHz) into the laser cavity reduced the linewidth to approximately 1.5Å. This was measured using a Jobin-Yvon HRS2 monochromator (1200 lines/mm; resolution 0.3Å). The etalon reduced the bandwidth of the laser and improved the spectral line shape (fig 2.5) by removing the asymmetry of the original line. The optimum position of the etalon was found to be between the dye cell and the telescope.

While the grating could be scanned under control of the PDP11/45 computer, the etalon had to be scanned manually. The procedure adopted when changing wavelength was to move the grating to the correct position and then rotate the etalon to obtain maximum output power.

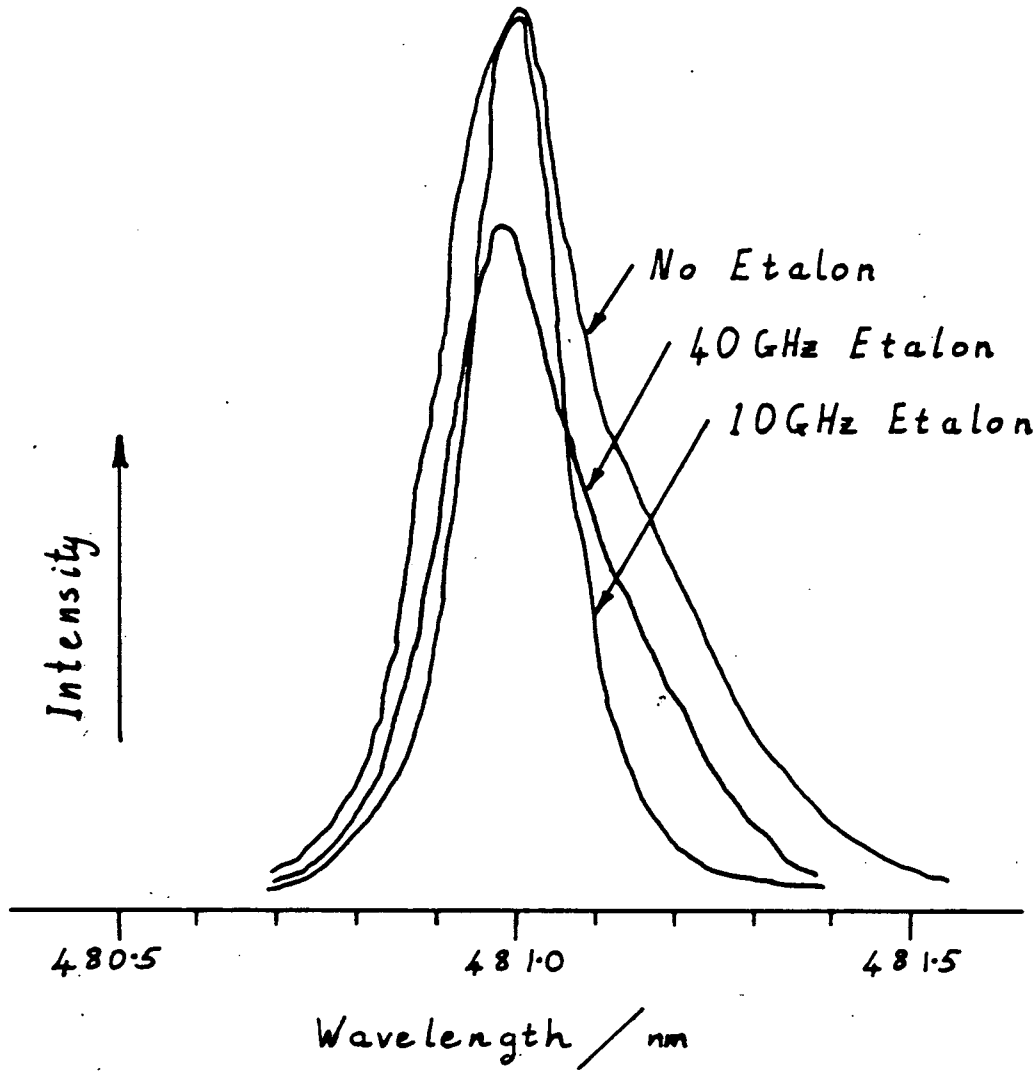

Figure 2.5 Dye laser bandwidth variation with etalon.

The divergance of the beam was too great to use without some correction. Using simple geometric optics the beam was shown to diverge from a point near the telescope. Two lenses were used to focus the beam at the tank centre (fig.2.6). They were chosen to produce a long narrow beam which would not scatter from the baffles. An aperture after the lenses removed any diffraction rings generated by the pinhole. Finally the beam was aligned with the tank by an adjustable periscope.

The resulting dye laser beam had a low divergance (1m rad) and a uniform diameter in the reaction zone. Dye laser parameters are summarised in table 2.1(a).

Bandwidth	1.3Å fwhm(i)
Pulse length	6ns fwhm
Output power	0.8KW/pulse(ii)
Repetition rate	100 Hz
Divergance	1 m Rad
Beam cross section	3.2 mm^2

Table 2.1a Dye laser parameters

(i) with 10GHz etalon (ii) measured at reaction zone; average power = 250 μW.

The laser dyes used cover the range 450nm - 500 nm. This allows several bands in the IF(X→B) spectrum to be studied. A slight gap did however exist at about 485nm due to the unfavourable properties of the Coumarin 152A/dioxin solution. The ranges of individual dyes were dependent on

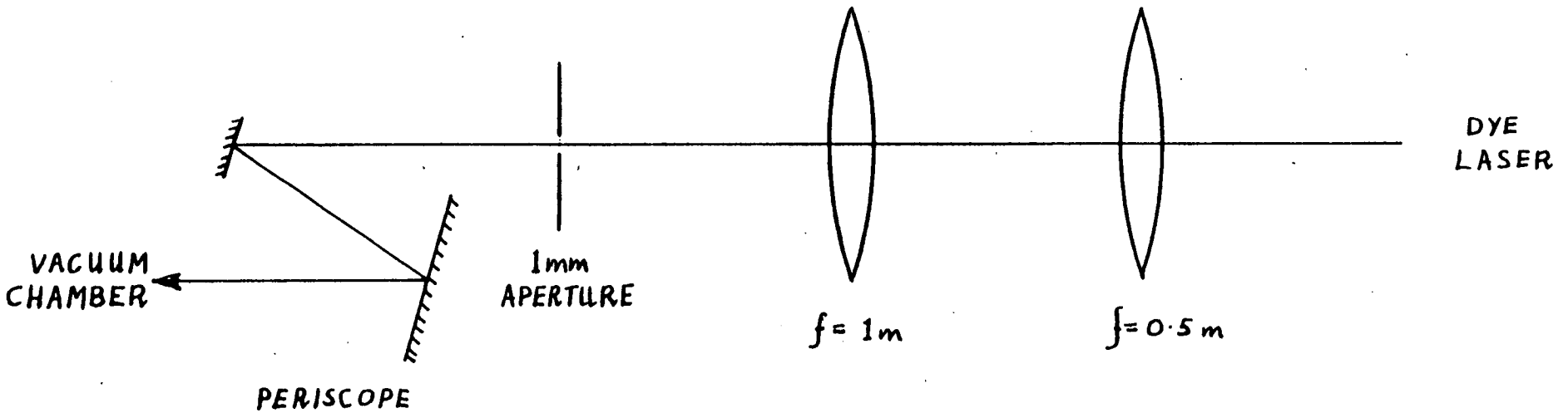

Figure 2.6 Collimating optics.

the adjustment of the dye laser and on the dye cell construction (GLE80). For a poor cell the maximum wavelength attainable for Coumarin 102 dye could be as low as 485 nm whereas for a good cell the range could extend to about 505 nm. Laser dyes used are listed in table 2.1(b).

Dye	Peak/nm	Range(i)/nm	Solvent	Concentration /M
Coumarin 47	460	450-475	Ethanol	5×10^{-3}
" 102	470	460-485	Ethanol	10^{-2}
" 152A	485	-	dioxan	10^{-2} (Rec)
" 307	500	485- 500	Ethanol	10^{-2}

Table 2.1b. Laser dyes suitable for the range 450-500nm

(i) Range of wavelength where the power is greater than $\frac{1}{2}$ peak.

2.23 Laser monitoring

The dye laser wavelength and intensity essential for normalisation, were measured after the beam left the tank (fig. 2.7). The wavelength was measured by diffusing the beam and using the monochromator. Measuring intensity however posed a problem. The average power as measured by the Laser Instrumentation Ltd. Power meter (154BT Mk.II) and 14BT thermopile was unreliable because the thermopile was very sensitive to the external environment. The method used was to reduce the intensity with interference filters and use a photomultiplier. The resulting pulsed output current was smoothed and averaged using a diode pump circuit (fig.2.8).

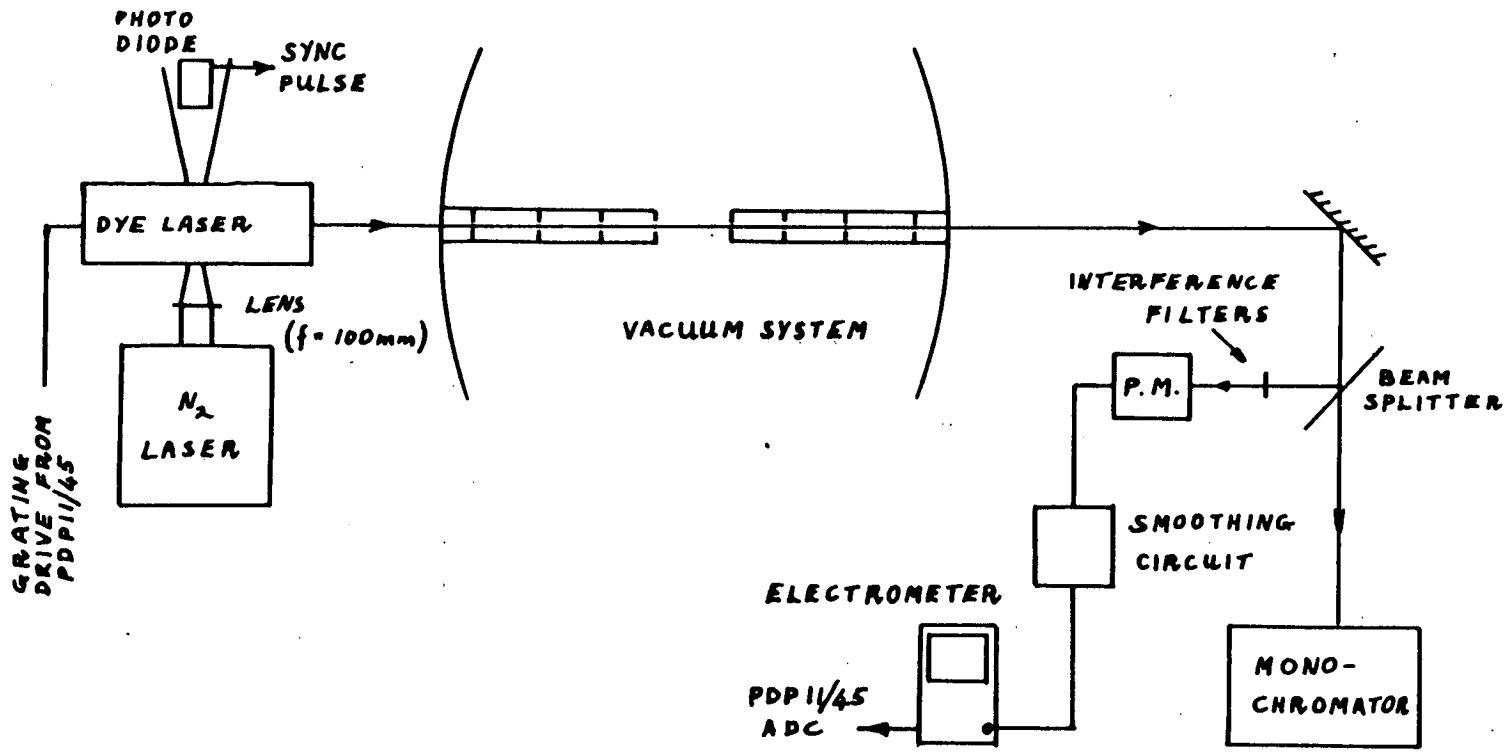

Figure 2.7 Schematic diagram of the laser monitoringsystem.

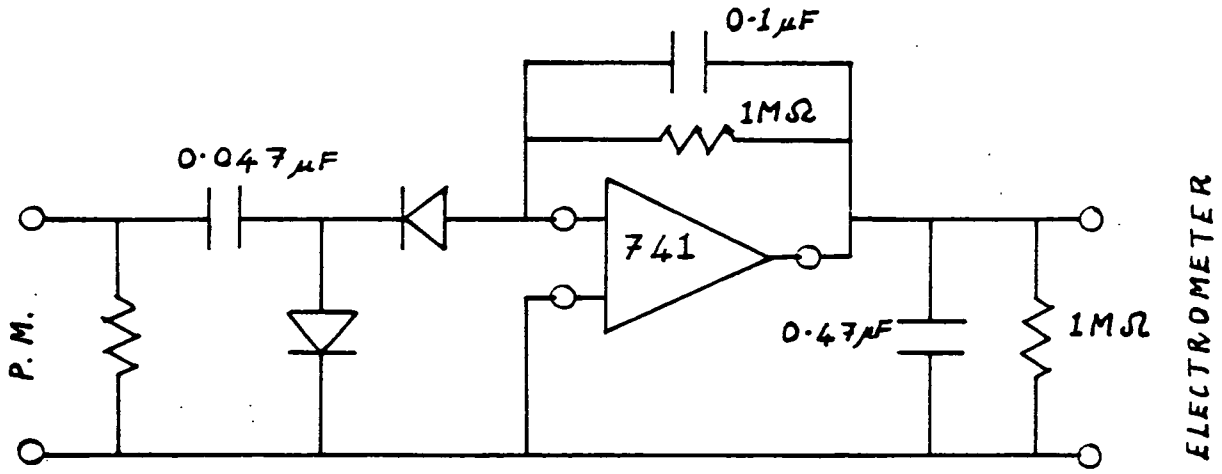

Figure 2.8. Photomultiplier output averaging circuit.

The output from this was measured by a Keithly electrometer (model 602) which was monitored by the PDP11/45 by its analogue to digital convertor.

A portion of the nitrogen laser beam was detected by a photo diode (ITTIL Type FD125) and this was used to initiate the counting system.

2.3 Molecular beam formation

2.3.1 Iodine beam.

The molecular Iodine beam was formed by a glass micro-capillary array of 10μm pore diameter, 1mm channel length and 75% transparency. The array was mounted on a stainless steel stem suspended from the differentially pumped chamber. The oven, also of stainless steel, pushed into the stem and a seal was effected with two Viton 'O'-rings (fig.2.9). The oven was sealed with a ptfe ring and had been vacuum tested to 10^{-5} Torr. The oven and stem could be heated separately so that the microcapillary array could be held at a slightly higher temperature to prevent blockage. The temperatures were monitored by two copper/constantan thermocouples.

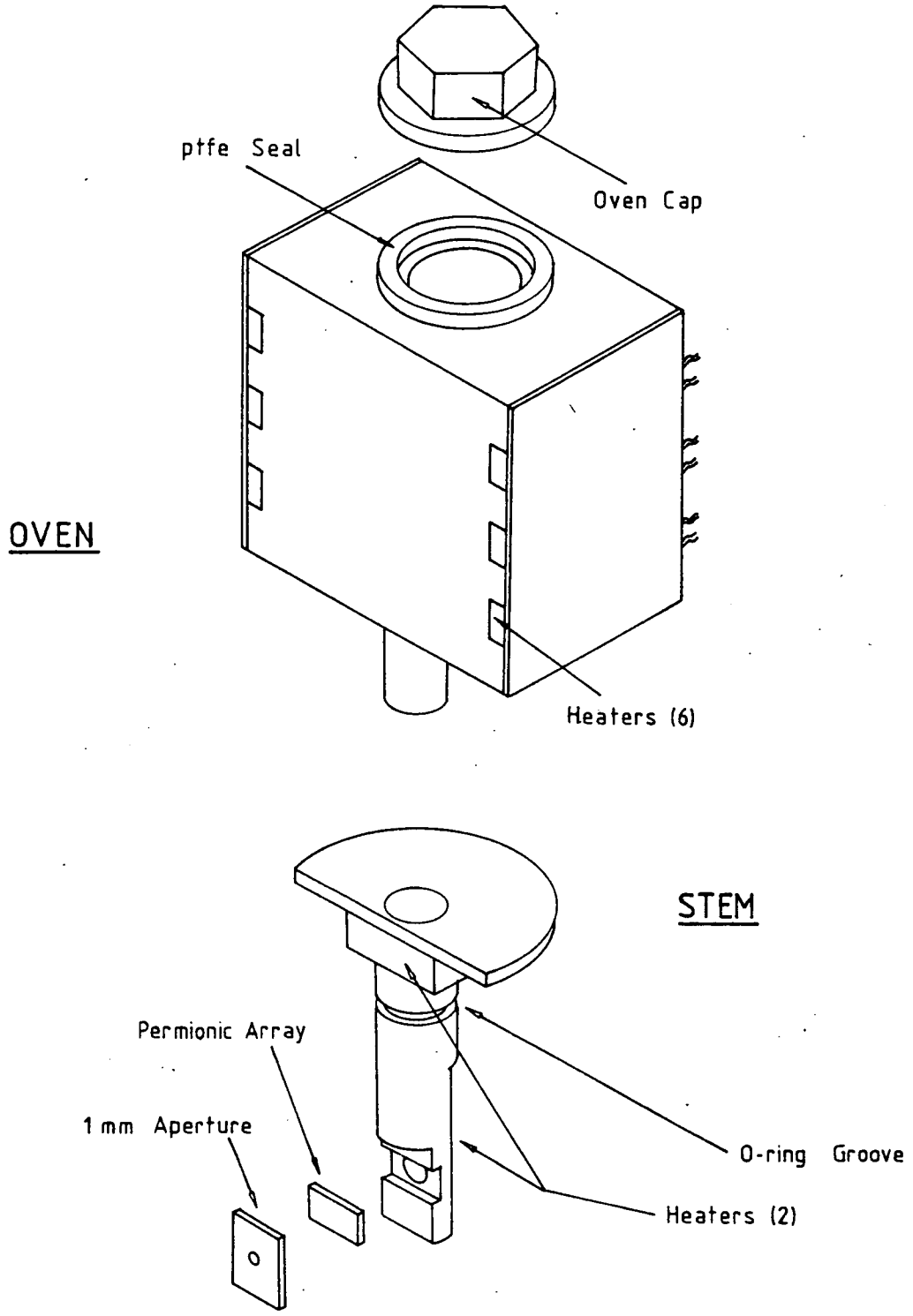

Figure 2·9 Iodine oven and stem.

This arrangement of a removable oven enabled the oven to be fitted last in the assembly of the experiment, leaving more space in which to work and reducing I_2 contamination of the apparatus.

The idea of the separate stem was that the cross beam reservoir was eventually to be situated outside the tank and connected by a heated glass pipe. The intention was that other gaseous reactants (e.g. CH_3I, Br_2) could then be used, extending the scope of the apparatus.

Although the stem was heated at two points, one above and below the DPC baseplate, a cold spot occassionally formed. This should be taken into account in any future design. However it was possible to produce a good I_2 beam by careful adjustment of the heater currents.

After leaving the reaction zone the I_2 beam impinged upon a copper reservoir filled with liquid nitrogen and was thereby removed from the vacuum system. The lowest pressure attainable with the I_2 beam running was less than 10^{-6} Torr but typically, running conditions were about 8×10^{-6} Torr.

2.3.2 Fluorine atom source.

The fluorine atom source was chosen to be a super-sonic nozzle beam source. The enhanced intensity of this type of source compared with an effusive beam (AND66) was necessary as only about 1% of the beam is atomic fluorine. Also, the improvements to directionality afforded by a glass permionic

array would have been more than offset by the attenuation in concentration due to the high reactivity of fluorine atoms with glass.

He/CF_4 mixtures were prepared at atmospheric pressure in a twenty litre reservoir, the composition being determined by the pressure ratio. The mixture was then bled through to a low pressure ballast volume (5 litres) via a needle valve. Beam stagnation pressures were measured by a Monitorr 162 pirani gauge (with He correction) or an oil monometer for pressures greater than 4 torr.

Chlorine and Bromine seeded in inert gases have been produced in a graphite oven at 2000K by dissociation of the parent molecules (VAL77). Fluorine, whose bond strength is much less, has been prepared by dissociation in a Nickel oven at the lower temperature of 1100K (PAR 72, FAR 75). Both ovens yielded better than 80% dissociation of the parent. The problem with this type of source is finding and machining suitably corrosion-resistant and thermally stable oven materials.

The alternative is to use a discharge through the parent gas. Miller and Patch (MIL69) first achieved an oxygen atom supersonic beam seeded in Helium buffer gas. The discharge was maintained by radio frequency excitation. Microwave excitation is often preferred over r.f. excitation due to stronger coupling to the discharge plasma, although Lee and co-workers have recently reported a supersonic $O(^3P)$ and $O(^1D)$ source formed by an r.f. discharge (SIB 80). Microwave discharges of SF_6, NF_3 and N_2F_4 in buffer gases have all been used to produce F atoms (FOO75) but CF_4/He and F_2/Ar mixture give very good results.

F_2/Ar mixtures can under favourable conditions form 100% dissociation products (FOO 75) but require special handling. When CF_4 is used, as in this study, other species will be present apart from $F^{\cdot}$. The principal contaminants are F_2, F^-, CF_2 and CF_3 whose concentrations vary with discharge power (POL 72). The effects of F^- and its recombination rate are unknown but are not thought to be important. CF_3 radicals react rapidly forming C_2F_6 ($K = 3 - 5.3 \times 10^{12} cm^3 mole^{-1} s^{-1}$; HIA72, BAS71) although CF_4 will also be reformed. CF_2 is relatively long lived but is also relatively inert. Any CF_3I formed will not be detected by the fluorescence technique as the lowest electronic transitions are in the u.v. (HER 51).

Many atom beams require for technical simplicity that the atom source and the reaction zone be separated by a considerable distance, e.g. RAD 75, STE 80. This involves a flow tube and for fluorine a reduction in atom concentration due to recombinations in the gas and, more critically, on the walls. This depletion can be severe, demanding low gas pressures and hence leading to loss of intensity. Attempts to reduce wall recombination with surface coatings have been successful to varying degrees. Phosphoric acid (POL 72) and boric acid (FOO 75) have both been recommended but teflon (BER 62) is generally regarded as the best (KOL 72). Homogeneous fluorine atom recombination is a 3 body process with a small rate constant ($K = 8 \pm 5 \times 10^{14}$ cm^6 $mole^{-2} s^{-1}$: FOO 75) which only becomes important for long flow tubes.

The F atom source described by Glen (GLE 80) and used to obtain preliminary results on the $F + I_2 \rightarrow IF + I$ vibrational specificity (DON 80) used a teflon dispersion to coat the flow system. (Du Pont FEP 856-200 in wetting agent Du Pont VM - 5336). To further reduce the F atom attenuation the nozzle diameter was increased to 1 mm. This increased the axial flow rate but forced a reduction in stagnation pressure in the source to about 1 torr.

A more productive beam could be formed if the source were situated directly over the nozzle as in Lee's r.f. source (SIB 80). Recently Gorry and Grice have constructed such a microwave source for an atomic oxygen super-sonic beam (GOR 80). Both groups report greatly increased atom beam fluxes over conventional sources i.e. $> 10^{18}$ atoms $s^{-1}s^{-1}$ and about 5×10^{17} atom $s^{-1}s^{-1}$ respectively.

For the studies reported here a fluorine atom source has been constructed which is similar in design to Gorry and Grice's oxygen source.

The microwave cavity was based on the design of Fehsenfeld et al. (FEH 65) and was similar to the EMS 214L cavity used previously. It was constructed of brass. The coupling scheme was identical to the commercial cavity and was simpler to use than that of GOR 80. It was cooled by water circulating in a jacket around its bulk (fig 2.10).

The impedance of the cavity was adjusted externally using a sealed bulb of gas and varied little with pressure. To permit fine tuning for different gas pressures and mixtures

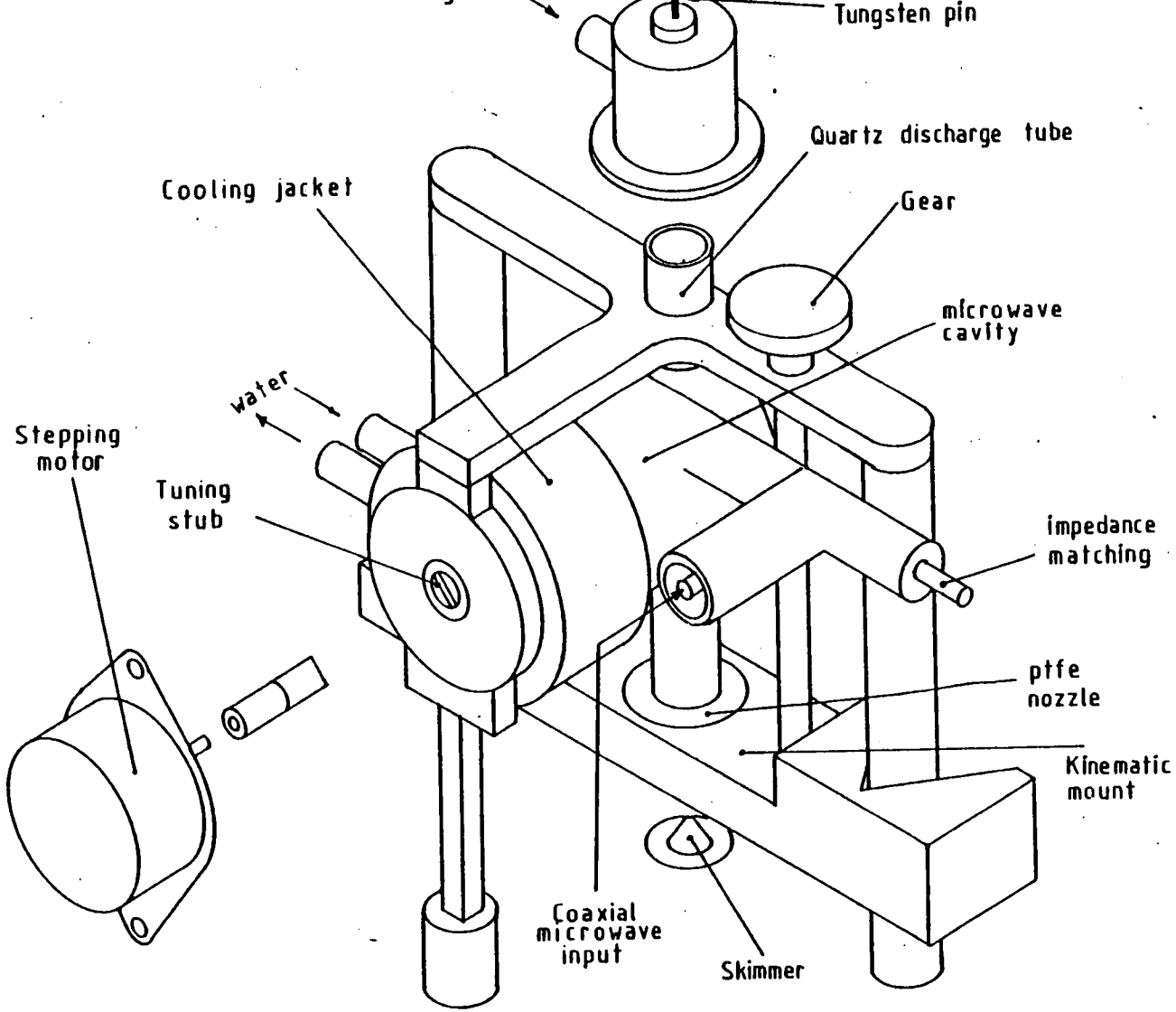

Figure 2.10 Fluorine atom source.

the tuning stub was adjusted in situ by a stepping motor.

The impedance matching gave very small reflected powers under favourable conditions, two watts or less, for incident powers of about 80W. No problems of damaged cables were encountered for these low powers.

The gas was supplied to the quartz discharge tube (13 mm o.d., 1 mm wall) via a stainless steel cap. The nozzle was immediately beneath the discharge region and the whole arrangement was sealed with four Viton 'O' rings. It was intended that the nozzle be mounted on a kinematic carriage. This was to allow optimisation of the nozzle-skimmer distance. The carriage, mounted on ptfe linear bearings was driven by a second stepping motor with a 90:1 gear reduction. Unfortunately, under the vacuum and temperature conditions the ptfe distorted sufficiently to cause the carriage to twist out of alignment with the skimmer. A later design which would not distort was built, but the nozzle skimmer distance could only be adjusted manually.

The nozzle itself was machined from ptfe rod. Its orifice was as small as could be reliably reproduced (0.3 mm) and its internal angle was 45°. As already mentioned teflon was not the best material for this environment but it was the only one which could be machined to such a delicate design. Metals being discounted, machinable glass and some ceramics were tried unsuccessfully.

The skimmer was constructed of stainless steel and had

a diameter of 0.5 mm. It had an internal angle of 25^{o} and external angle of 35^{o}. The skimmer to reaction zone distance was approximately 25 mm.

The stainless steel cap, as well as introducing the gas mixture, also housed a mechanism for initiating the discharge. (The vacuum system would not cope with a beam pressure high enough for the discharge to be self starting). To preionise the gas mixture a high voltage was applied to a tungsten pin mounted in a ceramic insulator in this stainless steel cap.

This pulse was supplied by a conventional tesla coil with the high step-up transformer mounted inside the vacuum system. This permitted ordinary high voltage feed-throughs to be employed without any arcing problems. Very little evidence of corrosion outside the discharge cavity indicated that the plasma was well confined, not extending through the nozzle as it can do (SIB 80).

The effective pumping speed of the DPC in the region of the source was calculated to be 490 ls^{-1} (conductance for the system was 750ls^{-1}, pump speed is 1400ls^{-1}). This allowed an upper limit on the flux through the nozzle to be set. The maximum pressure allowed was chosen as 10^{-3} torr since pressures above this would overload the pump, reduce its efficiency and interact with the atom beam. This set the maximum flow rate, $\dot{N}$, at $\dot{N} = 1.5 \times 10^{19}$ molecules S^{-1}.

The flow rate through the nozzle is

$$\dot{N} = n_o \; A \; \bar{v}_o \qquad 2.1$$

where n_o is the number density in the source, $\bar{v}_o$ is the mean velocity in the source and A is the orifice area. The gas mixture was largely Helium for which $\bar{v}_o = 10^3 ms^{-1}$. With a nozzle diameter of 0.3 mm the maximum source-pressure was 13 m bar. This agreed fairly well with the maximum running pressure measured of 15 m bar. This was much less than the pressures used by Gorry and Grice (260 m bar) and Lee (525 m bar). This of course limited the atom flux but also impaired the degree of dissociation.

The behaviour of the nozzle source was tested by observing the laser induced fluorescence from an NO_2/N_2 mixture. The resulting laser-induced fluorescence is shown in fig.2.11. The absolute values of the fluorescence were quite small as NO_2 emits preferentially in the red, where the photomultiplier had little sensitivity, and the radiative lifetime is very long (44 μs) (HER 51). The graph does however show the transition from effusive to supersonic flow, which occured at around 8 m bar.

2.3.3 Estimation of signal strength

2.3.3.1 Iodine beam intensity

The flow rate $\dot{N}$ of a gas with average molecular velocity $\bar{v}_o$ and source density n_o through a tube is given by

$$\dot{N} = \frac{2\pi}{3} \cdot \frac{a^3 \, n_o \, \bar{v}_o}{l} \qquad 2.2$$

where a is the tube radius and l the channel length. For a

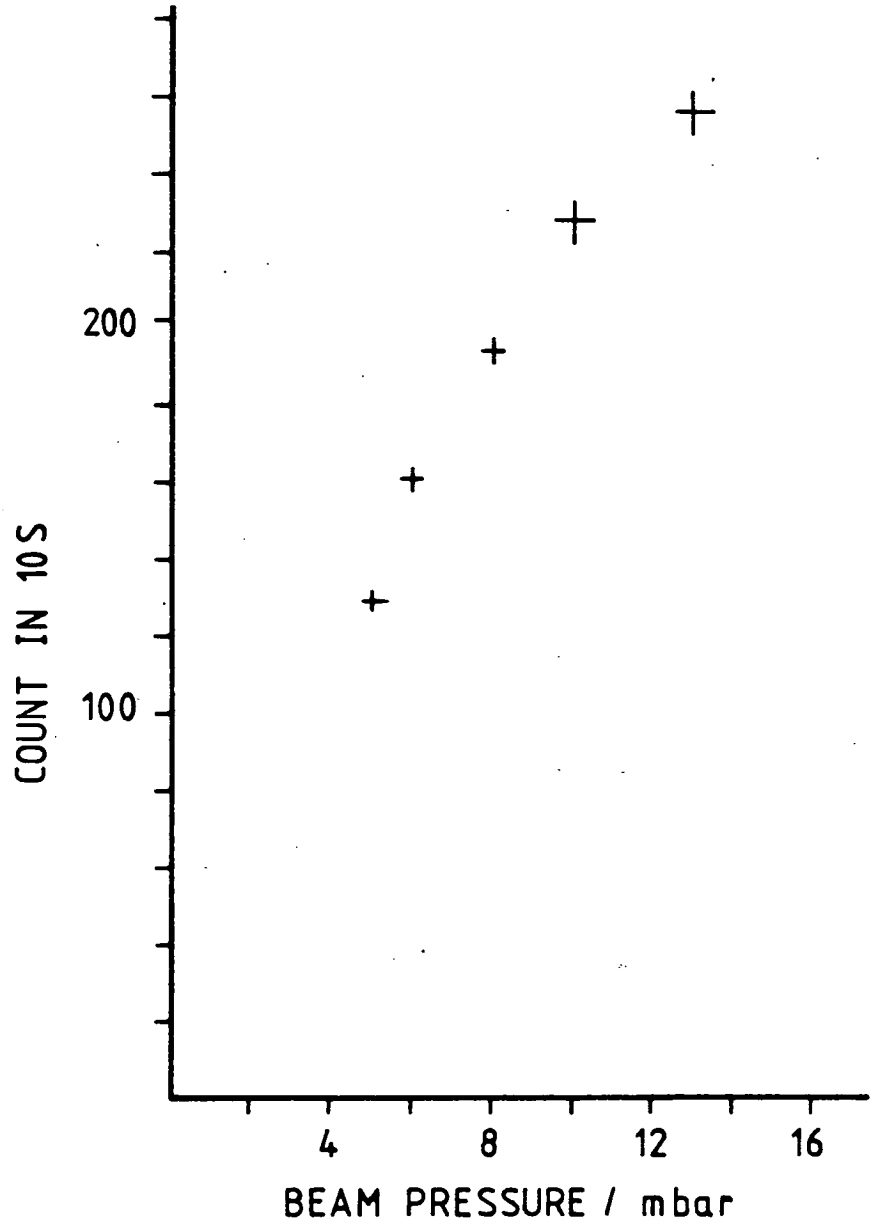

Figure 2.11 Laser induced fluorescence signal from NO_2 beam, variation with beam pressure. The transition from effusive to supersonic flow occurs at around 8 mbar.

single opaque tube, i.e. one whose length is greater than the mean free path in the source (λo), the forward intensity is given by (GIO 60)

$$I_1(o) = \frac{1}{8\sigma}\left(\frac{3\,\bar{v}_o\,\dot{N}\,a}{\sqrt{2}\,\pi}\right)^{\frac{1}{2}} \qquad 2.3$$

where σ = molecular diameter. For an array of m tubes the forward intensity becomes $Im\,(o) = m.I_1(o)$. m is calculated from

$$m = \frac{A\,\epsilon}{\pi a^2} \qquad 2.4$$

where A is the area of the array and ϵ is its transparency (75%). The angular half width at half maximum, $\Delta\theta_{\frac{1}{2}}$, for a single channel is calculated as (GIO 60)

$$\Delta\theta_{\frac{1}{2}} = \frac{\sigma}{1.78}\left(\frac{8^{\frac{1}{2}}\,3\,\dot{N}}{\bar{v}_o\,a}\right)^{\frac{1}{2}} \qquad 2.5$$

Empirically, however, these values must be corrected to account for interactions between tubes. The flow rate must be reduced by a factor of $\frac{2}{3}$ while $\Delta\theta_{\frac{1}{2}}$ increases by a factor of two (JOH 66).

Typical oven temperatures used were 60 - 70°C. This is equivalent to a vapour pressure of 7 - 13 mBar. Taking 10 m Bar as an average and an orifice diameter of 1 mm, the following values were obtained from equations 2.2 - 2.5.

$$\dot{N} = 7.2 \times 10^{12}\ s^{-1}$$

$$I_m\,(o) = 8.7 \times 10^{16}\ sr^{-1}\ s^{-1}$$

$$\Delta\theta_{\frac{1}{2}} = 38^{o}$$

The collision diameter for I_2 is assumed to be 6.5Å. The total flow rate ($\dot{mN}$) was 5.4×10^{16} s^{-1} which was more than adequately handled by the diffusion pumps.

2.3.3.2 Fluorine atom beam intensity.

The limit on the source pressure was set by equation 2.1 and the pumping capacity of the DPC. This set the maximum flow rate $\dot{N} \leqslant 1.5 \times 10^{19}\ s^{-1}$. The estimate for the F atom intensity given here is based on the arguments of Anderson and Fenn (AND 65) and only a resume of the calculation is offered.

The mean free path λ_o of F atoms in the source is to a good approximation that of He 10^{-2} mm at 10 Bar. This is less than the nozzle diameter d_o (0.3 mm) and will give a Knudsen number $K_n = \lambda_o/d_o$ less than unity, indicating non-molecular flow conditions. From this the terminal Mach number is given by

$$M_T = 2.05 \left(\frac{\epsilon}{K_n}\right)^{0.4} \qquad 2.6$$

The parameter ϵ, less than one, describes the efficiency of translational energy transfer in the fluid. This gives $M_T \simeq 8$. This is not as high as could be hoped; however Anderson and Fenn have found sources with such low Mach numbers work quite well (AND 65).

For a nozzle to skimmer distance l_s = 5 mm the atom density at the skimmer is calculated from

$$n_s = 0.157\ n_o \left(\frac{l_s}{d_o}\right)^{-2} \qquad \text{if } \frac{l_s}{d_o} > 4 \qquad 2.7$$

The flux through the skimmer, F_s, can be calculated from this and hence the forward intensity

$$I\ (o) = F_s\ l_s^2 \qquad 2.8$$

Taking a value for the degree of dissociation of 10% and a mixing ratio of CH_4/He of 10% the density of F atoms is estimated to be 1% of the total gas mixture. The forward intensity is then found to be I (o) = 6.0 x 10^{16} atoms sr^{-1} s^{-1}.

This is an order of magnitude less than that measured by Gorry and Grice for their oxygen atom source (d_o = 0.3 mm). They measure the degree of dissociation of O_2 molecules to be 35% and it would probably be larger for fluorine because of its low recombination rate. Even greater intensities could therefore be predicted for an F atom source showing the desirability of high differential pumping speeds.

2.3.3.3. Signal strength.

The estimation of the laser induced signal parallels that of Glen (GLE 80) using the revised estimates of beam intensities and the data from table 2.1. Details are given in the appendix.

The estimated count rate for the laser frequency λ_l close to the band head was determined to be

$$S\ (\lambda_l) = 5.9 \times 10^3\ p\ (v'')\ q_{v',v''} \quad s^{-1}$$

where $q_{v',v''}$ is the Franck - Condon factor for the transition, p(v") the relative population of the lower vibrational level. For wavelengths less than 500 nm the maximum Franck-Condon factor is 0.133 (for the (5,0) band : CLY 76) and, assuming 10% of the total population was in the v" = 0 state, the

expected count rate was of the order of 75 Hz. Due to the many approximations used this figure was likely to be an overestimate therefore low count rates are expected.

2.4 Noise reduction

Light scattered from the dye laser beam was a problem on two accounts. The instantaneous light pulse could be quite large, overloading the photomultiplier. It also caused after-pulsing in the photomultiplier. Directly scattered light could be reduced by careful collimation of the beam combined with extensive baffling.

2.4.1 Baffles.

The collimation of the laser beam prior to entering the vacuum system has already been described (section 2.2.2). The baffle arms were each over 500 mm long, with two sets of baffle apertures (fig 2.12). There was a number (5) of 10mm aperture secondary baffles along the length of the tube. The primary sets of baffles screwed directly on to the ends of the arms near the reaction zone. The design for these was loosely based on that of Pruett and Zare (PRU 76) although it was found that the actual arrangement of the apertures could only be settled by trial and error. The baffle arms could be aligned by means of three supporting screws in conjunction with the bellows.

2.4.2 Optics.

An optical system (fig. 2.13) consisting of two aspheric

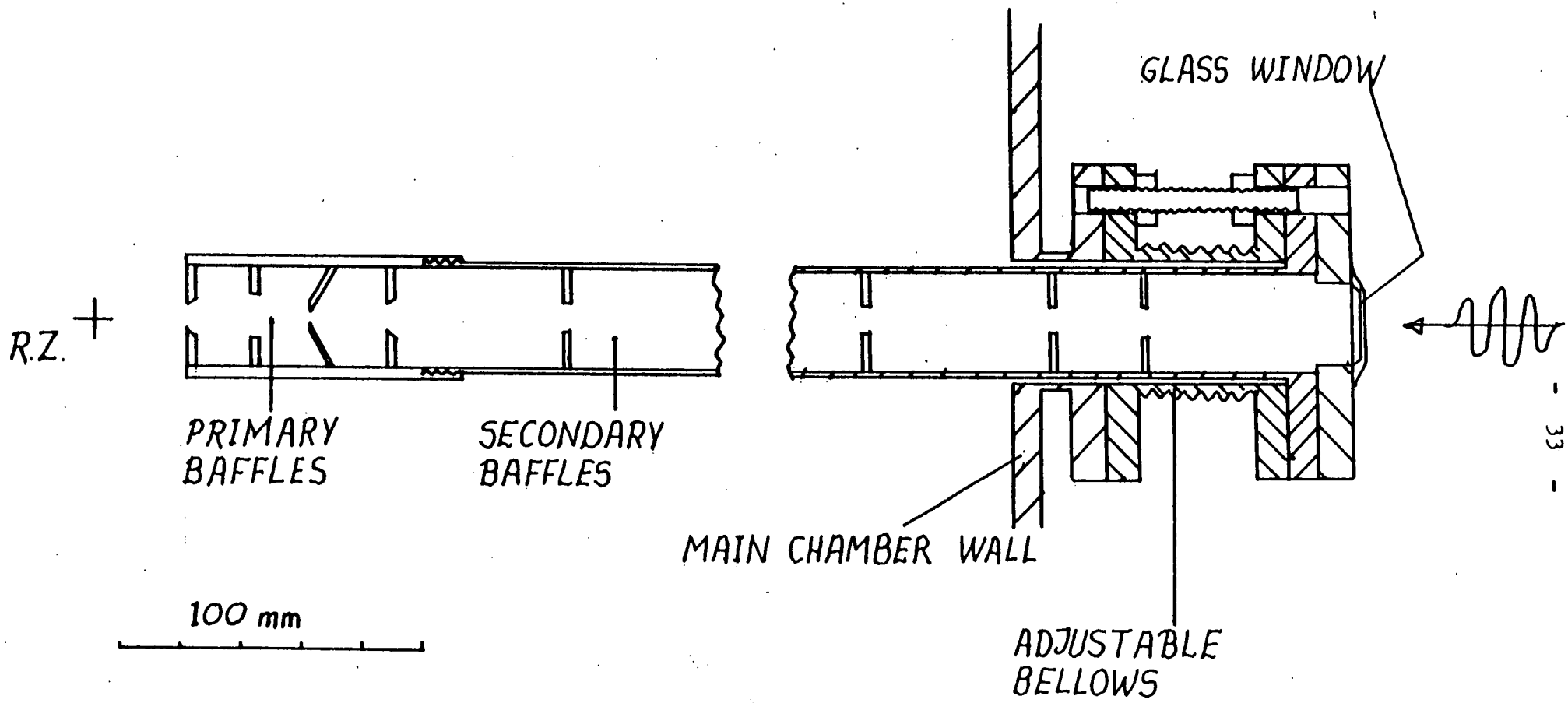

Figure 2.12 Baffle arms used to eliminate stray light from the reaction zone.

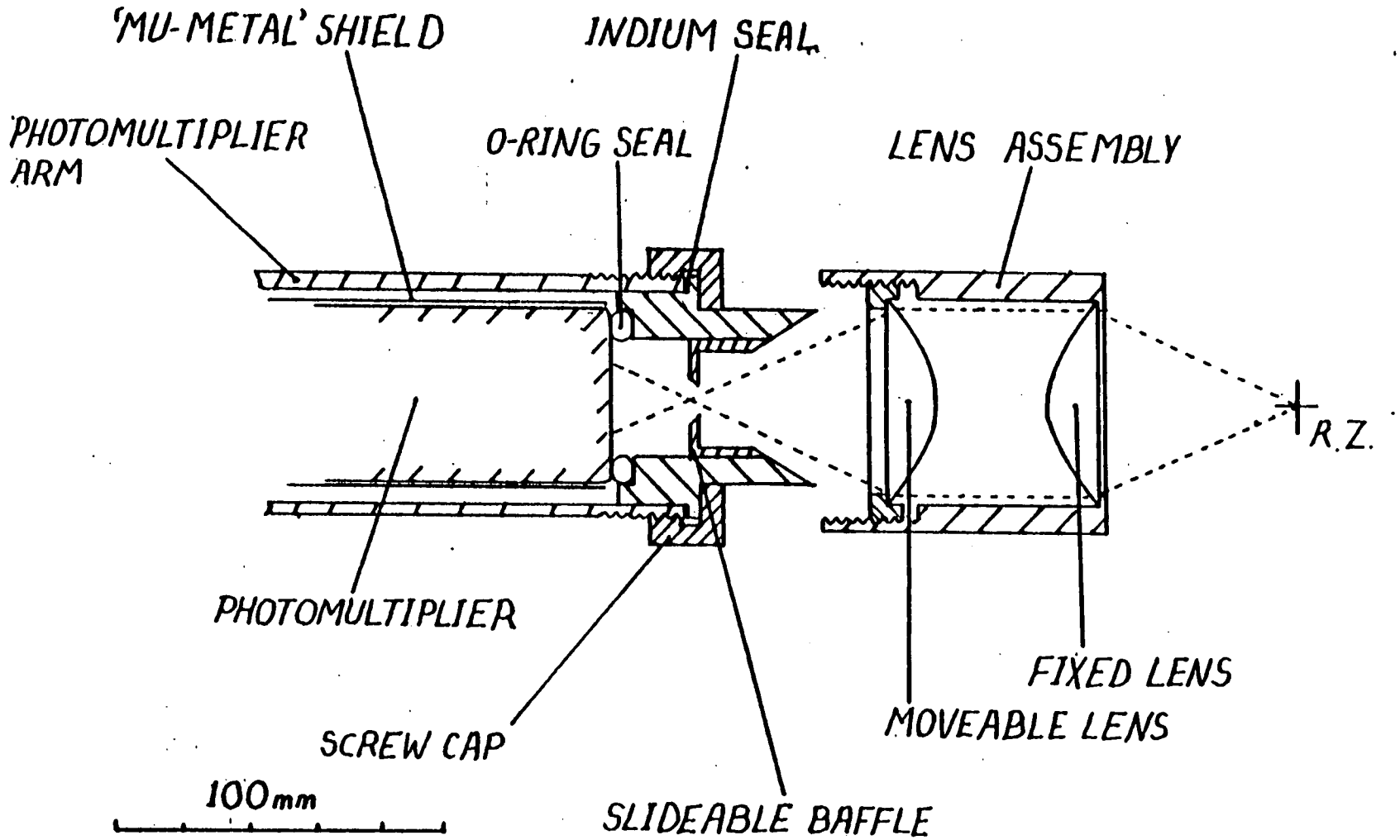

Fig. 2.13 Fluorescence collection optics

lenses (30 mm dia., 25 mm focal length) focused the fluorescence through an aperture (2mm) on to the photomultiplier. This arrangement enabled the p.m. to collect over a wide solid angle centred on the reaction zone while rejecting light from most other sources. With this arrangement the directly scattered light could be reduced to a few photons per pulse. Typically 10 photons per pulse, though with exceptional alignment as few as 2 or 3 per pulse, could be obtained. (This was measured using the pm and a Tektronix 7904 oscilloscope. The number of photons in a scattered light pulse was taken to be the ratio of pulse height to that of a single photon pulse.) The noise level although high compared with the signal could be completely overcome by the gating electronics described below. What could not be eliminated was the afterpulse induced by this scattered light, which arrived some 2 to 4 us afterwards.

2.4.3 Afterpulsing.

Afterpulsing is an effect which arises from the construction of the p.m. tube. The relatively large photocurrent induced by the scattered light ionises some of the residual gas in the p.m. The ions are accelerated towards and impinge on the photocathode, releasing secondary electrons (typically 4). The ions large mass compared with that of the electron means that the impact occurs, dependent on the p.m. construction, up to 10 us after the inducing photocurrent. These correlated p.m. pulses occurred in the

temporal region of interest (lifetime of IF ($B^3\Pi_{0+}$) = 7 μs: CLY 74) and therefore cannot be discriminated against. The only possibility was to reduce the probability of afterpulsing. As this was a function of the p.m. itself, a tube selected by EMI (9824A) for low afterpulsing was purchased. (A 50mm tube would have been better but the geometry of the experiment would not allow this.)

Figure 2.14 shows the afterpulse behaviour of two p.m.s. A measure of the probability of one photoelectron inducing an afterpulse is obtained by integrating the area under that part of the curve above the random background. Figure 2.14 (a) was the trace obtained from the original p.m. tube while 2.14(b) was the low afterpulsing tube operated at the same gain, 5×10^6.

2.4.4 Discharge noise.

Because of the proximity of the discharge to the data collection optics, light from the discharge contributed a significant proportion of the noise level. This therefore required that the light from the discharge could not illuminate any surface that the p.m. could 'see'.

Light from the discharge passed through the nozzle and skimmer apertures and was thereby collimated to a degree. The F atom beam dump was a convenient dump for the discharge light and was used as such. A baffle eliminated any light striking the optics and as many surfaces as possible were painted black. It was difficult to apply any other measures to the problem as they would interfere with the atom beam itself.

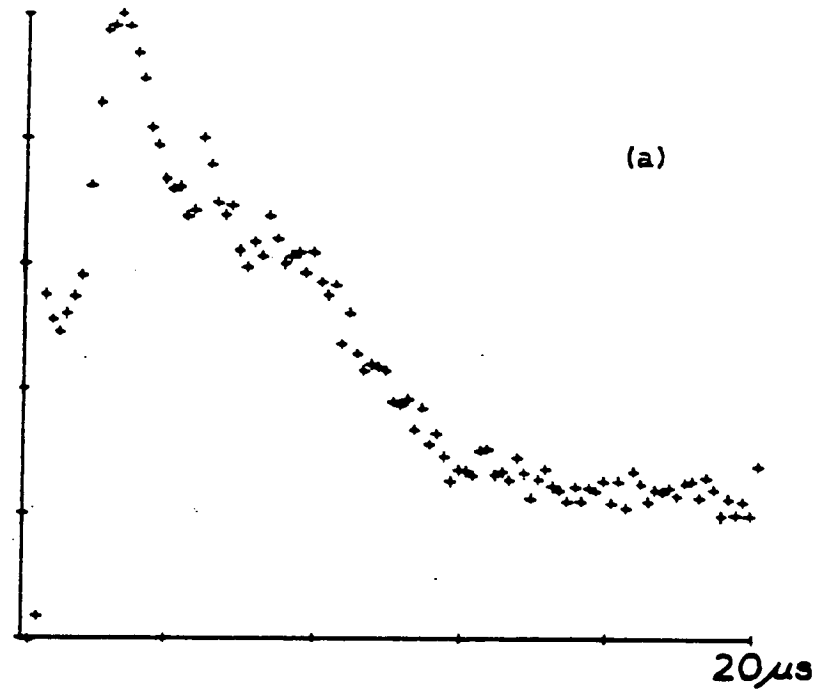

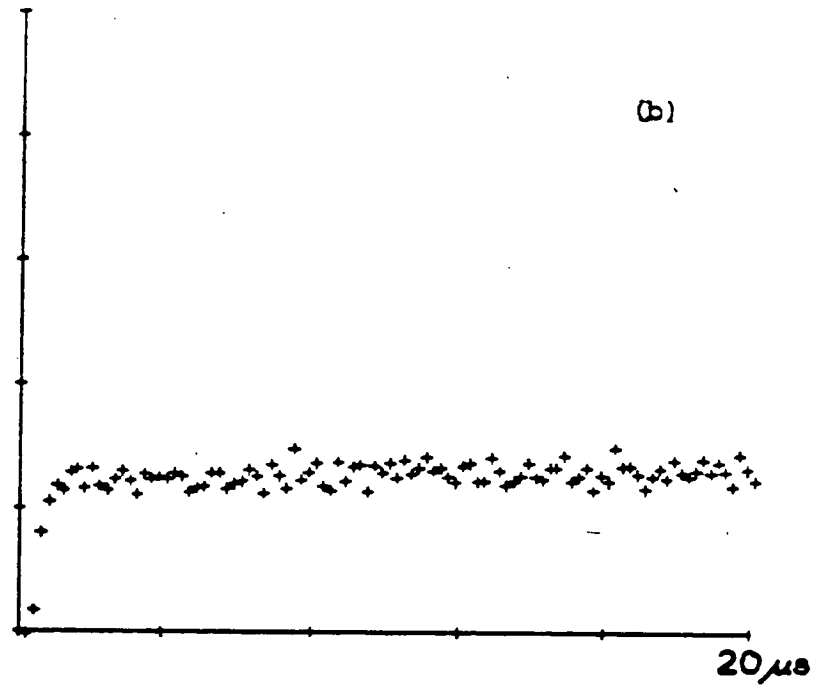

Fig 2.14 **Afterpulse distributions for two photomultipliers**

There seemed to be a limit to this aspect of noise reduction and it was noticed that the noise varied dramatically with atom beam pressure. Increasing the pressure would reduce the noise significantly. e.g.

Pressure	Noise rate
4 m Bar	11,400 Hz
11 m Bar	40 Hz

As the noise rate also varied with CF_4/He ratio it was concluded that metastable species were being swept along in the beam. As the atom beam was run at its maximum pressure throughout, the noise was conveniently minimised. It is probable that inview of high pressures attainable in the atom source described by Gorry and Grice it would not suffer unduly from this particular noise problem. Lee's source on the other hand, would probably give a poor S/N ratio in a laser induced fluorescence experiment as the plasma extended through the nozzle.

When the I_2 source was run alongside the atom beam the discharge noise apparently increased. No absolute measurements were obtained for this but it is thought that the increase was due to emission from the discharge causing the I_2 to fluoresce.

2.5 Data Collection

The aim of the data collection was to extract the fluorescence signal from the measured count with a maximum signal to noise ratio. This required that the noise contributions be reduced (see above), isolated and measured.

2.5.1 Noise classification.

There were three principal types of noise contributing to the overall background signal:

(1) Ambient light entering the tank.

(2) Light scattered out of the laser beam.

(3) Light from the discharge.

Dark noise from the p.m. could be treated as type (1) noise but it was sufficiently small to be ignored.

The three noise types were present simultaneously only when the signal, if any, was also present. If there had been a constant noise level and the signal was much stronger, then the noise would have manifested itself merely as a non-zero base line to the spectrum. However as the signal was small it was easily lost in the random fluctuations of the background. Also, as the laser intensity varied with wavelength, so part of the noise varies across the spectrum. The different noise types therefore had to be measured independantly for an accurate estimate of the signal.

Type (1) noise was completely random giving a constant background. This contribution was the least important as it could be almost completely eliminated by the electronics.

Type (2) noise was correlated with the laser intensity and had a time constant short compared with the laser period (10 ms). Directly scattered light arrived instantly and must not be collected. The resulting afterpulsing cannot be discriminated against and must be subtracted out. This

required counting with no product fluorescence present, that is with the discharge off. Noise arising from laser induced fluorescence of other species (e.g. I_2) could be treated similarly.

Type (3) noise was correlated with the discharge. This covered light scattered directly from the discharge, emission from metastable species and I_2 fluorescence caused by emission from the discharge. Chemiluminescence from the reaction of $F_2 + I_2$ has been reported (BIR 75). This has been attributed to the concerted reaction (KAH 80).

$$F_2 + I_2 \rightarrow F + I_2F \rightarrow IF + IF^*$$

Chemiluminescence has also been reported in a parallel molecular beam study of the $F + I_2$ system (TRI 81). This was reported as being very weak and was explained by secondary encounters of F atoms with a trihalogen complex. Any chemiluminescence involving F atoms or F_2 molecules will be type (3) noise, would only be present when the discharge was running and, would be independant of laser intesity.

2.5.2 Electronics.

The output from the p.m. was immediately amplified (fig. 2.15) by a unity gain preamplifier, Keithly model 111A, response time 3 ns. This acted mainly as an impedance matching device and gave a tenfold increase in the voltage output. Further amplification was still required and a 4 ns pulse amplifier, Hewlett Packard model 462A, was used. This gave a single photon pulse height of 50 mV. With a

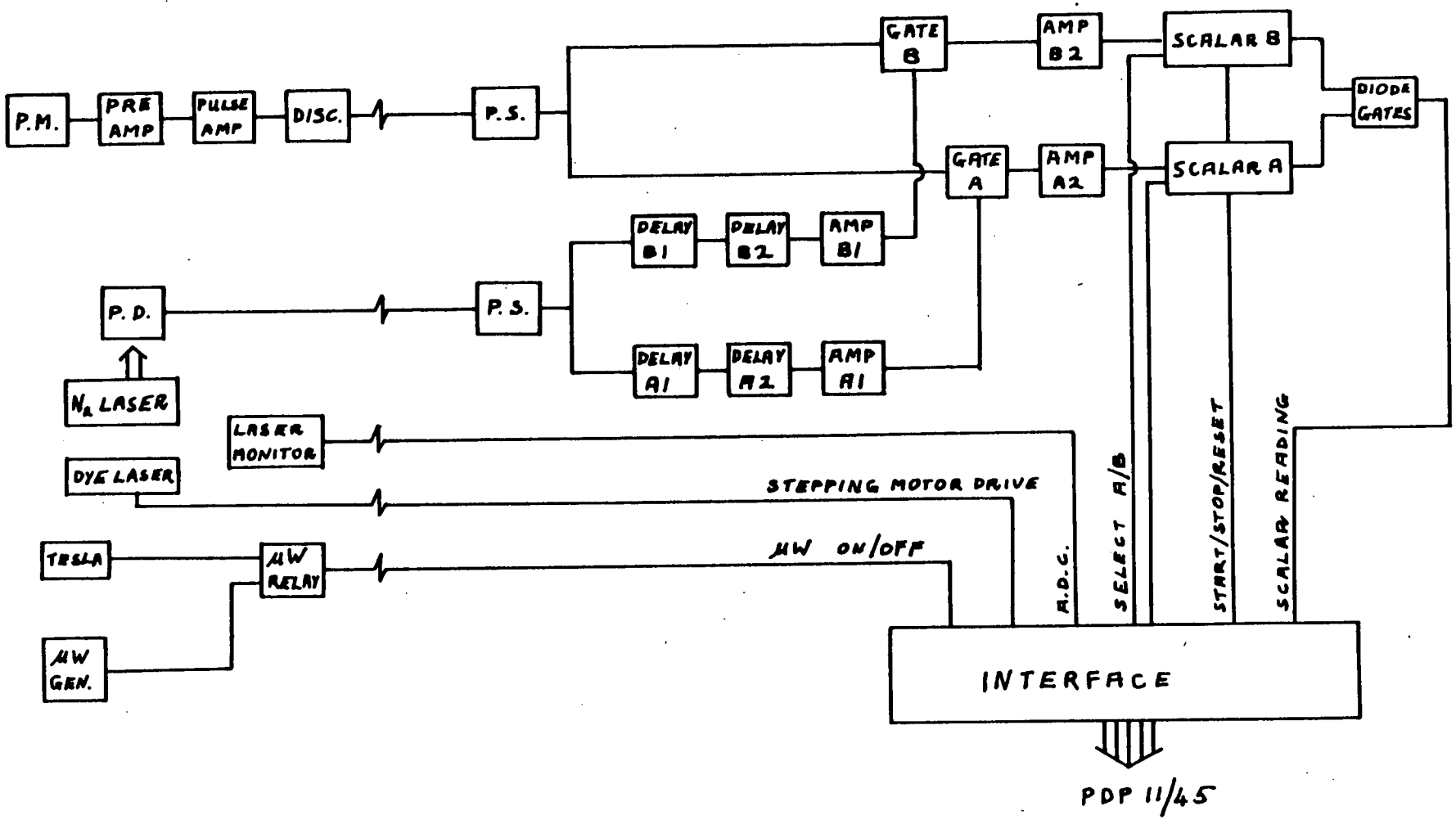

Figure 2.15 Block diagram of the data collection system.

discriminator threshold of 40 mV to limit the noise, the resulting digitised output was sent to the counting system. To further reduce noise all leads up to the discriminator were maintained as short as possible and all components were well shielded.

As the laser repetition rate 100Hz and the lifetime of IF is about 7 μs more than 9.9 ms of the counting period was redundant. A system of delays and gates (fig.2.15) allowed signal to be collected for only a short period after the laser pulse.

The signal from the discriminator was shaped and sent to two gates, A and B. A photodiode detected the N_2 laser pulse, which was shaped and initiated the count period. Delay A1 (0.5 μs) prevented the collection of scattered laser light while delay A_2 set the time that the gate remained open (10 μs). The amplifier inverted and shaped the delay pulse to drive the gate.

A similar arrangement of delays permitted one of the noise components to be counted. By setting delay B1 to 1.5 ms, which was much greater than the fluorescence life-time, scalar B registers the signal when the laser is not present.

These gated signals were counted by separate scalers. Five diode gates (fig.2.16) allowed a selected scaler to be interogated by the PDP 11/45.

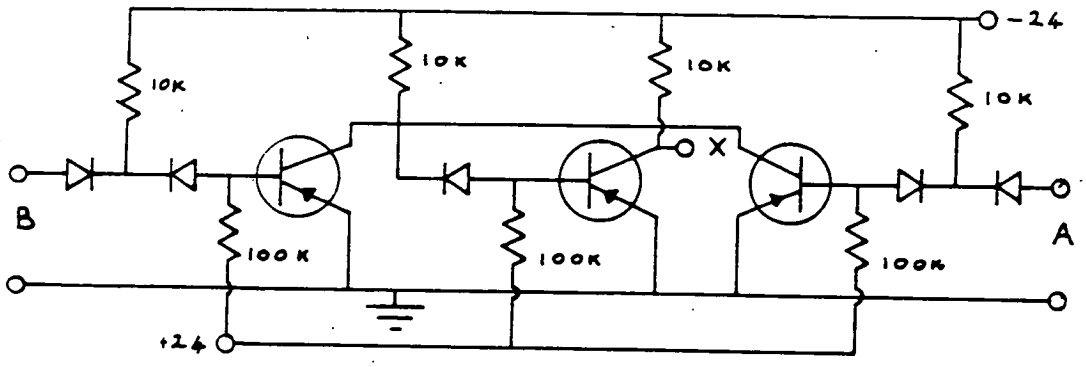

Figure 2.16 Circuit diagram for the diode gates used to read scalers A and B.

2.5.3 Computer Control.

As there are 3 noise types collected along with the fluorescence signal, ϕ, four measurements were required to extract that signal. From the total count, S_3, must be subtracted the total noise count.

S_3 was the count recorded by scaler A with the laser on and the atom source running. Simultaneously the count, S_2, in scaler B recorded the signal between laser pulses.

S_2 was the sum of noise types (1) and (3). The experiment collected for a short period (usually 10 s) in this mode, then the discharge was switched off. The experiment then collected for the same length of time with only the laser running. The count, S_1, of scaler A then recorded types (1) and (2) noise while scaler B recorded the ambient background, S_0. This procedure constituted a collection cycle.

The signal was given by the relationship

$$\phi' = S_3 - \delta S_2 - S_1 + \delta S_0 \qquad 2.9$$

where δ was the ratio of delays $A_2 : B_2$, i.e. the ratio of the duty factors. During each half of the collection cycle the laser intensity was monitored and averaged. This gave intensity values P_1 with discharge on and P_0 with discharge off. This allowed the signal to be determined with long term fluctuations in the laser intensity accounted for. The normalised signal was then given by

$$\phi = (S_3 - \delta S_2) / P_1 - (S_1 - \delta S_0) / P_0 \qquad 2.10$$

The collection cycle was repeated N_{co} times and constituted a block of data. The average signal from a data block was given by

$$\bar{\phi} = \frac{1}{N_{co}} \sum_{i=1}^{N_{co}} [(S_{3i} - \gamma S_{2i})/P_{1i} - (S_{1i} - \gamma S_{0i})/P_{0i}] \qquad 2.11$$

The standard error was calculated from the standard deviations of the individual counts, i.e.

$$\epsilon = \frac{1}{\sqrt{N_{co}}} \left(\frac{(\sigma_3^2 + \gamma\sigma_2^2)}{\bar{P}_1} + \frac{(\sigma_1^2 + \gamma\sigma_0^2)}{\bar{P}_0} \right)^{1/2} \qquad 2.12$$

The signal to noise ratio η was obtained from

$$\eta = \frac{\bar{\phi}}{\text{Total noise}} = N_{co}\,\bar{\phi} \left(\sum_i \frac{\gamma S_{2i}}{P_{1i}} - \frac{(S_{1i} - \gamma S_{0i})}{P_{0i}} \right)^{-1} \qquad 2.13$$

2.5.4 Programming.

Much of the data collection program was written by Robert Glen (GLE 80) but had been extensively amended as the experiment progressed. The most important change in the program was forced by the introduction of a second scalar. Another modification involved the separation of the program into three smaller units. The differences were large compared with the program described by Glen so the programs are listed in the appendix. Only those parts significantly altered are described in detail.

It was realised that the data collection routine spent 70 to 80% of its time waiting for the count to accumulate, while much of the remaining time was spent printing the results of the previous data block. The program was therefore divided into two main program units, one dedicated to collecting data, driving dye laser grating, etc., while the other

analysed the collected data blocks and performed other tasks not possible before. A third program unit was necessary to communicate between the two others and the teletype. Thus commands could be typed ahead without creating a bottle neck at the keyboard.

2.5.4.1 Interprogram communication.

Most of the input commands were entered to the programs through the interfacing unit **CDC3. The commands were simple, single alphabetic mnemonics and are listed in table 2.2.

Command	Action
K	Stop programs
W	Put programs in wait queue.
U	Update experimental variables.
D	Drive to new wavelength
C	Collect data.
M	Mark a data block as defective.
S	Review the data collected against wavelength
O	Analyse a block from disc.
T	Clear input buffer.
H	List Help information

Table 2.2 List of commands acceptable to **CDC3 program

**CDC3 monitored the keyboard constantly and when it needed a command it told the relevant unit by setting flags contained in the store's common area. The structure of the program was given in the flow chart - fig. 2.17.

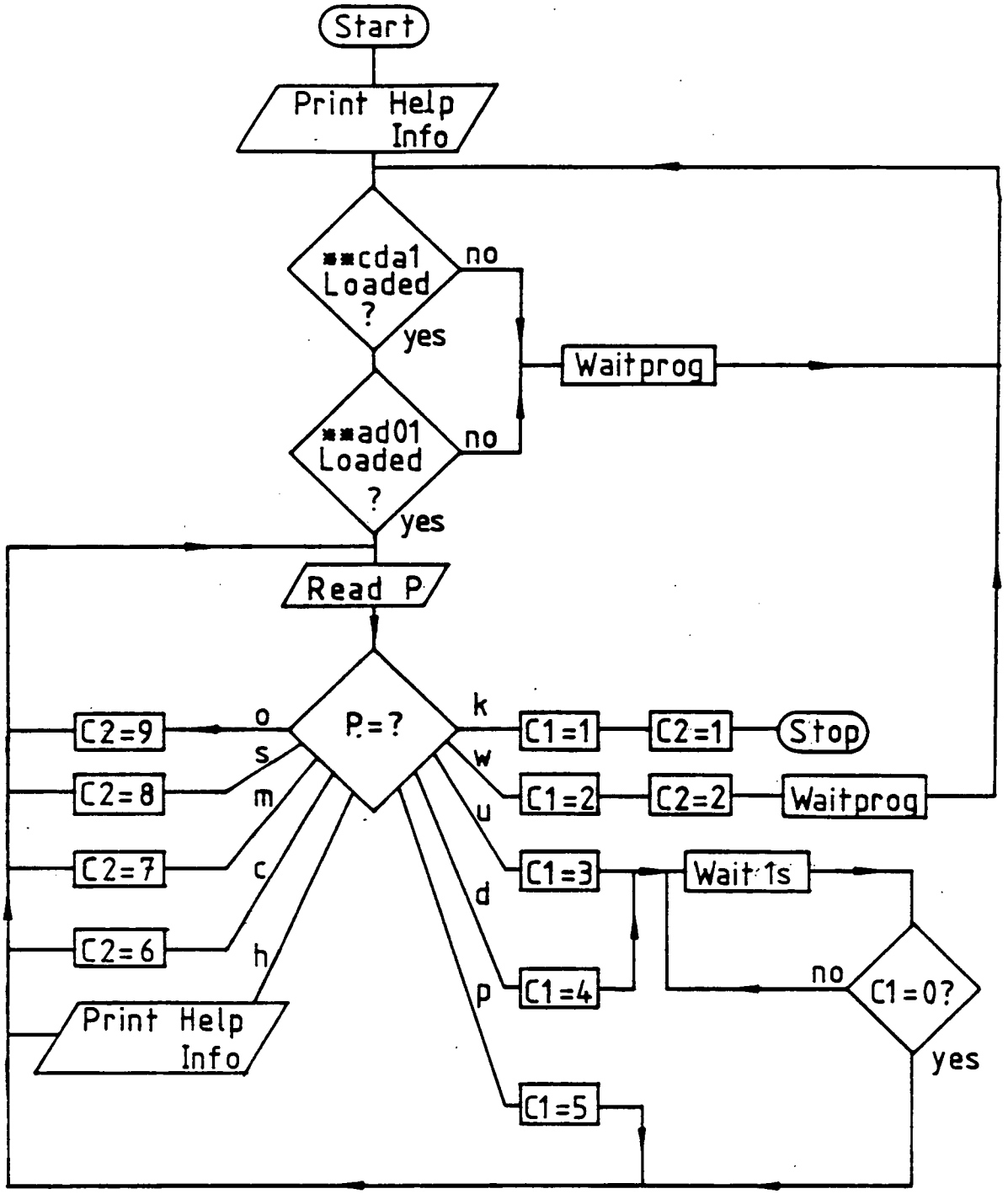

Figure 2.17 Diagram showing the structure of program **CDC3. C1 and C2 are variables used to communicate with the other programs which are stored in the common storage area.

2.5.4.2 Data collection program.

This program, **CDA1, controls the data aquisition and was written so that once it started to collect data it would stop only when specifically told to. Routines to drive the grating, read the scalars, update experimental variables, etc., are basically unchanged from those of reference GLE80. The structure of the program was however very different and was detailed in the flow chart (fig.2.18). The common variable C1, written by **CDC3, introduced the commands. If the program was left idle for too long it prompted for a command every 10 seconds.

2.5.4.3 Collect data routine.

The sequence of operations executed when a block of data was collected is shown in the flow diagram of figure 2.19. The number of entries per block was input as the variable NCO. Alternate count periods were taken with the F atom discharge on, then off. The data was retained in arrays which are held in a common area of store. When the requisite number of blocks had been collected, the data arrays were written to the direct access disc file. The analysis program **AD01 was notified that it was to examine the data and the collection program immediately started to execute its next task. An interrupt facility, which set bit 6 of the scalar to an impossible value, was introduced so that the progress of the experiment could be temporarily halted. If interrupted the routine would wait for a keyboard response.

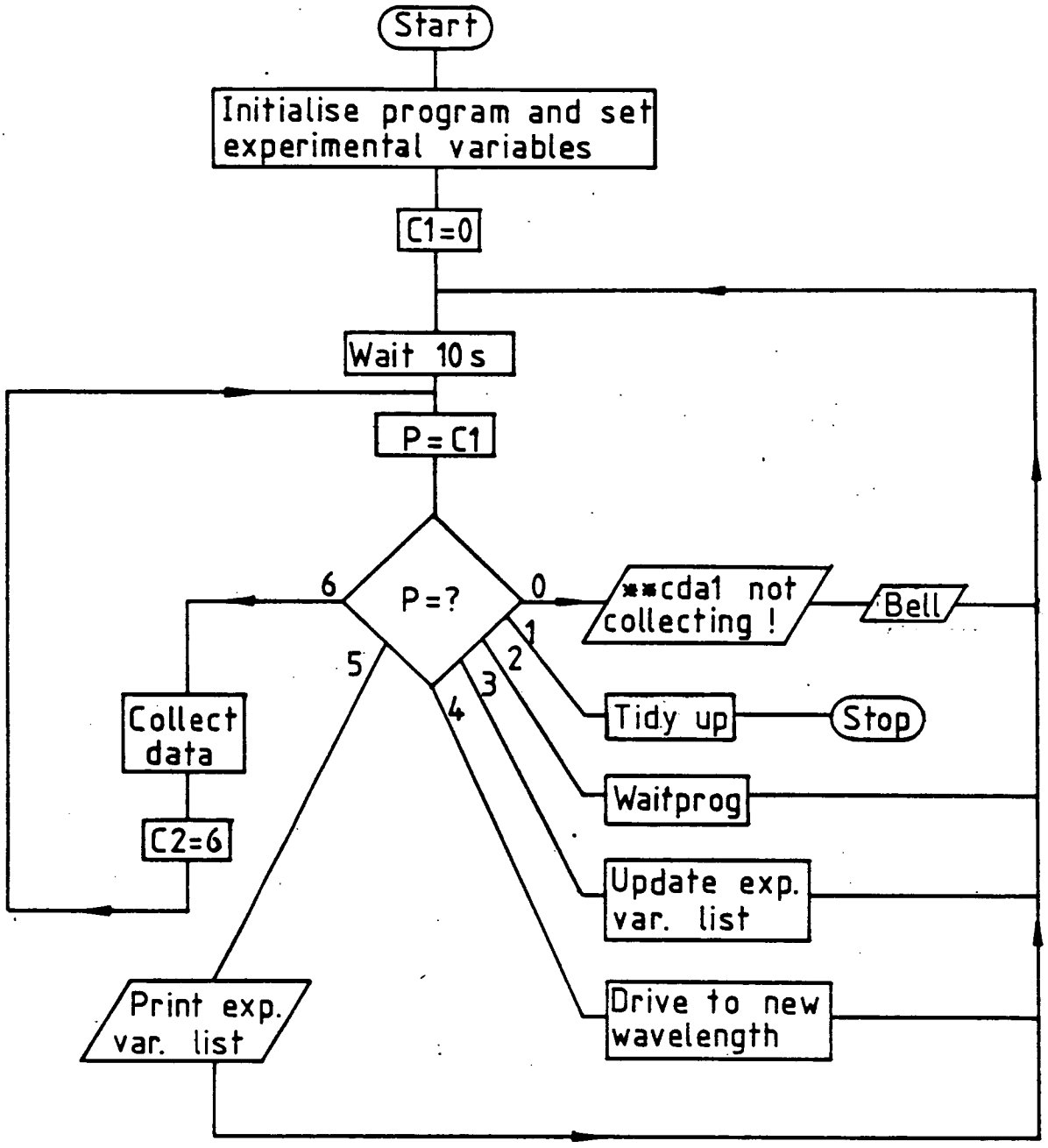

Figure 2.18 Diagram showing the structure of the program **CDA1. C1 and C2 are variables stored in a common area. Commands for the program are input through C1.

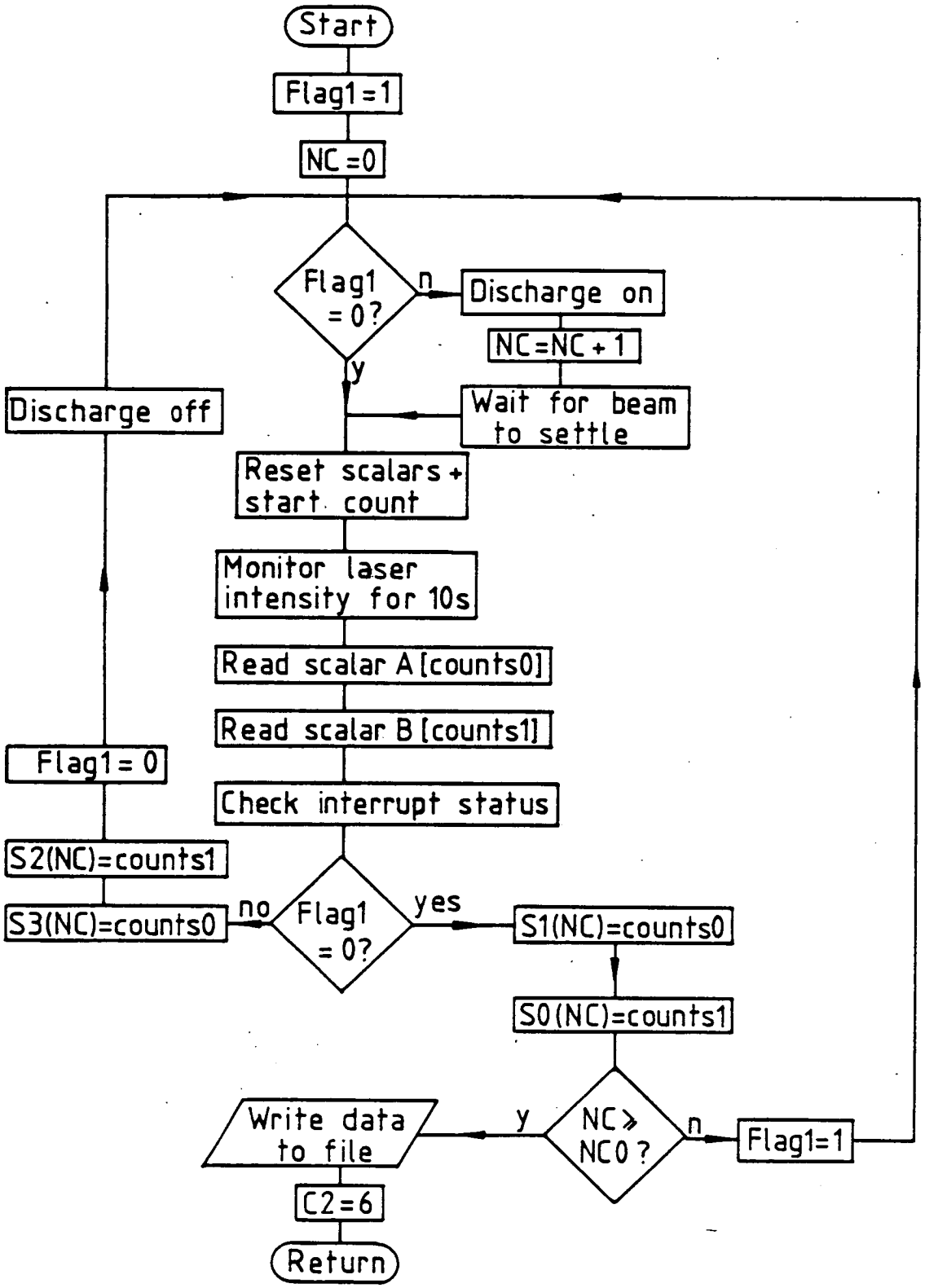

Figure 2.19 Flow chart for the data collection routine. Setting the common area variable C2 = 6 tells the analysis program to analyse the block of data just collected.

This routine was also required to check for the continuity of the experimental conditions. Facilities for on-line tank pressure measurement and beam monitoring were not available and these parameters had to be entered through the keyboard. Only the laser intensity could be monitored and if this drifted outside predetermined values warning messages were printed.

2.5.4.4 Data analysis program.

The data analysis program **AD01, figure 2.20, was intended to provide on-line analysis of the incoming data so that the experimeter could decide how best to proceed. The initial analysis was done according to equations 2.11, 2.12 and 2.13 but without normalisation for laser intensity. The quantity of output was optional, every data entry - useful for diagnostic purposes - or a brief list of the salient quantities could be printed as required.

Data blocks from the current data file could be analysed for comparison purposes when necessary. To obtain a listing of the spectrum collected it was necessary to be able to reject blocks of data when faulty, e.g. if the discharge fails to strike. This was done by setting a flag for that block which allowed the program to ignore it.

2.5.6 The experiment as a whole.

Experiments could, latterly, run for many days, the limiting factor often being the loss of I_2 beam pressure.

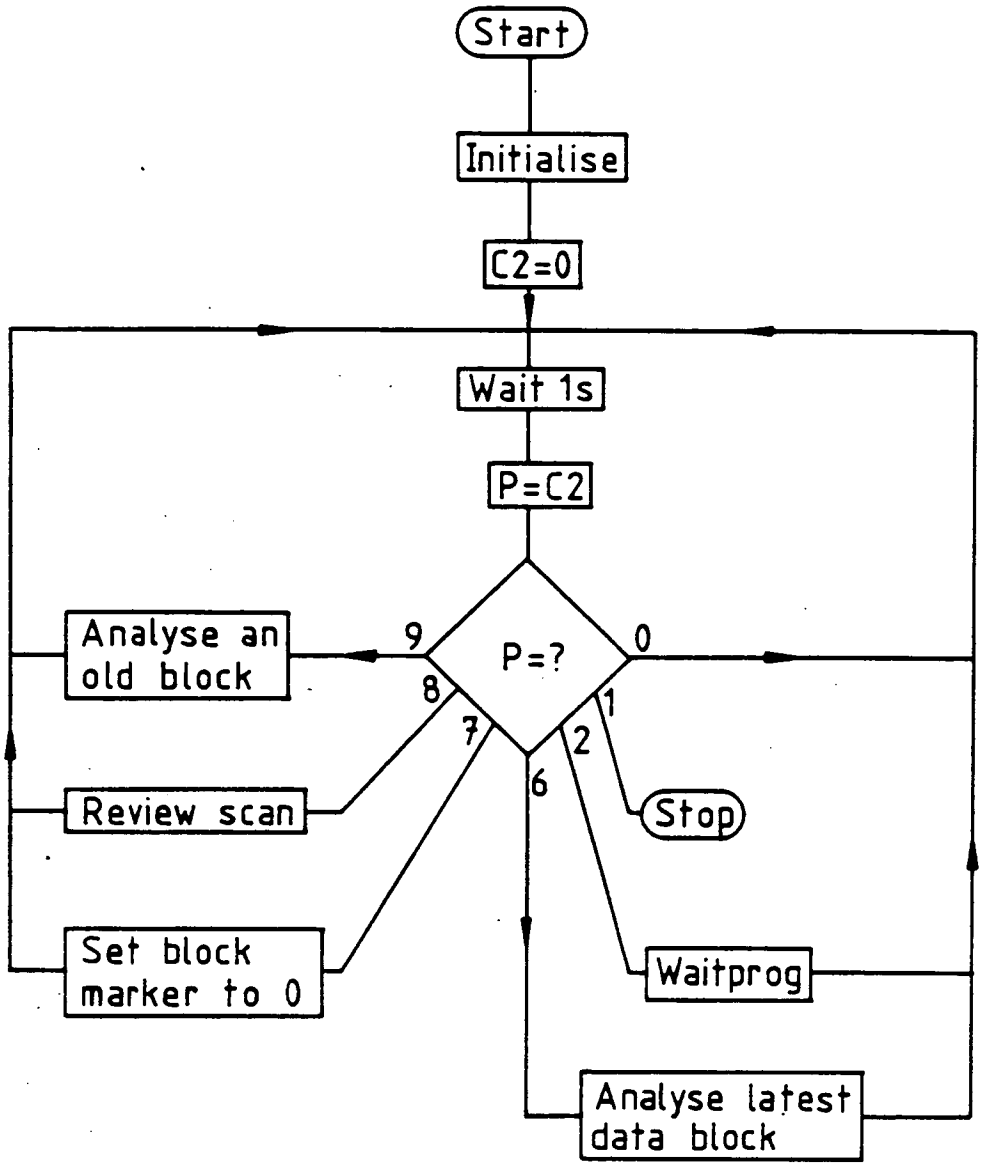

Figure 2.20 Flow diagram of the data analysis program.

After initial alignment of the laser and pumping down, the F beam source was checked for alignment by observation of NO_2 laser-induced fluorescence.

The apparatus then started to collect data at wavelengths close to IF(X)→IF(B) transition bandheads. Figure 2.21 shows a typical set of data. This particular data set was collected at a wavelength of 4782Å which is at the (5, 0) bandhead. The columns shown are (left to right) cycle number, S_0, S_1, S_2, S_3, P_0, P_1 (see section 2.5.3) and refer to a 10s counting period. The average laser intensity was 357.5 ± 0.3 mV.

Fluctuations in laser intensity were seldom greater than 1%.

The unnormalised signal for this data block is 36.5 ± 2.2 counts in 10s, i.e. the signal rate was nearly 4Hz. This low count rate resulted in long count periods.

2.6 Results

The results given here are those collected during the week beginning 22/9/80. The principal results are presented in table 2.3. It includes measurements that were intended to probe the v = 0, 1, 2, 3 product vibrational levels of $IF(X^1\Sigma^+)$. Franck Condon factors for the transitions accessible using the dyes of table 2.1 are shown in table 2.4 (CLY 76). All transitions involving the ground state were observed. Transitions not involving v = 0 proved to be much less easy to observe and much time was spent trying to obtain a measure of the v = 1 population from the (8, 1) band.

WAVELENGTH / A	FLUORESCENCE SIGNAL / ARB.UNITS.
4670.0 +/- 0.50	1.338 +/- 3.748
4673.0 +/- 0.50	0.173 +/- 1.686
4674.0 +/- 0.50	0.701 +/- 2.160
4675.0 +/- 0.50	-1.640 +/- 1.785
4677.0 +/- 0.50	0.367 +/- 1.008
4680.0 +/- 0.50	1.648 +/- 1.863
4682.0 +/- 0.50	-2.373 +/- 1.717
4684.0 +/- 0.50	-4.318 +/- 2.372
4686.0 +/- 0.50	2.586 +/- 2.225
4689.0 +/- 0.50	-3.256 +/- 1.921
4693.0 +/- 0.50	-1.352 +/- 1.617
4695.0 +/- 0.50	0.249 +/- 3.469
4696.0 +/- 0.50	-1.065 +/- 1.637
4698.0 +/- 0.50	2.877 +/- 1.579
4699.0 +/- 0.50	32.399 +/- 3.347
4700.0 +/- 0.50	25.104 +/- 2.643
4702.0 +/- 0.50	19.337 +/- 2.443
4705.0 +/- 0.50	14.274 +/- 1.683
4707.0 +/- 0.50	11.582 +/- 1.777
4708.0 +/- 0.50	9.766 +/- 1.578
4711.0 +/- 0.50	2.752 +/- 1.502
4713.0 +/- 0.50	3.751 +/- 2.111
4862.0 +/- 2.00	-1.067 +/- 1.713
4864.0 +/- 2.00	-2.606 +/- 1.859
4867.0 +/- 2.00	1.561 +/- 1.809
4871.0 +/- 2.00	26.117 +/- 2.177
4872.0 +/- 2.00	25.625 +/- 1.729
4874.0 +/- 2.00	27.344 +/- 2.203
4876.0 +/- 2.00	27.981 +/- 3.022
4945.0 +/- 0.50	-2.250 +/- 1.914
4949.0 +/- 0.50	-1.722 +/- 2.054
4951.0 +/- 0.50	-2.243 +/- 1.115
4953.0 +/- 0.50	-0.648 +/- 1.105
4955.0 +/- 0.50	1.660 +/- 1.379
4960.0 +/- 0.50	0.746 +/- 1.675
4963.0 +/- 0.50	4.310 +/- 1.509
4964.0 +/- 0.50	27.140 +/- 2.827
4965.0 +/- 0.50	20.218 +/- 2.030
4966.0 +/- 0.50	20.853 +/- 1.684
4967.0 +/- 0.50	8.884 +/- 1.590
4968.0 +/- 0.50	14.824 +/- 1.907
4975.0 +/- 0.50	5.012 +/- 1.851
4977.0 +/- 0.50	7.553 +/- 1.555
4979.0 +/- 0.50	3.930 +/- 1.834
4982.0 +/- 0.50	6.680 +/- 1.239
4982.0 +/- 0.50	5.808 +/- 1.649
4982.0 +/- 0.50	4.818 +/- 1.196
4982.0 +/- 0.50	2.069 +/- 1.953

Table 2.3 Fluorescence signal collected at wavelengths in the range 467 nm to 499 nm.

```
LISTING OF BLOCK NO    23 OF FILE LIF 205
 DATE= 2803.80
SIEF FUSN =     6
ENTRIES=   10
TIME AT START=  359.0414
TIME AT END=  364.4194

   1     31      4    3431      78  3.5726@ -1  3.5679@ -1
   2     29      6    3273      72  3.5762@ -1  3.5596@ -1
   3     27      6    3222      78  3.5767@ -1  3.5606@ -1
   4     41     10    3382      80  3.5662@ -1  3.5562@ -1
   5     39     10    3305      86  3.5809@ -1  3.5740@ -1
   6     45      6    3289      70  3.5839@ -1  3.5701@ -1
   7     43      6    3192      70  3.5828@ -1  3.5797@ -1
   8     40      3    3198      82  3.5912@ -1  3.5802@ -1
   9     40      7    3145      74  3.5804@ -1  3.5941@ -1
  10     44      8    3174      63  3.5792@ -1  3.5753@ -1
```

Figure 2.21 Sample data block.

V' \ V''	0	1	2	3
3	496.3 0.089			
4	486.9 0.119			
5	478.1 0.133	492.3 0.022		
6	469.8 0.131	483.5 0.000	497.9 0.066	
7	462.0 0.116	475.3 0.008	489.1 0.060	
8	454.7 0.096	467.5 0.031	481.0 0.033	495.1 0.024

Table 2.4 Band origins (nm) and Franck Condon factors for IF $(B^3\Pi_{0+}) \rightarrow$ IF $(X^1\Sigma^+)$ transitions accessible with the

dyes of table 2.1b and limited by the I_2 fluorescence at 500 nm.

The actual count rate was an order of magnitude down on that estimated but this was perhaps not too surprising, considering the high degree of approximation made. The most likely cause of the overestimate was probably too optimistic a guess of the F atom density. The signal to noise ratio of individual data blocks was relatively poor. The maximum of less than 30 was obtained with fresh dye, working at its peak gain near a bandhead. Often the signal to noise ratio was less than 10.

2.6.1 Data fits.

Conventional methods for determining vibrational populations from low resolution spectra rely on integration of the area under the band profile (STE80). For the quality of data presented here the preferred method of data fitting was by a simulation of the spectrum. The fit was then obtained by adjustment of vibrational and rotational distribution parameters (DAG 74, LIU 77). Ideally this procedure should involve parameterising the intensity function and using this for a non-linear least squares fit. This was not attempted as time did not permit and extensive adaptation of the simulation program necessary. Also lack of stability in such a procedure, for the data presented, could make any effort in this direction less than worthwhile.

The simulation program written by R. Glen is well documented and tested in reference GLE 80. It requires as input the spectroscopic constants of the molecule under consideration, its Franck Condon factors and the p.m. response function. The variable parameters governing the spectrum include $n_{v''}$, the vibrational populations, $T_{R''}(v'')$, rotational temperatures, $\Delta\lambda_l$ laser linewidth. The resulting simulation can be compared with the data and a fit obtained by eye. A better approach is to vary the parameters manually and obtain the standard deviation of the data points. The best fit was that which gave the lowest deviation.

2.6.1.1 Rotational distribution.

The peak intensity for a vibrational band varies sharply with the laser linewidth and rotational temperature. As the linewidth measurements gave consistent values when the etalon was used $\Delta\lambda_l$ was fixed at 1.3Å.

The rotational temperature for low lying vibrational bands is unlikely to vary much. It is frequently found that the energy disposal in rotation, $g_{R'}$, follows (LEV72)

$$g_{R'} = \frac{f_{R'}}{1 - f_{v'}} = \text{constant} \qquad 2.14$$

with $f_{R'}$, $f_{v'}$ the fractions of total energy available in rotation and vibration respectively. For a highly exothermic reaction $f_{v'}$ changes little for the low lying vibrational levels, implying $K.\langle T_{R'}\rangle \simeq g_{R'}.E_{Tot} = \text{const.}$ It was therefore assumed that the rotational temperature obtained for $v'' = o$ held for the levels up to $v'' = 3$, all of which were

less well characterised.

The resulting best fits to the data are shown in figures 2.22 and 2.23. The rotational temperatures $T_{R'}$, are

Vibrational Band	$T_{R'}$/K
(5,0)	240
(6,0)	227.5
(3,0)	227.5

As the deviation in the points cannot readily be related to the Boltzmann temperature the error in the temperature was estimated from the spread in the values for the three individual bands. $\langle T_{R'} \rangle$ was therefore, after averaging and rounding, 230K $\pm$ 10K.

2.6.1.2 Vibrational distribution.

Because of the combination of the high efficiency of the dye Coumarin 307 and the Franck Condon factors for the (8,3), (3,0) and (6,2) bands it was hoped to obtain their relative populations with some accuracy. The data, along with the best fit to the vibrational populations at the previously determined $T_{R'}$ is shown in figure 2.23. This simulation corresponds to the populations $n_{v''}$ shown in table 2.5.

V''	$N_{v''}$	Error limits
0	1.0	-
1	0.1	-
2	0.15	0.13 - 0.20
3	0.2	0 - 0.3

Table 2.5 Measured populations of product IF vibrational levels relative to the ground state.

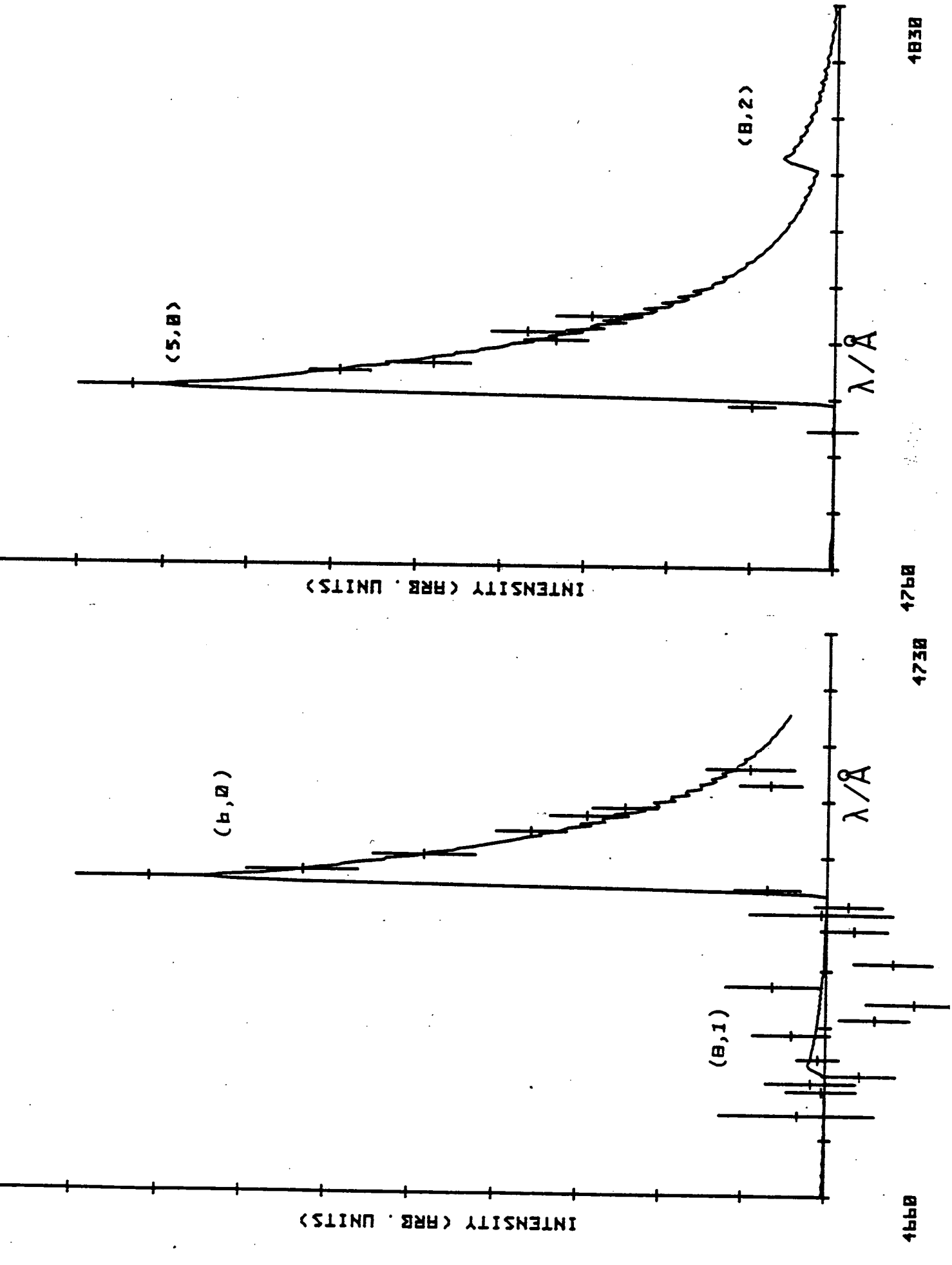
(5,0)
(6,2)
λ/Å
4830
4760
INTENSITY (ARB. UNITS)
(6,0)
(6,1)
λ/Å
4730
4660
INTENSITY (ARB. UNITS)

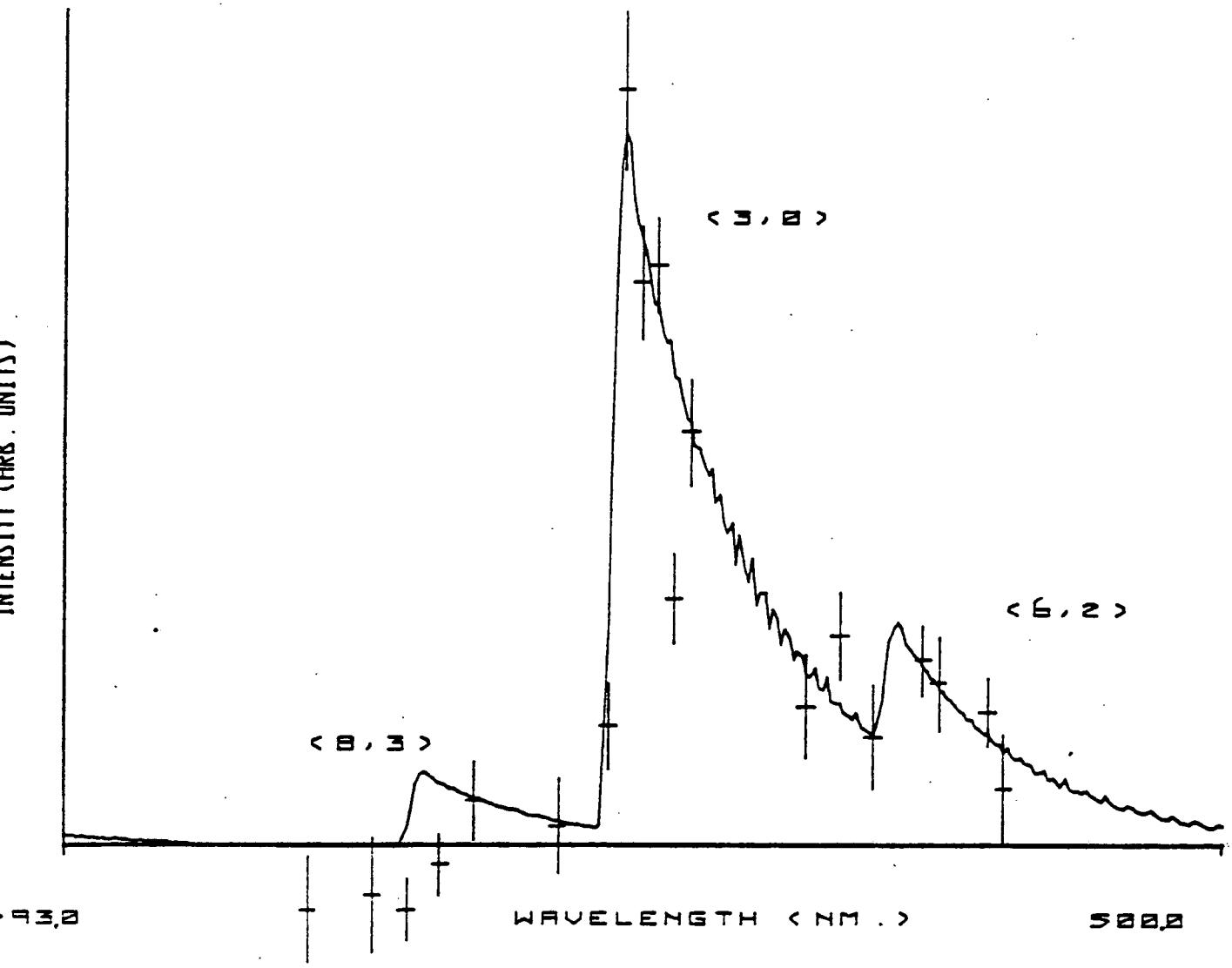

Fig. 2.23 Best fit to the data for the (8,3), (3,0) and (6,2) vibrational bands.

Previous Page:

Fig. 2.22 Best fit to the data for the (8,1), (6,0) and (5,0) vibrational bands.

For overlapping bands the deviation of the points cannot be related to $n_{v''}$. The errors quoted in the table are maximum and minimum $n_{v''}$ consistent with the error limits of the data points.

As can be seen from the (8,1) band (fig.2.22) the population in the $v''= 1$ level must be very small. All that can be said from the data is that it is less than 10% of the $v''= 0$ population.

2.6.2 Relaxation effects.

(a) Contribution of background.

IF could have formed a proportion of the residual gas background. Any present in the background could only be formed by reaction at the tank centre. The mole fractions would therefore be approximatdy the same in the backgound as in the detection zone. The contribution of background IF was then given by the ratio of pressures in these two regions. However as cryotrapping efficiently pumps I_2 vapour (vapour press 10^{-29}m Bar at 100K) IF should be pumped with the same efficiency. This suggested that background contributions to the signal would be negligible.

(b) Quenching.

If the estimated reagent fluxes are converted to densities and a generous collision diameter of 10Å is assumed then the mean free path of molecular species is calculated to be about 50mm at the reaction zone. As the size of the reaction zone was approximately 5mm across and the product velocity was of the order of 10^6mms^{-1} the fraction of molecules

which suffer a single collision was 1 - exp (-5/50) ≈ 10%. Thus, at most, 10% of the observed rotational distribution may have suffered some relaxation. Vibrational quenching is much less efficient than its rotational counterpart and is probably several orders of magnitude smaller. As the cross section for rotational relaxation is likely to be less than the hard sphere cross section it is assumed that the measured distributions reflect the unperturbed populations.

2.6.3 Information theoretic analysis.

It is often helpful to compare a measured distribution with the prior distribution, a statistical model which maximises the entropy of the distribution. The surprisal, I, is a measure of the deviation from this model, related to the entropy deficiency (BEN 72). The surprisal is given by

$$I(v) = -\ln\left(\frac{P(v)}{P^{o}(v)}\right) \qquad 2.15$$

where P is the measured probability distribution while P^{o} is the prior distribution.

In the vibrating rotor approximation for diatomics the expression for the rotational energy is truncated to $E_R = B_{v'} J(J+1)hc$ where the conventional notation has been used. This allows integration over the rotational quantum number, giving (LEV 75)

$$P^{o}(E_{v'}|E) = \frac{B_{v'}^{-1}(E - E_{v'})^{3/2}}{\sum_{v'=0}^{v'^{*}} B_{v'}^{-1}(E - E_{v'})^{3/2}} \qquad 2.16$$

as the expression for the vibrational prior distribution at a total energy E. v'^{*} is the maximum accessible vibrational level.

The surprisal plot shown in figure 2.24 is derived from the data of table 2.5, normalised so that $P(v' = o) = P^{o}(v' = o)$. This clearly shows that although there is a large uncertainty in the individual points, and contrary to many other reactive scattering results (LEV79), the plot is non-linear.

2.6.4 Comparison with other data.

Previous measurements on the F + I_2 system (DON80) indicated a population inversion with the populations of $v' = o,1,2$ approximately equal. These measurements agreed qualitatively with a similar study of the F + ICL system (STE79) and with trajectory results (see chapter 3) which showed a peak at high v'.

The results presented here are substantially different from those earlier measurements.

The results presented in reference DON80 prompted the construction of the atom source described in section 2.3.2. This was deemed necessary because the signal to noise ratios obtained with the previous atom source were extremely low and an increased atom concentration at the reaction zone was sought. Along with other modifications such as the counting technique and laser bandwidth, the improved apparatus gave a more reliable signal. In addition, by working with vibrational bands with larger Franck-Condon factors the uncertainty in assigning the relative populations was reduced.

In comparing the two sets of data (figure 1 of DON80 and

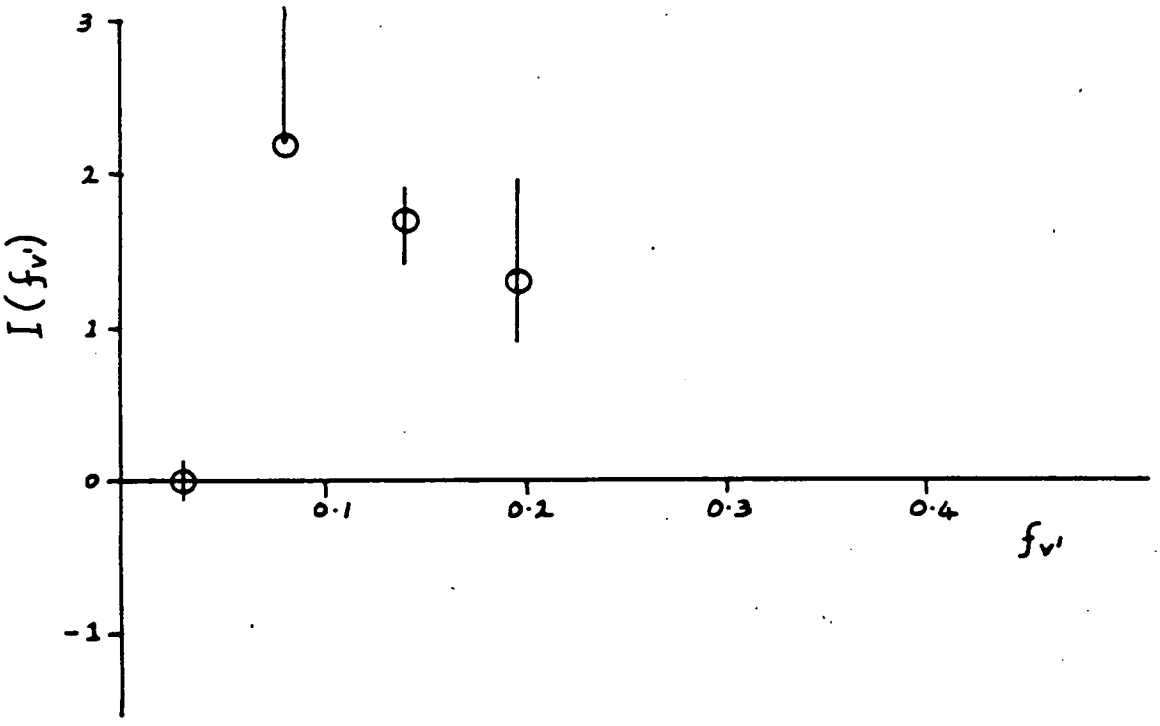

Figure 2.24 Surprisal plot of the first four vibrational levels of the IF product.

figures 2.22/2.23) the latest results for the (5,0) band are seen to give a much closer fit to the simulated spectrum. The previous result for the (8,1) band rests almost entirely upon a single data point with that for the (8,2) band not much better. While it is felt that the early results are most likely a misinterpretation of the data it is possible that a different distribution of vibrational energy could have arisen from different operating conditions such as beam energies or atom beam composition.

Further evidence is given to the present results by the results of Wanner's group which have recently been extended and show that the vibrational energy distribution for F + ICl also peaks sharply at v' = 0 (TRI80). This reference also reports a similar bimodal vibrational energy distribution for F + I_2 (and F + IBr) which agree in part with the more limited data presented here.

Chapter 3

Classical trajectory study of $F + I_2$ reactive scattering

3.1 Introduction

Quasi-classical trajectory calculations have been widely used in attempts to understand the energetics and dynamics of molecular reactions. Several reviews of trajectory studies have been published (BUN71, POR76, MUC79) giving details of the method and specific examples. The method has been extensively applied to reactive scattering systems but has also been used for in elastic/elastic systems and other studies which are strictly the domain of quantum mechanics e.g. surface hopping trajectories (TUL76, BLA81).

The calculation of a single trajectory involves the solution of the appropriate equations of motion. These are often the canonical equations of Hamilton (GOL50)

$$\dot{q}_i = \frac{\partial H}{\partial p_i} \quad : \quad -\dot{p}_i = \frac{\partial H}{\partial q_i} \qquad 3.1$$

where q_i, p_i are generalised coordinates and conjugate momenta. The Hamiltonian, H, is defined classically as the sum of kinetic and potential energies. The evaluation of the trajectory then consists of integrating the 6N first order differential equations until the trajectory has passed into a region of phase space identified with product states. This generates P_r, the probability of reaction as a function of the initial coordinates and momenta. To obtain the reactive cross section σ_R (T, V, J) (POR76) for an atom-diatom collision P_r must be integrated with respect to the initial conditions and is given by

$$\sigma_R\ (T,\ V,\ J) = \int_0^{\infty} 2\pi b\,db \int_0^{\pi} \tfrac{1}{2}\sin\theta\ d\theta \int_0^{2\pi} \frac{d\phi}{2\pi}\ .$$

$$\int_{\int_-}^{\int_+} G\ (r_{BC};\ V,\ J)\ dr_{BC} \int_{\eta=0}^{2\pi} \frac{d\eta}{2}\ P_r(T,\ V,\ J,\ b,\ \theta,\phi,\ r_{BC},\eta\ ) \qquad 3.2$$

where b = impact parameter

$\int_+, \int_-$ = inner and outer classical turning points

$G\ (r_{BC};\ V,\ J)$ = density function for internuclear distance, r_{BC}.

$\theta\ ,\ \phi$ = spherical polar orientation angles

V, J = internal action (vibrational and rotational energy)

η = BC rotation plane.

Because P_r (0 or 1) cannot be expressed analytically the multidimensional integral for σ_R, and other quantities, must be evaluated approximately. A numerical integration would be prohibitively expensive. Monte Carlo and Diophantine methods (POR76) however, permit many fewer trajectories to be calculated for the same accuracy and converge at a rate independent of the dimensionality of the integral. If the required integral is

$$I = \int dx_k \ldots\ldots \int dx_1\ .\ f\ (x_k,\ x_{k-1},\ \ldots x_1) \qquad 3.3$$

then the M.C. approximant to the integral is (HAM64)

$$I \simeq I' = \frac{1}{N} \sum_{i=1}^{N} f\ (\eta_i) \qquad 3.4$$

η_i is a vector whose elements are chosen randomly from a uniform distribution. The error inherent in this procedure is proportional to $N^{-\frac{1}{2}}$ and is independent of the dimensionality of the integration.

3.2 Selection of variables and coordinate system

For a triatomic system there are 18 coordinates needed to describe the system. Six of these can be discarded as they govern the motion of the centre of mass which is a constant. To simplify the selection procedure some variables are often fixed or scanned, while others are selected in a truly random manner. Several authors have scanned variables that hold a particular physical significance. For example the vibrational energy of the diatomic is usually assigned a fixed value while less well defined quantities such as vibrational phase are randomly selected. This allows the selectivity of the reaction to be investigated.

Schemes for selection of initial variables exist which attempt to accelerate the convergence of the M.C. integral. Two such schemes are stratified sampling (PAR73) and importance sampling (FAI 78, FAI79). By biasing the initial distributions the variance of a particular reaction attribute (e.g. cross section) is reduced. This is undeniably useful but can lead to an increased variance in other reaction attributes (FAI76). As a more general approach is intended here the unbiased distributions were used.

The program used was based on that described by Fernie (FER80) which was developed for an investigation of the $O + I_2$ reaction. Details of the coordinate system along with expressions for the derived quantities such as energies, scattering angle etc. are given by Fernie.

The program was updated to accept the random number generators G05CAF and G05DDF of the mark 7 NAG library (NAG78), giving uniform and gaussian distributions respectively. These routines are called a fixed number of times per trajectory and a record is kept for backward integration checks.

3.3 Integration of the equations of motion

Algorithms for integrating classical trajectories vary from the comparatively simple, single step Runga Kutta Gill procedure (BLA65, RAF66) to multi-step predictor corrector methods up to eleventh order (MUC73). For very long-lived trajectories, demanding many integration steps, highly stable routines are required. Gear's 6th order hybrid method (GEA71) has been used with some success (BRU73, FIT79). As many trihalogen molecules are known to be stable (VAL77) long lived trajectories involving a complex mechanism could have been expected for fluorine atom - iodine molecule reactions.

Fernie's program was adapted to utilise Gear's hybrid, variable step, variable order method. The NAG library routine (NAG78) D02QBF appeared to be suitable as it allowed the trajectory to be monitored throughout the integration. The results were very disappointing in that the accuracy demanded to reproduce previous results required a substantial increase in CPU time over the more conventional Hamming's method. This inefficiency was attributed to the low maximum order of the routine (5th c.f. 6th of BRU73) forcing an excessive number of steps to be taken. Also, being a library routine,

it was of a general nature and not available for adapting to a specific task. In particular the stability matrix (12 * 12) for the system of equations had to be evaluated to determine the order used for each step. The physics of the problem could have been used to speed up the calculation of this matrix, as 70% of the elements can be shown to be zero. Elements of the form

$$\frac{\partial \dot{q}_i}{\partial q_j} = \frac{\partial}{\partial q_j} \cdot \left(\frac{\partial T(p_i)}{\partial p_i} \right) = 0 \qquad 3.5$$

where $T(p_i)$ is the kinetic energy term which is independent of q_j, are identically equal to zero.

As no other version of Gear's algorithm was readily available it was decided to retain the routine used by Fernie. Hamming's algorithm (RAL60) is a modified version of Milne's predictor corrector method. It uses a special Runga Kutta Gill start up procedure, is fourth order and is stable for a wide range of step sizes. This method has been used for many cases e.g. long lived trajectories of Li_2 + Na (WHI76), surface hopping trajectories (TUL71) and large atom interations with laser fields (POP80). The method is prone to suffer from a build-up of rounding errors when very many steps are required (FIT79) and therefore such trajectories need to be checked.

For the trajectories of F + I_2 Hamming's method was found to be sufficiently accurate. The initial step size and local truncation error were adjusted for optimum performance. The best value for the initial step size was found to be 10^{-15} sec. This was a relatively large increment but allowed the

program to integrate the uncomplicated approach of the reactants very efficiently while a rigorous value for the relative error (10^{-5}) forced the step size to be reduced when necessary. Typically the integration step length was halved two or three times.

The accuracy of a trajectory integration is subject to differing definitions. Early results often quoted the degree of conservation of energy or angular momentum as a guide to the accuracy of a trajectory. While these are obviously necessary, they are seldom good measures of the quality of the integration. Other criteria exist for the accuracy but the most demanding condition is that of backward integration.

The trajectory is integrated to conclusion, the momenta reversed and integrated until the original coordinates and momenta are achieved.

If the starting point is not reached then the trajectory is discarded. This procedure is sometimes over rigorous in that the forward integration may be satisfactory while an error occurs on the backward section. It is also wasteful of CPU time as each trajectory would require double the time.

The optimum running conditions mentioned above gave energy conservation to better than one part in 10^5 in most cases. A sequence of trajectories was run with full backward integration to see if this level of energy conservation was sufficiently accurate. It was found that the vast bulk of trajectories reproduced initial coordinates and energies to a good degree of accuracy, while under these conditions at 0.025 V about 4% of the trajectories did not.* As a proportion of the

integration errors could be seen to have occurred on the backward step (by observing the total energy changes) this was taken to be an acceptable accuracy for the calculation.

* A few trajectories were found for which it was impossible to recover the initial coordinates under any conditions. These possibly pass through a region of the surface where points adjacent in phase space diverge exponetially (DUF79).

3.4 Potential energy surface

The potential energy surface governs the nuclear motion of the system and numerous reviews of this interesting topic exist (KUN76, MUR78, TUL81) Some guidelines for any surface are

i) The surface must accurately describe the potential in the assymptotic limits, thus obeying the known thermodynamic data.

ii) It should smoothly connect the reactant and product states through the interaction region, obeying any symmetry properties.

iii) Any known data, expirical or otherwise concerning the interaction region should be incorporated and outside these regions it should behave in a physically reasonable manner.

Many potential energy constructs are very elegant but of little practical use for trajectory calculation. Recourse is often made to arbitrary methods. The switching functions and hyperbolic map functions devised by Bunker (BUN71) have been used extensively (BLA63, KAR64, FLU76, SAN77). They both allow manipulation of topological features of the surface and produce the correct asymptotic limits. While the switching function

formalism is often an adequate description of an A + BC $\rightarrow$ AB + C system, it can be troublesome when BC is an homonuclear diatomic. Although discontinuities in the derivatives at $r_{AB} = r_{AC}$ are not severe it can trigger instability in the integration routine.

The London equation (LON29) relates the ground state energy of three ^2S atoms in terms of their respective diatomic singlet and triplet energies. This equation is appropriate for H_3 but has been modified (SAT55) and extended (KUN66) to incorporate much empirical information. The resulting LEPS construction has been used to describe many triatomic and tetratomic systems (WHI75, SMI75 for example).

The LEPS potential for a triatomic system is given in terms of the interatomic distances by

$$V(r_1, r_2, r_3) = Q_1 + Q_2 + Q_3 - (J_1^2+J_2^2+J_3^2-J_1J_2-J_2J_3-J_3J_1)^{\frac{1}{2}} \qquad 3.6$$

where $Q_i\ (r_i) = \frac{1}{2}(^1E_i + {}^3E_i)$ is nominally associated with couloumb integral and $J_i(r_i) = \frac{1}{2}\ (^1E_i - {}^3E_i)$ is nominally associated with the exchange term. ^1E_i and ^3E_i refer to the singlet and triplet energies of the separated diatomic fragments. As the ground state surface is sought, the ^1E_i are chosen to best represent the asymptotic regions for which the Morse potential is adequate.

$$^1E_i = {}^1D_i \left[1 - \exp\left[-{}^1\beta_i\ (r_i - {}^1r_i^o)\right]\right]^2 - {}^1D_i \qquad 3.7$$

^1D_i = dissociation energy

$^1r_i^o$ = equilibrium bond length

$$^1\beta_i = \left(\frac{\omega_{ei}^2\ \mu_i}{^1D_i}\right)^{\frac{1}{2}}$$

The repulsive ^3E_i state is given by the so called anti Morse function.

$$^3E_i = {}^3D_i\left[\,1 + \exp\left[\,-{}^3\beta_i(r_i - {}^3r_i^o)\right]\right]^2 - {}^3D_i \qquad 3.8$$

$^3\beta_i$ and $^3r_i^o$ are often (as here) equated with their singlet values. ^3D_i is given by the prescription

$$^3D_i = {}^1\frac{D_i}{2} \cdot \frac{(1 - s_i^2)}{(1 + s_i^2)} \qquad 3.9$$

s_i is an adjustable parameter allowing properties of the surface to be varied. $s_i = 1$ eliminates the triplet component giving a deep well. Reducing s_i adds a repulsive component to the corresponding bond and changes the position of the potential minimum with respect to that band.

For $F + I_2$ symmetry requires that $s_1 = s_3$. Allowing the proximity of the F atom to vary the ratio s_1/s_3 could be a way of accounting to some extent for change transfer effects. However the complexities introduced may overwhelm any benefits and this was not tried.

The spectroscopic data for ground state I_2 is quite detailed (COX72). In particular the RKR turning points are available to very high levels, nearly to the dissociation limit (LER70). The Morse curve obtained in the usual way from equation 3.7 gives a good fit to the part of the curve near the minimum but tends to deviate from the data points for the higher levels. This was particularly noticeable in the attractive portion of the curve. As the

repulsive part of the potential is never used for near thermal trajectories while the attractive part helps to form the exit channel, a least squares fit of the $^1\beta_i$ parameter to the outer turning points alone was carried out. The resulting potential energy curve is shown in figure 3.1 giving good agreement with the measured data. The remaining spectroscopic constants are given in table 3.1.

	IF $(X^1\Sigma^+)^{(i)}$	$I_2(X^1\Sigma_g^+)^{(ii)}$
De/cm^{-1}	22333 (iii)	12 435
$B/\text{Å}^{-1}$	2.021	2.33 (iv)
$r_o/\text{Å}$	1.9089	2.667

Table 3.1 Spectroscopic parameters for IF and I_2. From (i) CLY76, (ii) COX72, (iii) CLY78, (iv) see text.

Appleman and Clyne have measured the rate constant for reaction (1) (APP75) as $(4.3 \pm 1.1) \times 10^{-10} cm^3 molecule^{-1} s^{-1}$. This is, within experimental error, equal to the hard sphere collision frequency indicating that there is effectively no activation energy, nor a strong steric effect. Scattering measurements (CAR73, WON73) for F + I_2 show an isotropic or sideways peaked angular distribution consistent with the formation of a complex, albeit short lived. I_2F has been observed as one of the products of the F_2 + I_2 reaction (COG76) and is estimated to be stable by 12.6 KJ mol^{-1}. (VAL77)

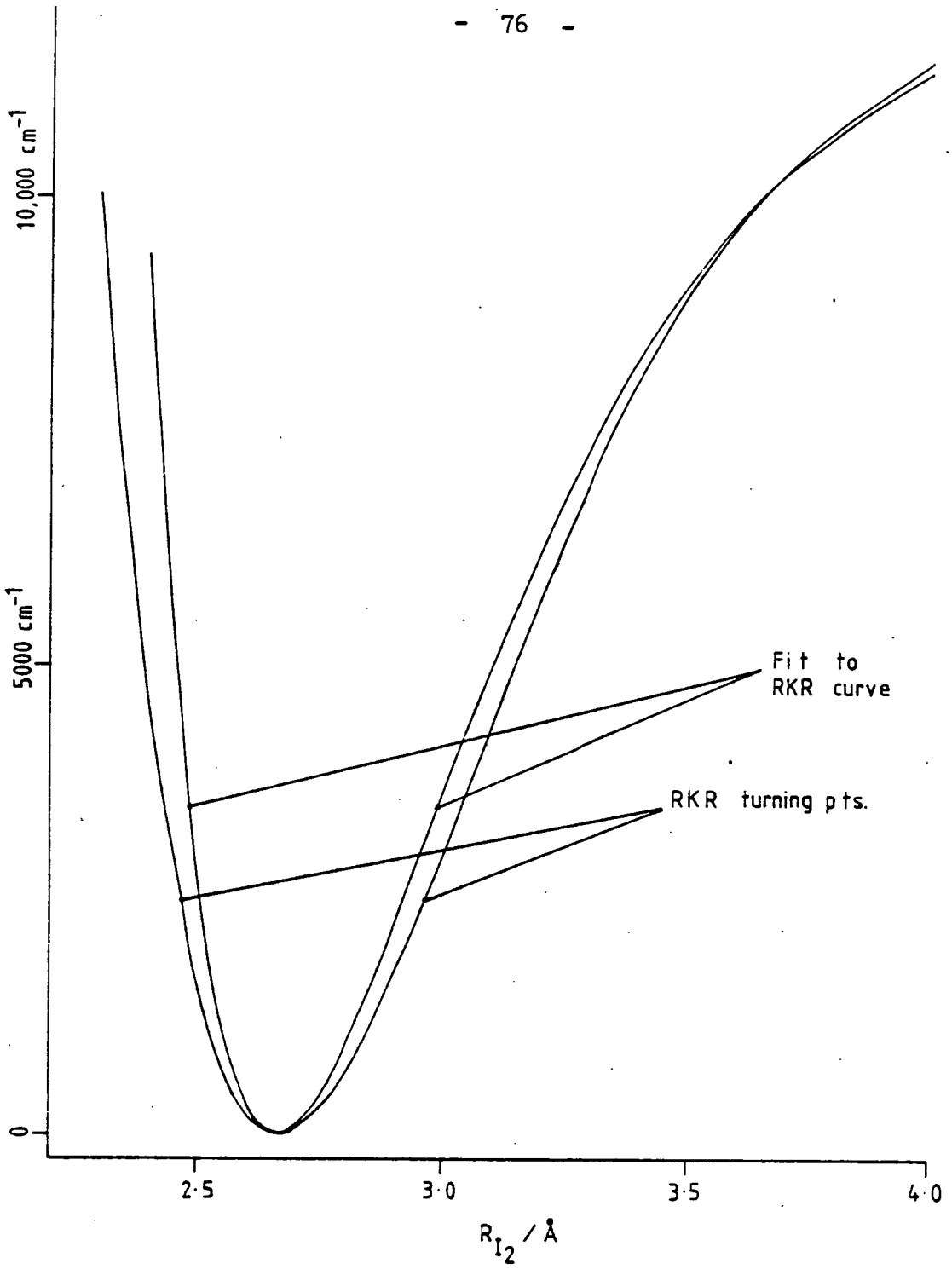

Figure 3.1 RKR turning points and Morse curve approximation as described in the text.

No 21 valence electron structures have been reported in the literature. Cl_2F, Br_2F, CLF_2, BrF_2 and tentatively I_2F have been observed in matrix isolation studies (PRO78) where an angle of 150^o was assumed for Cl_2F. Walsh's rules are inconclusive for such systems and are even less reliable when the system contains iodine, well known for charge transfer effects. Lee predicts a bent configuration for the tri-halogens they studied (VAL77) from the form of the distribution of the products. Schaefer has reported ab initio geometry optimisation calculations on the triatomic ClF_2 (UNG76). Although it was shown that the ground state was bent (148.8^o), the geometry changed between basis sets and has a low lying linear excited state. Inclusion of d orbitals on the central atom markedly improved the resulting energy and increased the bond angle for the ground state showing the importance of delocalisation.

Trajectories were run over nine LEPS surfaces details of which are shown in table 3.2. The surfaces are labelled S_o to S_8 as indicated in the table. The only restriction on the adjustable parameters s_i was that the well depth be approximately 12.6 KJ mol^{-1}. Only surface S_o has a barrier in the reaction coordinate, albeit small (1.71 KJ mol^{-1}).

Fixed angle scans of a few of the surfaces are plotted in figure 3.2 using mass weighted coordinates. (KUN76)

i.e. $$\int_{IF_2} = \beta\, r_{IF_2} \cos\phi \qquad 3.10$$

$$\int_{IF} = r_{IF} + \beta\, r_{IF_2} \sin\phi \qquad 3.11$$

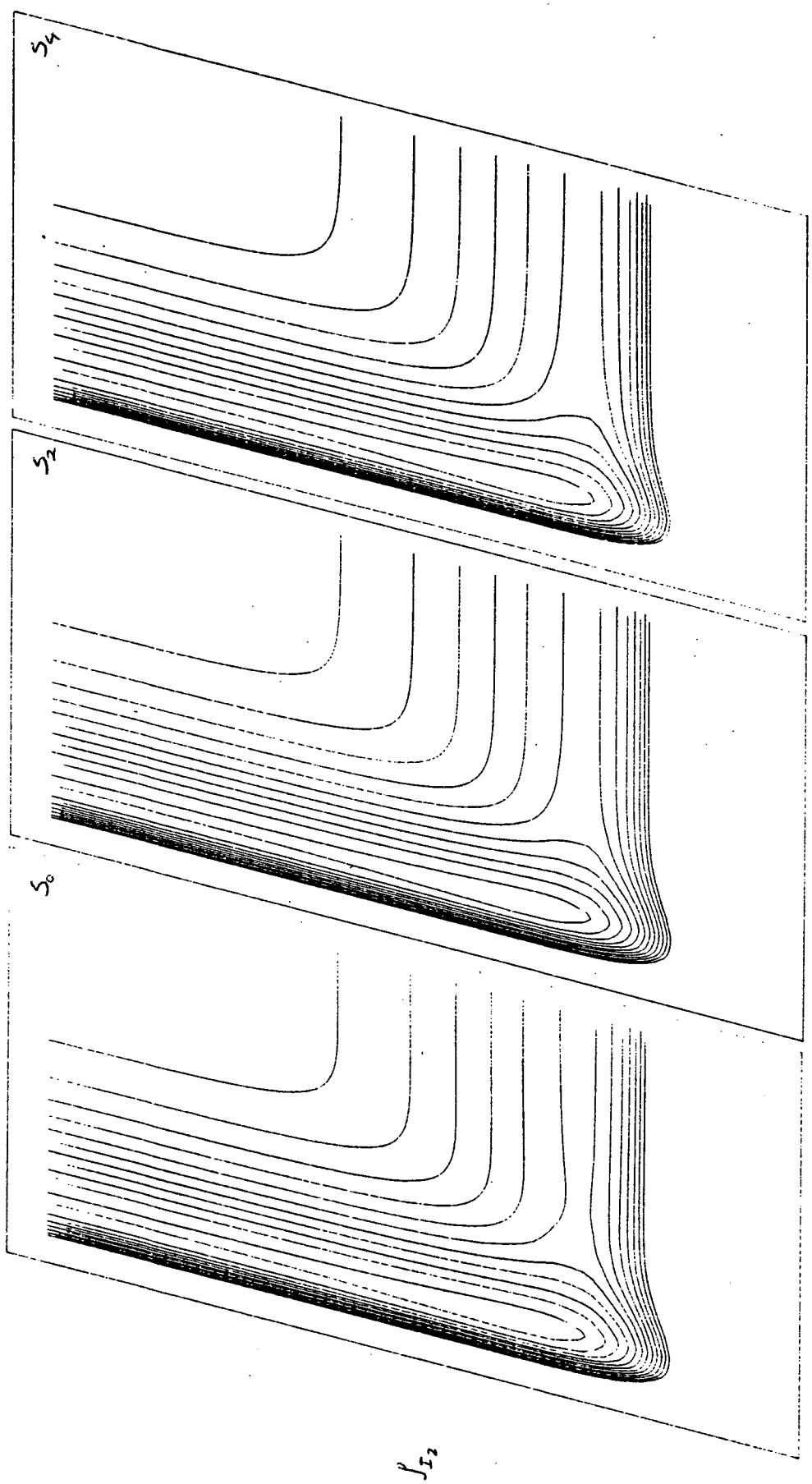

Figure 3.2 Fixed angle scan contour plots of the potential energy surfaces using skewed and scaled coordinates. The contours are shown at 0.25 eV intervals. A slight barrier is apparent for surface S_0.

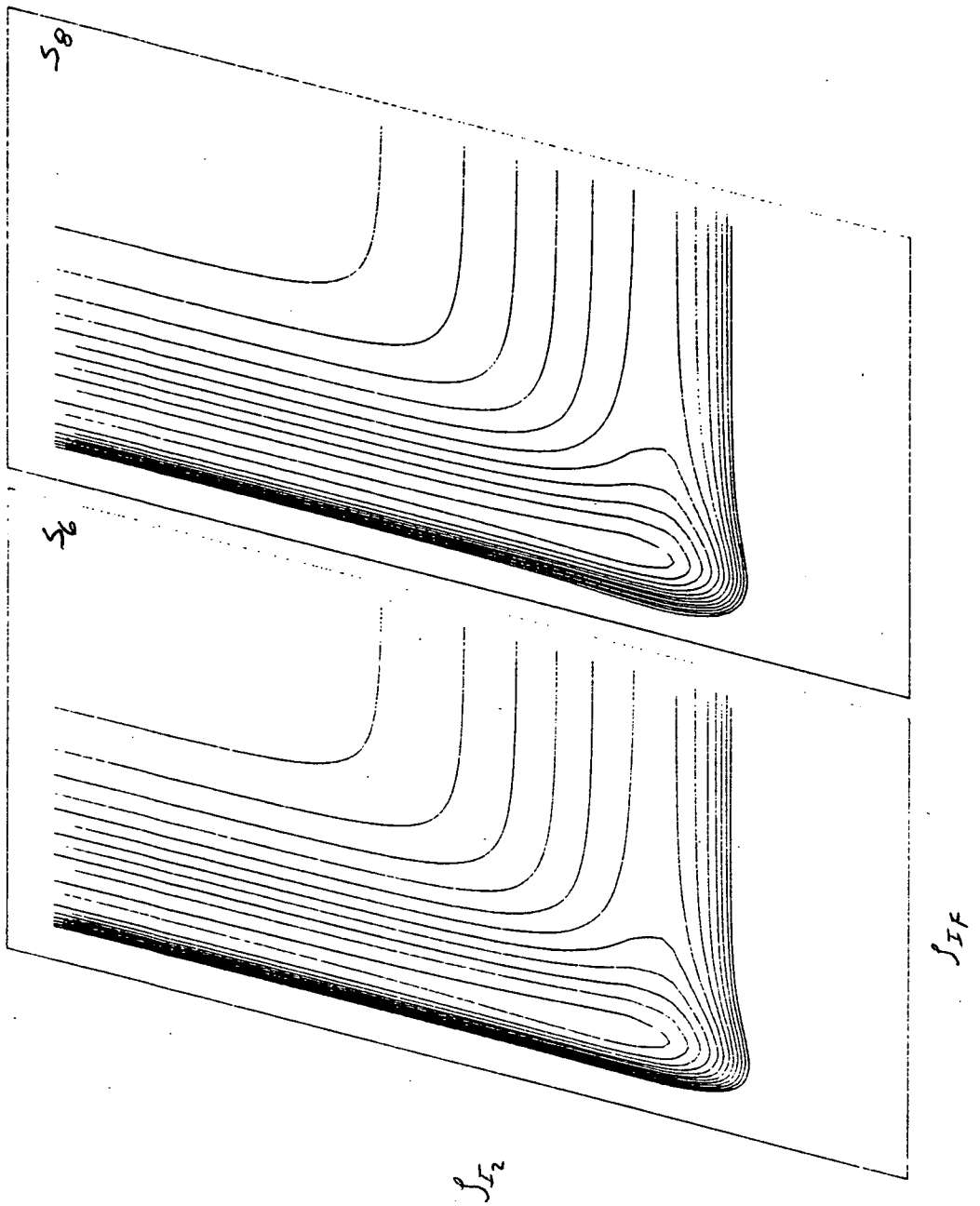
58
56
f_{I_2}
f_{I_F}

with $\beta = \left((M_I + M_F)/2M_F\right)^{1/2} = 1.960$ and $\sin\phi = 1/2\beta$ such that $\phi = 14.8^{\circ}$.

Surface	Sato Parameters		Well depth ($KJmol^{-1}$)	Well Position	
	s_{IF}^2	$s_{I_2}^2$		$r_{IF}/\text{Å}$	$r_{I_2}/\text{Å}$
S_o	0.0	0.533	12.5	1.9152	2.924
S_1	0.1	0.515	12.7	1.9159	2.917
S_2	0.2	0.494	12.6	1.9165	2.904
S_3	0.3	0.473	12.6	1.9171	2.899
S_4	0.4	0.450	12.5	1.9177	2.8 6
S_5	0.5	0.420	12.5	1.9180	2.875
S_6	0.6	0.390	12.6	1.9182	2.859
S_7	0.7	0.355	12.6	1.9179	2.842
S_8	0.8	0.310	12.6	1.9168	2.825

Table 3.2 The nine surfaces used in the study labelled S_o to S_8 with the Sato parameter s_{I_2} adjusted so that the well depth was close to the experimental value 12.6 KJ mol^{-1} (VAL77). Also shown are the well and positions of the well. Barrier in s_o, 1.71 KJ mol^{-1}, at r_{IF} = 2.998Å, r_{I_2} = 2.680Å.

From figure 3.2 and table 3.2 the surfaces are seen to satisfy the experimental criteria of well and activation energy. The situation of the well in the exit channel is physically plausible considering the strength of the I - F interaction. The surface is very attractive implying a large cross section,

again agreeing with the measured data.

In figure 3.3 the variation of the well position is shown for the surfaces used. From S_8 to S_o the well is seen to move further out into the exit channel, r_{I_2} increasing with s_{I2}. r_{IF} initially increases with its Sato parameter s_{IF} but decreases again for s_{IF}^2 greater than 0.6.

3.5.1 Colinear Trajectories

In Table 3.3 the rectilinear and trajectory classifications (KUN76) are used to describe the surfaces. In the colinear case the product vibrational energy V' is usually proportional to $\%A_T + \%M_T$, the sum of the attractive and mixed energy release. If however the approaching atom is very light then V' scales with $\%A_\perp$ and exhibits the light atom anomaly.

To prevent the repulsive components appearing negative $\%A_T$, $\%A_\perp$ etc. have been calculated relative to the bottom of the well. It is seen that the surfaces are very attractive in the rectilinear classification, even given the barrier of S_o. In the trajectory classification $\%A_T$ increases from S_1 to S_8 with a corresponding decrease in $\%M_T$ so that their sum is almost constant over the entire range. These values would suggest that a highly vibrationally excited diatomic product might be expected.

A caveat must be raised however when the one dimensional trajectory of figure 3.4 is considered. This trajectory, used to calculate $\%A_T$ (no reactant vibration), and the few run with reactant vibration were nearly always non-reactive. Because of the high attraction of the surface and the mass combination,

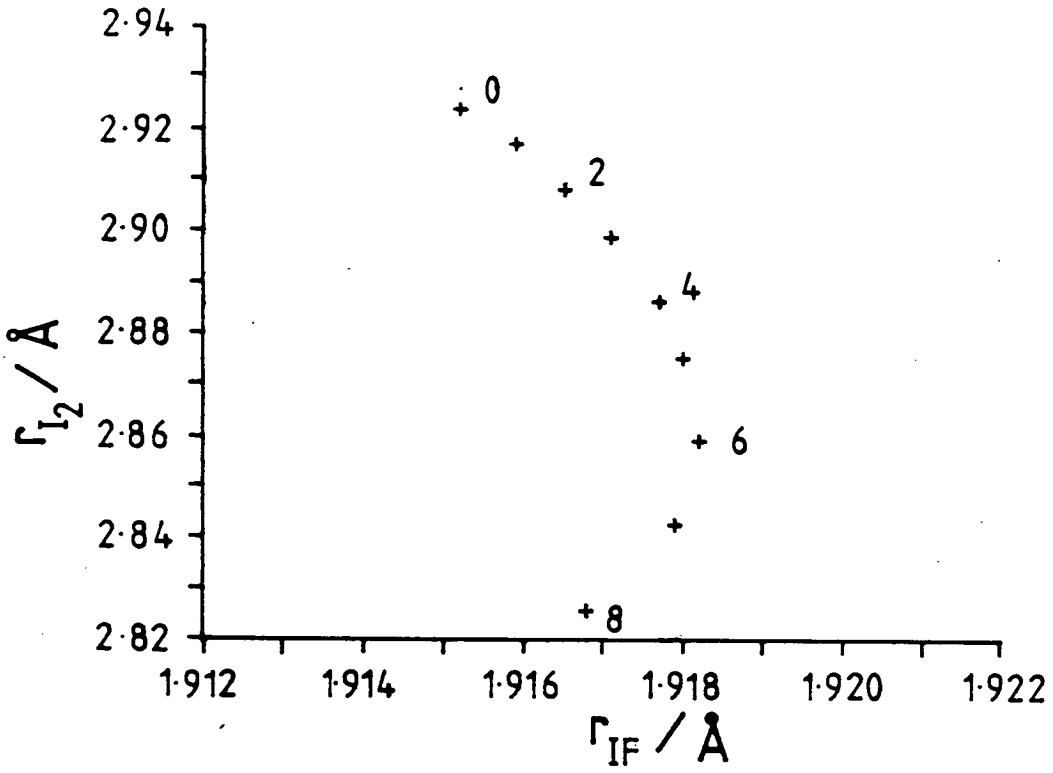

Figure 3.3 Variation of well position with Sato parameters for surfaces S_0 to S_8.

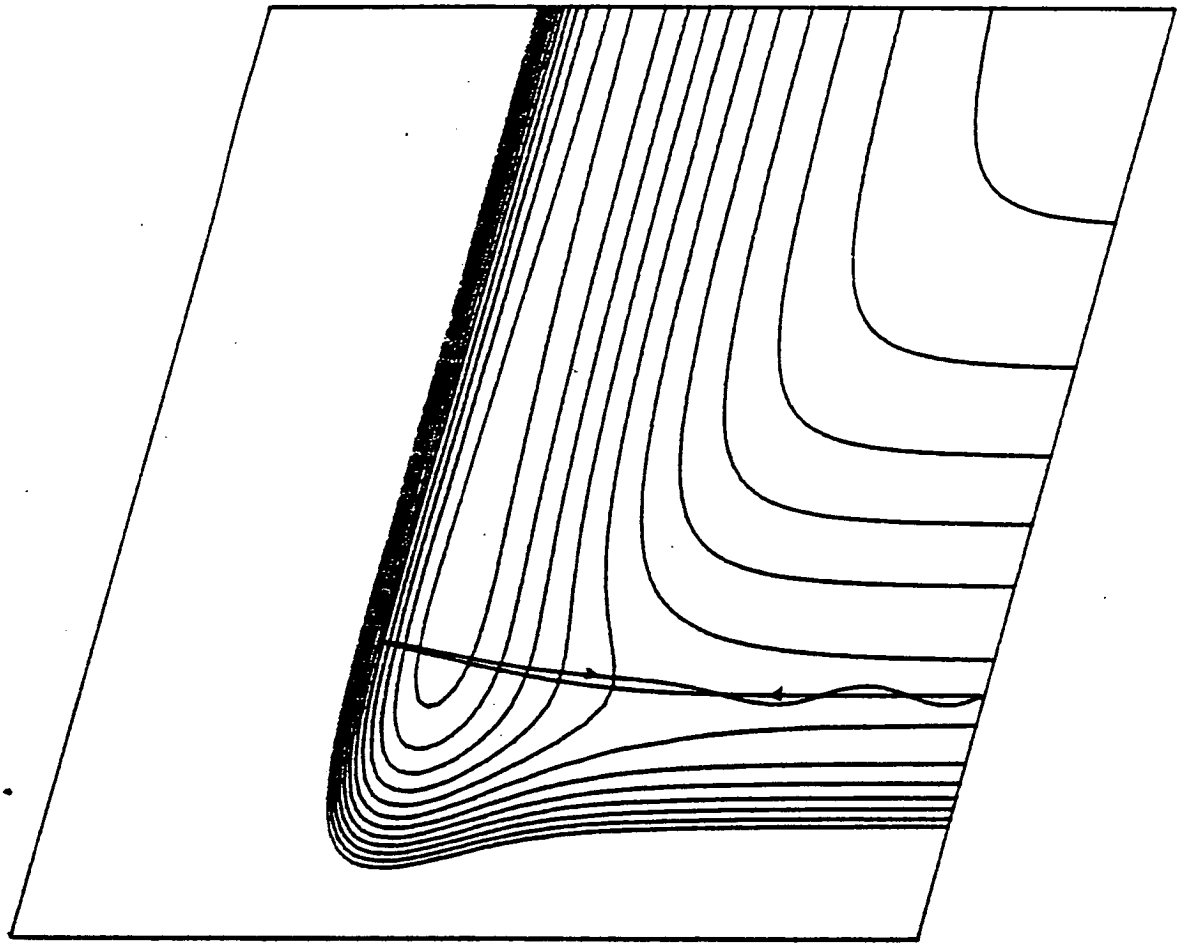

Figure 3.4 Colinear Trajectory with no reactant vibration run at 0.025 eV translational energy.

the trajectory was reflected straight back along the entrance channel. This effect was not evident in the three dimensional studies showing the pitfalls of a one dimensional calculation.

Surface	$\%A_T$	$\%M_T$	$\%R_T$	$\%A_\perp$	$\%R_\perp$
S_o	-	-	-	90.6	9.4
S_1	40.1	56.7	3.2	90.7	9.3
S_2	51.0	46.6	2.4	90.8	9.2
S_3	57.2	40.1	2.7	91.0	9.0
S_4	65.4	30.9	3.7	91.2	8.8
S_5	69.7	27.2	3.1	91.3	8.7
S_6	77.1	19.2	3.7	91.6	8.4
S_7	82.7	14.2	3.1	92.0	8.0
S_8	84.3	14.3	1.4	92.2	7.8

Table 3.3 Energy release for surfaces S_o to S_8 for colinear geometry, given for the trajectory and rectilinear classifications. For S_o the 0.025 trajectory used did not cross the RKR turning point of I_2 (v = o) so that $\%A_T$ is not available.

3.5.2 Reaction models

Simple physical models are widely used to try to gain an understanding of the more complex physics associated with collisions. Depending on the lifetime of the collision a reaction can be classed as either direct or complex. A direct trajectory is the result of a single encounter and 'remembers' its immediate past. Complex trajectories generally behave statistically and RRKM theory (SAF72, HOL77) and Phase Space

Theory, PST, (LIG67) have been used to describe such reactions.

While models of direct reactions are numerous, they tend to be much less general. Several good models based upon repulsion in the retreat reaction coordinate exist, such as the Impulsive, Gradual Force (POL74) and DIPR (KUN70) models. Very few allow for any approach coordinate interaction. Those that do, such as the harpooning mechanism (MAG40) or the polarisation model of ion-molecule reactions (GI058), tend to be very specific. Usually these models only give reaction cross sections and energy dependence, without attempting to predict any properties of the product.

Some of the models that could be applied to the F + I_2 system are shown in table 3.4 along with some of the properties that they would predict.

3.6 Results

Surfaces S_o and S_1 both exhibited some characteristics of reactions with energy barriers. These surfaces were only investigated at a single energy. Surfaces S_2 to S_7 were investigated at four translational energies, T, 0.25 eV, 0.06eV, 0.09eV and 0.2eV. The narrow range was chosen to cover the experimental data. The trajectories were all run with a rotational energy corresponding to J = 55 including a batch at T = 1.0eV for surface S_3. One batch for surface S_3 at T = 0.06eV was run at J = 150.

Surface S_8 introduces a deep well in the surface for the I - F - I configuration. This is a known defect of the LEPS formation (MUR78) and is unlikely to be a realistic representation. A restricted range of T was used for this surface.

	Model	T'	V'	R'	χ	σ_R	t_c	Comment
Complex	RRKM (SAF72,HOL77)	$\langle T' \rangle = E/3$ $P(T') = (E-T')$	$\langle V' \rangle = E/3$	$\langle R' \rangle = E/3$	Symmetric about 90°	$\sigma_R \propto E^{-\frac{1}{3}}$	$t_c \geq t_r$	
	PST/Prior (LIG67,LEV79)	$\langle T' \rangle = 3/7\ E$ $P(T') = T'^{\frac{1}{2}}(E-T')$	$\langle V' \rangle = 2/7\ E$ $P(V') = (E-V')^{\frac{3}{2}}$	$\langle R' \rangle = 2/7\ E$	"	-	"	
Direct	Impulsive (POL74)	$\langle T' \rangle = E - C_{ac}E_R$	$\langle V' \rangle = C_{ac}E_R \cos^2 \alpha$	$\langle R' \rangle = C_{ac}E_R - V'$	Backward peak	-	$t_c < t_r$	Often underestimates V'
	Gradual Force (POL74)	$\langle T' \rangle \geq \langle T' \rangle_{imp}$	$\langle V' \rangle \leq \langle V' \rangle_{imp}$	$\langle R' \rangle \leq \langle R' \rangle_{imp}$	"	-	"	DIPR model is in this category
	Spectator Stripping (HEN65)	$\langle T' \rangle = C_{ac}T$	-	$\langle R' \rangle$ = fract. of T.	Forward	large	"	No provision for H. Usually gives high energy limit.
	Colinear Surface (KUN70)	$\langle T' \rangle = \%R.E$	$\langle V' \rangle = (\%A_T + \%M_T)E$	-	-	-	-	See section 3.5.11

$C_{ac} = \frac{m_A}{m_A + m_B} \frac{m_C}{m_B + m_C} = 0.065$ for $F + I_2$; α = bond angle ; E_R = Repulsive energy release (POL74)

Table 3.4 Some reaction models and their predicted product properties.

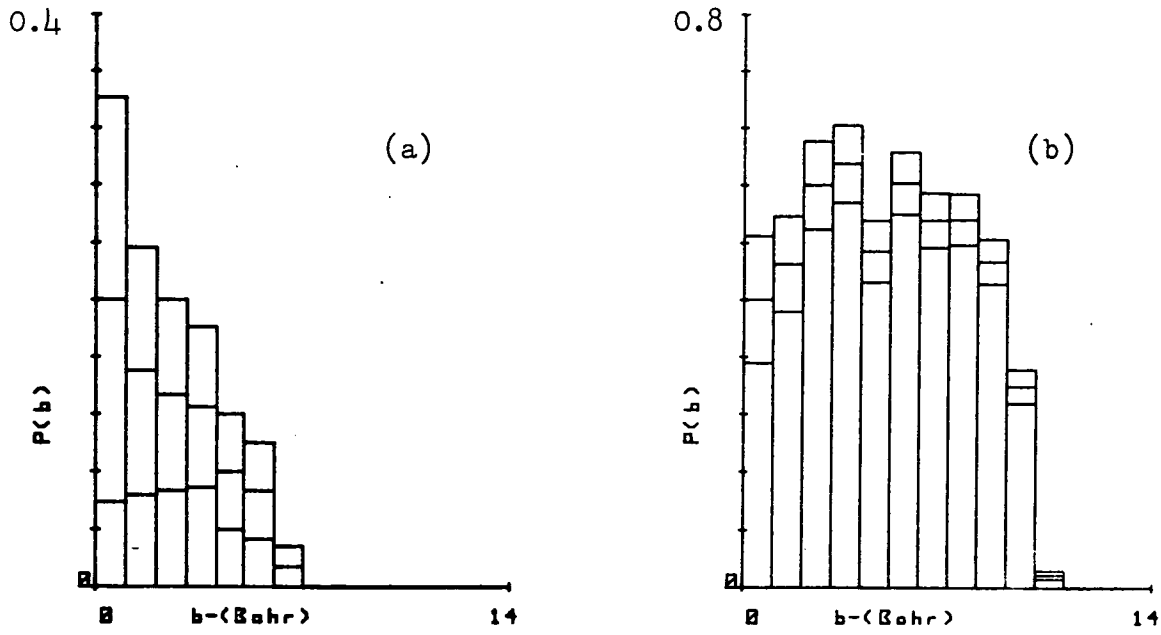

Figure 3.5 Opacity functions for surfaces S_0 (a) and S_2 (b) showing the effect of the barrier in surface S_0.

3.6.1 Cross Sections and Opacity

The impact parameter, b, for the trajectories was scanned from 1 a.u. up to a maximum, b_m, in steps of 1 a.u. The number of trajectories run at each impact parameter was weighted according to $n(b) = b$. b_m was determined by a test batch and was found to be fairly constant for S_3 to S_8 but fell sharply from 10 a.u. for S_2 to 7 a.u. for S_0.

Figure 3.5 shows the opacity functions $p_r(b)$ for surfaces S_0 and S_2 at 0.06eV. Figure 3.5a shows $p_r(b)$ decreasing with b which is characteristic of reactions proceeding via a barrier (GRI75), while figure 3.5b shows the nearly constant behaviour expected from reactions with no activation energy. Figure 3.6 shows the behaviour of $p_r(b)$ for surface S_3 across the range of energies used. These results are typical of all

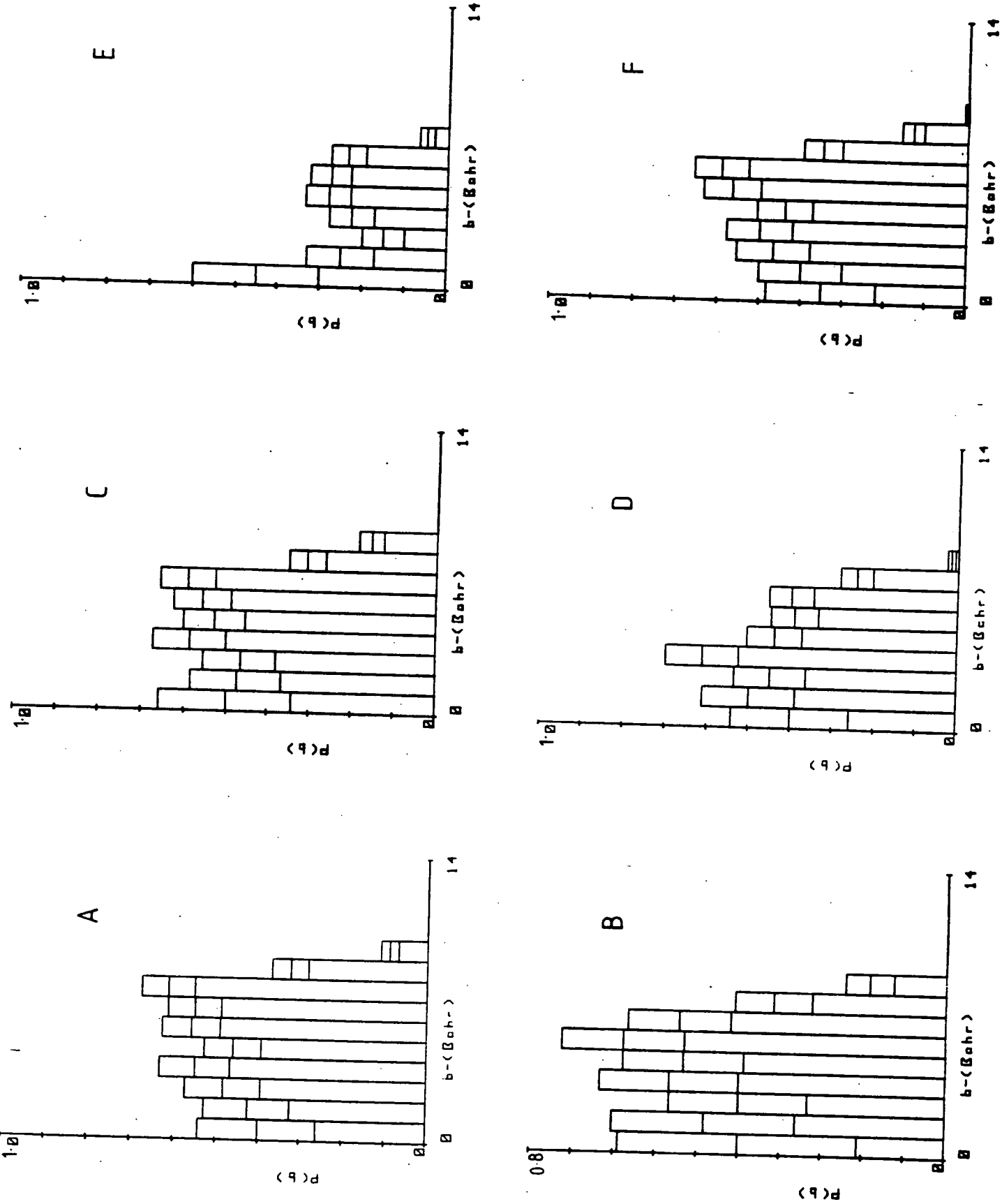

Figure 3.6 Opacity functions for surface S_3 for energies (A) 0.025 eV (B) 0.06 eV (C) 0.09 eV (D) 0.2 eV (E) 1.0 eV. (F) rotationally excited reactant.

the surfaces employed showing a decrease in b_m with translational energy input as would be expected.

The reactive cross section σ_r for the trajectory calculation is obtained from

$$\sigma_r = b_m^2 \frac{N_r}{N} \qquad 3.12$$

where N is the number of trajectories run and N_r is the number that react. The error in σ_r is given by

$$\Delta\sigma_r = b_m^2 \frac{N_r}{N} \frac{(N - N_r)^{\frac{1}{2}}}{N_r N} \qquad 3.13$$

Results for the calculations are listed in table 3.5.

A monotonic decrease of σ_r with T is observed for all surfaces except S_2. These points qualitatively follow the statistical complex model (MIL67) that σ_r varies with $T^{-\frac{1}{3}}$ for reactions proceeding without activation energy. Log-log plots (fig.3.7) are approximately linear with gradients given in table 3.5. Centrifugal narrowing of the reactant channel is probably the cause of the rising cross section obtained for surface S_2 at low energies.

It is interesting to note that for most energies the cross section is a maximum for surface S_6. This parallels quite closely the position of the well with respect to the I - F coordinate, r_{IF}. r_{IF} reaches a peak for the Sato parameter $s_{IF} = 0.6$ (figure 3.3) while $\%A_T$ and $\%A_\perp$ continue to increase with s_{IF}. Quite why this occurs is uncertain as the potential energy along the reaction coordinate for S_6 is greater than that for S_7 for all r_{IF} less than 10 Å.

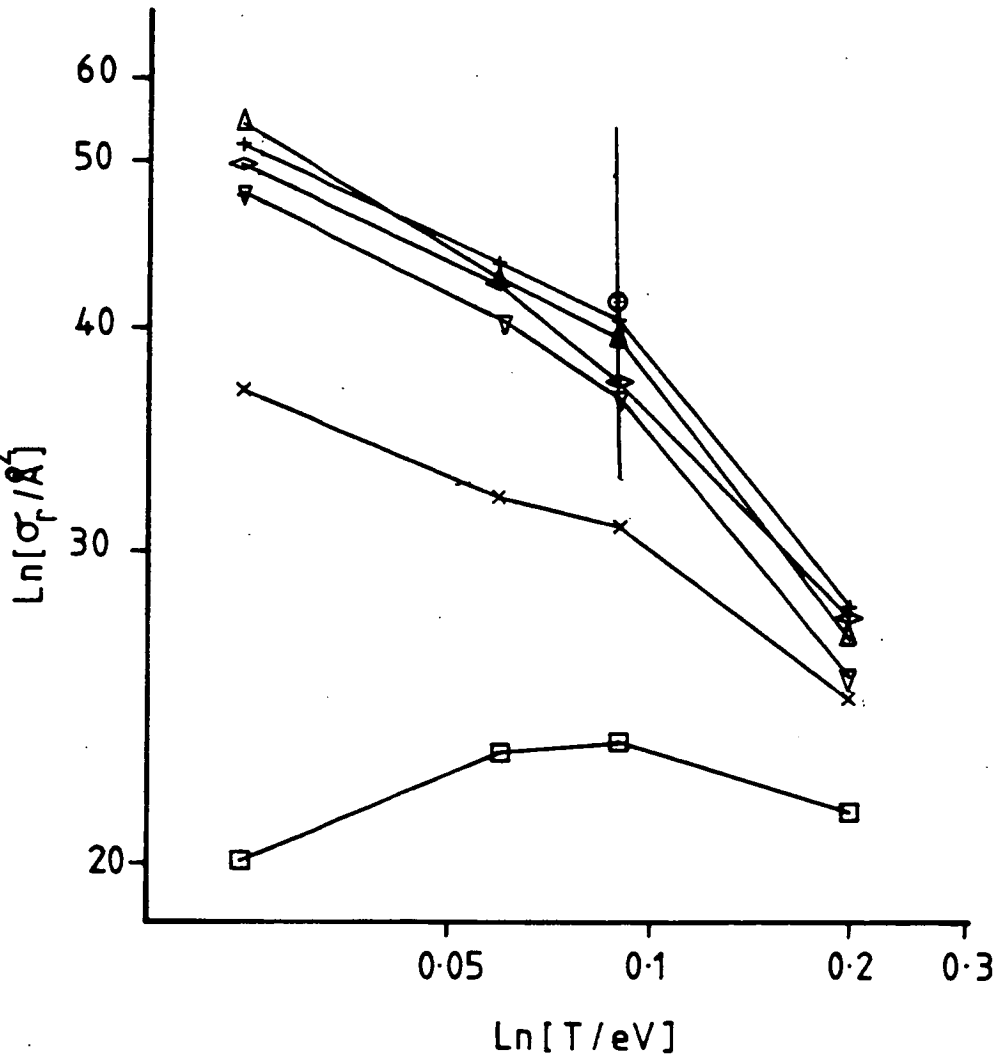

Figure 3.7 Log-log plot of the reaction cross section against initial translational energy for surfaces S_2 to S_7. The experimental result is also shown.

Key: □ - S_2 ∇ - S_4 + - S_6
× - S_3 ◇ - S_5 Δ - S_7
○ - exp. value

T/eV	0.025	0.06	0.09	0.20	g
S_0		2.99 ± 0.62			
S_1		12.9 ± 1.2			
S_2	20.2 ± 1.1	23.2 ± 1.2	23.3 ± 1.2	21.3 ± 1.3	
S_3	37.1 ± 1.3	32.1 ± 2.3	30.8 ± 1.3	24.8 ± 1.2	-0.19
S_4	47.5 ± 2.1	40.4 ± 2.0	36.3 ± 2.0	25.2 ± 1.8	-0.30
S_5	49.4 ± 2.0	42.5 ± 2.0	36.8 ± 2.0	27.4 ± 1.8	-0.28
S_6	50.8 ± 1.5	43.3 ± 2.0	40.5 ± 2.0	27.7 ± 1.8	-0.27
S_7	52.3 ± 2.1	42.5 ± 2.0	39.7 ± 2.0	26.9 ± 1.8	-0.31
S_8		41.9 ± 0.9	37.2 ± 0.9		

Table 3.5 Reaction cross sections ($\AA^2$) for surfaces S_0 to S_8 for each energy used. The errors are calculated from equation 3.14. Also shown is the power dependence of σ_R on the initial energy. At 1.0 eV and for J = 150 the cross sections are 11.8 ± 0.6$\AA^2$ and 31.0 ± 1.3$\AA^2$ respectively.

T/ev	0.025	0.06	0.09	0.20	1.00	0.06:J=150
S_0		*				
S_1		*				
S_2	1.4	1.4	1.1	1.0		
S_3	1.8	1.7	1.2	1.0	0.5	1.3
S_4	1.6	1.2	1.2	1.1		
S_5	1.7	1.4	0.9	0.8		
S_6	1.7	*	*	0.8		
S_7	1.5	1.2	0.9	0.8		
S_8		1.2	0.9			

Table 3.6 Collisional lifetimes (picoseconds) for surfaces S_0 to S_8 calculated from distributions of integration times.

* - Statistics too poor to obtain a value for lifetime.

The measured value for the rate constant for the reaction is $(4.3 \pm 1.1) \times 10^{-10}$ cm^3 molecule^{-1}s^{-1} (APP75), which corresponds to $\sigma_R = (43 \pm 11)$ Å^2. This result is plotted in figure 3.7. The agreement between this value and that of most of the surfaces explored is very good, with only surfaces S_0, S_1 and S_2 well outside the experimental bounds. These surfaces exhibit the least attraction, indicating that the large experimental result can be explained by an attractive surface.

3.6.2 Collision Lifetime

The lifetime of a collision is often determined by the time for which all internuclear distances are less than a fixed value. This value must be sufficiently large for the interaction to be complete. This definition can include some trajectories that are not truly long lived. Such trajectories form products which have very small translational velocities and hence take a significant time to exit from the interation region. This effect was judged to be small in this study and such cases were not specially treated.

Lifetime distributions for different energies on a few surfaces are shown in figure 3.8(a). Statistical theories demand that any long lived species decay in a random manner. This implies that the distribution of integration times should decay exponentially with time. Plots of Ln [P(t)] vs time can be used to assign a lifetime t_c to the collisional complex. Some of these are shown in figure 3.8(b). The shorter lifetime

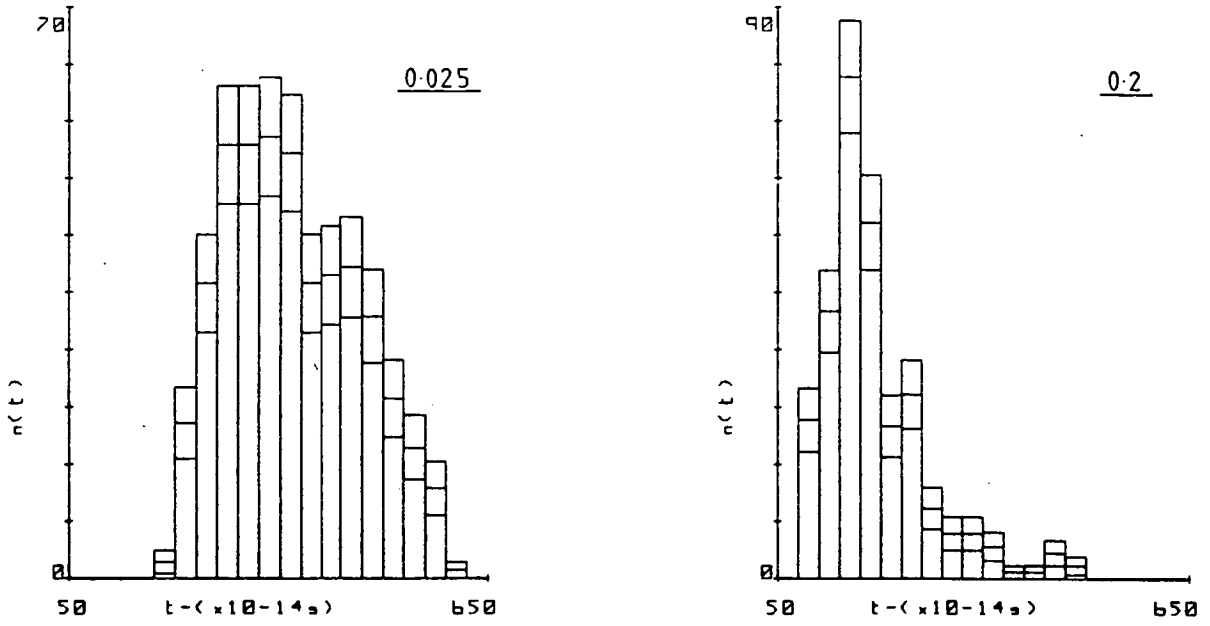

Figure 3.8a Integration time distributions for surface S_3 for energies 0.025 eV and 0.2 eV.

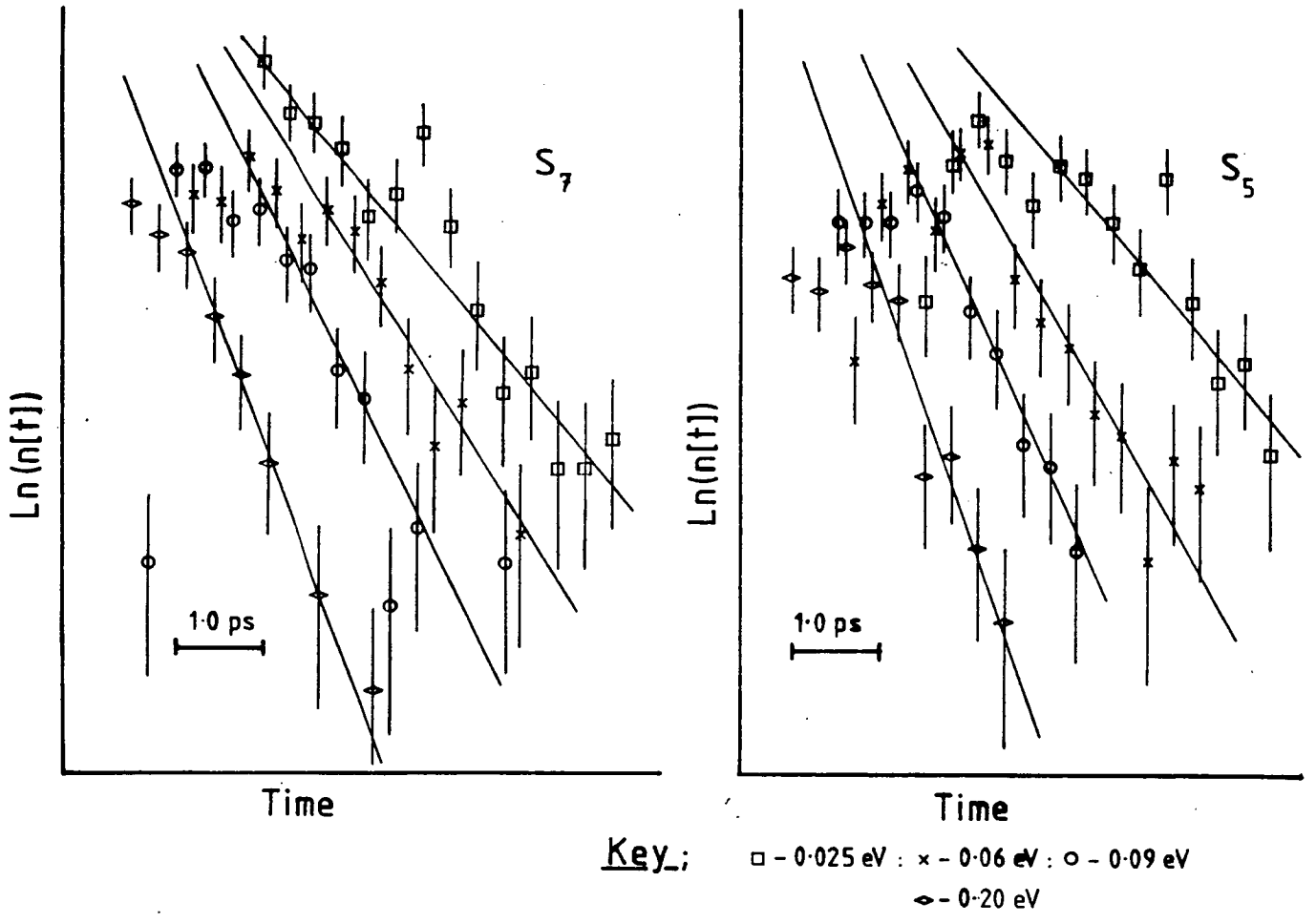

Figure 3.8b Log plots of the integration time distributions for surfaces S_5 and S_7.

points arose mainly from direct trajectories and consequently did not behave statistically. The longer lived ones behaved approximately exponentially and the lifetime was taken from this portion of the graph. Lifetimes calculated in this manner are listed in table 3.6.

RRKM theory gives an estimate for the lifetime t_o as

$$t_o = t_v \cdot \left(\frac{E + \epsilon}{E} \right)^n \qquad 3.14$$

where ϵ is the well depth with respect to the products

E is the total energy

t_v is a representative vibrational period for the complex. For a tight complex, n = 3 while n = 5/2 for a loose complex. Modifications to this expression to include angular momentum effects can be introduced (MIL73) but for the case of I_2 + F the exoergicity is the dominant term in the expression. This gives the statistical lifetime of the complex as t_o = 0.13 ps (if t_v is taken as 10^{-13}s). More information on t_v would be required for a detailed comparison however the values given in table 3.6 are on average an order of magnitude greater than t_v.

The critical lifetime for a complex is the rotational period, t_R. If the complex lifetime exceeds t_R then a statistical redistribution of energy along with a differential cross section peaked at the forward and backward poles can be expected (FLU73). If t_c is approximately equal to t_R then their ratio can sometimes be inferred from the ratio of the forward peak intensity to that of the backward peak (MIL67).

The rotational period can be calculated from the angular

momentum components of the reactants. Assuming all the translational energy appears as rotation then the following t_R are minimum for each T

T/eV	0.025	0.06	0.09	0.2	1.0	0.06 (J = 150)
t_R/ps	5.5	4.2	3.6	2.6	1.2	2.5

These are longer than any of the calculated lifetimes, implying that a direct mechanism is dominant for this system.

3.6.3.1 Scattering Angle

The angular distributions for the surface S_3 are shown in figure 3.9 with average values and widths for all the surfaces listed in table 3.7. The distributions for surface S_3 are typical of all the surfaces employed. At low energies the distributions are very similar, mostly broad and symmetric about $\chi = 90^{\circ}$. Only when T = 1.0 eV does the symmetry disappear and a modest backward peak forms.

To facilitate the analysis of these results the data can be compared with the uniform phase space (UPS) distribution (MUC79). Equal volumes of phase space correspond to equal partitions of the solid angle Ω Transforming the scattering angle χ to u according to

$$du = \tfrac{1}{2} \sin\chi \, d\chi \qquad 3.15$$

and binning with respect to u gives each bin equal weight in phase space. Distributions over u are shown in figure 3.10. Here variations with scattering angle are more obvious. At T = 0.025eV the distribution is almost constant with u. As the energy increases towards 0.2 eV, peaks in the distribution appear at the forward and backward poles while retaining the

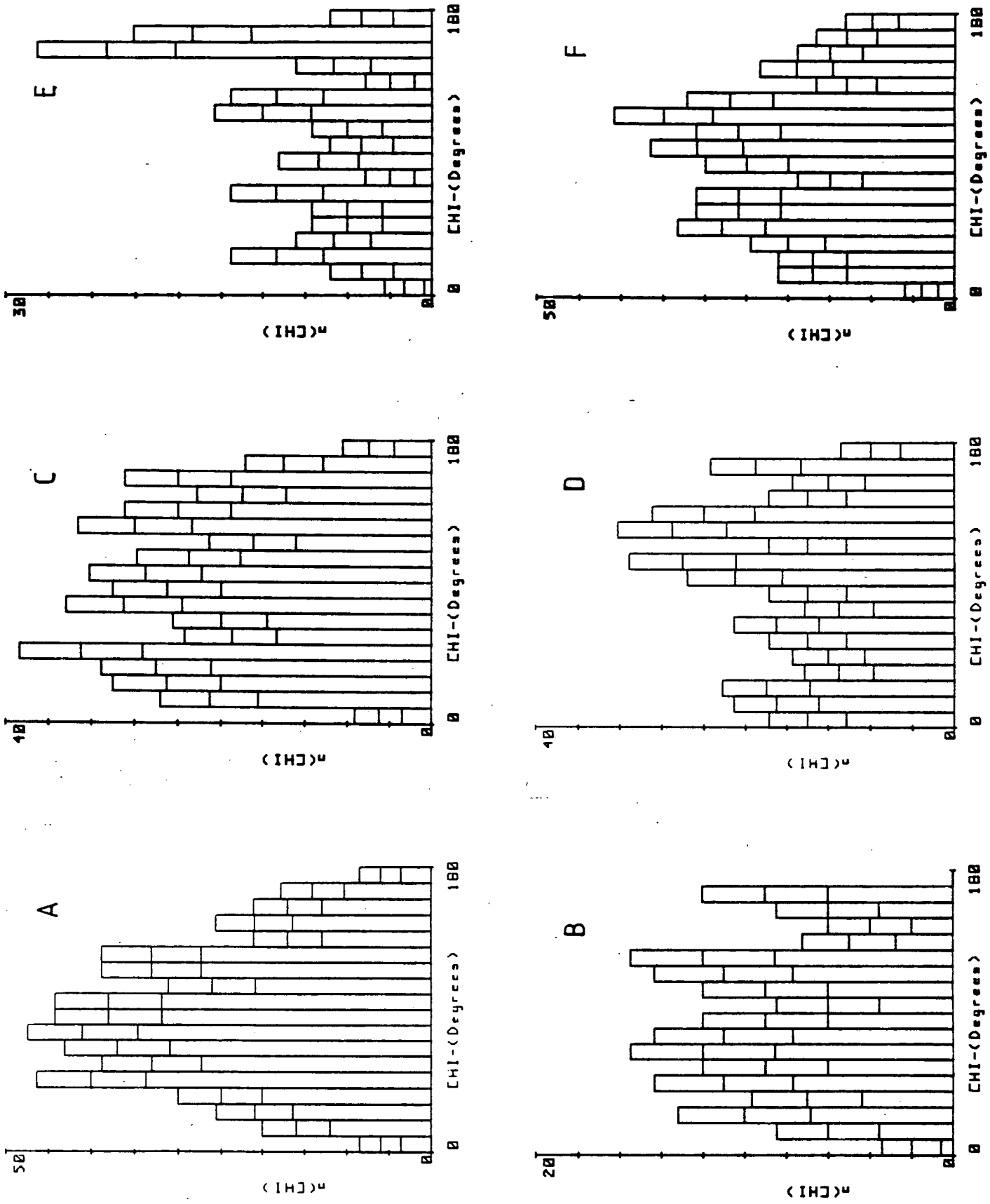

Figure 3.9 Angular scattering distributions for surface S_3. See fig. 3.6 for key.

T/eV	0.025	0.06	0.09	0.2	1.0	0.06:J=150
S_0		84.3 ± 7.2 34				
S_1		87.9 ± 4.0 40				
S_2	91.1 ± 2.5 40	85.3 ± 2.6 44	80.7 ± 2.6 44	93.3 ± 3.4 48		
S_3	85.9 ± 1.9 42	85.7 ± 3.7 44	87.2 ± 2.4 46	92.5 ± 2.9 50	104.0 ± 4.2 51	89.6 ± 2.3 44
S_4	88.8 ± 2.5 43	96.2 ± 2.9 46	88.0 ± 3.1 46	95.2 ± 3.9 48		
S_5	93.4 ± 2.6 45	88.5 ± 3.0 48	96.4 ± 3.1 46	97.4 ± 3.6 47		
S_6	95.7 ± 1.8 44	92.2 ± 2.9 47	94.8 ± 3.0 48	93.3 ± 3.7 48		
S_7	96.9 ± 2.5 45	92.5 ± 3.0 49	94.9 ± 2.9 46	97.5 ± 3.6 46		
S_8		93.0 ± 1.3 46	94.5 ± 1.3 45			

Table 3.7 Average values (upper figure) and widths (standard deviation) in degrees of the angular scattering distributions for surfaces S_0 to S_8.

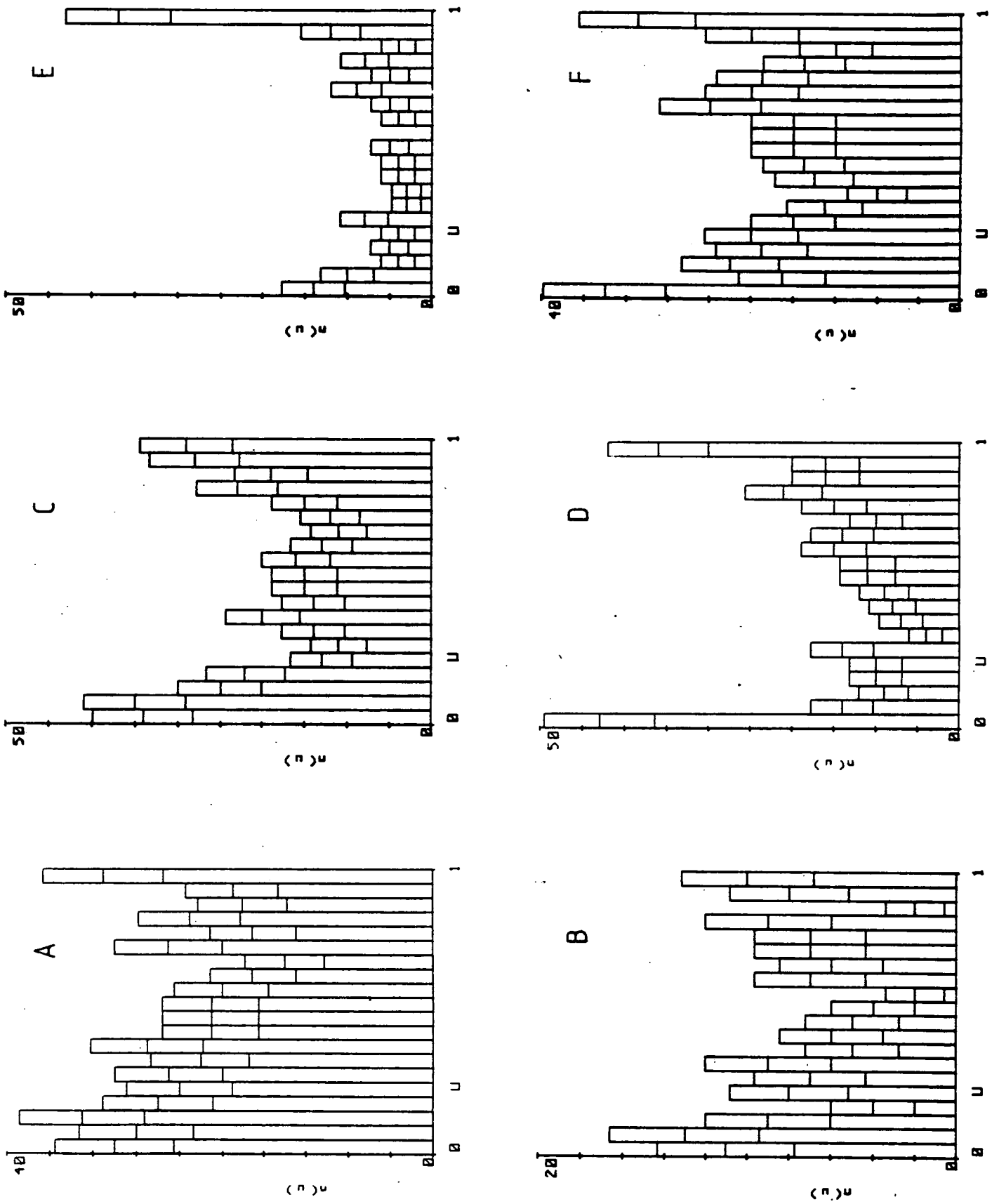

Figure 3.10 Scattering distributions for surface S_3 plotted against the transformed variable u , see text for details. See fig. 3.6 for key.

symmetry about $\chi = 90^{o}$. At T = 1.0eV the backward peak is very evident in this UPS analysis.

The change in angular distribution occurs because of the increase in orbital angular mementum (OAM) of the system. The average OAM, L, for the different energies are

T/eV	0.25	.06	.09	.20	1.0
L/$\hbar$	49	75	92	137	259

compared with the rotational angular momentum (RAM) J = 55 $\hbar$.

At very low T the major contribution to the angular momentum of the system is the rotation of I_2. If the products depart along the line of the dissolving I - I bond then the scattering angle will simply reflect the distribution of initial I_2 orientations. This distribution is random in phase space, that is P(u) = constant or P (χ) = $\frac{1}{2}$ sinχ which is approximately what is observed at low energy. As the OAM increases, the total angular momentum increasingly correlates with $\underline{L}$. This tends to force a correlation between $\underline{L}'$ and $\underline{L}$, similar to the statistical complex model (MIL67). This effect is slight and is only obvious in the UPS analysis.

This simple model would be quite sensitive to changes in $\underline{L}$ or $\underline{J}$ when they are nearly equal and could account for the difference in the measured angular distributions (CAR73, WON73). Increasing $\underline{J}$ from J = 55 to J = 150 had little effect at the energy used. A more extensive investigation of the rotational effects would be useful.

The measured angular distributions for $O + I_2/Br_2$ at nearly thermal energies gave similar distributions to those calculated here (RAD75). However at higher energy, 0.3 eV, the distribution for the similar mass combination of $O + I_2$ is backward peaked (CLO78) so that the 1.0eV result obtained here is probably realistic.

3.6.3.2 Rotational angular momentum reorientation angle

Distributions of θ, the angle between the initial $\underline{J}$ and final $\underline{J}'$ rotational angular momenta, are broad and peaked near 90° (figure 3.11, table 3.8) The similarity between these distributions and a sine distribution is very close, for higher energies in particular. For all the surfaces the similarity of the distributions at 0.2 eV to the sine distribution is statistically significant at the 10% level or greater. The lower energy results, while visually similar, have means significantly removed from 90°.

A sine distribution would suggest $\underline{J}$ and $\underline{J}'$ were uncorrelated. A small correlation may therefore exist for the low T results but is lost as the OAM of the reactants increases. This is emphasised when the distributions for T = 1.0eV, J = 55 and T = 0.06, J = 150 are considered. The former agrees extremely well with the sine distribution with a level of significance of more than 75%. The h igh RAM case seems to be biased towards $\theta = 0^\circ$ and its level of significance is very much less than 0.2%.

3.6.3.3 Orbital angular momentum reorientation angle

In all cases the OAM reorientation angle, ϕ the angle between $\underline{L}$ and $\underline{L}'$ was peaked between 0° and 90°, decreasing with T as would be expected, figure 3.12, table 3.9.

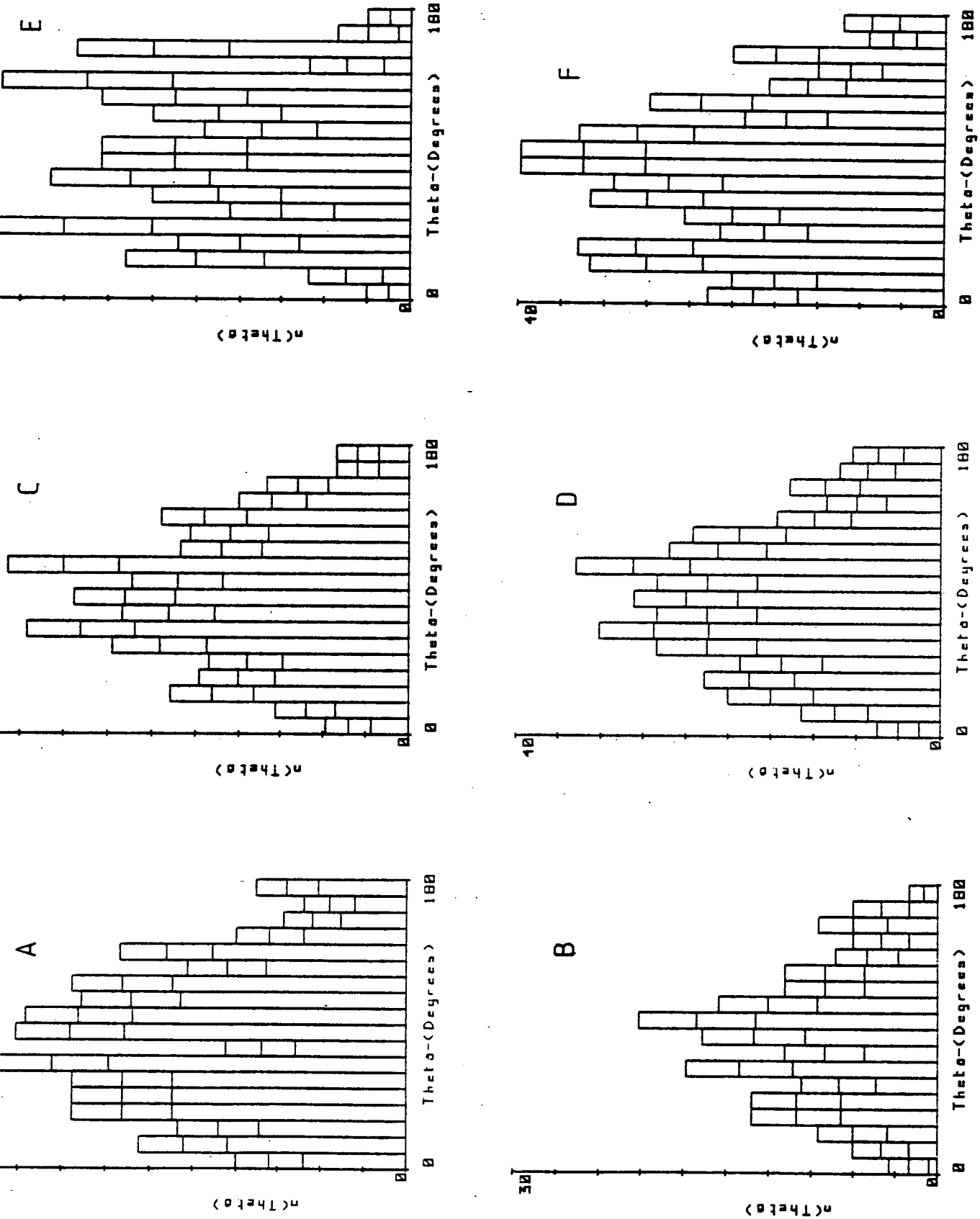

Figure 3.11 Rotational angular momentum reorientation angle distribution for surface S_3. See fig. 3.6 for key.

T/eV	0.025	0.06	0.09	0.20	1.0	0.06:J=150
S_0		70 ± 10				
S_1		82 ± 5				
S_2	79.9 ± 2.8	85.1 ± 2.5	84.5 ± 2.5	88.9 ± 2.7		
S_3	82.1 ± 2.1	86.7 ± 3.4	85.5 ± 2.1	86.1 ± 2.4	90.0 ± 3.5	79.2 ± 2.3
S_4	84.4 ± 2.6	84.1 ± 2.8	84.5 ± 2.7	96.6 ± 3.1		
S_5	85.5 ± 2.5	84.8 ± 2.8	87.6 ± 2.8	94.6 ± 3.2		
S_6	86.1 ± 1.9	85.0 ± 2.6	85.3 ± 2.8	92.4 ± 2.9		
S_7	88.1 ± 2.5	84.9 ± 2.7	85.7 ± 2.7	93.1 ± 3.0		
S_8		87.6 ± 1.2	84.4 ± 1.2			

Table 3.8 Average values (degrees) for the rotational angular momentum reorientation angle $\langle\theta\rangle$, for surfaces S_0 to S_8.

T/eV	0.025	0.06	0.09	0.20	1.0	0.06:J=150
S_0		53 ± 8				
S_1		50 ± 4				
S_2	60.3 ± 2.6	50.3 ± 2.2	49.5 ± 2.2	48.0 ± 2.4		
S_3	61.0 ± 1.9	50.0 ± 3.6	51.4 ± 1.9	49.1 ± 2.1	42.0 ± 2.7	72.9 ± 2.3
S_4	67.0 ± 2.6	56.1 ± 2.7	53.4 ± 2.4	53.0 ± 2.8		
S_5	66.4 ± 2.4	53.8 ± 2.5	56.3 ± 2.6	56.0 ± 2.8		
S_6	65.2 ± 1.7	57.9 ± 2.4	54.2 ± 2.3	49.6 ± 2.5		
S_7	67.4 ± 2.3	56.1 ± 2.4	59.4 ± 2.6	54.2 ± 2.8		
S_8		61.7 ± 1.1	55.6 ± 1.1			

Table 3.9 Average values (degrees) for the orbital angular momentum reorientation angle, $\langle\phi\rangle$, for surfaces S_0 to S_8.

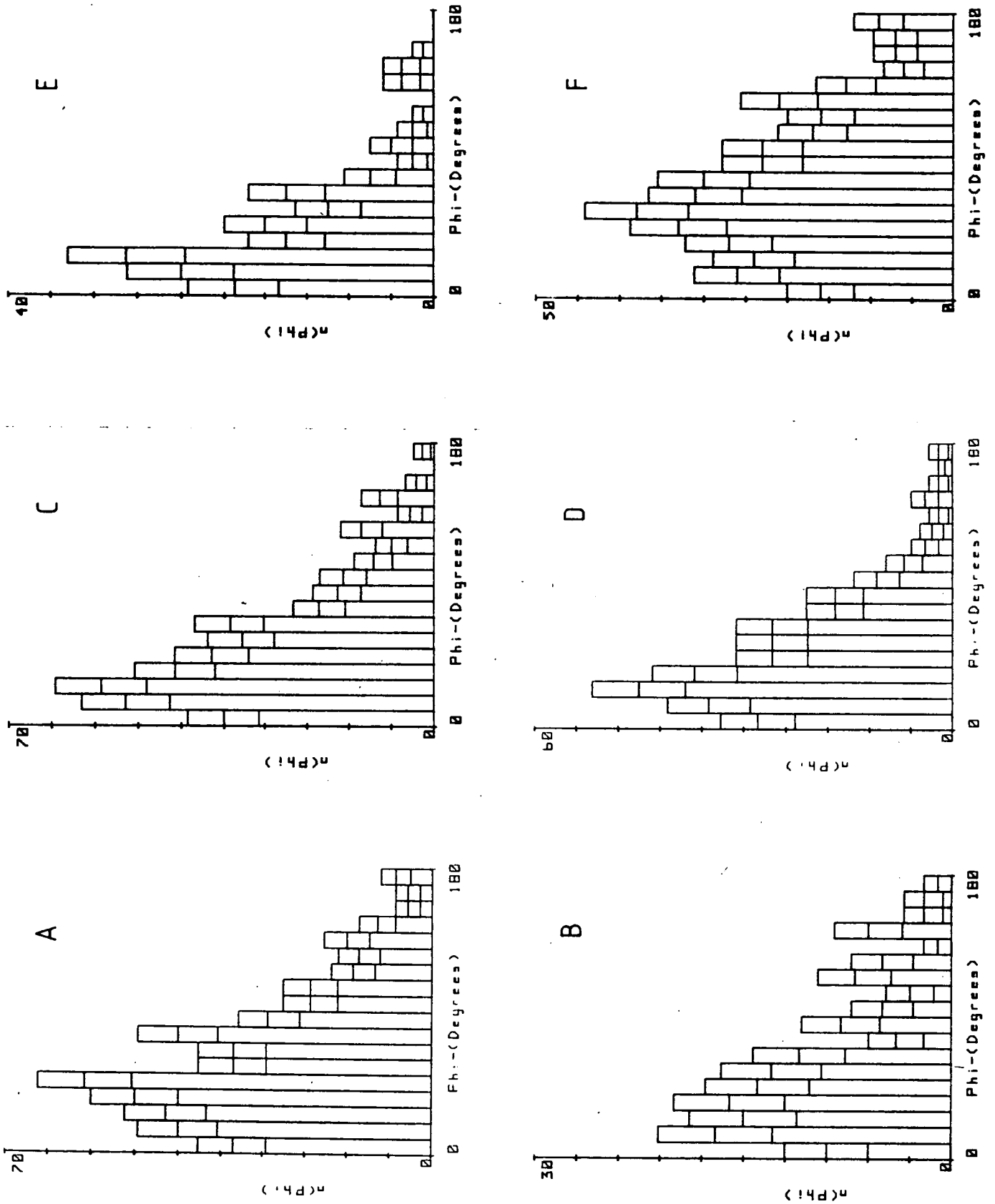

Figure 3.12 Orbital angular momentum reorientation angular distribution for surface S_3. See fig. 3.6 for key.

From the diagram

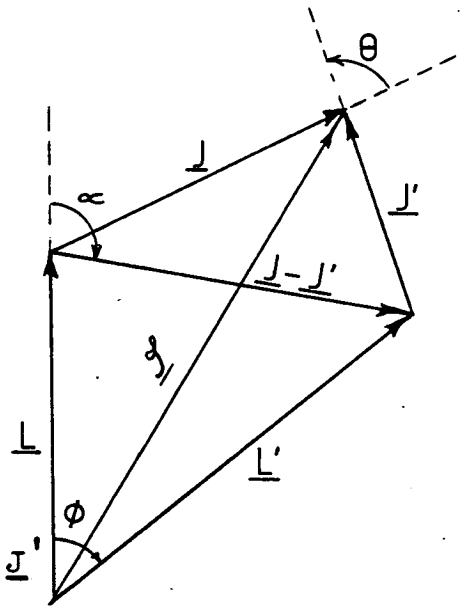

$$\phi = \tan^{-1}\left(\frac{|\underline{J} - \underline{J}'| / \sin\alpha}{L + |\underline{J} - \underline{J}'|/\cos\alpha}\right) \qquad 3.16$$

with α the angle formed between $\underline{J} - \underline{J}'$ and $\underline{L}$. If α averages to 90°, as would be the case for $\underline{J} - \underline{J}'$ randomly orientated with respect to $\underline{L}$, then as θ is about 90°.

$$\langle\phi\rangle \simeq \tan^{-1} \frac{(J^2 + J'^2)^{\frac{1}{2}}}{L} \qquad 3.17$$

Using the results for surface S_3 to obtain J', values of $\langle\phi\rangle_c$ were calculated. They are compared with $\langle\phi\rangle_T$ obtained directly from the trajectories in table 3.10.

	0.025	0.06	0.09	0.20	1.0	.06(J=150)
	56°	46°	41°	36°	27°	62°
	61° ± 2	60° ± 4	51° ± 2	49° ± 2	42° ± 3	73° ± 2
	62°	64°	60°	60°	60°	83°
	57°	56°	45°	38°	24°	67°

Table 3.10

The agreement with the trajectory results is quite poor. Re-analysing the trajectories and producing separate distributions for impact parameters less than and greater than the average value gives $\langle\phi\rangle_a$ and $\langle\phi\rangle_b$ respectively. It is seen that $\langle\phi\rangle_b$ agrees very well with $\langle\phi\rangle_c$ while $\langle\phi\rangle_a$ does not, but is fairly constant across T.

The discrepancy between $\langle\phi\rangle_a$ and $\langle\phi\rangle_c$ must be explained by α not averaging to 90°. If α does not average to 90° this suggests that there is some correlation between $\underline{L}$ and $\underline{J} - \underline{J}'$, that is between $\underline{J}'$ and $\underline{L}$, for small L.

With hindsight it would have been more informative to have computed the angles $\underline{L}\ \underline{J}'$ and $\underline{J}\ \underline{L}'$ directly.

3.6.4 Energy distributions

The product energy distributions, along with the differential cross section, are very important to the experimentalist because of their relative accessibility. These kinematic effects are therefore a strong test of any model - although such effects may not be unique.

3.6.4.1 Translational energy

The translational energy distributions for surface S_3 are shown in figure 3.13. The number of trajectories per bin is plotted against f_t', the fraction of available energy appearing as translation of the products. The distributions are peaked at low values of f_t' with the distributions becoming wider as the incoming velocity is increased.

The trend across the range of surfaces is very similar to the behaviour shown by S_3. The average values of f_t' are listed

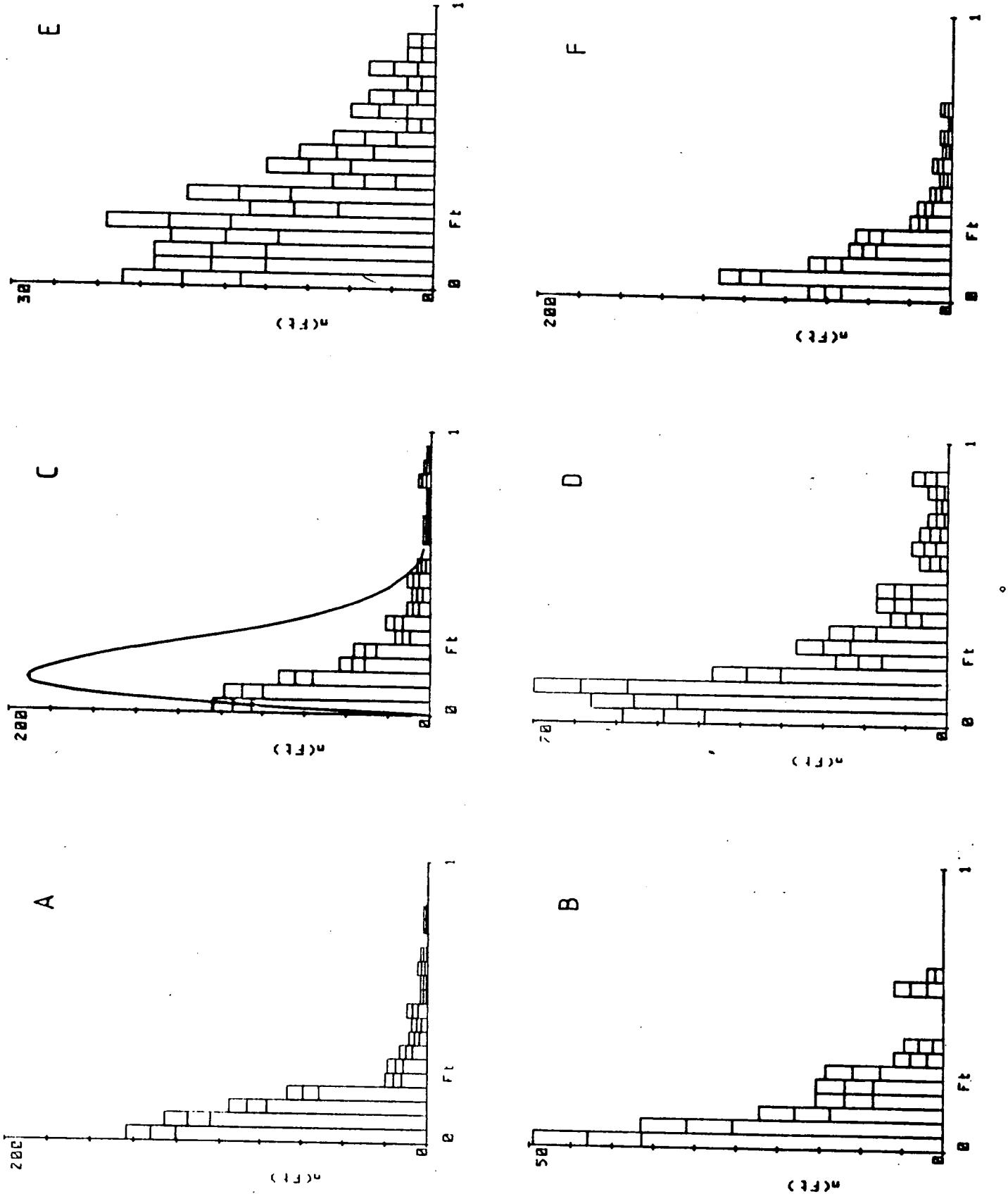

Figure 3.13 Translational energy distributions for surface S_3. See fig 3.6. The distribution measured at 0.083 eV is also shown .

in table 3.11 and plotted in figure 3.14 showing a general increase in $\langle f_t' \rangle$ from S_0 to S_8. The width of these distributions also increased along this series. For T = 0.06 eV the standard deviations σ_{SD} of the distributions are

Surface	S_2	S_3	S_4	S_5	S_6	S_7	S_8
σ_{SD}	0.11	0.13	0.17	0.18	0.23	0.23	0.22

For the colinear situation the highly attractive nature of the surface suggests that very little energy should appear as translation. Compared with the %R values of table 3.3 the relatively large values of T' must arise from nonlinear configurations. As with σ_R the increased $\langle f_T' \rangle$ across S_0 to S_8 may be accounted for by the increase in angular width of the well.

For a statistical distribution of T', distributions similar to those of figure 3.15 may be expected. Figure 3.15a is the Prior distribution which assumes equal product density in phase space. The prior for translation is (BER75)

$$P^o(T') = T'^{\frac{1}{2}} (E - T') / E^{5/2} \qquad 3.18$$

or

$$P^o(f_t') = \frac{15}{4} f_t'^{\frac{1}{2}} (1 - f_t') \qquad 3.19$$

Equal partitions in phase space are given by equal partitions of the variable z_t' such that

$$z_t' = \int_o^{f_t'} P^o(f_t') \, d f_t' = \tfrac{5}{2} f_t' (1 - 3/5 f_t') \qquad 3.20$$

T/eV	0.025	0.06	0.09	0.20	1.0	0.06:J=150
S_0		4.9 ± 0.8 4				
S_1		7.3 ± 0.7 7				
S_2	11.3 ± 0.8 13	11.4 ± 0.7 11	14.0 ± 0.8 13	16.8 ± 1.0 15		
S_3	12.7 ± 0.6 13	13.6 ± 1.1 13	15.8 ± 0.8 16	19.5 ± 1.1 18	26.6 ± 1.6 20	15.6 ± 0.7 13
S_4	13.6 ± 0.7 12	18.0 ± 1.0 16	20.0 ± 1.1 17	24.7 ± 1.5 19		
S_5	19.9 ± 1.1 19	22.6 ± 1.1 18	23.2 ± 1.2 18	24.9 ± 1.6 21		
S_6	23.1 ± 0.9 21	27.8 ± 1.4 23	24.7 ± 1.3 21	30.7 ± 1.7 22		
S_7	28.5 ± 1.3 24	28.4 ± 1.4 23	27.4 ± 1.4 21	31.1 ± 1.7 22		
S_8		30.8 ± 0.6 23	30.5 ± 0.7 22			

Table 3.11 $\langle f_T' \rangle$ (upper figure) and widths (standard deviations) of the translational energy distribution - % - for surfaces S_0 to S_8.

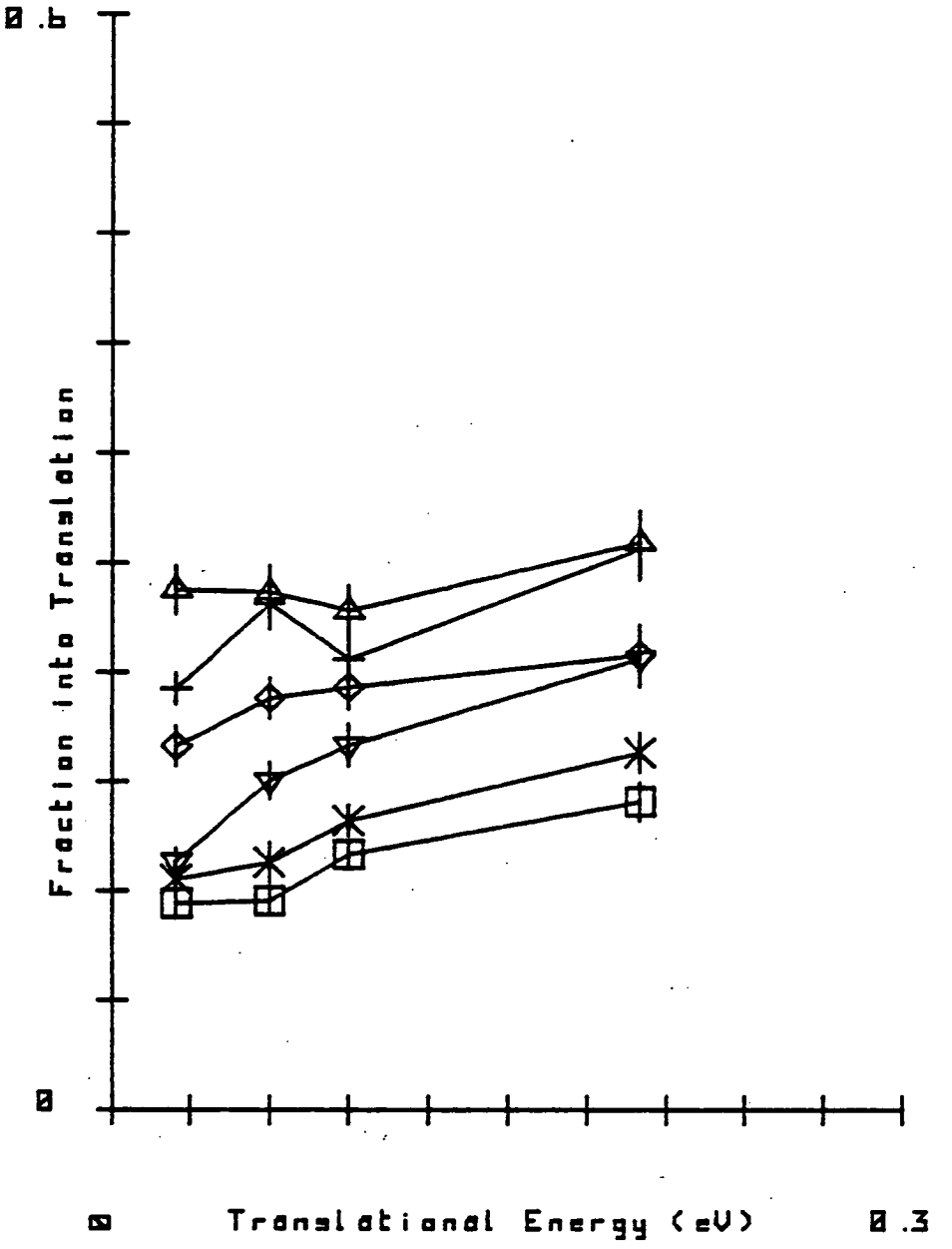

Figure 3.14 f_t' plotted against initial translational energy.
For key see figure 3.7.

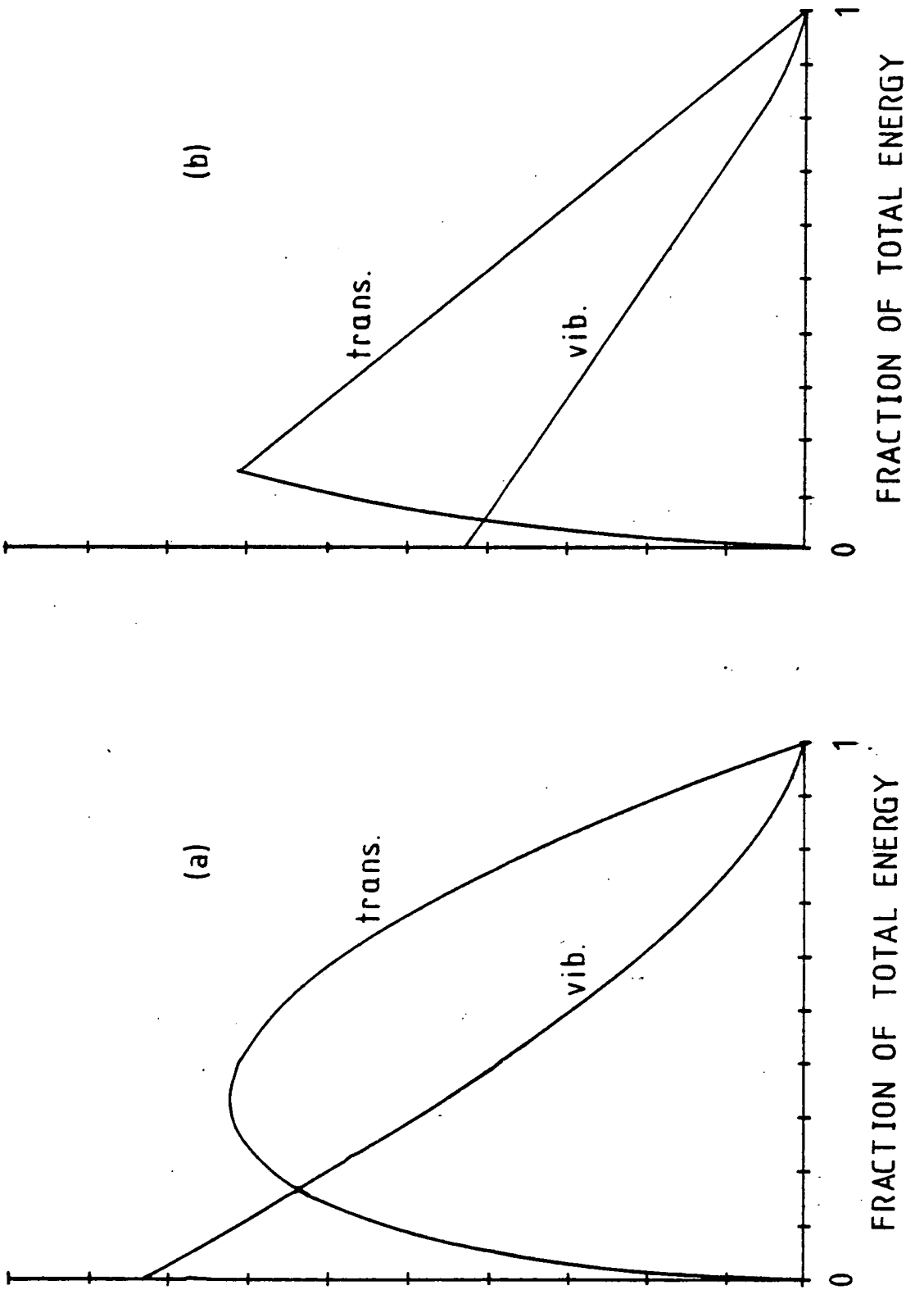

Figure 3.15 Translational and vibrational energy distributions for (a)Prior (PST) and (b) RRKM (0.2 eV).

The Prior distribution is then $P^o(Z_t') = \text{constant}$. The same results as in figure 3.13 are replotted in figure 3.16 against the transformed variable z_t'. These plots show the distributions to be strongly nonstatistical with this pattern repeated for all other surfaces.

The expected RRKM distributions are shown in figure 3.15b, given by (SAF72)

$$P_{RRKM}(T') = \begin{cases} \left(\frac{T'}{B_m'}\right)^{\frac{2}{3}} (E - T') & T' \ll B_m' \\ (E - T') & T' > B_m' \end{cases} \qquad 3.21$$

for a loose complex, where B_m' is the centrifugal exit barrier. Again the calculated distribution disagrees with the trajectory results, although $\langle f_t' \rangle$ does seem (figure 3.14) to approach the RRKM value $\langle f_t' \rangle = \frac{1}{3}$.

$\langle f_t' \rangle$ is consistently low for all surfaces investigated and is similar to the experimentally determined value, 15% (WON73, CAR73). The form of the distributions are also similar to the experimental distribution which is plotted in figure 3.13 alongside the data for surface S_3. These results are the best fit but those for surfaces S_2 to S_6 give results that are all close to the measured values.

3.6.4.2 Vibrational energy

The product vibrational energy distributions are plotted in figure 3.17 for surface S_3. They contrast sharply with the Prior distribution for vibration, which in the RRHO approximation is (BER75)

$$P^o(f_v') = \tfrac{5}{2}(1 - f_v')^{3/2} \qquad 3.22$$

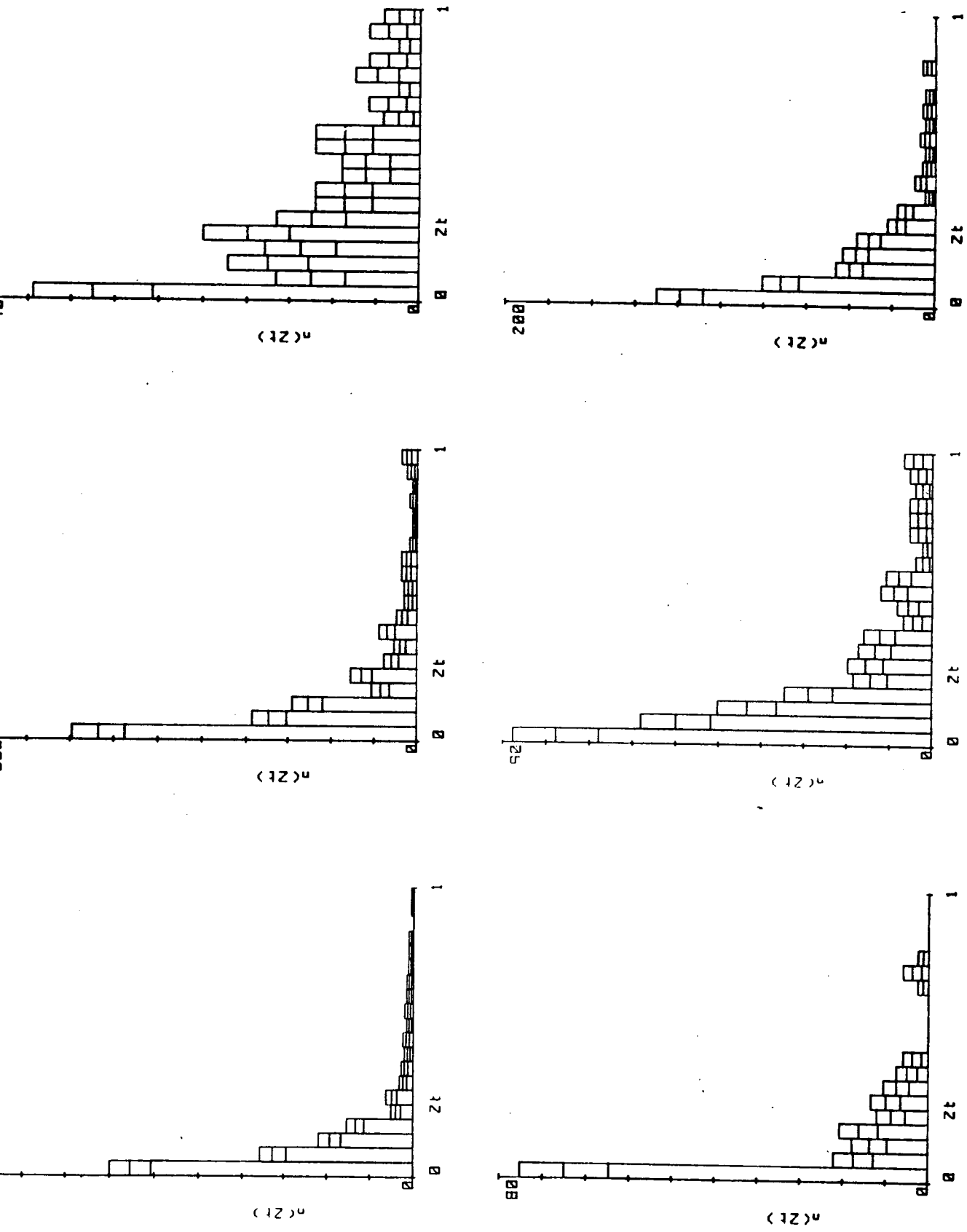

Figure 3.16 Translational energy distribution plotted against the transformed variable z'_t for surface S_3. See fig. 3.6 for key.

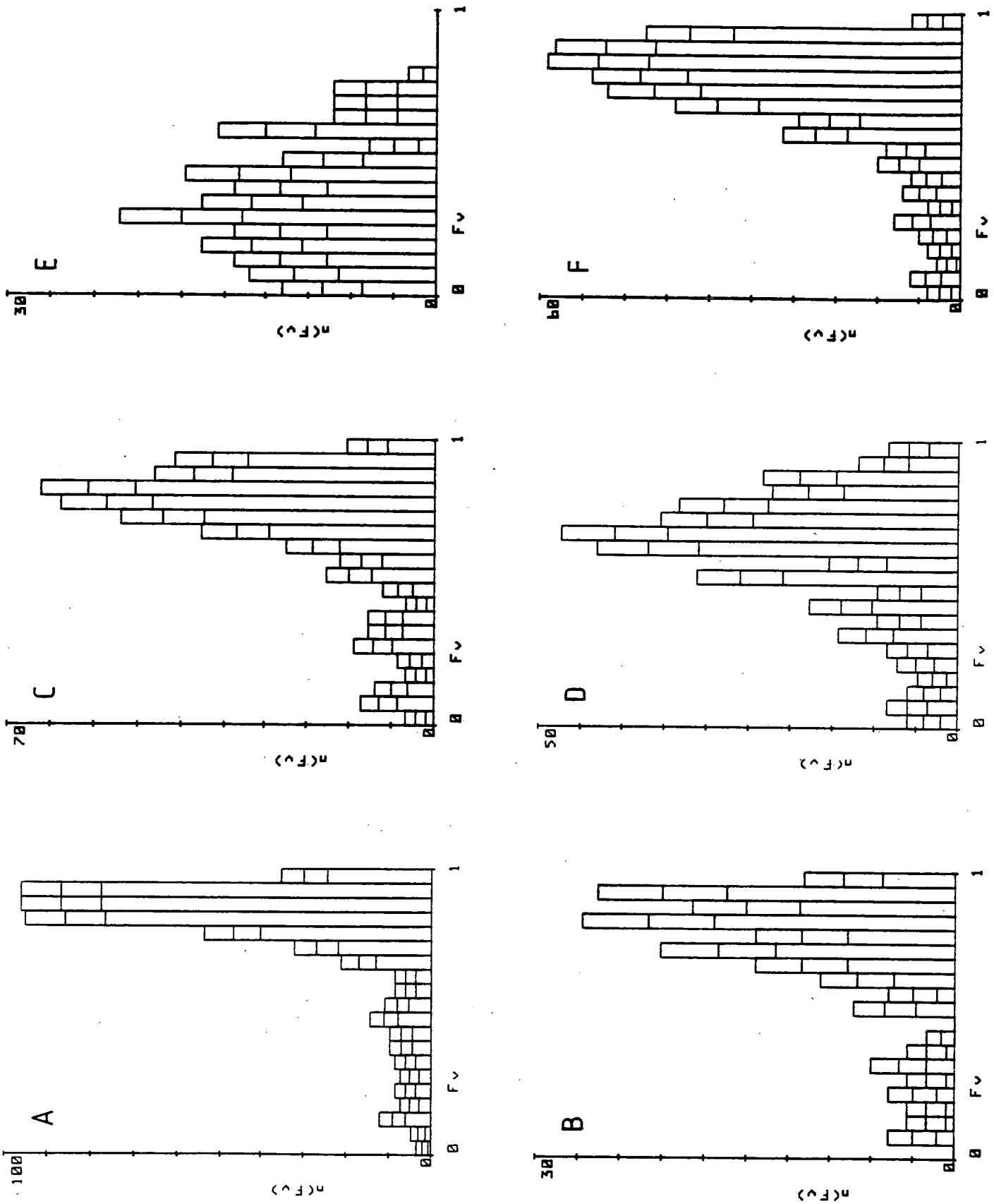

Figure 3.17 Vibrational energy distributions for surface S_3. See fig. 3.6 for key.

shown in figure 3.15(a). If a UPS analysis is done, as for translation the plots over the transformed variable

$$z_v' = \int_0^{f_v'} 5/2(1-f_v')^{3/2} d\, f_v' \qquad 3.23$$

only emphasise the population inversion, figure 3.18. The degree of the inversion decreases with increased T, shown by the decrease in $\langle f_v' \rangle$ of table 3.12 and figure 3.19. This decrease occurs because the high velocities over the surface cause the trajectories to deviate more from the minimum path, the effect of which is to randomise the energy distribution. Also a large fraction of energy is forced into rotational and translational modes by angular momentum conservation.

A surprisal analysis, figure 3.20, shows that the surprisal (LEV76) is approximately linear as is often the case (BER75, LEV79). The line may be slightly curved due to angular momentum constraints but the statistics are too poor to permit a full three parameter fit. For a linear surprisal plot the gradient λ_v can be related to a vibrational temperature

$$\lambda_v = \frac{E}{kT_v} \qquad 3.24$$

Gradients for all the trajectories are also listed in table 3.12. All the surfaces show $\lambda_v \ll 0$ indicating substantial population inversions.

Trajectories for surface S_0 must pass close to the position of the barrier in the surface, probably close to the colinear geometry. This gives the trajectory a large value for f_v', close to that predicted by $\%A_\perp$. σ_R is also very small, as already

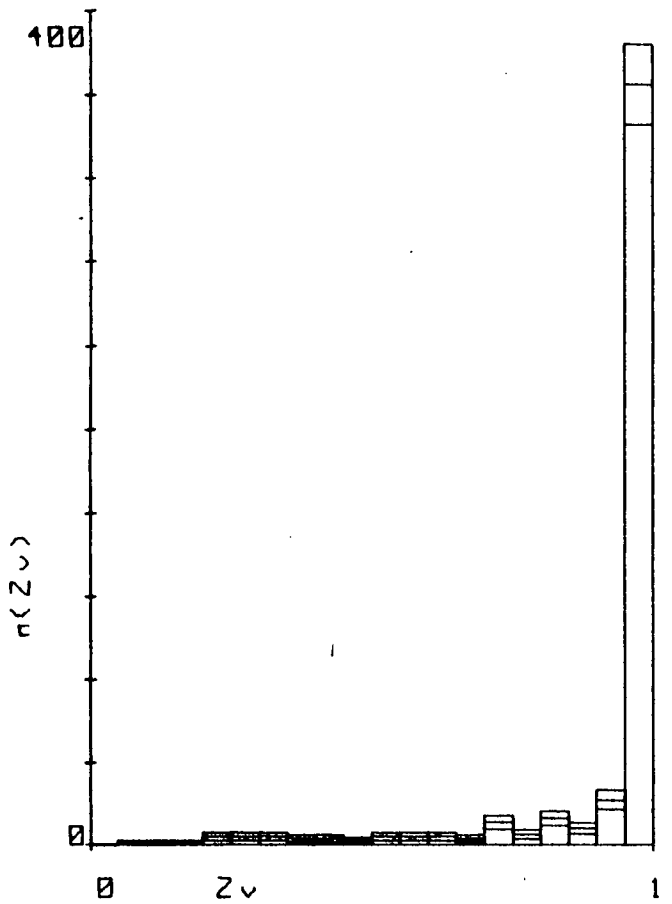

Figure 3.18 Vibrational energy dist. at 0.025eV for surface S_3 plotted against the variable z'_v showing the non-statistical form of the dist.

Figure 3.19 f'_v plotted against initial translational energy for surfaces S_2 to S_7 . See fig. 3.7 for key.

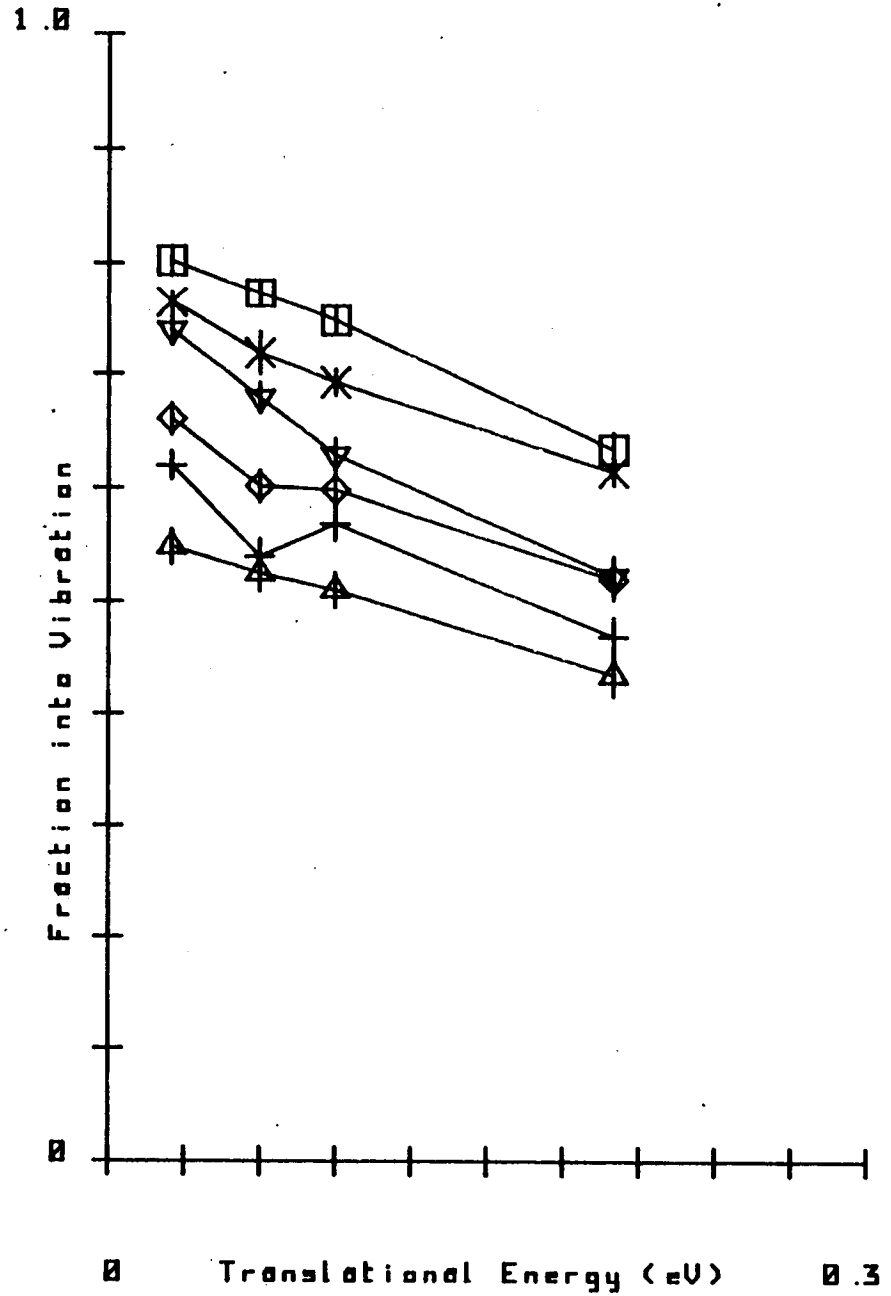

T/eV	0.025	0.06	0.09	0.2	1.0	0.06:J=150
S_0		92.9 ± 1.0 5 -42.5				
S_1		88.2 ± 0.9 9 -9.8				
S_2	80.2 ± 1.3 21 -7.6	77.2 ± 1.2 21 -7.9	74.8 ± 1.1 19 -8.5	63.5 ± 1.5 21 -6.5		
S_3	76.3 ± 1.0 21 -7.7	71.8 ± 1.9 22 -7.4	69.2 ± 1.1 22 -7.2	61.5 ± 1.2 21 -6.4	33.3 ± 1.6 19 -2.4	71.3 ± 1.0 20 -7.8
S_4	73.9 ± 1.2 21 -7.9	67.9 ± 1.3 21 -7.8	62.9 ± 1.4 21 -6.9	52.3 ± 1.7 22 -4.7		
S_5	66.1 ± 1.4 25 -6.8	60.1 ± 1.4 23 -6.3	59.8 ± 1.5 22 -6.5	52.0 ± 1.8 24 -4.8		
S_6	62.0 ± 1.1 26 -6.4	54.0 ± 1.6 26 -5.4	56.9 ± 1.5 24 -5.9	46.9 ± 1.8 23 -3.9		
S_7	54.9 ± 1.6 28 -5.1	52.5 ± 1.6 26 -5.3	51.0 ± 1.6 25 -5.1	43.5 ± 1.9 24 -3.8		
S_8		48.1 ± 0.7 25 -4.5	46.9 ± 0.7 25 -4.4			

Table 3.12 $\langle f_v' \rangle$ (upper figure) and widths (standard deviations) - % - for surfaces S_0 to S_8. The lower figure is the surprisal I (f_v').

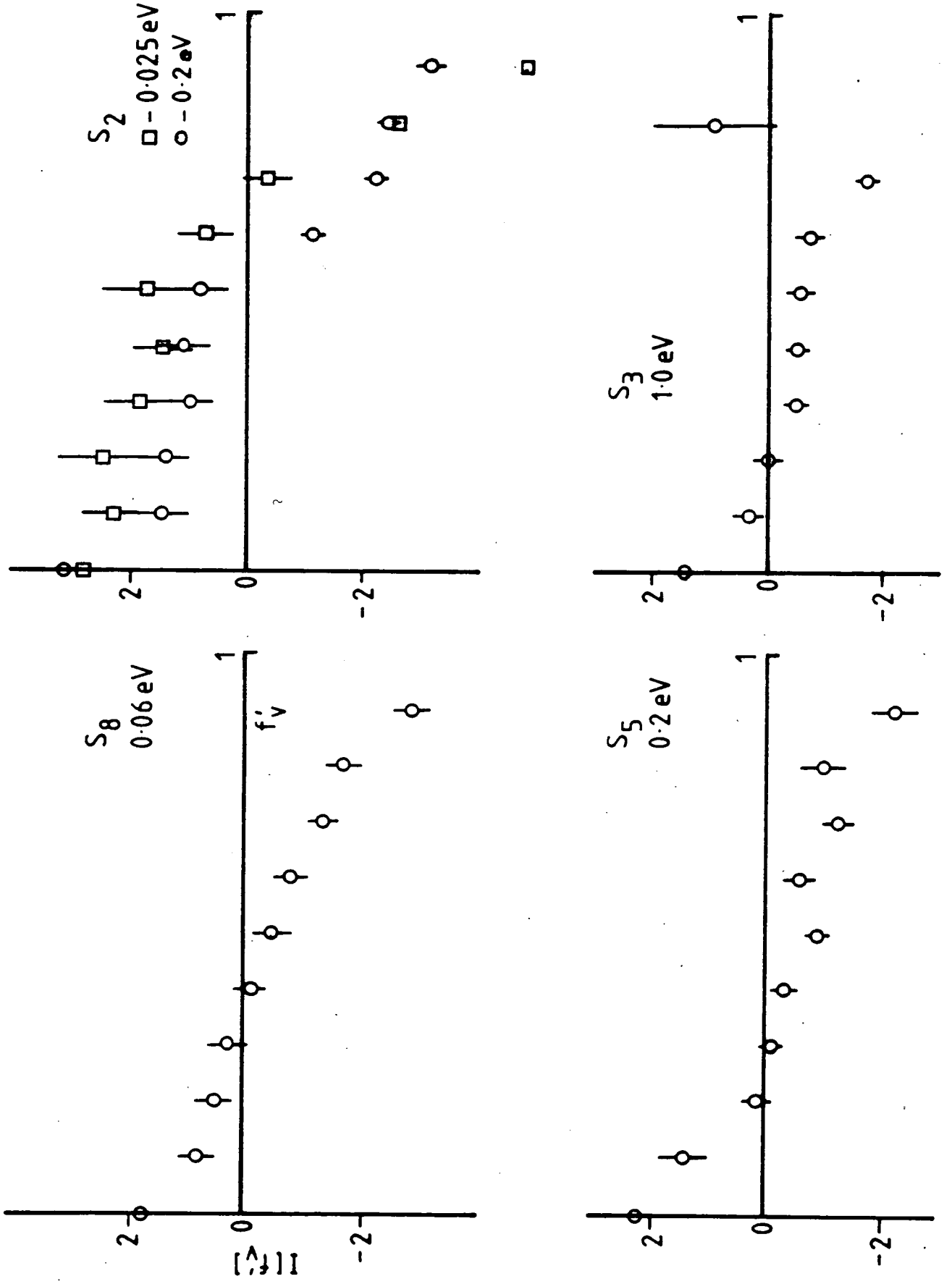

Figure 3.20 Surprisal plots of the vibrational energy for a few surfaces and energies.

noted for colinear trajectories, and the distribution is sharply peaked near $f_v' = 1.0$ (figure 3.21(a)). At the other end of the scale, surface S_8, the distribution is quite broad and $\langle f_v' \rangle$ is about half of $\%A_\perp$. Noting that the measured distribution peaks at low f_v' (figure 4.1), sixty batches of trajectories were run on this surface at T = 0.06eV and 0.09 eV to check that no peak in the distribution formed at low f_v'. None was observed in the distribution with respect to f_v' (figure 3.21(b)) or z_v', nor was any discernable in the surprisal plot.

The vibrational energy distribution from RRKM theory is (WHI76)

$$P_{RRKM}(V') = \begin{cases} (E - V' - 2/5B_m') \; B_m'^{\frac{2}{3}} & V' \leqslant E-B_m' \\ \frac{3}{5}(E - V')^{5/3} & V' > E-B_m' \end{cases} \qquad 3.25$$

and is plotted in figure 3.15(b). The vibrational distribution is obviously non-statistical when compared with both the RRKM and Prior distributions.

Comparison of the trajectory results with other models is equally unproductive. The impulsive model (table 3.4) predicts at most $\langle f_v' \rangle = 6.5\%$, with this as the upper limit for the Constant Gradual Force model. The DIPR model (KUN70) since it is basically a more sphisticated version of the gradual force family would give similarly low results for f_v'. The analysis which comes closest to predicting the energy distributions is the colinear classification of the potential energy surface.

3.6.4.3 Rotational Energy

The product rotational energy distributions are plotted in figure 3.22 for surface S_3. The distributions peak at low values of f_R', decreasing rapidly almost to zero. The distributions broaden with increased T so that the average value

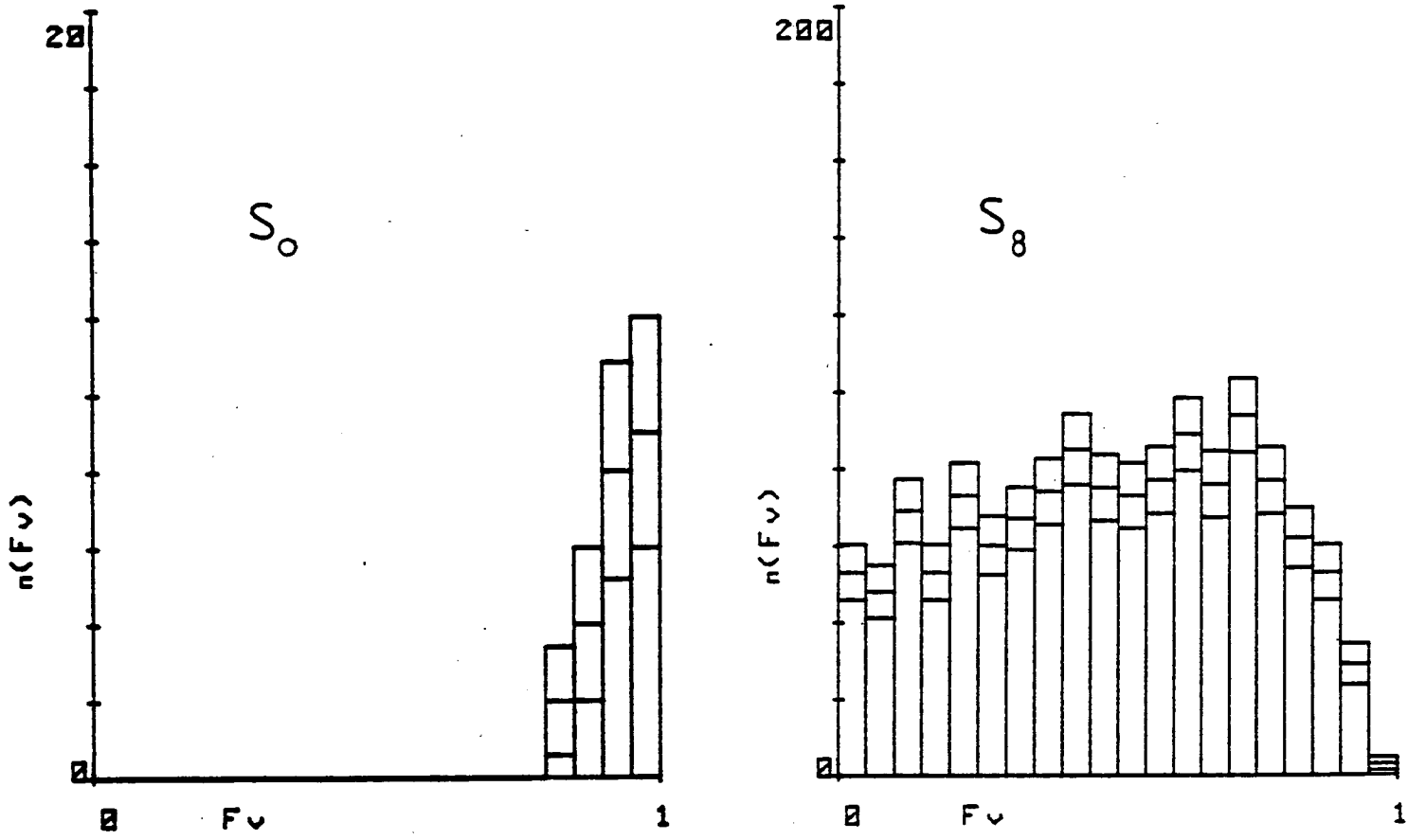

Figure 3.21 Vibrational energy distributions for surfaces S_0 and S_8.

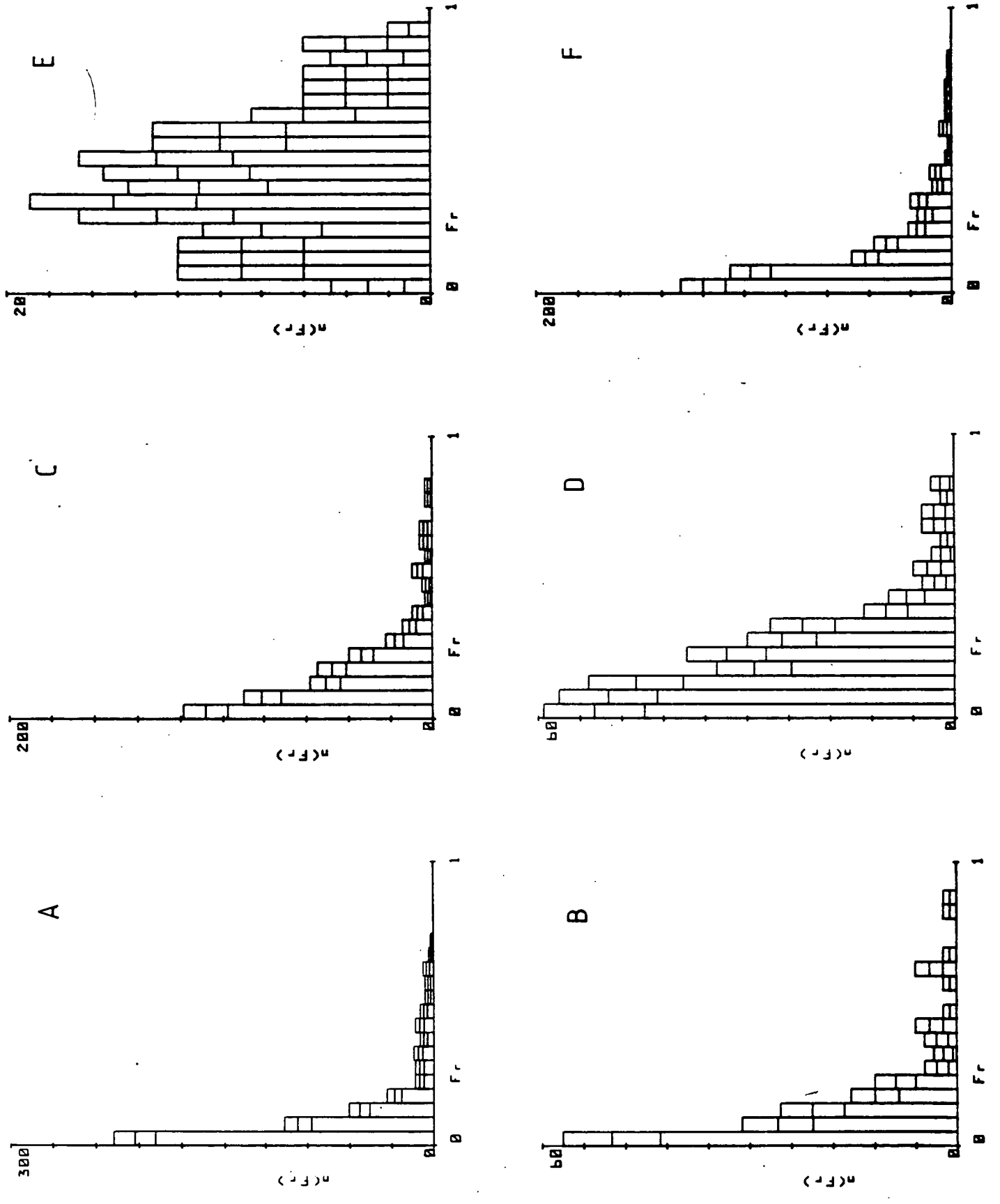

Figure 3.22 Rotational energy distributions for surface S_3. See fig. 3.6 for key.

$\langle f_R' \rangle$ also increases, table 3.13 and figure 3.23. This holds for all the surfaces and energies except that run at 1.0eV. At this energy the distribution is broad, peaking at around f_R' = 0.35. Low values for $\langle f_R' \rangle$ are typical for this mass combination, forced on the system by the angular momentum constraints.

The rotational distributions are similar for all the surfaces although $\langle f_R' \rangle$ increases from surface S_0 to S_8. Also across the range of surfaces the widths of the distributions increase as they do for translation. Again this can be explained by the greater angular width of the well in the surface. Smaller angles of the 'complex' when it breaks up permit larger angular momenta which in turn allow increased rotational energies.

Comparison with model distributions is again limited. Repulsive models - table 3.4 - do not in principle apply for this reaction although they give a better estimate for rotation than vibration. A surprisal analysis is not possible in this study because the Prior distribution for rotation (BER75) is conditional upon f_v' i.e.

$$P^o(f_R'/f_v') = \frac{(1 - f_v' - f_R')^{\frac{1}{2}}}{(1 - f_v')} \qquad 3.26$$

There were too few trajectories to analyse with respect to two variables. Another complicating factor is that the distribution is very dependent on the angular momentum.

Superficially the distributions are similar to a Boltzmann energy distribution and could be characterised by a rotational temperature, $T_R' = \langle R' \rangle / K_b$. These temperatures are shown in

T/eV	0.025	0.06	0.09	0.20	1.0	0.06:J=150
S_0		2.2 ± 0.5 2 330				
S_1		4.6 ± 0.5 5 680				
S_2	8.5 ± 0.8 13 1230	11.3 ± 0.9 14 1680	11.3 ± 0.7 12 1720	19.7 ± 1.1 16 3250		
S_3	11.0 ± 0.7 13 1590	14.6 ± 1.4 17 2170	14.9 ± 0.8 15 2270	19.0 ± 0.9 16 3140	40.1 ± 1.8 22 10.341	13.1 ± 0.8 15 2195
S_4	12.5 ± 0.9 15 1810	14.0 ± 0.9 14 1080	17.1 ± 1.1 16 1600	23.0 ± 1.4 18 3800		
S_5	14.0 ± 1.0 17 2030	17.3 ± 1.0 17 2570	17.0 ± 1.0 15 2590	23.1 ± 1.3 16 3810		
S_6	14.9 ± 0.7 16 2150	18.3 ± 1.1 19 2720	18.4 ± 0.9 15 2800	22.4 ± 1.2 16 3700		
S_7	16.6 ± 1.0 18 2400	19.1 ± 1.0 17 2840	21.6 ± 1.2 18 3290	25.5 ± 1.6 21 4210		
S_8		21.0 ± 0.5 18 3130	22.5 ± 0.6 19 3430			

Table 3.13 $\langle f_R' \rangle$ (upper figure) and widths (standard deviations) - % - for surfaces S_0 to S_8. The lower figure is the rotational temperature T_R' derived from $\langle f_R' \rangle$.

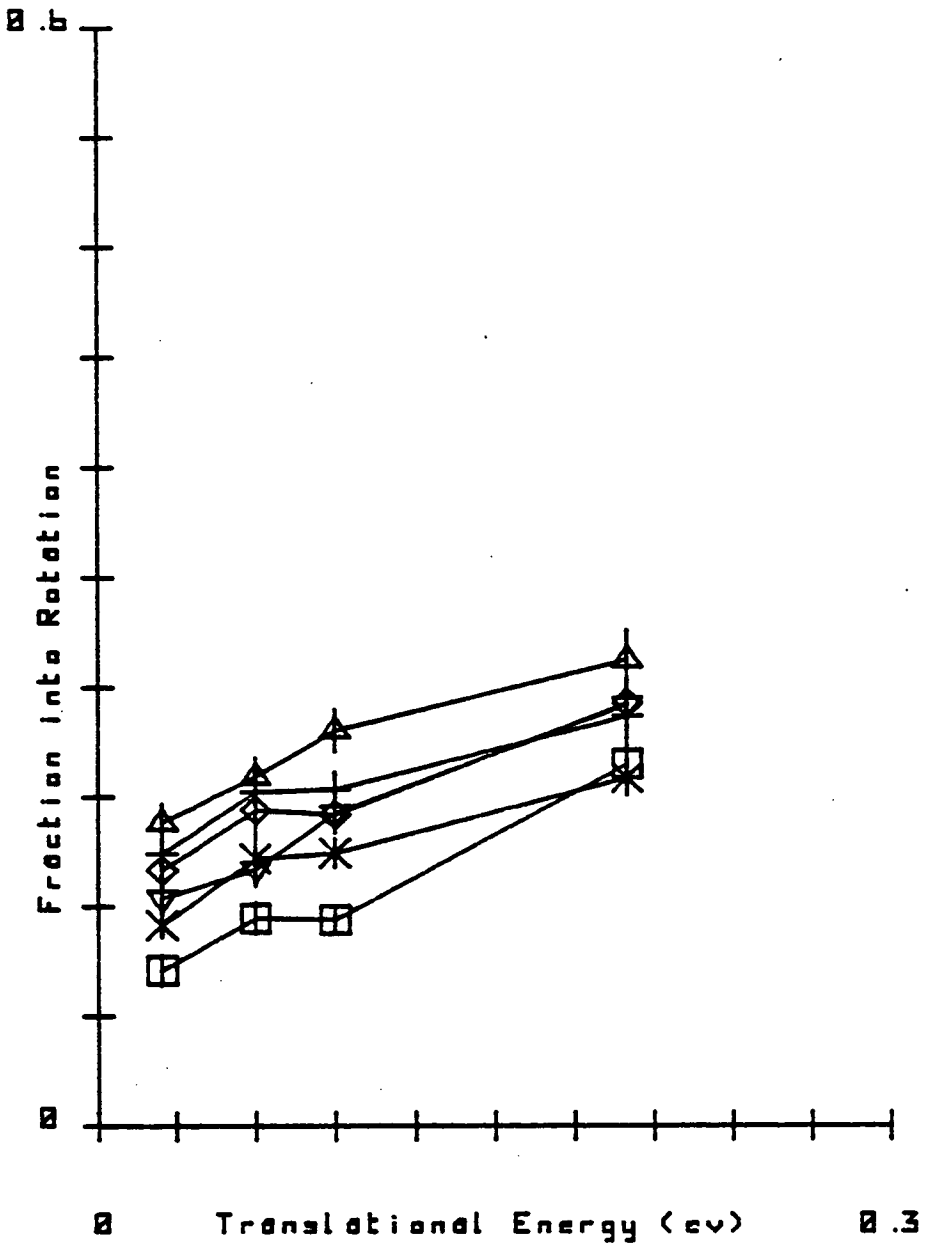

Figure 3.23 $\langle f_R' \rangle$ plotted against initial translational energy.
For key see figure 3.7.

table 3.13. Apart from surfaces S_0 and S_1 the rotational temperatures are all much higher than the experimental value of 230K reported in chapter 2.

3.7 Conclusions

The trajectory study shows that some aspects of the reaction suggest a complex mechanism. For example the reaction cross section varies approximately with $T^{-\frac{1}{3}}$ for most surfaces (fig 3.7), the angular distribution is almost symmetric about 90^o (fig.3.9) and the complex lifetime seems to behave statistically (fig.3.8). On the other hand the energy distributions are strongly non-statistical, in particular the vibrational energy distribution (fig 3.17). While the trajectory lifetimes (about 1ps) are significantly larger than the RRKM lifetime (0.1 ps) they are still less than the rotational period (5 ps). Obviously an intermediate region obtains where the lifetime is not long enough to give equipartition of energy in phase space (WHI75).

Whitehead has noted that σ_R and $\langle f_v' \rangle$ vary monotonically with the Sato parameter s_{IF} (FLE82). Also, it was found that the position of the well in the r_{I_2} coordinate increased with s_{IF}.

In this study σ_R was not found to be a monotomic function of s_{IF} (table 3.5) but decreases again for s^2_{IF} larger than 0.6. Although $\langle f_v' \rangle$ does decrease monotonically with s_{IF} (fig.3.19) σ_R seems to vary with the r_{IF} coordinate of the well position.*

Another difference between these results and FLE82 is the magnitude of the cross section (19Å^2 vs 20 to 50Å^2 of section 3.6). Obviously σ_R is quite sensitive to changes in the attractive component of the I_2 potential.

Detailed comparisons of the trajectory results with the experimental data is left to the next chapter. Suffice it to say however that there is a sizeable difference between the measured and calculated distribution of vibrational energy.

* The angle of the surface to the trajectory opposite the input channel is close to 90°. As the well moves towards the entrance channel this angle changes. This may cause fewer trajectories to be reflected back through the input channel, causing σ_R to vary with r_{IF}.

Chapter 4

Discussion

4.1 Summary of experimental work

Grice and co workers (CAR73) first reported angular distribution data for the reaction

$$F + I_2 \rightarrow IF + I \qquad (1)$$

These results were obtained at a translational energy of 2.9 kJ mol^{-1} with Fluorine atoms generated by a microwave discharge source similar to that used for O/I_2 reactive scattering (RAD73). At the same time Wong and Lee also reported results for reaction (1) (WON73). Here Fluorine atoms were produced by thermal dissociation of F_2 in a Nickel oven with velocity selection giving a collision energy of 8.1 kJ mol^{-1}. Both sets of workers showed that the translational energy distribution peaks at 15% of the available energy, assuming ground state products. However there was disagreement over the angular distribution. Grice reported a broad range from sideways to backward scattering while Lee reported a nearly isotropic distribution with a mild forward peak. Grice concluded that the product distribution varies appreciably with initial translational energy in the range 3 to 8 kJ mol^{-1}.

The work of Appelman and Clyne gave rate constants for Fluorine atom reactions with some halogens and interhalogens (APP75). They showed that the activation energy was negligible and the reaction rate is close to the hard sphere collision frequency.

The vibrational energy distribution reported in chapter 2 shows a significant population in the ground state of IF.

This is confirmed in similar measurements by Wanner's group (TRI80), where vibrational energy distributions for

$$F + ICl \longrightarrow IF + Cl \qquad (2)$$

$$F + IBr \longrightarrow IF + Br \qquad (3)$$

are also reported. The distributions are bimodal, a substantial peak at v = 0 with a smaller one at high vibrational quantum numbers. These results for reaction (1) are more extensive than those presented in chapter 2, high vibrational states were studied using a modulated atom beam to pick out the signal from I_2 fluorescence. These results are displayed in figure 4.1

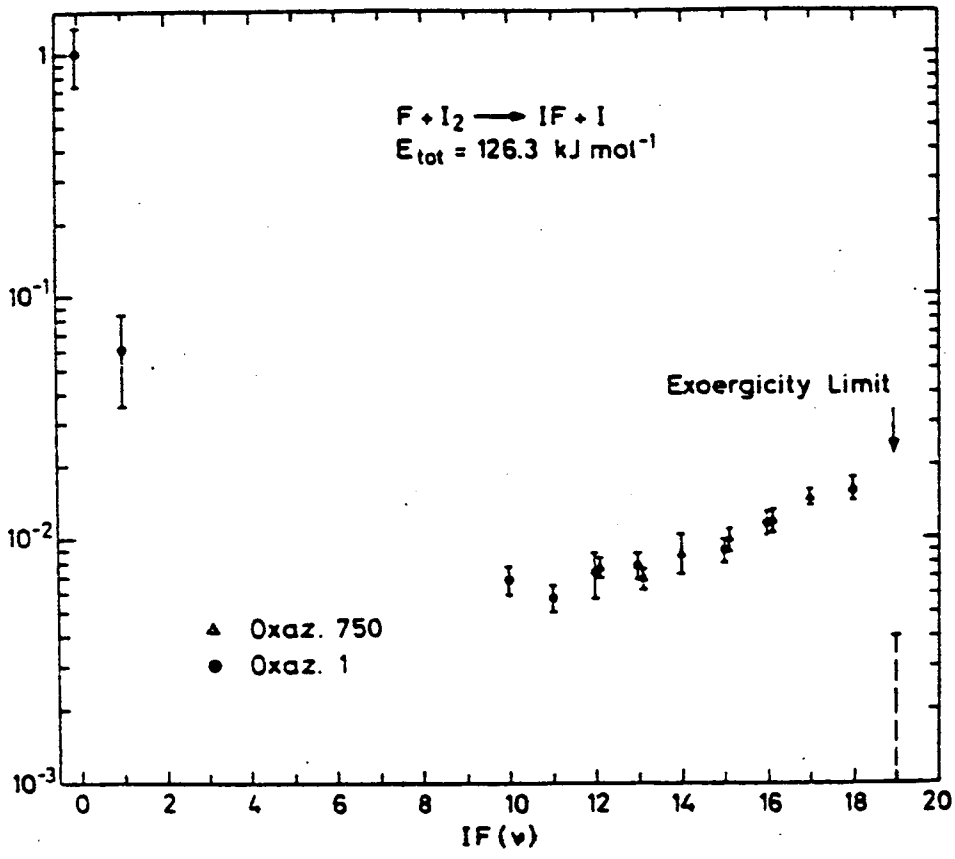

Vibrational product state distribution in the $X^1\Sigma^+$ state of IF. The population of $v = 19$ was estimated to be within the range of the broken error bar.

Figure 4.1 Vibrational energy distribution obtained for reaction (1). Reproduced from TRI81.

4.2 Comparison of Trajectory results with experiment

The results of chapter 3 for surfaces which agree with the known data, show that it is impossible to reproduce the measured vibrational energy distribution. Whitehead's recent results agree with this conclusion (FLE82)*

Essentially four properties of reaction (1) have been determined and a comparison of each with the trajectory calculations is attempted below.

a) The computed cross sections for many of the surfaces are nicely spanned by the experimentally obtained value. Those that give the best agreement are those which are most attractive. It is therefore reasonable to assume that no matter what the overall interaction, initially it occurs on the attractive ground state surface.

b) The fraction of energy channelled into translation of the products gives reasonably good agreement between the experimental and computed results (15% compared with 12% to 30%). A possible explanation of this low value is that it is constrained by the angular momentum. This is also suggested by the low rotational energy of the v = 0 state measured in chapter 2.

* In this study the parameter for the I_2 morse curve was not fitted to the RKR turning points but was calculated from ω_e. A smaller reactive cross section results but apart from this the study is almost identical to that of chapter 3.

c) The angular distribution from the calculations is approximately sideways scattered, corresponding to a random distribution in space, with a trend towards backward scattering at higher energies. The measurements of Wong and Lee were the better and gave an isotropic angular distribution with a slight forward peak. This suggests a long lived complex mechanism is the dominant process. By the ratio of forward to backward peaks (1:0.8) the complex lifetime is estimated (FIS67) to be one or two rotational periods (4 - 8ps). This is significantly longer than that given by RRKM theory - equation 3.14- and the values obtained from the trajectory calculations (less than 2ps). This tends to suggest that an intermediate is formed which is more stable, with respect to the products, than 12.6KJ mol^{-1}.

d) The form of the vibrational energy distribution produces the largest difference between calculations and experiment. For trajectories run on the LEPS surfaces of chapter 3 and reference FLE82 the vibrational distributions are very similar. They produced an inversion with the distribution peaking at high v. This is in sharp contrast to the measured distribution which shows the greatest proportion of the reaction produces low vibrational energies. Perhaps more surprising is the bimodal form of the measured distribution. Few bimolecular reactions produce this type of distribution, however Polanyi has shown that it occurs (POL77) for

$$H + ICl(v) \rightarrow HCl(v) + I \qquad (4)$$

In this case the bimodality could be identified with two dynamically different reaction paths traced out on a single surface. A direct path produced low internal excitation while a migratory path gave higher internal excitation (POL80). In the indirect path the labile Hydrogen, after an initial interaction with the attractive Iodine end of the molecule, migrated to the Chlorine. The resulting distribution was very sensitive to the initial energy of the reactants. This mechanism cannot be involved for reaction (1) as the reactant molecule is symmetric to approach at either end and has no barrier comparable to that of H··· CL···I. Any dynamical effect would be expected to show up in the trajectory results and if any exists it was not obvious. Most other bimodal distributions are found to have a dynamical explanation - see for example POL80, DIN73 and ref.s therein. Other distributions can however be formed by the action of more than one potential energy surface. (FLU73).

4.3 Energy conservation

Wanner's vibrational results give $\langle v \rangle = 1$ unless there is a further peak between levels 1 and 10 i.e. $\langle f_{v'} \rangle = 9\%$. As most of the reaction products are in the ground vibrational state, the average fraction of energy into rotation will be close to that measured in chapter 2 i.e. $\langle f_{R'} \rangle = 2\%$. Combining these results with the scattering results of Lee and Grice where $\langle f_{t'} \rangle = 15\%$ leaves about 74% of the available energy unaccounted for. Although these results are the sum of three different experiments a discrepancy of this

magnitude cannot be attributed to any sum of errors.

A possible conclusion is that the excess energy appears as electronic excitation, first hinted at by Lee (WON73). The relevant energy levels are shown in figure 4.2. The only accessible excited electronic state is that of $I(^2P_{\frac{1}{2}})$ with ground state $IF(X^1\Sigma^+)$. At 0.953eV the formation of $I(^2P_{\frac{1}{2}})$ (MOO58) would account for 78% of the exoergicity of reaction (1) or approximately 75% of the available energy at the energies used. This shows remarkable agreement with the energy deficiency estimated above.

The bimodal form of the vibrational energy distribution of figure 4.1 suggests there are two reaction paths. The smaller peak at high quantum numbers is quite like the trajectory results of chapter 3. A surprised plot of the best fitting trajectory results - surface S_4 - normalised to this data is shown in figure 4.3. The fit is very good and the two plots even exhibit the same curvature. Using the trajectory results to project to lower levels it is estimated that (9 ± 2)% of the reaction contributes to this channel.

The mechanism therefore put forward is that the reaction has two branches. One occurring solely on the ground electronic surface producing vibrationally excited IF. The other, principal channel producing excited Iodine, $^2P_{\frac{1}{2}}$ atoms.

4.4.1 Role of $F(^2P_{\frac{1}{2}})$

Without surface hopping $I(^2P_{\frac{1}{2}})$ can only be formed by the reaction of spin orbit excited Fluorine atoms, i.e.

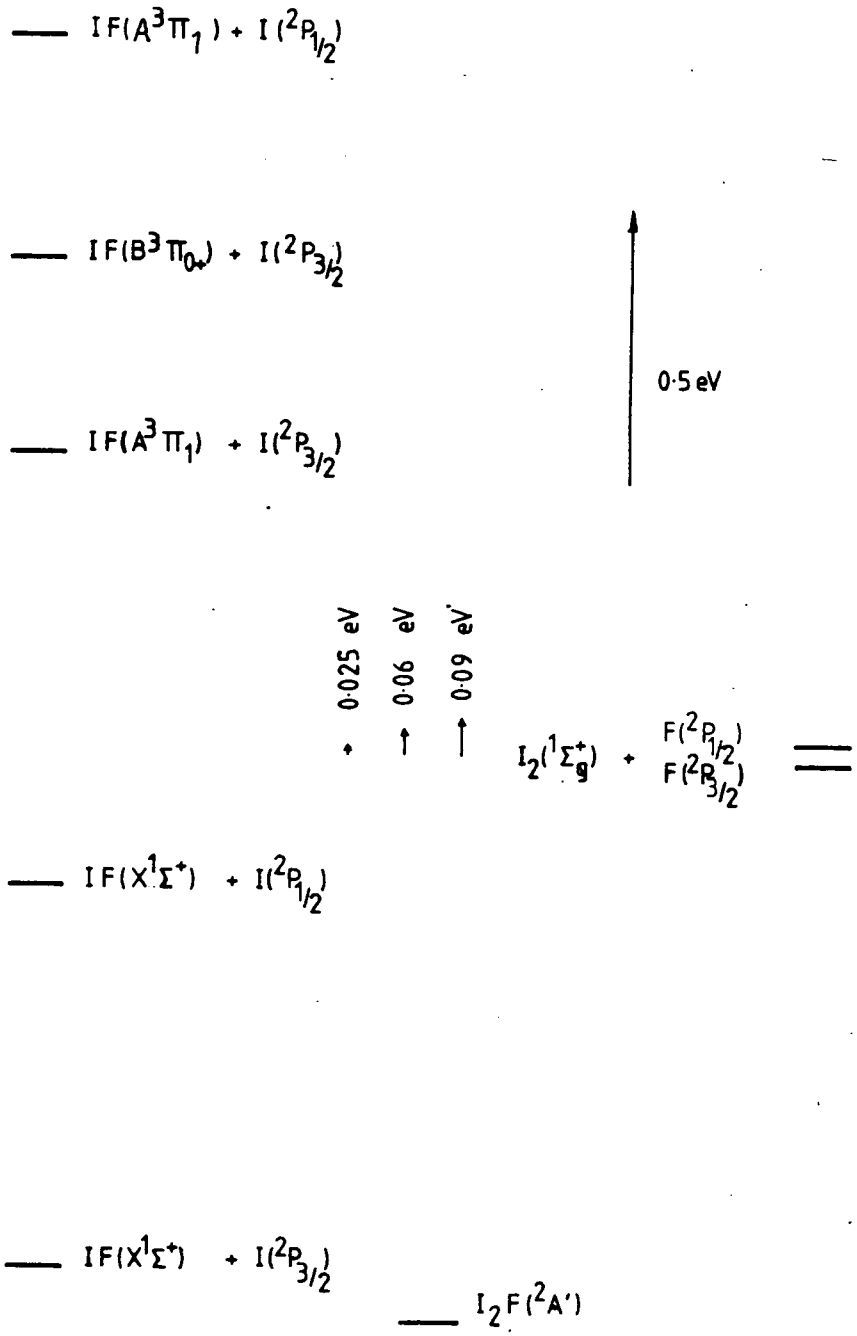

Figure 4.2 Electronic level scheme for the reaction showing the relative energies of the different states. The total available energy of the experiments to date is also shown.

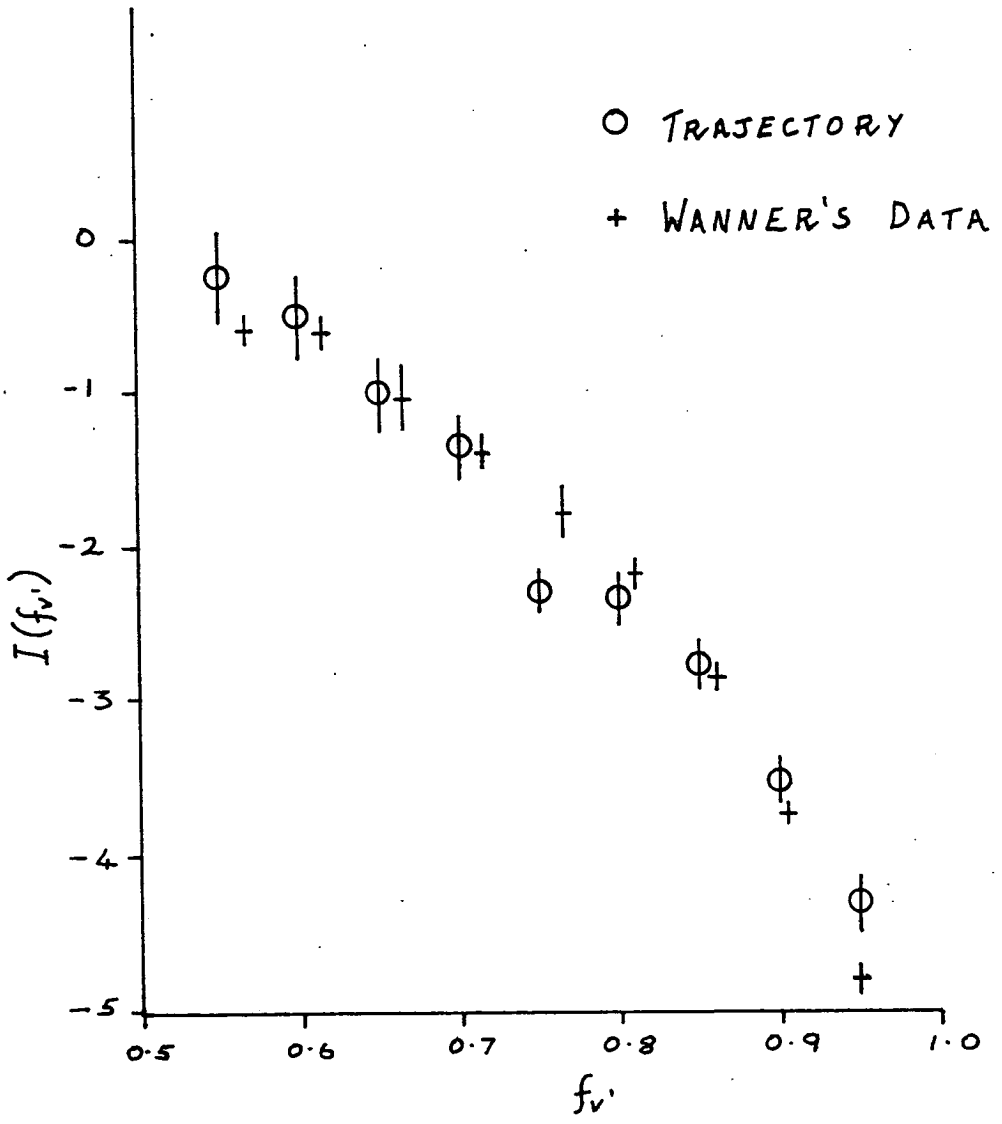

Figure 4.3 Surprisal plot of the trajectory results for surface S_4 at 0.06eV normalised to the surprisal obtained from figure 4.1.

$$F(^2P3/2) + I_2(X^1\Sigma_g^+) \rightarrow IF(X^1\Sigma^+) + I(^2P3/2) \qquad (5a)$$

$$F(^2P\,\tfrac{1}{2}) + I_2(X^1\Sigma_g^+) \rightarrow IF(X^1\Sigma^+) + I(^2P_{\frac{1}{2}}) \qquad (5b)$$

$F(^2P_{\frac{1}{2}})$ is present, at the energies used in concentrations of about 7% of the total Fluorine atom population. If the low energy vibrational peak corresponds to reaction (5b) then it must have a very large cross section to contribute 91% of the products. Crudely it could be estimated from the overall cross section (APP75) by

$$\sigma_R \simeq 43 * \frac{91\%}{7\%} = 560 \text{Å}^2$$

This is larger even than that for $K + Br_2$ (σ_R=200Å^2 : LOS79) where a harpooning mechanism predominates. While $F^{\cdot}$ has a large electron affinity (3.5eV : COT72) it is not expected to be sufficient to form an ion pair. (Chlorine has a larger electron affinity (3.61eV : COT72) and only short range attraction was found for $Cl + I_2$ reactive scattering (LEE69).

Some studies have found that the electronic state of Fluorine atoms is unimportant in reaction (SUN77). Others have found that in some instances $F(^2P_{\frac{1}{2}})$ atoms were less reactive than $F(^2P3/2)$ (FOO75). The relative reactivities of these two states must depend on any differences in the potential energy surfaces arising from the two electronic configurations.

4.4.2 Other systems

Reaction (1) is one of four bimolecular reactions whose exoergicity is sufficient to form $I(^2P_{\frac{1}{2}})$ as one of the products. An information theoretic study of this and the other three reactions (DIN75)

$$K + I_2 \rightarrow KI + I(^2P3/2)/I(^2P\tfrac{1}{2}) \qquad 6a/b$$

$$D + I_2 \rightarrow KI + \text{"} \qquad 7a/b$$

$$F + HI \rightarrow HF + \text{"} \qquad 8a/b$$

attempted to predict the branching ratios between excited and ground state products.

The experimental data for reaction (7) showed that channel (7a) dominates and no $I(^2P\tfrac{1}{2})$ was detected. For reaction (8) the predicted branching ratio of $\Gamma_8 = 0.5$ was on the threshold for chemical laser action. Experimentally $I(^2P\tfrac{1}{2})$ was detected for this reaction but was largely the result of secondary collisions with vibrationally excited HF (SUN77). While reaction (8) gave little $I(^2P\tfrac{1}{2})$ directly the analogous reaction

$$F + HBr \rightarrow HF + Br(^2P3/2)/Br(^2P\tfrac{1}{2}) \qquad 9a/b$$

produced 10 ± 4% in the excited branch. Here also vibrational to electronic energy transfer was important.

For reaction (1) the information theoretic value for the branching ratio was calculated to be $\Gamma_1 = 0.3$. Using this value a fit to the data of Wong and Lee was attempted with some success. However as some assumptions (DIN75) regarding the measured energy distribution were made, a quantitative agreement was not claimed.

The results for reactions (6) to (8) indicate that from energy considerations $I(^2P\tfrac{1}{2})$ would be expected as a significant branch in these reactions. The final outcome however must be governed by the exact nature of the electronic surfaces involved.

4.4.3 Correlation diagrams

Herschbach has argued the case for a triplet ground state for the O-Br-Br complex (DIX73). This arises from the possibility suggested by Walsh (WAL53) that the a' (σ)$^{4\sigma}$ orbital crosses the a"(3π) and a'(3π) orbitals and lies below them at large bond angles. (fig.4.4). This is explained by the strong O-Br interaction and noting that the a'(σ)$^{4\sigma}$ orbital is partly O-Br bonding and Br-Br antibonding. This gives the valence shell configuration

$$\ldots (4a')^2\ (2a")^2\ (5a')^2\ (6a')\ (3a") \qquad C_s \quad (^3A")$$

$$\ldots (2\pi)^4\ (4\sigma)^2\ (3\pi)^2 \qquad C_{\infty v} \quad (^3\Pi)$$

CNDO-UHF studies confirm that this configuration has the lowest energy for the linear case (DIX73).

The case for the trihalogens should provide a similar situation, with the lone electron in a 3π orbital in the linear case. However the bent geometry is probably lower in energy with an angle of about 150° (UNG76, PRO78). This would have the electronic configuration

$$\ldots (2a")^2\ (5a')^2\ (6a')^2\ (3a")^2\ (7a') \qquad {}^2A'$$

A possible correlation diagram for the system is given in figure 4.5 It shows how the electronic state might vary with bond angle given the orbital ordering of figure 4.4. The avoided crossing allows the configuration to change to

$$\ldots (2a")^2\ (5a')^2\ (6a')^2\ (7a')\ (3a")^2 \qquad {}^2A'$$

for angles close to 180°.

During the reaction the Fluorine atom and Iodine molecule approach on the ground state $^2A'$ surface as would be

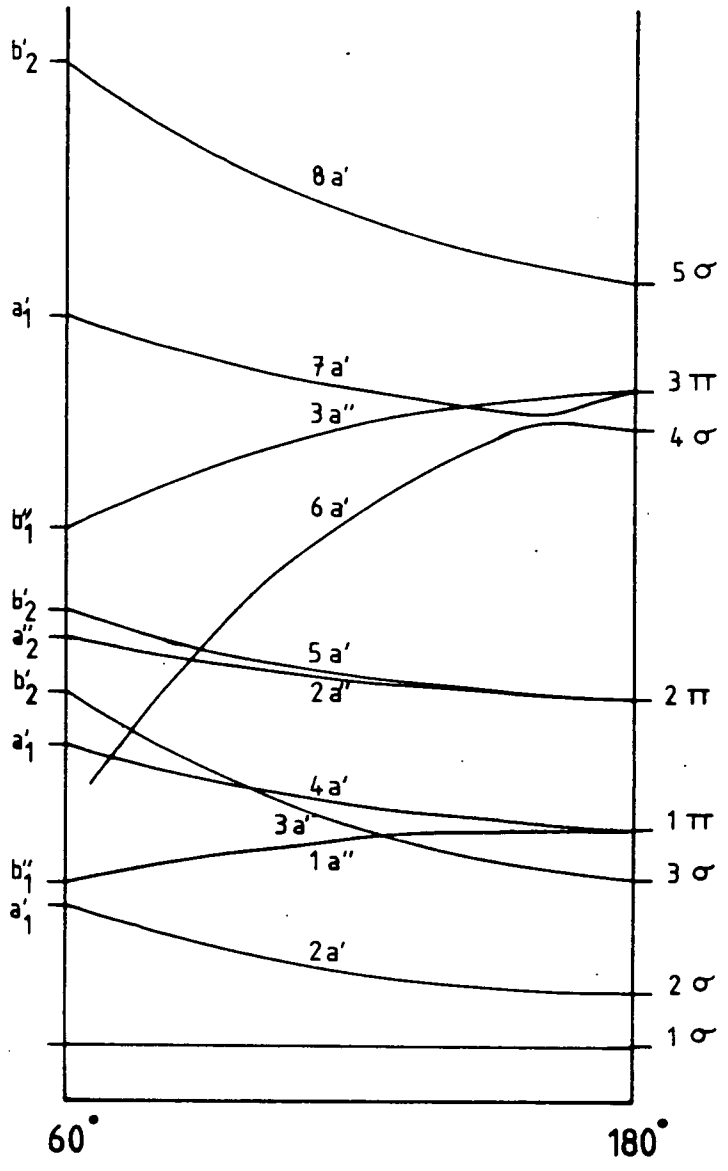

Figure 4.4 Walsh diagram for ABB system which shows the avoided crossing of the 3π and 4σ levels - after DIX73.

expected. The complex thus formed will have considerable vibrational energy. The lifetime of the complex as shown in chapter 3 is such that a few vibrational periods can be executed. It is thus quite likely that the complex will cross the linear geometry and that the electronic configuration corresponding to $^2\Pi_{\frac{1}{2}}$ will obtain. This doubly occupies an orbital which is I - I antibonding and would cause the complex to blow up. A second change of electronic configuration would be expected as the Iodine atom retreats so that the lowest energy surface is maintained. To form I* one or other of these avoided crossings must be followed diabatically. To account for the size of this channel the probability of surface hopping must be high. This probability, from the Landau Zener formula (BAT61), is

$$P = 1 - \frac{2\pi V_{12}}{\hbar v_r |S_1 - S_2|}$$

where V_{12} is the matrix element connecting the two states. r_{I2} is a strongly decreasing function of r_{I2}. Hence r_{I2} increases on the surface the system is likely to behave diabatically at the second crossing. If it is the second crossing that is followed diabatically, the difference in gradients $S_1 - S_2$ will be quite large (see fig 4.5). The radial velocity v_r can be large also and all of these conditions allow the probability to approach unity.

4.5 Reactions of Fluorine with interhalogens

Reactions (2) and (3) give vibrational energy distributions

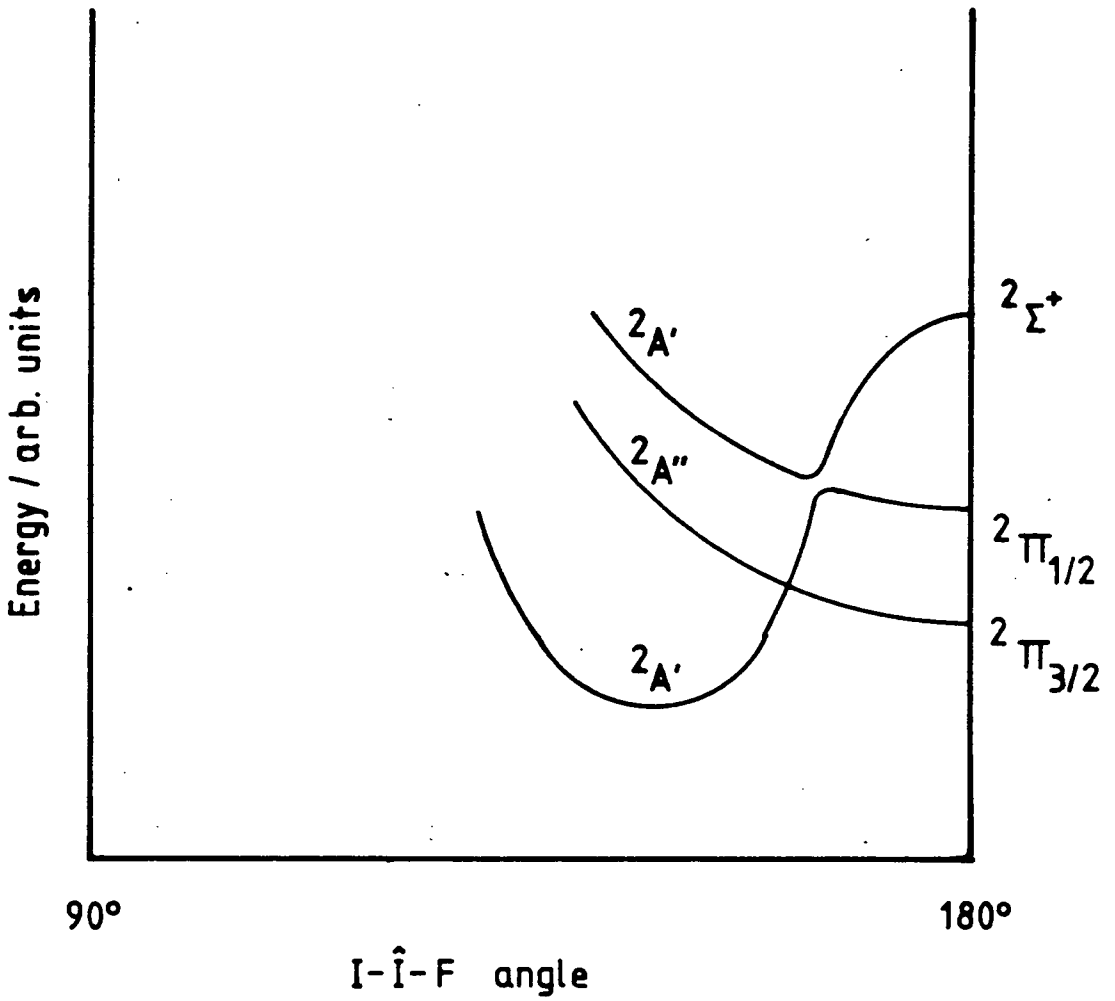

Figure 4.5 (a)
Possible correlation diagram for I_2F showing how the electronic states might vary with bond angle given the orbital scheme proposed by Herschbach.

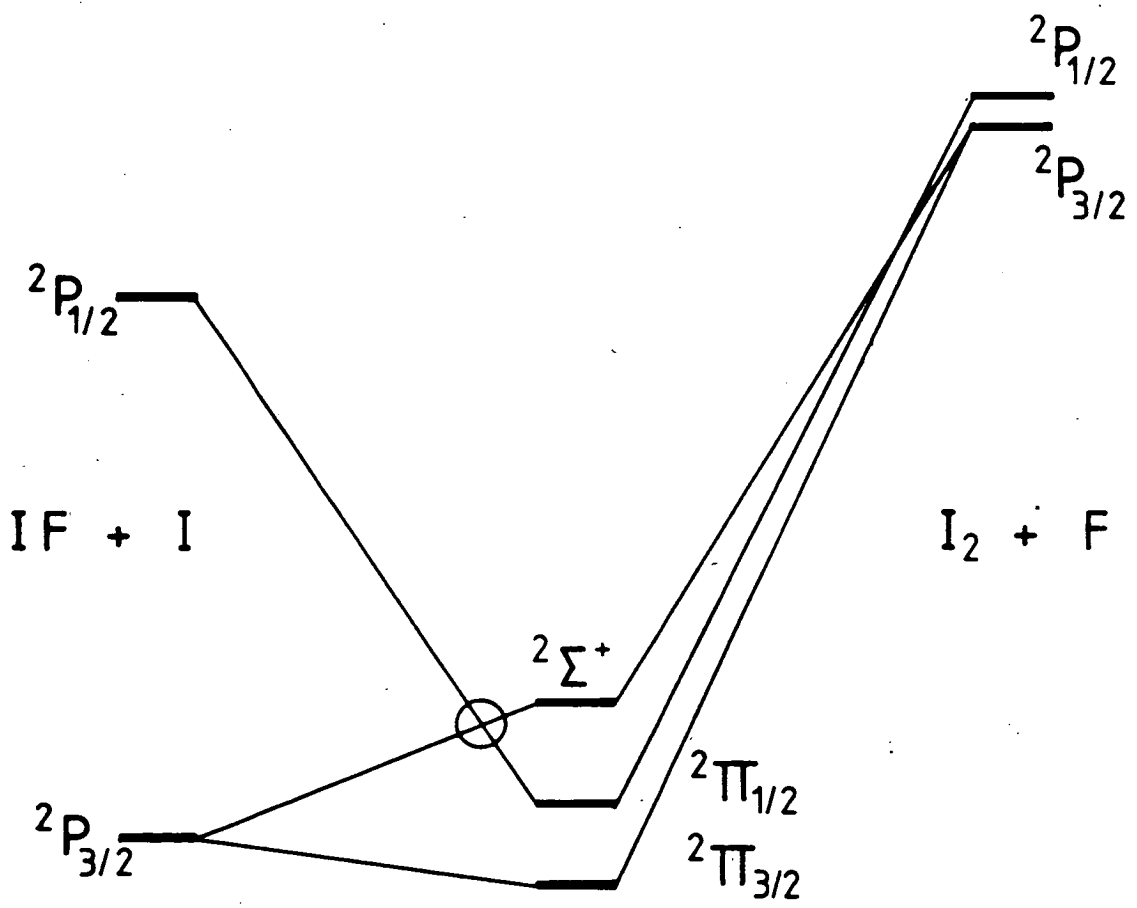

Figure 4.5(b) Correlation diagram for colinear I-I-F given the orbital scheme proposed by Herschbach. At the circled crossing the difference in gradients of the potential surfaces will be large because of the large difference in the energy of the two atomic states of iodine. If spin orbit interactions are strong in I_2F then these two states will adopt the same symmetry, $^2E_{\frac{1}{2}}$, and it becomes an avoided crossing.

(TRI 80) very similar to that of reaction (1). Bimodal distributions could be formed here by the migratory mechanism of Polanyi (POL80) since there is a barrier for the F - X - I geometry. However the strong similarity of the three distributions suggests a mechanism similar to that of reaction (1) where no such migratory mechanism was found.

If the distributions are separated into two channels as before then the relative populations of the high energy (direct) branch and the low energy (complex) branch can be estimated. These values are given in table 4.1 where no obvious pattern seems to emerge. Fig.4.6 shows surprisal plots for the three reactions taken from Wanner's data (TRI80). The high $f_{v'}$ points for the three reactions are very much alike. They have different intercepts but are otherwise similar, with the curvatures for $f_{v'}$ near unity almost identical. For the nearly linear region of the plot between $f_{v'} = 0.5$ and $f_{v'} = 0.8$ the gradients are shown in table 4.1. The strong agreement within the error limits suggests that the reactions proceed on qualitatively similar potential energy surfaces. The gradients g_c for the complex region $v = 0$ and $v = 1$ are positive and increase along the series ICl, IBr, I_2. If however these surprisals are calculated using the energy available when X^* is formed (table 4.2), the gradients g_c' agree very well. These points are also shown in figure 4.6. No error bars are plotted for these points, because the relative populations are likely to be close to the given values. The quoted error limits

IX	% direct	% complex	g_d	g_c	g_c'
I_2	9 ± 2	91 ± 2	-8.1 ± 1.0	48 ± 12	12 ± 4
IBr	70 ± 10	30 ± 10	-7.0 ± 0.4	20 ± 10	11 ± 4
ICl	50 ± 10	50 ± 10	-7.1 ± 0.8	14 ± 4	11 ± 4

Table 4.1 Relative populations of the peaks in the vibrational distributions of reference TRI80. Also the gradients from the surprisal plots of figure 4.6 - see text for details.

PRODUCTS \ IX	I_2	IB_r	ICl
IF + X	-118	- 90.3	- 57.2
IF + X^*	-27.1	- 46.1	- 46.6

Table 4.2 Exothermicities in $J\ mol^{-1}$ for each channel of reactions (1), (2) and (3).

(TRI 80) are probably large to take into account the normalisation to the higher v points which require different laser dyes and are masked by the fluorescence from IX.

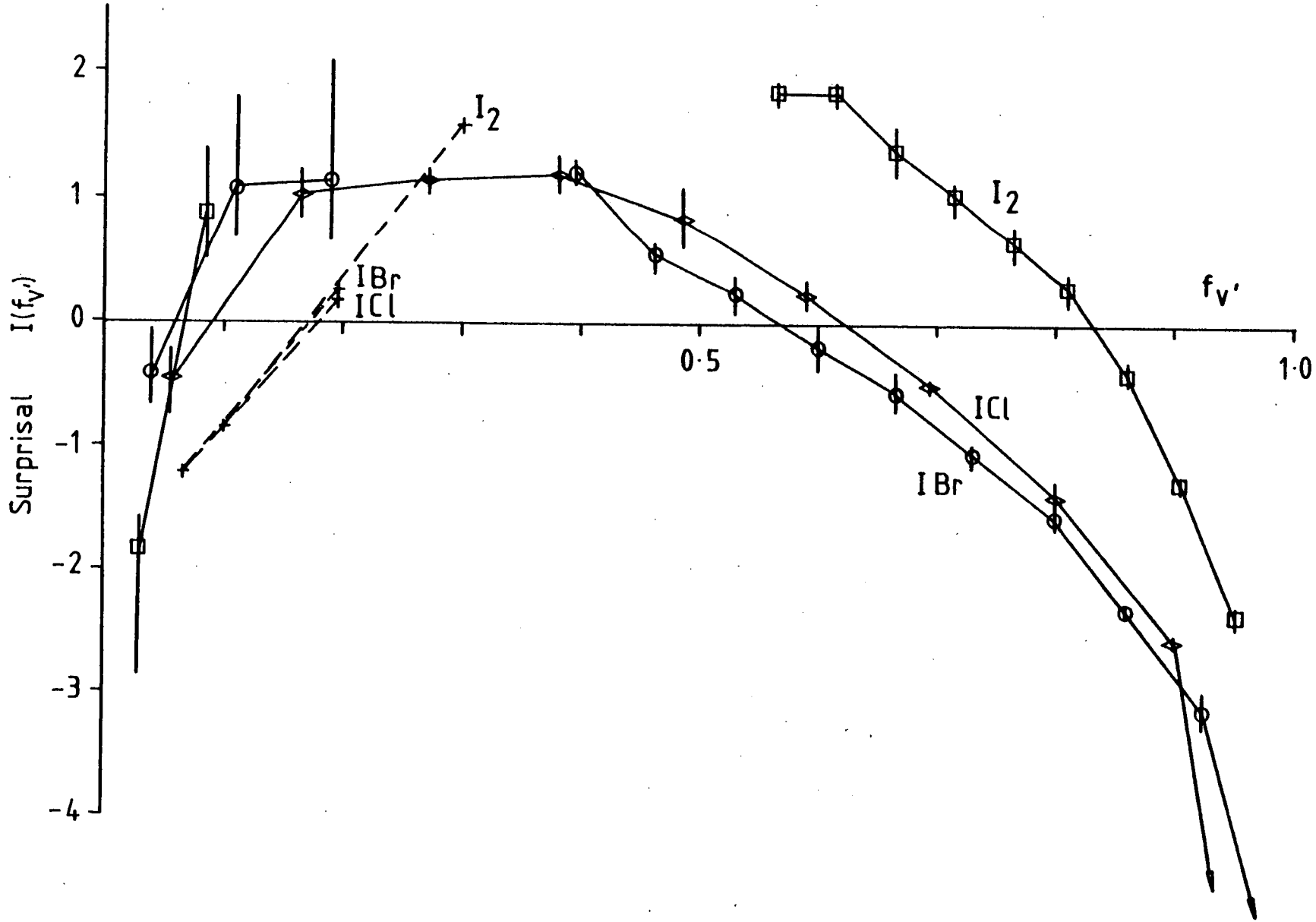

Figure 4.6 Surprisal plots of the data from ref. TRI80. See text for details.

If these reactions follow the argument of section 4.4.3 then the energy release will appear as a repulsion in FI...X. The energy distributions might then be predicted by one of the many retreat coordinate models (POL 74). The simplest of these is the 'Impulsive Model'. An instantaneous force acts between FI - X which represents the sudden transition to a repulsive surface. The resulting vibrational energy is given by

$$E_{v'} = E'_{tot} \cdot \frac{M_F}{M_F + M_I} \cdot \frac{M_F}{M_I + M_X} \cdot \cos^2 \alpha$$

with $\alpha = 0$ for the linear case. This model often underestimates $E_{v'}$ but gives a guide to the effect of the mass combination. The predicted values, for linear systems, for reactions (1), (2) and (3) are then

IX	I_2	IBr	ICl
$E_{v'}$	1.9	2.4	2.8 KJ mol^{-1}

all of which are less than the zero point energy of IF, 3.6 KJ mol^{-1}. The expected distribution would therefore strongly favour v = 0, which is observed.

The argument of section 4.4.3 also suggests that the impulse occurs near the linear configuration. As E_R, from the impulsive model varies with $1 - \cos^2\alpha$, very little of the available energy would appear as rotation agreeing with the observed results for reaction (1) given in chapter 2.

4.6 Summary and Conclusions

The experimental results for reaction (1) either conflict with each other or they point to the formation of electronically excited Iodine. Comparison of the form of the laser induced fluorescence results for reaction (1) with those of reactions (2) and (3) suggests that excited Bromine and Chlorine are also formed. As $^2P_{\frac{1}{2}}$ products do not correlate with the electronic states of the reactants a surface hopping mechanism must be involved. A possible route to the excited state, outlined above, also accounts for the observed energy distributions.

It had been thought that the predicted inversion of the product IF vibrational energy distribution for reaction (1) could have been used for a far infra-red chemical laser. However if $I(^2P_{\frac{1}{2}})$ is formed in the nine to one ratio inferred from the vibrational distribution, then a chemical laser working at 1.3 μm would be possible if it were technically feasible.

The observed chemiluminescence from $IF(A^3\Pi_1)$ and $IF(B^3\Pi o+)$ in $F_2 + I_2$ reactions (BIR 75, KAH 80) and reactions (1), (2) and (3) (TRI 81) might be easier to explain if an electronically excited halogen was already present from one of the previous steps in any reaction chain.

Although the indications from the experimental data are that the excited state atomic product is highly likely in these reactions, there is no direct evidence. Measurements of the $I(^2P_{\frac{1}{2}})$ to $I(^2P3/2)$ ratios, probably in a molecular beam environment, are needed to fully understand these interesting reactions.

Note added in proof.

Recently several papers have reported oxygen atom reactions with halogens and interhalogens (DAV82,FER82,DUR82,SMI82,HOF82). The reaction of oxygen with iodine could be expected to produce similar reaction dynamics to that of fluorine and iodine due to the similar mass combination. SMI82 reports a transition from complex dynamics to rebound scattering at higher energies, 0.45 ev, for this reaction. This is similar to the work already noted (CL078) and to the trajectory study of chapter 3 where this transition was also noticed. SMI82 suggests that different mechanisms occur at different impact parameters. The trajectory results for surface S_3 at 1.0 ev do show that small impact parameters tend to give backward scattering while large ones give a more symmetric distribution. $\langle\chi\rangle = 120^{\circ}$ for impact parameters less than the average and $\langle\chi\rangle = 88^{\circ}$ for those greater than average. Generally this was true for all the surfaces and energies used in the study but the difference was less pronounced at the lower energies. This effect did not lead to any bimodal energy distributions at a particular energy and it is thought unlikely to lead to any even if averaging over the reagent energy distributions is taken into account.

References.

DAV82 : F.E.Davidson, A.R.Clemo, G.L.Duncan, R.J.Browett, J.H.Hobson and R.Grice, Mole. Phys., 46, 33,(1982)

DUR82 : A.Durkin, D.J.Smith and R.Grice, Mole. Phys.,46, 55,(1982)

FER82 : D.P.Fernie,D.J.Smith, A.Durkin and R.Grice, Mole.Phys., 46, 41,(1982)

HOF82 : A.Durkin, D.J.Smith, S.M.A.Hoffman and R.Grice, Mole.Phys., 46, 1261,(1982)

SMI82 : A.Durkin, D.J.Smith and R.Grice, Mole. Phys., 46, 1251,(1982)

APPENDICES

Appendix A. Evaluation of expected signal rate

The reactive collision rate

$$\dot{Z} = n_F \, n_{I_2} \, \sigma_R \, \bar{v}_{rel} \qquad A1$$

is 2.4×10^{14} $cm^{-3}s^{-1}$ with n_F (6×10^{16} cm^{-3}) the fluorine atom density in the reaction zone, n_{I_2} (6×10^{12} cm^{-3}) the iodine molecule density in the reaction zone, σ_R (4.3×10^{-15} cm^2) the reaction cross section and $\bar{v}_{rel}$ (1.4×10^5 cm s^{-1}) the relative velocity. The number density of product species n_p is given by

$$n_p = \tfrac{1}{2} \dot{Z} C = \tfrac{1}{3} \dot{Z} \frac{\bar{r}}{\bar{v}'_{rel}} \qquad A2$$

Where C is a dwell time for the product in the reaction zone $\bar{r}$ is a representative dimension of the reaction zone, giving $n_p = 2.7 \times 10^8$ cm^{-3}. The fluorescence rate $\dot{n}$ is the product of n_p with the laser energy density $\int(t)$ and the transition probability $B(\lambda)$. If the laser pulse shape is assumed to be square then $\int(t) = \int_o = 4.5 \times 10^{-12}$ J cm^{-3} MHz^{-1}. The transition probability is determined from

$$B(\lambda_L) = q_{v'v''} \left| R_e(\bar{r}_{v'v''}) \right|^2 \sum_{\Delta J''} S_{J'J''} \exp \left(\frac{-J''(J''+1)}{Q_R(v'')} \right) \qquad A3$$

where $q_{v'v''}$ is the Franck-Condon factor and R_e ($\bar{r}_{v'v''}$) is the dipole moment. The summation over $\Delta J''$ in equation A3 accounts for the finite bandwidth of the laser and the relatively close spacing of the rotational transitions. Near a bandhead the exponential is approximately unity and $S_{J'J''}$, the line strength becomes $(2J'' + 1)$. This then gives, for a laser wavelength λ_L close to a bandhead $\dot{n}(\lambda_L) = 2.1 \times 10^{14}$ $p(v'')$. $q_{v'v''}$ cm^{-3} s^{-1} where $p(v'')$ is the fraction of

product molecules in the v" state. The absolute signal is then

$$S(\lambda_L) = \dot{n}(\lambda_L).\Delta t_L.V.f.\epsilon \qquad A4$$

with Δt_L (5ns) the laser pulse length, V ($9mm^3$) is the probe volume, f (100HZ) is the repetition rate and ϵ is the collection efficiency. The optics collect signal through a cone of full angle $\pi/4$ radians and the photomultiplier efficiency is around 10% giving ϵ = 0.6%. Therefore A4 gives $S(\lambda_L) = 5906, p(v'')_1 q_{v',v''}$.

For the accessible bands of IF, $q_{v',v''}$ = 0.1 is a reasonable value, then if p (v") is 10% (say) the expected count rate would be 55 S^{-1}.

Appendix B. Listing of programs **CDA1

**CDC1

**ADO1

POTFUN

```
%BEGIN
!
%OWNINTEGERARRAY REPLY(1:11)='K','W','U','D','P','C','M','S','T','H','O'
%INTEGER BASE,I,P,FLAG1
%SWITCH SW(1:11)
!
BASE= -8192
!..............ADDRESS OF SHARED AREA.................
%ROUTINE HELP
 %PRINTTEXT'  POSSIBLE REPLIES  ';NEWLINE
 %PRINTTEXT'--------------------';NEWLINE
 %PRINTTEXT'  K - KILL PROGRAM '
 %PRINTTEXT'  W - WAIT PROGRAM '
 %PRINTTEXT'  U - UPDATE VARIABLES IN DATA COLL. PROGRAM'
 %PRINTTEXT'  D - DRIVE GRATING TO NEW WAVELENGTH'
 %PRINTTEXT'  P - PRINT EXP. VAR. LIST'
 %PRINTTEXT'  C - COLLECT DATA '
 %PRINTTEXT'  S - REVIEW A SCAN WRT WAVELENGTH'
 %PRINTTEXT'  M - MARK AN OLD BLOCK AS DEFECTIVE'
 %PRINTTEXT'  O - ANALYSE AN OLD BLOCK'
 %PRINTTEXT'  H - LIST THIS FILE'
 %END ; ! OF HELP
!
!
%PRINTTEXT'HELP INFORMATION?'
READSYMBOL(P);NEWLINE
%IF P='Y' %THEN HELP
CHECK1:%IF INTEGER(BASE)=0 %THEN -> CHECK2
! C0 = 0 IMPLIES DATA COLL. PROG. LOADED
%PRINTTEXT' INSERT DATA COLLECTION PROGRAM';NEWLINE
WAITPROG
->CHECK1
CHECK2:%IF INTEGR(BASE+2)=0 %THEN -> PROMPT
! C1 = 0 IMPLIES DATA ANALYSIS PROGRAM LOADED.
%PRINTTEXT' INSERT DATA ANALYSIS PROGRAM';NEWLINE
WAITPROG
->CHECK1
!
!
PROMPT:READSYMBOL(P)
%CYCLE I=1,1,11
%IF P#REPLY(I) %THEN -> PASS
NEWLINE
->SW(I)
PASS:%REPEAT
%IF P#10 %AND P#32 %THEN %PRINTTEXT'?'
NEWLINE;->PROMPT
!
!
SW(9):->PROMPT
!
SW(1):INTEGER(BASE)=1
INTEGER(BASE+2)=1
STOPPROG
!
SW(2):INTEGER(BASE)=2
INTEGER(BASE+2)=2
WAITPROG
->CHECK1
!
```

```
SW(3):INTEGER(BASE)=3
U:WAIT(50)
%IF INTEGER(BASE)=0 %THEN -> PROMPT
->U
!
SW(4):INTEGER(BASE)=4
D:WAIT(50)
%IF INTEGER(BASE)=0 %THEN -> PROMPT
->D
!
SW(5):INTEGER(BASE)=5
->PROMPT
!
SW(6):INTEGER(BASE)=6
->PROMPT
!
SW(7):INTEGER(BASE+2)=7
->PROMPT
!
SW(8):INTEGER(BASE+2)=8
->PROMPT
SW(10):HELP
->PROMPT
!
SW(11):INTEGER(BASE+2)=11
->PROMPT
!
%ENDOFPROGRAM
```

```
E=RB03        COMPILED: 07/04/81  14.38.18
BLER FILE=.NULL

IMP-11 COMPILER 7.100
      1     %BEGIN
      2        *.NOLIST
      3        %ENDOFLIST
    412        *.LIST
    413        %ROUTINESPEC COLLECTDATA
    414        %ROUTINESPEC SETOUTPUT
    415        %ROUTINESPEC DECODE(%INTEGERNAME COUNTS,ERRCD,%INTEGER AB)
    416        %ROUTINESPEC STOPPROG
    417        %ROUTINESPEC WRITETODISC
    418        %ROUTINESPEC ANALYSE(%REALARRAYNAME D1,%REAL M1,LIM,%REALNAME MEAN,%C
                SIGMA,%INTEGERNAME N1)
    419        %ROUTINESPEC WAITPROG
    420        %ROUTINESPEC CHECKINTERRUPT
    421        %ROUTINESPEC LOADVARS
    422        %ROUTINESPEC INITIALISE(%INTEGER CHECK)
    423        %ROUTINESPEC MONITOR
    424        %ROUTINESPEC DRIVEGRATING
    425        %ROUTINESPEC CHECKERROR(%INTEGERNAME COUNTS,ERRCD,%INTEGER AB)
    426        %REALFNSPEC READLASER
    427        %INTEGER I,P,CTIME,COUNTS0,COUNTS1,MINT,MONIT,T1,DTIME
    428        %INTEGER ERRCD,NSETS,ERRCD1,IMONIT,IFLAG
    429        %INTEGER FLAG1,FLAG3,FLAG4,BASE
    430        %INTEGER ISET,STEPS,SEQNO,IINST,NC,NC0,QFLAG,IE,RTI
    431        %REAL MM,LL,TIMEIN,TIMEOUT
    432        %INTEGER NBLOCK,FBLOCKS
    433        %INTEGER OLDDIR,NEWDIR
    434        %REALARRAY P1(1:16)
    435        %REALARRAY PP1(1:16)
    436        %REALARRAY P0(1:16)
    437        %REALARRAY PP0(1:16)
    438        %REALARRAY ILASER(1:50)
    439        %REAL LPOW,LPOW1,LSIGMA,LFAC1,LFAC2,LSCALE
    440        %REAL MP0,MP1,MPP0,MPP1,Q0,Q1,QQ0,QQ1
    441        %REAL MTIME,SUMERR,FFAULT,FTIME
    442        %INTEGERARRAY S0(1:16)
    443        %INTEGERARRAY S1(1:16)
    444        %INTEGERARRAY S2(1:16)
    445        %INTEGERARRAY S3(1:16)
    446        %INTEGERARRAY FNAME(0:2)
    447        %INTEGERARRAY TNAME(0:2)
    448        %REALARRAY EXPVAR(0:31)
    449        %SWITCH EXEC(1:9)
    450        SETPOT(256,256)
    451        SETPOT(512,512)
    452        SETPOT(1024,1024)
    453        !COMMON BLOCK ADDRESS STARTS AT -8192
    454        BASE=-8192
    455        ! FIRST NO. IS CONTROL VARIABLE FOR COLLECT PROG
    456        ! SECOND CONTROLS ANALYSIS PROG (BASE+2)
    457        ! THIRD CONTAINS SEQNO(LIF***)   (BASE+4)
    458        !FOURTH CONTAINS MOST RECENT BLOCK NO.  (BASE+6)
    459        ! ENTRY TO PROGRAM HERE
```

```
460       ! INITIALISE VARIABLES
461       IINST=6  ;! NO. OF POSSIBLE ACTIONS
462       ISET=0
463       NSETS=0
464       NBLOCK=1
465       STEPS=0
466       FLAG3=0  ;!  SUPPRESSES ERROR MESSAGES FROM DECODE.
467       QFLAG=1  ;!DEFINE DAFILE ON FIRST PASS
468       IFLAG=0  ;!  INTERRUPT FLAG
469       LOADVARS   ;!READS DEFAULT VALUES OF EXPVAR FROM LIF000
470       INITIALISE(0)     ;!CHECKS THE VALUES OF EXPVAR ARE O.K.
471       %CYCLE I=1,1,16
472       S0(I)=0;S1(I)=0
473       P0(I)=0;P1(I)=0
474       PP0(I)=0;PP1(I)=0
475       %REPEAT
476       PROMPT2:INTEGER(BASE)=0
477       WAIT(500)
478       PROMPT1:P=INTEGER(BASE)
479       %IF P=0 %THENSTART
480          %PRINTTEXT'COLLECTION PROGRAM AWAITING INSTRUCTIONS'
481          RINGBELL(2);NEWLINE
482          WAIT(500)
483          ->PROMPT1
484          %FINISH
485       %CYCLE IE=1,1,IINST
486       %IF P=IE %THEN ->EXEC(IE)
487       %REPEAT
488       %PRINTTEXT' INVALID COMMON VARIABLE';NEWLINE
489       WAITPROG;->PROMPT2
490       EXEC(1):STOPPROG
491       !
492       EXEC(2):WAITPROG
493       ->PROMPT2
494       !
495       EXEC(3):INITIALISE(1)
496       ->PROMPT2
497       !
498       EXEC(4):DRIVEGRATING
499       -> PROMPT2
500       !
501       EXEC(5):%PRINTTEXT'VARIABLE LISTING';NEWLINE
502       %CYCLE I=0,4,28
503       %CYCLE P=0,1,3
504       PRINTFL(EXPVAR(I+P),11);SPACES(6)
505       %REPEAT
506       NEWLINES(2)
507       %REPEAT
508       ->PROMPT2
509       !
510       EXEC(6):COLLECTDATA
511       ->PROMPT1
512       !
513       %ROUTINE COLLECTDATA
514          %INTEGER AB
515          SELECTOUTPUT(0)
```

```
516         TIMEIN=RTIME
517         SUMERR=0
518         FLAG1=1 ;!ENTRY WITH BEAM ON
519         NC=0 ;!NO OF PAIRS AT THIS W.
520         LPOW=1  ;  LSIGMA=1    ;!    SET LASER POWER=1 FOR MONITOR OFF
521         RESET:%IF IFLAG=1 %THENSTART
522         CHECKINTERRUPT
523         %RETURNIF RTI=0
524         %FINISH
525         %IF FLAG1=1 %THEN NC=NC+1
526         SKIPINC:IFLAG=0
527         ERRCD=0
528         %IF FLAG1=1 %THENSTART
529         SETPOT(0,1024) ;!TESLA ON,DISCHARGE ON
530         WAIT(DTIME+120) ;!WAIT FOR TESLA OFF AND BEAM SETTLE
531         %FINISH
532         SETPOT(0,512)
533         SETPOT(512,512)   ;  !RESET SCALAR
534         SETPOT(0,256)
535         SETPOT(256,256)   ;  !START SCALAR
536         ERRCD1=0
537         %IF IMONIT=0 %THENSTART
538         WAIT(CTIME*50+1)
539         ->NOLASER
540         %FINISH
541         MTIME=RTIME
542         LPOW1=LPOW ;!OLD LASER POWER
543         MONITOR
544         MTIME=(RTIME-MTIME)*3000
545         T1=INTPT(CTIME*50-MTIME)
546         WAIT(T1+1) %IF T1>0
547         NOLASER:
548         %IF FLAG1=1 %THEN SETPOT(1024,1024) ;! DISCHARGE OFF
549         AB=1            ;!   SELECT SCALER A
550         DECODE(COUNTS0,ERRCD,AB)  ;!  READ SCALAR A
551         %IF ERRCD#0 %THEN CHECKERROR(COUNTS0,ERRCD,AB)
552         %IF ERRCD#0 %THEN ->SKIPINC
553         AB=0              ;!    SELECT SCALAR B
554         DECODE(COUNTS1,ERRCD,AB)  ;!     READ SCALAR B
555         %IF ERRCD#0 %THEN CHECKERROR(COUNTS1,ERRCD,AB)
556         %IF ERRCD#0 %THEN -> SKIPINC
557         %IF ERRCD1>1 %THENSTART
558             RINGBELL(3)
559             %PRINTTEXT'LASER POWER VARYING.';NEWLINE
560             ERRCD1=ERRCD1-2;%FINISH
561         %IF ERRCD1=1 %THENSTART
562             RINGBELL(3)
563             %PRINTTEXT'LASER POWER CHANGED';NEWLINE
564             %FINISH
565         %IF FLAG1=1 %THENSTART
566         S3(NC)=COUNTS0
567         S2(NC)=COUNTS1
568         P1(NC)=LPOW
569         PP1(NC)=LSIGMA
570         FLAG1=0;! DISCHARGE OFF
571         WAIT(100) ;! WAIT FOR BEAM TO SETTLE
```

```
572          -> RESET
573          %FINISH
574          ! FLAG1=0 FOR THIS DATUM HERE,SO PROCESS ONE PAIR OF COUNTS
575          S1(NC)=COUNTS0
576          S0(NC)=COUNTS1
577          P0(NC)=LPOW
578          PP0(NC)=LSIGMA
579          %IF NC=NC0 %THENSTART
580          TIMEOUT=RTIME
581          SETPOT(0,512)
582          SETPOT(512,512)
583          WRITETODISC
584          INTEGER(BASE+6)=NBLOCK-1 ; !THE NUMBER OF THE BLOCK JUST COLLECTED
585          INTEGER(BASE+2)=6 ; !TELL ANAL TO ANALYSE THE BLOCK JUST COLLECTED
586          %RETURN
587          %FINISH
588          ! PROCEED TO BEAM ON
589          FLAG1=1
590          ->RESET
591          %END ;! COLLECTDATA
592       !
593       %ROUTINE DECODE(%INTEGERNAME COUNTS,ERRCD,%INTEGER AB)
594          !
595          %INTEGER I,J,N,R,II,K
596          %OWNINTEGERARRAY PRIORITY(0:11)=0,1,0,1,0,1,0,1,0,1,0,1
597          %OWNINTEGERARRAY IMAXD(0:5) = 7,6,7,2,3,0
598          %INTEGERARRAY BIT(0:4)
599          %INTEGERARRAY SETBIT(0:11)
600          %INTEGERARRAY DIGIT(0:5)
601          %INTEGERARRAY A(0:11)
602          %INTEGERARRAY STORE(0:11)
603          %ROUTINE GETDATA
604             ! READS BINARY DATA (12 BYTES OF 5 BITS EACH) FROM INTERFACE
605             %INTEGERFNSPEC READBIN
606             %INTEGER I
607             %CYCLE I=0,1,11
608             STORE(I)=21
609             %REPEAT
610             %CYCLE I=0,1,11
611             STORE(I)=READBIN
612             WAIT(5)
613             %REPEAT
614             %INTEGERFN READBIN
615                *EMT+336
616                *MOV+12. (R1),R1
617                *RTS+PC
618                %END ;!READBIN
619             %END ;!GETDATA
620          !
621          SETPOT(AB*2048,2048)
622          GETDATA
623          %CYCLE I=0,1,11
624          %IF STORE(I)=31 %THENSTART
625          NEWLINE
626          RINGBELL(3)
627          %PRINTTEXT' MODE FAULT';NEWLINE
```

```
628         ERRCD=1
629         K=0
630         -> TRANSFER
631         %FINISH
632         %REPEAT
633         %CYCLE I=0,1,11
634         %IF STORE(I)=20 %THEN ->PERM ;!START CODE IN HIGHEST BYTE
635         %REPEAT
636         ERRCD=4
637         %RETURNIF FLAG3=1
638         RINGBELL(3);%PRINTTEXT' STARTCODE FAULT'
639         NEWLINE
640         K=0
641         -> TRANSFER
642         PERM:
643         %CYCLE II=I,1,11
644         A(II-I)=STORE(II)
645         %REPEAT
646         -> CHECK RANK %IF I=0 ;! NO CYCLING OF ELEMENTS
647         K=11-I+1
648         TRANSFER:%CYCLE II=K,1,11
649         A(II)=STORE(II-K)
650         %REPEAT
651         %IF ERRCD#0 %THEN ->DIAGS
652         CHECKRANK:
653         %IF A(1)=10 %THENSTART
654         IFLAG=1 ;!INTERRUPT REQUEST CODE
655         %FINISH
656         %CYCLE I=2,1,11
657         %IF PRIORITY(I)=0 %AND ((A(I)=0 %AND A(I+1)=0) %OR     %C
            (A(I)#0 %AND A(I+1)#0)) %THENSTART
658         ERRCD=2
659         %RETURNIF FLAG3=1
660         NEWLINE
661         RINGBELL(3)
662         %PRINTTEXT' READOUT FAULT'
663         NEWLINE
664         ->DIAGS
665         %FINISH
666         %REPEAT
667         %CYCLE I=2,1,11 ;! SKIP STARTCODE
668         %IF A(I)=0 %THEN -> PASSBYTE
669         %CYCLE J=0,1,4
670         BIT(J)=A(I)<<J&16              ;!GET BIT
671         %IF BIT(J)=16 %THENSTART       ;!TEST FOR SET BIT
672         SETBIT(I)=4-J                 ;!POSITFLAG1 OF SET BIT
673         N=5-(I-(PRIORITY(I)))//2   ;!POWER OF TEN
674         DIGIT(N)=SETBIT(I)+5*(1-(PRIORITY(I)))
675                                       ;!VALUE OF BYTE
676         %FINISH
677         %REPEAT
678         PASSBYTE:%REPEAT
679         N=4
680         TESTDIGIT:R=DIGIT(N)-IMAXD(N)
681         %IF R<0 %THEN -> COUNTSOK
682         %IF R=0 %AND N#0 %THENSTART
```

```
683           N=N-1
684           -> TESTDIGIT
685           %FINISH
686           ERRCD=3
687           %RETURNIF FLAG3=1
688           NEWLINE
689           RINGBELL(3)
690           %PRINTTEXT' OVERFLOW FAULT'
691           NEWLINE
692           ->DIAGS
693           COUNTSOK:COUNTS=0
694           %CYCLE N=0,1,4
695           COUNTS=COUNTS+DIGIT(N)*10**N
696           %REPEAT
697           ERRCD=0
698           FLAG3=0
699           %RETURN
700           DIAGS:%RETURNIF EXPVAR(31)=0
701           %CYCLE I=0,1,11
702           WRITE(A(I),4)
703           %REPEAT
704           NEWLINE
705           %END ;! DECODE
706        !
707        %ROUTINE MONITOR
708           %INTEGER I
709           %REAL MM,LL
710           %CYCLE I=1,1,MONIT
711           ILASER(I)=READLASER
712           WAIT(MINT)
713           %REPEAT
714           MM=0
715           LL=30000
716           %IF MONIT=1 %THENSTART
717           LPOW=ILASER(1)
718           ->SKIPANALYSIS
719           %FINISH
720           ANALYSE(ILASER,MM,LL,LPOW,LSIGMA,MONIT)
721           SKIPANALYSIS:
722           %IF ABS(1-LPOW/LPOW1)>LFAC1 %THENSTART
723           %RETURNIF NC=1 ;! NO DIAG ON FIRST PASS
724           ERRCD1=1
725           %FINISH
726           %IF MONIT=1 %THENRETURN
727           %IF LSIGMA>LPOW*LFAC2 %THENSTART
728           ERRCD1=ERRCD1+2
729           %FINISH
730           %END ;!MONITOR LASER
731        !
732        %ROUTINE ANALYSE(%REALARRAYNAME D1,%REAL M1,LIM,%REALNAME MEAN,%C
                    SIGMA,%INTEGERNAME N1)
733           %INTEGER NA,NB,C
734           %REAL E,M2,SD
735           NA=1
736           NB=N1
737           SD=0.
```

```
738          M2=0
739          C=0
740          %IF LIM<=0. %THEN LIM=.0001 ;! SMALL PERTURBATION
741          %CYCLE I=NA,1,NB
742          E=D1(I)
743          %IF ABS(E-M1)<LIM %THENSTART
744          M2=M2+E
745          C=C+1 ;! ACCEPTED ELEMENTS
746          %FINISH
747          %REPEAT
748          ->OK %UNLESS C<2
749          RINGBELL(10)
750          NEWLINE ;%PRINTTEXT' DIVISION BY ZERO IN ANALYSE';NEWLINE
751          WRITE(C,4);WRITE(NA,4);WRITE(NB,4)
752          NEWLINE
753          PRINT(M1,6,4);PRINT(LIM,6,4);PRINT(E,6,4);NEWLINE
754          MEAN=1;SIGMA=1
755          %PRINTTEXT' DATA COLLECTION STOPPED'
756          WAITPROG
757          %RETURN
758          OK:M2=M2/C ;! NEW ESTIMATE OF MEAN
759          %CYCLE I=NA,1,NB
760          E=D1(I) ;! SUBTRACT MEAN TO AVOID LOSS OF PRECISFLAG1
761          %IF ABS(E-M1)<LIM %THEN SD=SD+(E-M2)*(E-M2)
762          %REPEAT
763           N1=C
764          MEAN=M2
765          SIGMA=SQRT(SD/(C-1)) ;! STANDARD DEVN.
766          %END ;!ANALYSE
767       !
768       !
769       %ROUTINE STOPPROG
770          NEWLINE;WRITE(NSETS,3)
771          %PRINTTEXT'DATA SETS CREATED';NEWLINE
772          %PRINTTEXT'LAST SEQ NO. = ';WRITE(SEQNO,4)
773          NEWLINES(2)
774          *EMT+372
775          %END ;!STOPPROG
776       !
777       %ROUTINE INITIALISE(%INTEGER CHECKONLY)
778          %INTEGER IDEFN,IMAX,I,JJ
779          IDEFN=30
780          IMAX=0
781          JJ=1
782          %IF CHECKONLY=0 %THEN ->CHECKVARS
783          NEWLINE;%PRINTTEXT' TYPE INDEX=-1 TO END ALTERATIONS'
784          READINDEX:NEWLINE
785          %PRINTTEXT'INDEX NO:';READ(I)
786          %IF I<=0 %THEN -> CHECKVARS
787          %IF I>31 %THENSTART
788          %PRINTTEXT'OUT OF RANGE'
789          -> READINDEX
790          %FINISH
791          %IF I>=23  %AND I<=27 %THENSTART
792          NEWLINE;%PRINTTEXT' NOT ACCESSIBLE'
793          ->READINDEX
```

```
794         %FINISH
795         %IF I>IDEFN %THENSTART
796         %PRINTTEXT'WARNING-VARIABLE NO.';WRITE(I,3)
797         %PRINTTEXT'NOT DEFINED'
798         %FINISH
799         %IF I=18 %THEN QFLAG=1
800         %IF I=11 %THEN STEPS=0
801         READVARS:
802         %PRINTTEXT'VAR.SETTING:';READF(EXPVAR(I))
803         %IF I>IMAX %THEN IMAX=I
804         JJ=JJ+1
805         -> READINDEX
806         CHECKVARS:%IF IMAX>IDEFN %THEN ISET=IMAX %ELSE ISET=IDEFN
807         EXPVAR(0) =ISET
808         ! CHECK FOR FAULTY PARAMS
809         LSCALE=EXPVAR(9)
810         %IF LSCALE<0.001 %OR LSCALE>10.0 %THENSTART
811         NEWLINE;%PRINTTEXT'INVALID MONITOR FSD'
812         I=9;JJ=JJ-1
813         ->READVARS
814         %FINISH
815         DTIME=INTPT(50*EXPVAR(16)+0.001)
816         CTIME=INTPT(EXPVAR(17)+0.001)
817         %IF CTIME#1 %AND CTIME#10 %AND CTIME#100 %THENSTART
818         NEWLINE;%PRINTTEXT'INVALID COUNT TIME';NEWLINE
819         I=17;JJ=JJ-1
820         ->READVARS
821         %FINISH
822         SEQNO=INTPT(EXPVAR(18)+0.001)
823         %IF SEQNO=0 %OR SEQNO>999 %THENSTART
824         NEWLINE;%PRINTTEXT 'INVALID SEQ.NO.';NEWLINE
825         I=18;JJ=JJ-1
826         ->READVARS
827         %FINISH
828         INTEGER(BASE+4)=SEQNO
829         MONIT=INTPT(EXPVAR(19)+.01)
830         %IF MONIT<0 %OR MONIT>50 %THENSTART
831         %PRINTTEXT'INVALID NO. OF MONITORINGS';NEWLINE
832         I=19;JJ=JJ-1
833         ->READVARS
834         %FINISH
835         LFAC1=EXPVAR(20)
836         LFAC2=EXPVAR(21)
837         NC0=INTPT(EXPVAR(22)+0.001)
838         %IF NC0>16 %OR NC0<1 %THENSTART
839         %PRINTTEXT'INVALID NO OF DATA POINTS';NEWLINE
840         I=22;JJ=JJ-1
841         ->READVARS
842         %FINISH
843         FLAG4=INTPT(EXPVAR(28)+0.001)
844         %IF FLAG4#0 %AND FLAG4#1 %THENSTART
845         %PRINTTEXT'INVALID VARIABLE 28-FLAG';NEWLINE
846         I=28;JJ=JJ-1
847         ->READVARS
848         %FINISH
849         %IF EXPVAR(29) <0 %OR EXPVAR(29)>30 %THENSTART
```

```
850           %PRINTTEXT'INVALID SIGNAL GATE';NEWLINE
851           I=29;JJ=JJ-1
852           ->READVARS
853           %FINISH
854         %IF EXPVAR(30)<1 %OR EXPVAR(30)>10 %THENSTART
855           %PRINTTEXT'INVALID NOISE GATE';NEWLINE
856           I=30;JJ=JJ-1
857           ->READVARS
858           %FINISH
859         !
860         ! ALTER OUTPUT STREAM IF SEQNO HAS BEEN CHANGED
861         !
862         %IF QFLAG=1 %THENSTART
863         SETOUTPUT
864         QFLAG=0
865         %FINISH
866         %IF MONIT=0 %THENSTART
867         NEWLINE;%PRINTTEXT' LASER MONITORING OFF';NEWLINE
868         IMONIT=0;%RETURN
869         %FINISH
870         IMONIT=1
871         MINT=INTPT(CTIME/MONIT*50+0.001);! LASER MONITORING INTERVAL
872         %END ;!INITIALISE
873       !
874       %ROUTINE WRITE TO DISC
875         %REALARRAY DA(0:127)
876         %INTEGER I,K,ADR,K0,BASE1
877         NEWLINE
878         %CYCLE K=0,1,127
879         DA(K)=0
880         %REPEAT
881         DA(0)=NBLOCK
882         DA(1)=STEPS
883         DA(2)=NC
884         DA(3)=TIMEIN
885         DA(4)=TIMEOUT
886         K0=5
887         %CYCLE K=0,1,31
888         DA(K+K0)=EXPVAR(K)
889         %REPEAT
890         K0=K0+K
891         ADR=ADDR(S0(1))
892         %CYCLE K=1,1,8
893         DA(K+K0)=MAKEREAL(ADR)
894         ADR=ADR+4
895         %REPEAT
896         K0=K0+K
897         ADR=ADDR(S1(1))
898         %CYCLE K=1,1,8
899         DA(K+K0)=MAKEREAL(ADR)
900         ADR=ADR+4
901         %REPEAT
902         K0=K0+K
903         %CYCLE K=1,1,16
904         DA(K+K0)=P0(K)
905         %REPEAT
```

```
906           K0=K0+K
907           %CYCLE K=1,1,16
908           DA(K+K0)=P1(K)
909           %REPEAT
910           K0=K0+K
911           ADR=ADDR(S2(1))
912           %CYCLE K=1,1,8
913           DA(K+K0)=MAKEREAL(ADR)
914           ADR=ADR+4
915           %REPEAT
916           K0=K0+K
917           ADR=ADDR(S3(1))
918           %CYCLE K=1,1,8
919           DA(K+K0)=MAKEREAL(ADR)
920           ADR=ADR+4
921           %REPEAT
922           WRITEDA(NBLOCK,ADDR(DA(0)))
923           NBLOCK=NBLOCK+1
924           NSETS=NSETS+1
925           BASE1=BASE+10
926           COMMONSEND(ADDR(DA(0)),127,BASE1)
927           %END ;!WRITETODISC
928        !
929        %ROUTINE SETOUTPUT
930           %INTEGER N,I
931           %INTEGERARRAY DIG(0:2)
932           SELECTOUTPUT(0)
933           N=SEQNO
934           %CYCLE I=0,1,2
935           DIG(I)=INTPT(N/10**(2-I))
936           N=N-DIG(I)*10**(2-I)
937           DIG(I)=DIG(I)+48
938           %REPEAT
939           ! DIG(I) CONTAINS THE DIGITAL PART OF THE OUTPUT FILE NAME
940           FNAME(0)='I'<<8+'L'
941           FNAME(1)=DIG(0)<<8+'F'
942           FNAME(2)=DIG(2)<<8+DIG(1)
943           NEWLINE
944           %PRINTTEXT' OUTPUTFILE IS LIF'
945           %CYCLE I=0,1,2
946           PRINTSYMBOL(DIG(I))
947           %REPEAT
948           NEWLINE
949           !OPEN FILE
950           OPENDA(FNAME)
951           FBLOCKS=FILESIZE(FNAME)
952           NEWLINE;%PRINTTEXT' FILE CONTAINS';WRITE(FBLOCKS,6)
953           %PRINTTEXT' BLOCKS'
954           NBLOCK=FBLOCKS+1
955           %PRINTTEXT' NEXT BLOCK NO.=';WRITE(NBLOCK,6)
956           NEWLINE
957           %END ;!SETOUTPUT
958        !
959        %ROUTINE LOADVARS
960           %INTEGER I
961           SELECTINPUT(21) ;!FILE LIF000
```

```
962         %CYCLE I=0,1,31
963         READF(EXPVAR(I))
964         %REPEAT
965         SELECTINPUT(20)
966         CLOSESTREAM(21)
967         %END ;!LOADVARS
968      !
969      %REALFN READLASER
970         !
971         !     READS LASERBEAM MONITOR ON ADC CHANNEL 5
972         !     USES AUTO RANGING FOR MAX PRECISION
973         !
974         %OWNREALARRAY FACT(0:3)= 10.,5.,2.5,1.25
975         %INTEGER GAIN,VAL
976         GAIN=3 ;! START ON MOST SENSITIVE RANGE
977         1: VAL=VOLT(5,GAIN)
978         %IF MOD(VAL)>1000 %THENSTART
979         GAIN=GAIN-1
980         ->1 %IF GAIN>=0 ;! KNOCK DOWN GAIN-
981         NEWLINE
982         RINGBELL(40)
983         %PRINTTEXT' OUTPUT CLOSE TO 10 VOLTS';NEWLINE
984         %PRINTTEXT' LEVEL TAKEN AS 10 VOLTS';NEWLINE
985         GAIN=0
986         VAL=1023
987         %FINISH
988         %RESULT=VAL*FACT(GAIN)/1023*LSCALE ;! MULTIPLY IN RANGE FACTOR & NORMALISE
989         %END ;! READLASER
990      !
991      %ROUTINE DRIVEGRATING
992         %INTEGER DSTEPS,DD
993         %ROUTINESPEC DRIVEMOTOR(%INTEGER UNIT,STEPS)
994         NEWLINE;%PRINTTEXT' STEPS:';READ(DSTEPS)
995         %RETURNIF DSTEPS=0
996         NEWDIR=DSTEPS//IABS(DSTEPS)
997         !NEWDIR=+1:=>RED
998         !      =-1:=>BLUE
999         %IF NEWDIR=OLDDIR %THEN  DD=1 %ELSE DD=3
1000        STEPS=STEPS+DSTEPS
1001        DSTEPS=DSTEPS+NEWDIR*DD ;!COMPENSATION
1002        OLDDIR=NEWDIR
1003        DRIVEMOTOR(1,DSTEPS)
1004        !
1005        %ROUTINE DRIVEMOTOR(%INTEGER UNIT,STEPS)
1006           *MOV+R1,-(SP)
1007           *MOV+14.(R1),R0
1008           *MOV+16.(R1),R1
1009           *EMT+355
1010           *MOV+(SP)+,R1
1011           %END ;!DRIVEMOTOR
1012        !
1013        %END ;!DRIVEGRATING
1014     !
1015     %ROUTINE CHECKINTERRUPT
1016        %INTEGER P,IREP
1017        NEWLINE;%PRINTTEXT' INTERRUPT REQUEST:'
```

```
1018          READINT:READSYMBOL(P)
1019          %IF P#'X' %AND P#'C' %THEN -> READINT
1020          NEWLINE
1021          %IF P='X' %THEN RTI=0
1022          %IF P='C' %THEN RTI=1
1023          IFLAG=0
1024          %END ;!CHECKINTERRUPT
1025       !
1026       %ROUTINE WAITPROG
1027          NEWLINE
1028          *EMT+301
1029          NEWLINE
1030          %END ;!WAITPROG
1031       !
1032       %ROUTINE CHECKERROR(%INTEGERNAME COUNTS,ERRCD,%INTEGER AB)
1033          %INTEGER J,H
1034          SETPOT(AB*2048,2048)
1035          FLAG3=1;H=0 ;!DISABLE FAULT DIAG
1036          H=CTIME %IF ERRCD=1
1037          %CYCLE J=1,1,10
1038          ERRCD=0
1039          WAIT(H)
1040          DECODE(COUNTS,ERRCD,AB)
1041          %IF ERRCD=0 %THEN -> DIAG
1042          %REPEAT
1043          SUMERR=SUMERR+1
1044          FFAULT=SUMERR/NC
1045          %IF NC>3 %AND FFAULT>0.5 %THENSTART
1046          NEWLINE;%PRINTTEXT' FAULT RATE EXCEEDED'
1047          WAITPROG
1048          %RETURN
1049          %FINISH
1050          %PRINTTEXT'BAD COUNT '  ;  ->L1
1051          DIAG:FTIME=RTIME
1052          %PRINTTEXT'O.K. '
1053          L1:WRITE(NC,4);WRITE(FLAG1,2)  ;  ! NC=WHICH PAIR,FLAG1= DISCH ON/OFF
1054          WRITE(J,3);WRITE(AB,2);NEWLINE  ;  !J=NO OF TIMES READ, AB=SCALAR A/B
1055          %END ;!CHECKERROR
1056       !
1057       !
1058       %ENDOFPROGRAM
```

```
4        COMPILED: 09/04/81  19.13.31
FILE=.NULL

1 COMPILER 7.100
 1      %ENDOFLIST
92         %ROUTINESPEC SETOUTPUT(%INTEGERARRAYNAME F)
93         %ROUTINESPEC SETINPUT(%INTEGERARRAYNAME F)
94         %ROUTINESPEC ANALYSEBLOCK(%INTEGERNAME N,%REALNAME M,S,E,LDA,BG,SN,L)
95         %ROUTINESPEC INTANALYSE(%INTEGERARRAYNAME A,%REALNAME M,S, %C
             %INTEGERNAME N,N0)
96         %ROUTINESPEC SCANSPEC
97         %REALARRAY LAMBDA(1:200)
98         %INTEGERARRAY MARK(1:200)
99         %INTEGERARRAY FNAME(0:2)
00         %INTEGERARRAY FNAME1(0:2)
01         %INTEGER BASE,P,N,SEQNO,FBLOCKS,TEXTNO,I
02         %REAL M,S,E,LDA,BG,SN,LASER
03         BASE=-8192
04         SEQNO=-1000
05         INTEGER(BASE+2) = 0
06         N=1
07         WAIT(250)
08         !
09         PROMPT:P=INTEGER(BASE+2)
10         %IF P#1 %AND P#2 %AND P#6 %AND P#8 %AND P#7 %AND P#9 %THENSTART
11             WAIT(50)
12             ->PROMPT
13             %FINISH
14         INTEGER(BASE+2)=0
15         %IF P=1 %THEN STOPPROG
16         %IF P=2 %THENSTART
17             WAITPROG;->PROMPT
18             %FINISH
19         %IF P=7 %THENSTART
20             FAU:%PRINTTEXT'BLOCK NO:';READ(N);NEWLINE
21             %IF N<2 %OR N>200 %THEN ->FAU
22             MARK(N) = 0
23             %PRINTTEXT'BLOCK MARKED AS DUD.';NEWLINE
24             %FINISH
25         %IF P=8 %THEN SCANSPEC
26         %IF P=9 %THENSTART
27             %PRINTTEXT'BLOCK NO:'
28             READ(N);NEWLINE
29             ->SAMEFILE
30             %FINISH
31         %IF P#6 %THEN ->PROMPT
32           N=INTEGER(BASE+6)
33           %IF SEQNO=INTEGER(BASE+4) %THEN ->SAMEFILE
34             SEQNO=INTEGER(BASE+4)
35             SETINPUT(FNAME)
36             OPENREADDA(FNAME)
37             %CYCLE I=1,1,200
38             LAMBDA(I)=0;MARK(I)=1
39             %REPEAT
40           SAMEFILE:  ANALYSEBLOCK(N,M,S,E,LDA,BG,SN,LASER)
41           LAMBDA(N)=LDA
```

```
42          %PRINTTEXT'BLOCK NO: ';WRITE(N,3);NEWLINE
43          %PRINTTEXT'WAVELENGTH: ';PRINT(LDA,5,1);%PRINTTEXT'A '
44          %PRINTTEXT'LASER: ';PRINT(LASER,2,3);NEWLINE
45          %PRINTTEXT'MEAN SIG= ';PRINT(M,3,3);%PRINTTEXT'+/-'
46        PRINT(E,3,3);%PRINTTEXT'S:N= ';PRINT(SN,3,3);NEWLINE
47        ->PROMPT
48        !
49        !
50        %ROUTINE ANALYSEBLOCK(%INTEGERNAME BLOCKNO,%REALNAME SIG,DEV,ERR,%C
              LDA,BG,SN,POW)
51          %ROUTINESPEC READFROMDISC
52          %INTEGER NC,STEPS,CHBLOCK,ADR,ENTRIES,FBLOCKS
53          %INTEGER I,N0,N1,N2,N3
54          %REAL TIMEIN, TIMEOUT
55          %REAL M0,M1,M2,M3,E,SDPOW,X0,X1,X2,X3
56          %REALARRAY DA(0:127)
57          %INTEGERARRAY S0(1:16)
58          %INTEGERARRAY S1(1:16)
59          %INTEGERARRAY S2(1:16)
60          %INTEGERARRAY S3(1:16)
61          %REALARRAY P0(1:16)
62          %REALARRAY P1(1:16)
63          %REALARRAY EXPVAR(0:31)
64          !
65          READFROMDISC
66          !
67          %STOP %IF NC<2
68          !
69          %IF P=6 %AND EXPVAR(31)=2 %THENSTART
70          %CYCLE I=1,1,NC
71          WRITE(S0(I),5);WRITE(S1(I),5);WRITE(S2(I),5);WRITE(S3(I),5)
72          PRINT(P0(I),2,3);PRINT(P1(I),2,3);NEWLINE
73          %REPEAT
74          %FINISH
75          !
76          E=EXPVAR(29)/EXPVAR(30)/1000
77          !
78          LDA=EXPVAR(11) + STEPS
79          !
80          POW=0  ;  SDPOW=0
81          %CYCLE I=1,1,NC
82          POW=POW+P0(I)+P1(I)
83          SDPOW=SDPOW + P0(I)*P0(I) + P1(I)*P1(I)
84          %REPEAT
85          !SDPOW=SQRT((SDPOW-POW*POW/NC/2)/(2*NC-1))
86          POW=POW/NC/2
87          !
88          INTANALYSE(S0,M0,X0,N0,NC)
89          INTANALYSE(S1,M1,X1,N1,NC)
90          INTANALYSE(S2,M2,X2,N2,NC)
91          INTANALYSE(S3,M3,X3,N3,NC)
92          !
93          BG=M1 + E*(M2-M0)
94          SIG=M3 - BG
95          %IF BG#0 %THEN SN=SIG/SQRT(BG/NC) %ELSE SN=999
96          E=E*E
```

```
97          DEV=SQRT((X0*X0 + X2*X2)*E + X1*X1 + X3*X3)
98          ERR=DEV/SQRT(NC)
99          !
00          %ROUTINE READFROMDISC
01             %INTEGER BASE1
02             %IF P=6 %THENSTART
03               BASE1=BASE+10
04               COMMONREAD(ADDR(DA(0)),127,BASE1)
05               %FINISH %ELSE READDA(BLOCKNO,ADDR(DA(0)))
06             CHBLOCK=INTPT(DA(0)+0.01)
07             %IF CHBLOCK#BLOCKNO %THENSTART
08             NEWLINE;%PRINTTEXT' BLOCK CHECK ERROR'
09             WRITE(CHBLOCK,6);WRITE(BLOCKNO,6)
10             %FINISH
11             DA(1)=DA(1)-1 %IF DA(1)<0
12             STEPS=INTPT(DA(1)+0.01)
13             NC=INTPT(DA(2)+0.01)
14             TIMEIN=DA(3)
15             TIMEOUT=DA(4)
16             %CYCLE I=0,1,31
17             EXPVAR(I)=DA(I+5)
18             %REPEAT
19             ADR=ADDR(DA(37))
20             %CYCLE I=1,1,16
21             S0(I)=INTEGER(ADR)
22             ADR=ADR+2
23             %REPEAT
24             %CYCLE I=1,1,16
25             S1(I)=INTEGER(ADR)
26             ADR=ADR+2
27             %REPEAT
28             !
29             %CYCLE I=1,1,16
30             P0(I)=DA(I+52)
31             %REPEAT
32             %CYCLE I=1,1,16
33             P1(I)=DA(I+68)
34             %REPEAT
35             ADR=ADDR(DA(85))
36             %CYCLE I=1,1,16
37             S2(I)=INTEGER(ADR)
38             ADR=ADR+2
39             %REPEAT
40             ADR=ADDR(DA(93))
41             %CYCLE I=1,1,16
42             S3(I)=INTEGER(ADR)
43             ADR=ADR+2
44             %REPEAT
45             %END ;!READFROMDISC
46          !
47          %END ; !ANALYSEBLOCK
48       !
49       %ROUTINE SETOUTPUT(%INTEGERARRAYNAME FNAME1)
50          %INTEGER N,I
51          %INTEGERARRAY DIG(0:1)
52          N=TEXTNO
```

```
53          %CYCLE I=0,1,1
54          DIG(I)=INTPT(N/10**(1-I))
55          N=N-DIG(I)*10**(1-I)
56          DIG(I)=DIG(I)+48
57          %REPEAT
58          ! DIG(I) CONTAINS THE DIGITAL PART OF THE OUTPUT FILE NAME
59          FNAME1(0)='A'<<8+'D'
60          FNAME1(1)='A'<<8+'T'
61          FNAME1(2)=DIG(1)<<8+DIG(0)
62          %END ;!SETOUTPUT
63       !
64       %ROUTINE SETINPUT(%INTEGERARRAYNAME FNAME)
65          %INTEGER N,I
66          %INTEGERARRAY DIG(0:2)
67          SELECTINPUT(20)
68          N=SEQNO
69          %CYCLE I=0,1,2
70          DIG(I)=INTPT(N/10**(2-I))
71          N=N-DIG(I)*10**(2-I)
72          DIG(I)=DIG(I)+48
73          %REPEAT
74          ! DIG(I) CONTAINS THE DIGITAL PART OF THE INPUT FILE NAME
75          FNAME(0)='I'<<8+'L'
76          FNAME(1)=DIG(0)<<8+'F'
77          FNAME(2)=DIG(2)<<8+DIG(1)
78          NEWLINE
79          !OPEN FILE FOR READ ONLY
80          OPENREADDA(FNAME)
81          FBLOCKS=FILESIZE(FNAME)
82          NEWLINE
83          %END ;!SETINPUT
84       !
85       %ROUTINE SCANSPEC
86          %REAL DL,L0,LF,L,SM,SE,SBG
87          %REAL M,E,S,LDA,BG,SN,LASER
88          %INTEGER I,N,DISC
89          !
90          DL=1
91          %PRINTTEXT'WRITE TO DISC?'
92          READSYMBOL(I) %UNTIL I='Y' %OR I='N'
93          NEWLINE
94          DISC=0
95          %IF I='Y' %THENSTART
96             DISC=1
97             AGAIN:%PRINTTEXT'FILE NO.:';READ(TEXTNO)
98             %IF TEXTNO>99 %OR TEXTNO<0 %THEN ->AGAIN
99             SETOUTPUT(FNAME1)
00             DEFINEOUTPUT(FNAME1)
01             %FINISH
02          %PRINTTEXT'START WAVELENGTH:';READF(L0)
03          %PRINTTEXT' STOP WAVELENGTH:';READF(LF)
04          L=L0
05          !
06          CLOSESTREAM(0)
07          SELECTOUTPUT(DISC)
08          NEWLINES(2)
```

```
09          %PRINTTEXT'WLENGTH   ENTRIES  SIGNAL    B/G'
10          NEWLINES(2)
11          !
12          FBLOCKS=FILESIZE(FNAME)
13          L1:I=2
14          N=0;SM=0;SE=0;SBG=0
15          !
16          L2:%IF L=LAMBDA(I)*MARK(I) %THEN ->L4
17          !
18          L3:I=I+1
19          %IF I>FBLOCKS %THEN ->L5
20          ->L2
21          !
22          L4:ANALYSEBLOCK(I,M,S,E,LDA,BG,SN,LASER)
23          SM=SM+M
24          SE=SE+E*E
25          SBG=SBG+BG
26          N=N+1
27          ->L3
28          !
29          L5:%IF N=0 %THENSTART
30          M=0;E=0;BG=0
31          ->L6
32          %FINISH
33          %IF N=1 %THEN ->L6
34          M=SM/N
35          E=SQRT(SE)/N
36          BG=SBG/N
37          !
38          L6:PRINT(L,5,1);SPACES(5)
39          WRITE(N,2);SPACES(5)
40          PRINT(M,3,3);%PRINTTEXT'+/-';PRINT(E,3,3)
41          SPACES(5);PRINT(BG,3,3);NEWLINE
42          !
43          L=L+DL
44          %IF L<=LF %THEN ->L1
45          !
46          CLOSESTREAM(DISC)
47          SELECTOUTPUT(0)
48          NEWLINE
49          %PRINTTEXT'SPECTRUM COMPLETE'
50          NEWLINE
51          !
52          %END ; !OF SCANSPEC
53      !
54      !
55      %ROUTINE INTANALYSE(%INTEGERARRAYNAME D,%REALNAME M,S %C
        ,%INTEGERNAME N,N0)
56          %REAL E,M0,S0
57          %INTEGER I
58          M=0;N=0;S=0
59          M0=0 ; S0=10000
60          %CYCLE I=1,1,N0
61          E=D(I)-D(1)
62          %IF ABS(E)<S0 %THENSTART
63                M=M+E
```

```
64              S=S+E*E
65              N=N+1
66              %FINISH
67          %REPEAT
68          %IF N<2 %THENSTART
69              M=M+D(1);S=1;%RETURN
70              %FINISH
71          M0=M/N+D(1)
72          S0=SQRT((S-N*(M0-D(1))*(M0-D(1)))/(N-1))
73          N=0;M=0;S=0
74          %CYCLE I=1,1,N0
75          E=D(I)-M0
76          %IF ABS(E)<=2*S0 %THENSTART
77              M=M+E
78              S=S+E*E
79              N=N+1
80              %FINISH
81          %REPEAT
82          M=M/N+M0
83          S=SQRT((S-N*(M-M0)*(M-M0))/(N-1))
84          %END
85      !
86      %ENDOFPROGRAM
```

```
      SUBROUTINE POTFUN(T,C,CDOT)
      IMPLICIT REAL*8(A-H,L,M,O-Z)
      COMMON/BLKO1/MA,MB,MC
      COMMON/BLKO2/MMOL,M,RMMOL,MU1,MU2,RMU1,RMU2
      COMMON/BLKO5/BETAAB,BETAAC,BETABC,DAB,DAC,DBC,RO1,RO2,RO3,SD1,SD2
     1,SD3,DD1,DD2,DD3
      COMMON/BLK14/S,SS
      COMMON/BLK4O/IFLAG,ENDT
      COMMON/BLK99/ISUM1
      DIMENSION C(12),CDOT(12),PDOT(6),QDOT(6),DR1DQ(6),DR2DQ(6)
      DIMENSION DR3DQ(6)
      ISUM1=ISUM1 + 1
      Z1=C(1) + S*C(4)
      Z2=C(2) + S*C(5)
      Z3=C(3) + S*C(6)
      R1=DSQRT(Z1*Z1+Z2*Z2+Z3*Z3)
      X1=C(1) - SS*C(4)
      X2=C(2) - SS*C(5)
      X3=C(3) - SS*C(6)
      R3=DSQRT(X1*X1+X2*X2+X3*X3)
      R2=DSQRT(C(4)*C(4) + C(5)*C(5) + C(6)*C(6))
      RR1=1/R1
      RR2=1/R2
      RR3=1/R3
      XX1=DEXP(-BETAAB*(R1-RO1))
      XX2=DEXP(-BETABC*(R2-RO2))
      XX3=DEXP(-BETAAC*(R3-RO3))
      X21=XX1*XX1
      X22=XX2*XX2
      X23=XX3*XX3
      EJ1=DD1*X21 - 2*XX1*SD1
      EJ2=DD2*X22 - 2*XX2*SD2
      EJ3=DD3*X23 - 2*XX3*SD3
      DENOM=(EJ1-EJ2)*(EJ1-EJ2)+(EJ1-EJ3)*(EJ1-EJ3)+(EJ2-EJ3)*(EJ2-EJ3)
      DENOM=DSQRT(DENOM/2)
      ENTRY HAMPOT(HAM)
      QQ1=SD1*X21 - 2*XX1*DD1
      QQ2=SD2*X22 - 2*XX2*DD2
      QQ3=SD3*X23 - 2*XX3*DD3
      POT=QQ1+QQ2+QQ3 - DENOM
      S1=O
      S2=O
      DO 21 J=1,3
      S1=S1+(C(J+6)*TRED*O.529177D-8)**2
      S2=S2+(C(J+9)*TRED*O.529177D-8)**2
   21 CONTINUE
      HAM=POT + O.5*RMU1*O.103641D-11*S1 + O.5*RMU2*O.103641D-11*S2
      IF(IFLAG.EQ.1) GO TO 7
      RETURN
    7 DQ1DR1=-2*BETAAB*X21*SD1 + 2*BETAAB*XX1*DD1
      DQ2DR2=-2*BETABC*X22*SD2 + 2*BETABC*XX2*DD2
      DQ3DR3=-2*BETAAC*X23*SD3 + 2*BETAAC*XX3*DD3
      DJ1DR1=-2*BETAAB*X21*DD1 + 2*BETAAB*XX1*SD1
      DJ2DR2=-2*BETABC*X22*DD2 + 2*BETABC*XX2*SD2
      DJ3DR3=-2*BETAAC*X23*DD3 + 2*BETAAC*XX3*SD3
      DENOM2=DENOM*2
      DVDR1=DQ1DR1 - (2*EJ1-EJ2-EJ3)*DJ1DR1/DENOM2
      DVDR2=DQ2DR2 - (2*EJ2-EJ3-EJ1)*DJ2DR2/DENOM2
      DVDR3=DQ3DR3 - (2*EJ3-EJ1-EJ2)*DJ3DR3/DENOM2
    8 DR1DQ(1)=RR1*Z1
      DR1DQ(2)=RR1*Z2
      DR1DQ(3)=RR1*Z3
      SRR1=S*RR1
      DR1DQ(4)=Z1*SRR1
      DR1DQ(5)=Z2*SRR1
      DR1DQ(6)=Z3*SRR1
      DR3DQ(1)=RR3*X1
      DR3DQ(2)=RR3*X2
      DR3DQ(3)=RR3*X3
      SSRR3=-SS*RR3
      DR3DQ(4)=X1*SSRR3
      DR3DQ(5)=X2*SSRR3
      DR3DQ(6)=X3*SSRR3
      DO 1 J=1,3
    1 DR2DQ(J)=0.ODO
      DO 2 J=4,6
    2 DR2DQ(J)=C(J)*RR2
      DO 3 J=1,6
    3 PDOT(J)=-DVDR1*DR1DQ(J)-DVDR2*DR2DQ(J)-DVDR3*DR3DQ(J)
```

```
      DO 4 J=1,3
    4 QDOT(J)=RMU1*C(J+6)
      DO 5 J=4,6
    5 QDOT(J)=RMU2*C(J+6)
      DO 6 J=1,6
      CDOT(J)=QDOT(J)
    6 CDOT(J+6)=PDOT(J)/TRED**2
      RETURN
      END
```

Appendix C. Publications

Volume 69, number 3 CHEMICAL PHYSICS LETTERS 1 February 1980

ENERGY PARTITIONING IN THE REACTION F + I_2

R.J. DONOVAN, D.P. FERNIE, M.A.D. FLUENDY, R.M. GLEN, A.G.A. RAE and J.R. WHEELER
Department of Physics, University of Edinburgh, Edinburgh EH9 3JJ, UK

Received 8 November 1979

The vibrational populations and rotational temperature of the IF product formed in the reaction F + I_2 → IF + I have been measured using a crossed-beam laser-induced fluorescence technique. The relative collision energy was 90 meV. Measurements of the relative populations in the v = 0, 1 and 2 levels showed a strong population inversion with an effective temperature of −3000 K, corresponding to a fraction of the total energy, $\langle f_v \rangle = 0.6 \pm 0.1$, appearing in product IF vibration. In contrast, the product was rotationally cold with $\langle f_R \rangle \approx 0.02$. The results are consistent with a direct dynamical process for this reaction.

. Introduction

The F + I_2 reaction is of interest as one of a series or which quite detailed dynamical information is now vailable. The reaction has been studied at thermal energies [1] and a rate constant corresponding to a reaction cross section σ_R = 43 Å^2 found. Molecular beam cattering experiments [2,3] on this system have produced rather disparate results. Grice et al. [2] observed redominantly backwards and sideways product scattering at an initial collision energy of 35 meV while at he higher collision energy of 100 meV Wong and Lee 3] observed a more isotropic distribution with some xcess forward scattering. Both groups reported a fraction $\langle f_T \rangle \approx 0.15$ of the total energy appearing in product translation.

In the closely analogous reaction F + ICl [4] substantial IF product excitation was observed with $\langle f_v \rangle$ 0.63 indicating a very nonstatistical energy disposal robably as a result of a direct dynamical process. The eactions Cl + I_2 and Cl + Br_2 have also been studied y beam scattering methods [5–7]. The former reaction showed stripping dynamics with $\langle f_T \rangle \approx 0.3$, while he Cl + Br_2 reaction proceeded via a short-lived complex again with $\langle f_T \rangle \approx 0.3$.

As might be expected from the greater density of cessible states the process F + CH_3I → FI + CH_3 has een shown to proceed via a long-lived complex at ermal collision energies and the lifetime of this complex has been estimated from molecular scattering measurements for a range of initial collision energies [8,9]. In the long-lived complex regime approximately 30% of the total energy appeared as translational motion of the products. Laser-induced fluorescence measurements [10] confirmed the expected statistical distribution of energy, the CH_3 fragment emerging with about 40% of the total energy and 30% being evenly divided between rotation and vibration in the IF product.

This family of reactions reveals an interesting graduation of behaviour at thermal collision energies, spanning the range from direct to long-lived complex dynamics. The system investigated here, F + I_2, will thus be of interest in exploring the effects of changes in the mass ratio and in revealing any novel features in the potential surface associated with fluorine atom reactions.

2. Experimental

The experiment was performed in a crossed molecular beam laser induced fluorescence apparatus. An effusive I_2 beam was produced using a 10 μm microcapillary array with the reagents supplied from a reservoir at 370 K (≈10 Torr). F atoms were generated by a microwave discharge in a mixture of 10% CF_4 in He, at a total pressure of 5 Torr and were delivered to a nozzle of diameter 1 mm, mounted in a differentially pumped chamber, via a glass pipe coated in "Teflon" (Dupont

FEP 856-200) [11]. The reaction zone was approximately spherical in shape with diameter ≈ 5 mm and the IF concentration was estimated to be $\approx 10^7$ cm^{-3}. The background pressure with beams running was $\approx 4 \times 10^{-5}$ Torr. The reaction zone was illuminated by a tuneable dye laser. This was pumped by a nitrogen laser of original design [12] operated at a 50 Hz repetition rate. The dye laser pulse was <5 ns (fwhm) in duration and had a band width of 2–3 Å. Rotational structure was thus not resolvable. The dyes used were Coumarin 47 and Coumarin 102 (Applied Photophysics Ltd.) covering the region 460–490 nm. In this region the (5,0), (6,0), (7,0), (8,1), (8,2) bands have Franck–Condon factors > 0.03 [13]. Beyond 500 nm fluorescence from IF is obscured by that from the I_2. The fluorescence from the product was viewed at right angles to the laser beam through an aspheric lens and aperture system and was detected by a photomultiplier (EMI 9824). The photon-counting system was gated open 2 μs after each laser flash and closed 10 μs later. Since the IF(B) lifetime is about 8 μs [14] this technique helps to discriminate against noise from other species and against after-pulsing in the photomultiplier. Data was accumulated in this way for 10 or 100 s periods with the laser and F atom discharge each alternately on and off. The count accumulated in each mode together with a measurement of the laser intensity, taken with a sample and hold A–D converter, was captured by a PDP11/45 computer.

Noise from both photomultiplier dark count and stray light was negligible (< 0.1 s^{-1}) and the main noise arose from laser-induced after-pulsing in the photomultiplier. This resulted from a rather poor beam profile and amounted to about 1 s^{-1}. The signal rate was also low, due principally to the low mean laser power (≈100 μW), being comparable with or less than the noise rate. Counting times were therefore long and data could only be collected at a few selected wavelengths to map out the gross features of the vibrational distribution. Bands with $v = 0$ were relatively easy to see but $v = 1$ and 2 were more difficult due to the small Frank–Condon factors from these levels.

3. Results

The (5,0), (6,0), (8,1) and (8,2) bands have been observed. The net signal, the difference in the signals

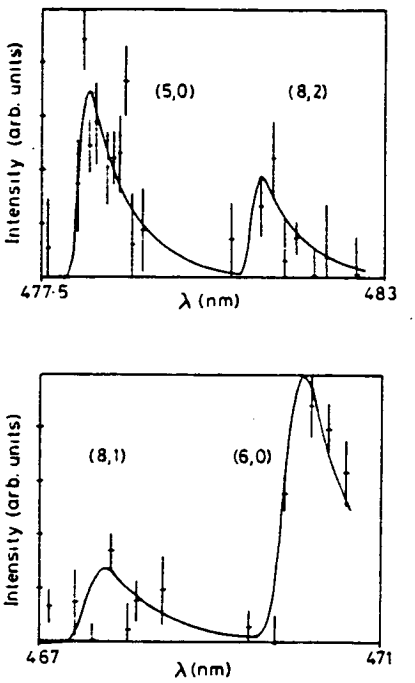

Fig. 1. Fluorescence intensity in the (5,0), (8,2), (8,1) and (6,0) bands of IF product as a function of the wavelength of the incident laser light.

with the F atom discharge on and off, was corrected for background and normalised using the recorded laser intensity (corrected as necessary for wavelength sensitivity). The results are shown as a function of wavelength in fig. 1. The error bounds are largely determined by the after-pulsing effects discussed previously.

The data have been fitted to a simulated spectrum [15] calculated by convoluting the line frequencies with a triangular laser bandwidth function determined experimentally and using the Franck–Condon factors reported by Clyne et al. [13]. A Boltzmann distribution of rotational states was assumed and all the bands were constrained to the same rotational temperature. The only variable parameters in the fit were the level populations, $N(v)$, which are proportional to the cross sections for the reaction into that channel. The population ratios calculated in this way, relative to $N(0) = 1.0$, are shown in table 1. Good agreement is observed for independent estimates via the (6,0) and (5,0) bands and a rotational temperature of about 200 K satisfactorily describes all the observed levels. The rotational temperature could not be determined to better than 100 K.

able 1
opulation observed in various vibrational levels

Band $v' \leftarrow v''$	$N(v'')$
(5,0)	1.00 ± 0.15
(6,0)	1.16 ± 0.12
(8,1)	1.38 ± 0.28
(8,2)	1.60 ± 0.24

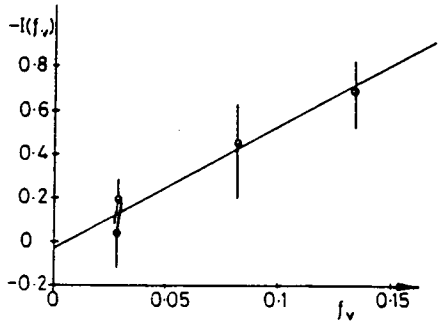

Fig. 2. Plot of the surprisal $-I(f_v)$ against f_v for the four observed bands of IF.

Discussion

The relative populations in the 0, 1 and 2 vibrational ates of the IF product, as shown in table 1, reveal a ıbstantial population inversion. Higher states, up to v 19 are energetically available but are not measurable xperimentally due to predissociation, which sets in at = 9, and interference by fluorescence from the I_2 re- gent. Nevertheless, an effective vibrational tempera- ıre for the product can be estimated via the surprisal ot, fig. 2. Such plots are very frequently linear [16] ver most of the energetically accessible range and so ın provide an estimate of the population in the higher ates. The gradient in fig. 2 corresponds to an effec- ve vibrational temperature of −3000 K and a most robable vibrational state of $v = 13$–14 in the product. his extrapolation then yields a fraction of total energy vibration $\langle f_v \rangle = 0.6 \pm 0.1$.

The rotational temperature is less well defined since dividual rotational transitions cannot be resolved. owever, information on the average rotational tem- erature is available from the band profile. The accuracy this estimate is contingent on relaxation effects but except in the case of the $v = 0$ state, where signals from cold product in the background might interfere, this should not be a substantial effect. The average rotational temperature observed, about 200 K, is equivalent to a rotational fraction $\langle f_R \rangle \approx 0.02$. The energy disposal estimated from these measurements is compared with that for analogous reactions in table 2.

The F + I_2 reaction releases the major fraction of its exothermicity as product vibration and in this respect is similar to the ICl reaction. The disposal is highly nonstatistical and this pattern is characteristic of direct dynamics of reaction with a substantial attractive energy release in the entrance valley of the potential surface. For L + HH mass ratios the relative vibrational and translational disposals can be expected to correlate with the attractive entrance and repulsive exit behaviour of the potential.

The rotational excitation observed is much smaller than in ICl. This may arise from the mass ratio since the exit I atom carries away most of the incident angular momentum associated with I_2 rotation as orbital

able 2
nergy disposal

isposal action	System				
	F + I_2	F + ICl	Cl + I_2	Cl + Br_2	F + CH_3I
$_v\rangle$	0.6	0.55 [b]	–	–	0.15 [d]
$_R\rangle$	0.02	0.14 [b]	–	–	0.14 [d]
$_T\rangle$ beam measurement	0.15 [a]	–	≈0.3 [c]	≈0.3 [c]	≈0.3 [e]
$_T\rangle$ by difference	0.4	0.31	–	–	(0.4 in CH_3) [d]

Refs. [2,3]. [b] Ref. [4]. [c] Ref. [6]. [d] Ref. [10]. [e] Ref. [8].

gular momentum and acts as an effective sink for gular momentum. The low rotational excitation obved may also be associated with a much slower relaxon, compared with ICl, of the I_2 bond during the lision.

ferences

] E.H. Appelman and M.A.A. Clyne, J. Chem. Soc. Faraday I 71 (1975) 2072.
] C.F. Carter, M.R. Levy, K.B. Woodall and R. Grice, Faraday Discussions Chem. Soc. 55 (1973) 381.
] Y.C. Wong and Y.T. Lee, Faraday Discussions Chem. Soc. 55 (1973) 383.
] L. Stein, J. Wanner, H. Figger and H. Walther, in: Laser induced processes in molecules, Springer series in chemical phys. Vol. 6, eds. K.L. Kompa and S.D. Smith (Springer, Berlin, 1974) p. 232.
] Y.T. Lee, P.R. LeBreton, J.D. McDonald and D.R. Herschbach, J. Chem. Phys. 51 (1969) 455.
[6] H.J. Loesch and D. Beck, Ber. Bunsenges. Physik. Chem. 75 (1971) 736.
[7] Y.T. Lee, J.D. McDonald, P.R. LeBreton and D.R. Herschbach, J. Chem. Phys. 49 (1968) 2447.
[8] J.M. Farrar and Y.T. Lee, J. Chem. Phys. 63 (1975) 3639.
[9] J.J. Valentini, M.J. Coggiola and Y.T. Lee, Faraday Discussions Chem. Soc. 62 (1977) 232.
[10] L. Stein, J. Wanner and H. Walther, J. Chem. Phys., to be published.
[11] H.C. Berg and D. Kleppner, Rev. Sci. Instr. 33 (1962) 248.
[12] D.P. Fernie, unpublished.
[13] M.A.A. Clyne and I.S. McDermid, J. Chem. Soc. Faraday II 72 (1976) 2242.
[14] M.A.A. Clyne and I.S. McDermid, J. Chem. Soc. Faraday II 74 (1978) 1644.
[15] R.M. Glen, Ph.D. Thesis, University of Edinburgh, to be published.
[16] R.D. Levine and J.C. Kinsey, in: Atom–molecule collision theory, ed. R.B. Bernstein (Plenum Press, New York, 1979).

J. Chem. Soc., Faraday Trans. 2, 1981, 77, 1133–1141

Efficient Calculation of Bands of Eigenvalues and Eigenvectors in One Dimension

BY KENNETH LAWLEY* AND ROSS WHEELER

Department of Chemistry, University of Edinburgh, West Mains Road, Edinburgh EH9 3JJ

Received 22nd September, 1980

It is suggested that the most efficient way of calculating large numbers of sequential eigenvalues and eigenvectors lying between specified limits is through the replacement of the second-order differential operator by the second central difference, followed by a matrix formulation of the eigenvalue problem. The capabilities of this neglected method are illustrated by the calculation of shape resonances in scattering and of Franck–Condon factors in the spectroscopy of high vibrational states.

1. INTRODUCTION

The numerical solution of the Schrodinger equation in one dimension,

$$\{-d^2/dr^2 + V^*(r)\}\psi(r) = E^*\psi(r) \tag{1}$$

[$E^* = 2\mu\sigma^2 E/\hbar^2$, $r = R/\sigma$, $V^*(r) = 2\mu\sigma^2 V(R)/\hbar^2$ where σ is any convenient length parameter] presents no particular problem nowadays, but it remains a time consuming operation when carried out repeatedly. Popular methods are those of Numerov or a predictor–corrector based algorithm[1,2] which often yield eigenvalues and eigenfunctions of unnecessarily high precision. The main alternatives are spectral decomposition (Rayleigh-Ritz) methods[3,4] and the use of various semi-classical solutions, either in the form of the Bohr–Sommerfeld quantisation rule[5] for eigenvalues and the classical action integral for the phase,[6,7] or in the form of various uniform WKB treatments. In 1974 Tobin and Hinze[8] suggested using an old finite difference method whereby the problem is converted to a matrix eigenvalue one in which the basic vectors are essentially Dirac delta functions $\delta(r - r_n)$ for a finite number of grid points, $r_1, \ldots, r_N$.

While there cannot be any uniquely best method of tackling the general eigenvalue problem, eqn (1), it is the purpose of this paper to suggest that for large scale calculations, those involving wide bands of eigenstates, the hitherto rather neglected matrix method is the preferred one. We briefly outline the method in section 2 and then apply it to two problems where it seems particularly well suited: the calculation of resonances in elastic scattering (section 3) and of Franck–Condon factors (section 4).

2. OUTLINE OF THE METHOD

The operator d^2/dr^2 is replaced by an expansion in central differences δ^n and only the leading term retained;

$$\begin{aligned} d^2\psi/dr^2 &= \xi^{-2}[\delta^2 - \tfrac{1}{12}\delta^4 + \mathcal{O}(\delta^6)]\psi(r) \\ &\approx \xi^{-2}[-\psi(r_{i+1}) + 2\psi(r_i) - \psi(r_{i-1})] \end{aligned} \tag{2}$$

where ξ is the grid spacing $(r_{i+1} - r_i)$ and the wave function is replaced by a one-dimensional array containing the values at the grid points. The differential equation, eqn (1), then becomes a matrix eigenvalue equation

$$^{(2)}\mathbf{H}\psi^{(2)} = \{\xi^{-2}\boldsymbol{\delta}^{(2)} + \mathbf{V}\}\psi^{(2)} = {}^{(2)}\mathbf{E}^*\psi^{(2)} \tag{3}$$

where

$$\boldsymbol{\delta}^{(2)} = \begin{pmatrix} 2 & -1 & 0 & 0 \\ -1 & 2 & -1 & 0 \\ 0 & -1 & 2 & -1 \\ \cdots & \cdots & \cdots & \cdots \end{pmatrix} \tag{4}$$

and $\mathbf{V}$ is the diagonal matrix containing values of the potential at the grid points. The superscript (n) indicates that the eigensolutions refer to an nth finite difference operator. $\mathbf{H}$ is thus tridiagonal and, as Tobin and Hinze pointed out, the roots (eigenvalues) are very readily found by the standard method of bisection based upon the Sturm sequence.[9] The fact that the off-diagonal elements in $\mathbf{H}$ are all equal to -1 makes the coding of the problem particularly simple and the storage space small. Among the many advantages we would only draw attention to the well known fact that for tridiagonal matrices the time taken to find a root is proportional to N (the dimension of the matrix) rather than to N^2 for the general eigenvalue problem. If eigenvectors are required, these can be obtained by only two cycles of inverse iteration. The time taken for this is again proportional to N and is anyway inherently faster than the first stage of finding the eigenvalues. The factoring into upper and lower triangular form proceeds without pivoting.

The great advantage of the method over the Rayleigh–Ritz approach (expansion of ψ in known eigenfunctions of a model Hamiltonian) is that no preliminary quadrature is necessary in setting up $\mathbf{H}$.

In his comparison of matrix methods, Shore[10] missed the decisive numerical advantage of the finite difference method in allowing the method of bisection to be used. However, he correctly identified the weakness of the Rayleigh–Ritz approach from a computational point of view.

The radial boundaries, $r_{\min}$ and $r_{\max}$ [at which $V(r)$ is effectively infinite], are placed so that they lie just outside the inner and outer classical turning points of the highest quantum state to be included. The grid spacing is assigned so that the highest frequency oscillation in ψ is spanned by *ca.* 10 grid points. In the problems to be described, N typically lies between 1000 and 2000. The energy range in which the eigenvalues are required is then decided. It is another advantage of the method of bisection that the number, although not the position, of quantum states in the pre-assigned energy range is obtained after only two cycles of bisection. Use of this knowledge of the average density of states makes the search for eigenvalues very efficient when a band of eigenvalues is to be calculated.

"Exact" eigenvalues are not required for the method of inverse iteration. The number of stages of bisection needed to produce an eigenvalue of sufficient quality depends on the density of states. For the rather closely spaced quantum states studied below, we have found that 4–6 bisections are adequate, giving an error in the eigenvalue of *ca.* 1% of the local level spacing.

The error in eigenvalues obtained in this way comes from the neglect of the fourth- and higher-order differences in eqn (2) (assuming that the machine arithmetic is carried out to the necessary precision).

Tobin and Hinze used a quadratic extrapolation of ${}^{(2)}E(\xi)$ to obtain the true eigenvalue $E^*[\equiv {}^{(2)}E^*(0)]$. However, if eigenfunctions are also to be calculated, the effect on the eigenenergy of the first neglected term in eqn (2), δ^4, can be obtained to $\mathcal{O}(\xi^4)$ by first-order perturbation theory

$$E^* = {}^{(2)}E^*(\xi) + {}^{(4)}E^*(\xi) + \mathcal{O}(\xi^4)$$

where

$${}^{(4)}E^*(\xi) = -(12\xi^2)^{-1}\psi^{(2)}\delta^{(4)}\psi^{(2)} \tag{5}$$

and $\delta^{(4)}$ is the matrix

$$\begin{pmatrix} -6 & 4 & -1 & 0 & 0 & \cdot \\ 4 & -6 & 4 & -1 & 0 & \cdot \\ -1 & 4 & -6 & 4 & -1 & \cdot \\ 0 & -1 & 4 & -6 & 4 & -1 \\ \cdot & \cdot & \cdot & \cdot & \cdot & \cdot \end{pmatrix}$$

3. PHASE SHIFTS AND RESONANCES

A resonance in the lth partial wave is marked by a rapid rise of π in the phase shift as the resonance energy E_n is passed through. The general behaviour is

$$\eta_l = \eta_l^{(0)} + \tan^{-1}\left\{\frac{\Gamma_{nl}}{2(E - E_{nl})}\right\} \tag{6}$$

where $\eta_l^{(0)}$ is the smooth outer branch contribution and the width Γ_{nl} can be found from the Breit-Wigner formula

$$\frac{\mathrm{d}(\eta_l - \eta_l^{(0)})}{\mathrm{d}E} = \frac{\Gamma_{nl}}{2(E - E_{nl})^2 + \Gamma_{nl}^2/2}. \tag{7}$$

The search for resonances by conventional methods is time consuming. The complete range of positive E below the orbiting limit for a particular l value must be scanned fairly densely in order to locate the regions of anomalous phase shift and then each of these regions scanned more carefully so that the phase shifts can be fitted by the functional form, eqn (6). Milne's method[11] has been used for this problem, but requires one quadrature and the solution of a transcendental equation for each phase shift.

Using the present method, the outer boundary is placed slightly beyond the maximum in the centrifugal potential where the true potential can be regarded as essentially zero. The continuum of positive energy states is thereby quantised with a density that is sufficiently great for adjacent resonances to be resolved. The eigenvectors are not explicitly needed in this problem since they are all characterised by having a node at r_{max}, where we can write

$$\psi(r_{max})/r_{max} = A_l j_l(kr_{max}) + B_l n_l(kr_{max}) \tag{8}$$
$$= 0$$

and so the phase shift is given by

$$\tan \eta_l = -B_l/A_l = j_l(kr_{max})/n_l(kr_{max}). \tag{9}$$

η_l is thus obtained in the interval $(0, 2\pi)$ (making use of the signs of j_l and n_l). In the present context of shape resonances, all the relevant η_l are positive. We can then use Levinson's theorem,[12]

$$\eta_l(k=0) = n\pi \tag{10}$$

to locate η_l within the complete interval $(0, \infty)$.

Taking as a model calculation the resonances supported by the Lennard-Jones potential having $\varepsilon = 1\times10^{-21}$ J, $\sigma = 3.61$ Å, $\mu = 6.33\times10^{-26}$ kg, we consider the partial wave $l = 10$. A portion of the eigenenergy spectrum for a sequence of outer boundary positions is displayed in fig. 1, many more than would be used in an actual

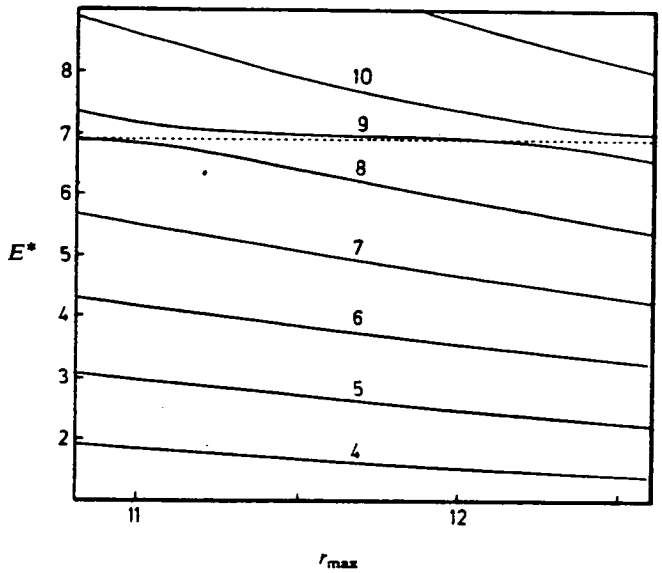

FIG. 1.—Behaviour of a band of roots of the second difference Hamiltonian matrix as a function of r_{max}. The potential is a Lennard-Jones one, reduced well depth 200; $l = 10$ and the reduced centrifugal barrier height is 8.7. The boundary positions are indicated on the lowest plot.

calculation ($r_{min} = 0.982$; $r_{max} = 10$–12; $N = 600$). At any boundary position one anomalous eigenvalue is apparent at around $\varepsilon = 7$. In contrast to the other roots, this one is insensitive to r_{max}, whereas the others show the r_{max}^{-2} behaviour characteristic of the particle in a box problem. This behaviour is quite general for resonances; because such states have a large amplitude inside the centrifugal barrier, their energy is essentially determined by the expectation value of $\mathcal{H}$ in this restricted region of space (this is the basis of the stabilisation method of Hazi and Taylor[13]). In the present example, only one resonance is seen (and can be approximately located from only one position of the outer wall). The phase-shift function for this resonance can be adequately fixed from four values of r_{max}, fig. 2; from the value of the phase shift extrapolated to zero energy, $\eta_{10}(k=0) \rightarrow 4\pi$, there are clearly four bound states remaining in the well for the tenth partial wave and one metastable state having an energy $E_0^* = 6.95$.

Turning to a slightly larger-scale problem, we investigated all the resonant states for the Ar+Ar scattering problem using the Lennard-Jones potential with $\varepsilon =$

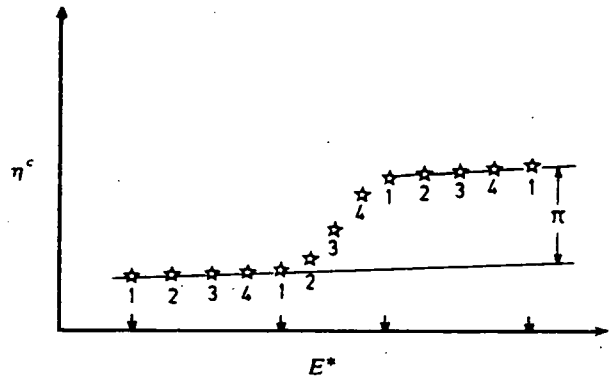

FIG. 2.—Schematic behaviour of the reduced energy behaviour of a phase shift in radians. The energy scan is induced by moving the outer boundary and four values of r_{max} are shown. Each position results in a coarse energy scan equivalent to a vertical cut through fig. 1; the eigenvalues at the first boundary position are arrowed.

1.7×10^{-21} J, $\sigma = 3.418$ Å, $\mu = 3.145\times10^{-26}$ kg. A portion of the family of $\eta_l(E)$ plots is illustrated in fig. 3, again obtained with four values of r_{max}. Of the five resonances that are visible, only the one for $l = 23$ will have a measurable width Γ. Using eqn (7) gives $E_{2,23} = 49.7$ cm^{-1}, $\Gamma_{2,23} = 0.67$ cm^{-1}.

As a final example, we turn to the $H_2 + Ar$ system, where three resonances have been detected experimentally. The favoured potential is a Lennard-Jones one of LeRoy and van Kranendonk[14] having $D_e = 52.2$ cm^{-1} and $R_e = 5.557$ Å. In order to obtain the highest accuracy for the resonance energy, we have extrapolated from values at $\xi = 0.03$, 0.02, 0.015 to zero step length to obtain the value $E_{res} = 13.25 \pm 0.02$ cm^{-1} for the $l = 8$ partial wave. This value is in better agreement with the observed value of 13.45 ± 0.45 cm^{-1} than the calculated (by an unspecified method) value of Toennies *et al.*[15] While not ideal for work of the highest accuracy, the method nevertheless gives results of "experimental" accuracy in times faster than that of the Numerov routine when the position of the resonance is initially completely unknown.

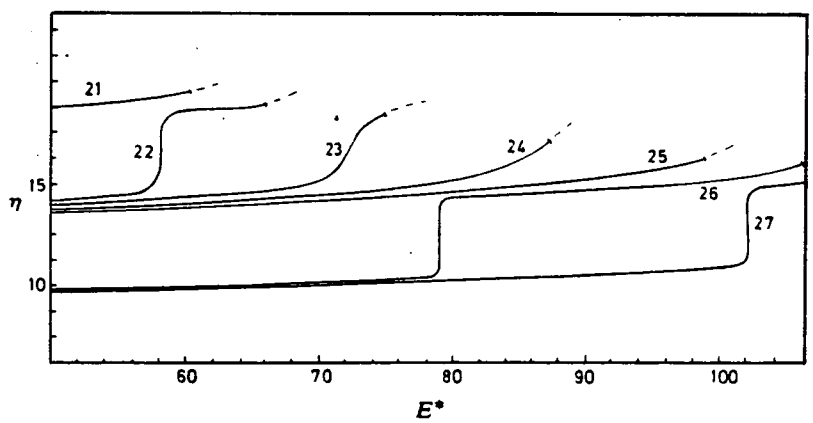

FIG. 3.—Extended diagram of $\eta_l(E)$ for Ar → Ar. Partial waves $l = 21$–27 are shown and each phase-shift curve is broken off when E^* reaches the centrifugal barrier height for the l value. Four resonances are visible, but only one has an appreciable width.

The width of the resonance in the $H_2 + Ar$ system for $l = 8$ is calculated to be $2\,cm^{-1}$, a typical value for levels close to the top of the centrifugal barrier. An appreciably larger value of Γ (or a shorter time delay $\tau = 2\hbar\,\partial\eta_l/\partial E$) would be associated with an energy just above the centrifugal barrier height.

4. FRANK-CONDON FACTORS

For the purpose of numerical evaluation, a Franck–Condon (FC) factor essentially involves a single quadrature of the product of two functions which are rapidly oscillating when initial and final states are highly excited vibrationally. We concentrate on the efficient generation of the wave functions appearing in the matrix element of the dipole moment operator, $\mu(R)$:

$$f_{n''n'} = \frac{64\pi^4\nu^3}{3h} S_{n''n'} \tag{11}$$

$$S_{n''n'} = \left\{ \int \psi_{n''}^{(1)}(r)\mu_n(r)\psi_{n''}^{(2)}\,dr \right\}^2 . \tag{12}$$

Various stationary-phase methods naturally suggest themselves in the evaluation of eqn (12) and some of these are explored in a subsequent paper.[16] As in scattering theory, these methods are at their most useful in delineating and classifying the broad features of interference phenomena. However, laser-induced fluorescence studies tend to produce rather extensive high resolution spectra spanning a wide band of final vibrational states. In order to extract the details of the potential energy curves from such data by trial and error fitting, what is needed is an accurate and rapid method of generating the eigenfunctions appearing in eqn (12) from, probably, a tabulated rather than an analytical potential. If the lower state is a continuum, then perhaps 50 different final state energies will have to be included in order to reproduce the spectrum, $I(\nu)$. We suggest that the matrix method is ideally suited for this problem. The eigenvectors can be used directly to evaluate the integral in eqn (12) using Simpson's rule.

In the bound → free case, the outer wall at r_{max} discretizes the continuum states and introduces a graininess into the simulated spectrum. The choice $5 \leq R_{max}/\text{Å} \leq 6$ usually leads to an adequate density of states for heavier systems. Perhaps the most attractive of alternative approaches is the uniform WKB method of generating wave functions proposed by Eu[17] and applied to the FC factor problem by Golde and Kvaran[18] (a very similar method has been used by Kruger[19] based on the work of Miller and Good[20]). The method, however, suffers from two minor disadvantages. The first is one of speed; at each point in the quadrature, eqn (12), the wave functions themselves have to be obtained by a quadrature followed by the solution of a transcendental equation then the generation of the appropriate Hermite polynomial or Bessel function. The second disadvantage is that convergence to the exact solution cannot be tested; the convergence of the quadrature with respect to step length can certainly be demonstrated, but the wave functions converge on the WKB solutions, not the exact eigenfunctions. We have carried out a comparison of the wave functions obtained by the uniform WKB method, supplied by Dr. Kvaran, and those obtained by the matrix method for the $v' = 133$ level of the D state of I_2. The matrix wave function was constructed from 1750 and 3500 grid points and was found to be effectively converged at the larger grid spacing. The nodal positions of the two functions were identical to 0.005 Å, but the overall appearance of the envelope of the JWKB wave function was much flatter than the matrix function. The ratio of the

first maximum, near the inner turning point, to the mid-point amplitude was larger by *ca.* 30% in the matrix function case and the discrepancy was even more marked at the outer turning point. This would have a noticeable effect on calculated FC factors if the classical turning point of transition lay close to a turning point of the motion, or involved interference between the turning and mid points.

We illustrate the matrix method by simulating the $B(n'=43) \rightarrow X(n''=1,\ldots,9)$ spectrum of I_2. While not a large scale calculation, only nine final vibrational states are included, the results of the present approach can be compared with the Numerov "shooting" technique used for this system by Allegrini *et al.*[21] For the B state potential, the RKR data of Barrow and Yee[22] were interpolated at the grid points and the X state potential obtained in the same way from the results of LeRoy.[23] The classical turning points for $n'=43$ are at 2.65 and 4.47 Å; the boundary positions $R_{min}=2.5$ Å, $R_{max}=5$ Å were used, with 1250 grid points. A dimension of 600 points would suffice for a reliable picture of the relative line strengths, but the use of the finer grid spacing of 0.002 Å allows the effect of small displacements of the upper and lower potential curves to be explored. The results are illustrated in fig. 4 with

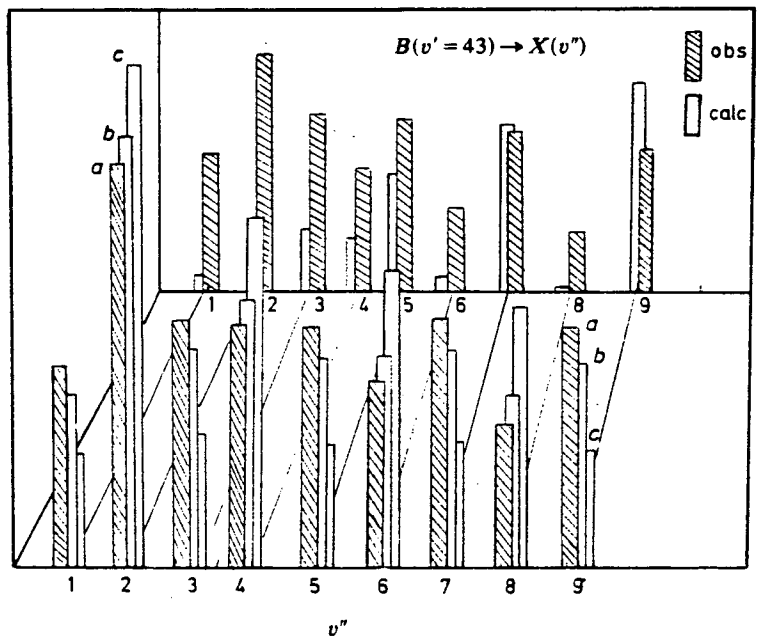

FIG. 4.—Overlap integral for a portion of the $B \rightarrow X$ spectrum of I_2. The upper histograms are the observed intensities (divided by v^4) and the results of Allegrini *et al.*[21] normalised to the observed intensity for the (43, 2) band. The lower histograms are computed by the present method for three, (*a*)-(*c*), sequential radial displacements of the B state with respect to the X state. Position (*a*) clearly gives the best fit to the observed intensity profile.

$\mu(R)=1$. The lower state was shifted by +0.002 and +0.004 Å from the initial choice dictated by the published potentials. It is clear that a displacement of roughly −0.002 Å would bring the calculated and observed line intensities into even better agreement. For any particular line, the variation in intensity with relative displacement of upper and lower states is cyclical with a periodicity, in the present case, of *ca.* 0.03 Å. This is simply the result of the upper and lower state eigenfunctions passing

in and out of phase at the classical point of transition (where the momenta in the two states are equal) as the potential wells are displaced.

The method has been extensively used for the bound → free transitions from the $n' = 195$ and 133 levels of the D state with, typically, 1000–1500 grid points. Extrapolation to zero step length does not alter the pattern of intensities, though a slight shift of *ca.* 10 cm^{-1} in the peak positions can be seen. For the $B(n' = 43)$ state, the first-order perturbed energy, defined in eqn (5), was 7 cm^{-1} and the eigenvalue $E_0 = 3765$ cm^{-1}. The observed energy is 3771.72 cm^{-1}. It is a general observation that the sum of the unperturbed and first-order perturbed energy of $\delta^{(4)}$

$$E^* = {}^{(2)}E^*(\xi) + {}^{(4)}E^*(\xi) \tag{13}$$

is nearly independent of step length and may be taken as the converged eigenvalue to 1 part in 10^5. We report these calculations of FC factors associated with higher vibrational states in a following paper.

5. CONCLUSIONS

The sample calculations presented above illustrate the high quality of the wave functions and eigenvalues obtained from a simple central difference formulation of the wave equation. The numerical algorithms are all exceptionally simple, fast and well tried in other fields. We have not found them to exhibit any instability in classically forbidden regions and parasitic solutions cannot appear. The only requirement is, naturally, that the grid spacing be small compared with the local wavelength of the motion, but this is also true of step-wise integration methods. Eigenfunctions obtained after only two stages of inverse iteration from crude eigenvalues bear a strong resemblance to the fully converged functions and are adequate for many purposes where the solutions obtained by step-wise integration are unnecessarily precise.

The potential functions need not be in analytical form and exactly the same routines can be applied to either discrete or continuum states. The great strength of the method is that it proceeds directly to eigenvalues and the general disposition of states can be seen at a glance. A particularly simple application would be in the evaluation of partition functions where even semi-classical methods[24] can be time consuming. Anomalies due to resonances can be picked out from anomalies in the eigenvalue spacing in the discretized continuum. Observed energy levels can be fitted by adjusting the potential energy parameters before proceeding to eigenfunctions.

For single-shot applications, the finite difference method has no particular advantages but we suggest that for wide-scale applications involving many eigenstates or a dense sampling of the continuum, the present method is the preferred one.

[1] J. W. Cooley, *Math. Comp.*, 1961, **15**, 363.
[2] S. M. Roberts and J. S. Shipman, *Two-Point Boundary Value Problems: Shooting Methods* (American Elsevier, New York, 1972). For a sample application to the orbiting resonances problem, see R. I. Price, *Mol. Phys.*, 1977, **33**, 559, and to FC factors, see J. Tellinghuisen, *J. Quant. Spectrosc. Radiat. Transfer*, 1978, **19**, 149.
[3] C. S. Lin and G. M. F. Drake, *Chem. Phys. Lett.*, 1972, **16**, 35.
[4] J. Romelt and R. Runau, *Theor. Chim. Acta*, 1980, **54**, 171.
[5] The method is widely used. Two representative medium scale calculations are: P. D. Gait, *Chem. Phys. Lett.*, 1977, **51**, 506 and J. P. Flamme and J. Momigny, *Chem. Phys.*, 1978, **34**, 303.
[6] W. I. Newman and W. R. Thorson, *Can. J. Phys.*, 1972, **50**, 2997.
[7] M. V. Berry, *Proc. Phys. Soc. London*, 1966, **80**, 479.
[8] F. L. Tobin and J. Hinze, *J. Chem. Phys.*, 1975, **63**, 1034.

[9] J. H. Wilkinson, *The Algebraic Eigenvalue Problem* (Clarendon Press, Oxford, 1965).
[10] B. W. Shore, *J. Chem. Phys.*, 1973, **59**, 6450.
[11] S-Y. Lee and J. C. Light, *Chem. Phys. Lett.*, 1974, **25**, 435.
[12] M. S. Child, *Molecular Collision Theory* (Academic Press, London, 1974).
[13] A. U. Hazi and H. S. Taylor, *Phys. Rev. A*, 1970, **1**, 1109.
[14] R. J. LeRoy and J. van Kranendonk, *J. Chem. Phys.*, 1974, **61**, 4750.
[15] J. P. Toennies, W. Welz and G. Wolf, *J. Chem. Phys.*, 1976, **64**, 5305.
[16] R. J. Donovan, A. Kvaran and K. P. Lawley, to be submitted.
[17] U.-I. Cho and B. C. Eu, *J. Korean Chem. Soc.*, 1974, **18**, 307.
[18] M. F. Golde and A. Kvaran, *J. Chem. Phys.*, 1980, **72**, 442.
[19] H. Kruger, *Theor. Chim. Acta*, 1979, **51**, 311.
[20] S. C. Miller and R. H. Good, *Phys. Rev.*, 1953, **91**, 174.
[21] M. Allegrini, G. Alzetta and M. Civilini, *Chem. Phys. Lett.*, 1980, **70**, 454.
[22] R. F. Barrow and K. K. Yee, *J. Chem. Soc., Faraday Trans. 1*, 1973, **69**, 684.
[23] R. J. LeRoy, *J. Chem. Phys.*, 1970, **52**, 2686.
[24] W. Witschel, *Chem. Phys.*, 1980, **50**, 265.

(PAPER 0/1458)

Journal of Molecular Structure, 86 (1981) 193—195
THEOCHEM
Elsevier Scientific Publishing Company, Amsterdam — Printed in The Netherlands

Short communication

THE MOLECULAR AND ELECTRONIC STRUCTURE OF TETRASULPHURDINITRIDE; A STUDY BY AB INITIO MOLECULAR ORBITAL METHODS

MICHAEL H. PALMER*, J. ROSS WHEELER and ROBERT H. FINDLAY
Department of Chemistry, University of Edinburgh, West Mains Road, Edinburgh EH9 3JJ (Scotland)
N. P. C. WESTWOOD and W. M. LAU
Department of Chemistry, University of British Columbia, 2036 Main Mall, Vancouver V6T 1Y6 (Canada)

(Received 27 May 1981)

The low-melting red compound S_4N_2 occurs widely in reactions of sulphur—nitrogen compounds, and has been known for many years. It appears that only one isomer is as yet known, and that three different environments can be postulated for the S atoms on the basis of its reactivity. The nitrogen atoms appear to be equivalent [1]. This has led to the proposal that the molecule is a 6-membered ring (1).

The use of Hückel rule arguments [2, 3] and aromaticity (as a 10 π electron system) have indicated a planar C_{2v} structure, but an alternative boat (or chair) form (C_s symmetry) has been proposed [4]. No molecular structure has yet been published, which is remarkable for such a small molecule.

The present paper gives the results of ab initio molecular orbital studies in which the two structural forms, C_{2v} and C_s, were completely optimised by a full gradients procedure. The principal results are shown in Table 1, and the final structure in Fig. 1.

The non-planar C_s structure is found to be the most stable by about 60 kJ-mol^{-1}; five of the atoms are nearly co-planar, with only the *para*-S atom (S-4) markedly away from this plane. This is in good agreement with the predictions by Jolly [4], and suggests that aromaticity is not present in S_4N_2. Indeed, it can be argued that for C_{2v} symmetry the distinction between $4n$ and $(4n + 2)$ π-electron systems is not fundamental, since the Hückel rule is based upon Hund's rule of maximum multiplicity coupled with the presence of degenerate levels in the cyclic hydrocarbons for which it is normally invoked. There are no degenerate levels in C_{2v} molecules.

*Author for correspondence.

0166—1280/81/0000—0000/$02.75

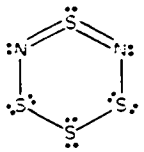

1

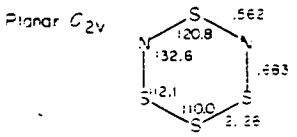

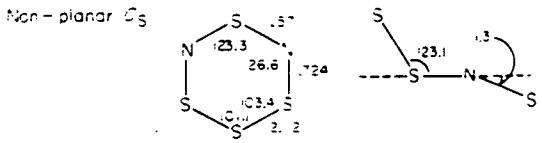

Fig. 1. Final geometries (HONDO Program).

Conversion of the delocalised MO's to a localised orbital system [5] yields a bonding system of classical type (1) with the 3 contiguous S atoms having normal covalent σ-bonds and two lone pairs each. The nitrogen atoms are each doubly bound to the single S(IV) centre and each of these three has a

TABLE 1

Best total energies (a.u.). Optimised geometry starred

Symmetry		C_{2v}	C_s
Basis set			
S	N		
MB 10*s* 6*p*1*d*	7*s* 3*p*	−1695.6347*	−1695.6571*
DZ 12*s* 9*p*1*d*	9*s* 5*p*	−1698.8251	−1698.8301
Virial theorem (DZ)		1.9999	1.9994
Dipole moment (Debye) (DZ)		0.560	0.823
Atomic populations (DZ)			
S-1		15.5054	15.5047
S-3/5		15.8554	15.8637
S-4		16.0719	16.0388
N-2/6		7.3568	7.3646
Orbital energies (eV) (DZ)		8.62 ($3a_2$)	8.61 (a'')
		9.46 ($6b_1$)	9.44 (a')
		11.81 ($12b_2$)	11.96 (a'')
		13.11 ($18a_1$)	13.06 (a')
		13.43 ($5b_1$)	13.97 (a')
		13.52 ($17a_1$)	14.16 (a')
		14.41 ($11b_2$)	14.32 (a'')
		14.80 ($2a_2$)	14.87 (a'')

single lone pair. The molecule is found to have a highly polarised structure (Table 1). The $3d_s$ orbital populations are never high, bearing in mind that six $3d_s$ cartesian functions implicitly include a further $3s$ orbital together with the usual five "chemical" $3d_s$ orbitals. Total $3d_s$ populations are: S-1, 0.7330; S-3/5, 0.4784; and S-4, 0.4364 electrons. The higher value at S-1 is consistent with the cumulative nature of the bonding, but is much lower than might be expected on *spd* hybridisation grounds.

When the basis sets are markedly increased to better than double zeta [5], the effect of the $3d_s$ orbitals on the total energy are nearly halved from 0.6232 a.u. to 0.3300 a.u. (1 a.u. = 2626 kJmol^{-1}). The largest basis set consisting of an S($12s9p1d$) and N($9s5p$) contracted as in our previous work [6] yielded a total energy of $-$ 1698.83018 a.u. and a Virial theorem value of 1.99935 to be compared with the theoretical value of 2.00000.

Further details of these calculations and the results of extended basis set calculations will be given in a further paper together with an interpretation of the UV-photoelectron spectrum.

REFERENCES

1 H. G. Heal, The Inorganic Heterocyclic Chemistry of Sulfur, Nitrogen and Phosphorus, Academic Press, 1980, Chap. 6, p. 115.
2 A. J. Bannister, Nature, 237 (1972) 92.
3 H. W. Roesky, Angew. Chem. Int. Ed. Engl., 18 (1979) 91.
4 W. L. Jolly, Sulfur Research Trends, Adv. Chem. Ser., 110 (1972) 92.
5 R. H. Findlay, M. H. Palmer, A. J. Downs, R. G. Egdell and R. Evans, Inorg. Chem., 1980, 19, 1307.
6 M. Redshaw, M. H. Palmer and R. H. Findlay, Z. Naturforsch., Teil A 34 (1978) 220.

Gas-Phase Tautomerism in the Triazoles and Tetrazoles: A Study by Photoelectron Spectroscopy and ab Initio Molecular Orbital Calculations

Michael H. Palmer, Isobel Simpson, and J. Ross Wheeler
Department of Chemistry, University of Edinburgh, Edinburgh, Scotland

Z. Naturforsch. 36a, 1246–1252 (1981); received September 28, 1981

The photoelectron spectra of the tautomeric 1,2,3,- and 1,2,4-triazole and 1,2,3,4-tetrazole systems have been compared with the corresponding N-methyl derivatives. The dominant tautomers in the gas phase have been identified as 2H-1,2,3-triazole, 1H-1,2,4-triazole and 2H-tetrazole.

Full optimisation of the equilibrium geometry by ab initio molecular orbital methods leads to the same conclusions, for relative stability of the tautomers in each of the triazoles, but the calculations wrongly predict the tetrazole tautomerism.

Introduction

In a previous study [1] one of us reported the gas phase He(I) photoelectron spectra for the aza derivatives of pyrrole (1a), derived by progressive substitution of ≧CH by ≧N, namely pyrazole (2a), imidazole (3a), 1,2,3-triazole (4a), 1,2,4-triazole (5a) and tetrazole (6a). The spectra obtained in the latter three cases relate to tautomeric mixtures, namely 4a ⇋ 7a, 5a ⇋ 8a, 6a ⇋ 9a, and it had been assumed that the tautomer present in the gas phase would be the same as in the solid state or solution, there being no evidence to the contrary; thus we assigned the spectra on the basis of 4a, 5a and 6a rather than 7a, 8a or 9a, respectively [2, 3, 4].

Two pieces of information have subsequently made us reconsider this topic. The dominant tautomer present in the (gas-phase) microwave spectrum of 1,2,3-triazole is now thought to be the 2H-form (7a), previously not identified because of its very low dipole moment (relative to 4a) [5]. Secondly, as part of an investigation of nuclear quadrupole coupling using large basis sets [6], we unexpectedly found that assigned geometries for some of the un-observed tautomers (7a, 8a, 9a) led to energies very similar to those using known structures for the other compounds (e.g. 4a und 5a); optimisation could lead to a reversal of assignment for the thermodynamically most stable tautomer.

Reprint requests to Dr. M. H. Palmer, Department of Chemistry, University of Edinburgh, West Mains Road, Edinburgh EH9 3JJ, Scotland.

In the present paper we report (a) a comparison of the photoelectron spectra of the tautomeric mixtures with the corresponding N-methyl compounds of each type, e.g. 1,2,3-triazole with 4b and 7b; (b) ab initio calculations of the optimum geometry for each tautomeric form, with a view to determining the calculated equilibrium ratio from the energy difference (Figure 1).

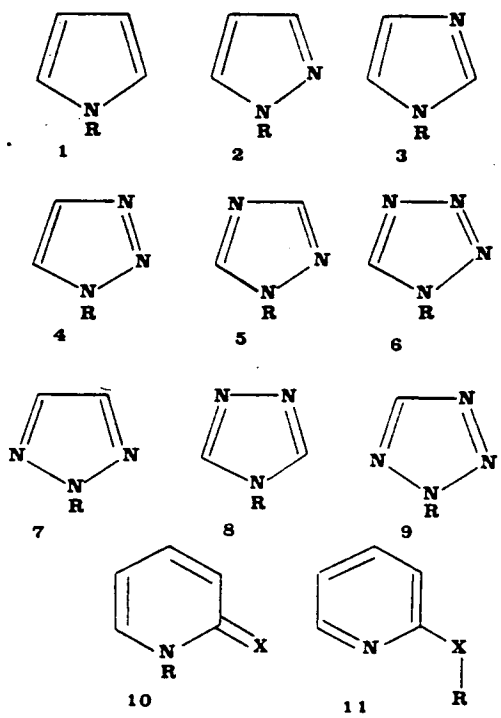

Fig. 1. Molecular structures. 1–9: (a) R=H, (b) R=Me; 10, 11: (a) R=H, X=O, (b) R=H, X=S, (c) R=Me, X=O, (d) R=Me, X=S.

0340-4811 / 81 / 1100-1246 $ 01.00/0. — Please order a reprint rather than making your own copy.

Methods

(a) *The Photoelectron Spectra*

These were obtained from the previous samples [6] on a Perkin Elmer PS 16 Spectrometer, modified by incorporation of a Helectros hollow cathode lamp and Vacuum Science Workshop power supply. A Varian C1024 signal averaging device was used to repetitively scan and increase signal-to-noise for some of the compounds, which have comparatively low vapour pressure at normal temperatures, but which require to be drawn into the spectrometer from an external reservoir. Calibration was by means of $Xe/Ar/N_2$ mixtures (IP's 12.13, 15.75 and 18.6 eV, respectively) and He^+ self-ionisation (26.2 eV).

(b) *Ab Initio Electronic Structure Calculations*

These proceded in stages as follows: — (i) a minimal basis (7s3p/3s; MB) for (C, N/H) was used for a full gradients procedure search for the lowest energy structure. This is a different procedure to that adopted in our recent paper on 9-membered ring heterocycles [7] where the method involved gradients of total energy with respect to cartezian coordinate followed by up-dating of a Hessian matrix; the new method, using the HONDO program [8, 9], uses a gradient procedure based upon derivatives of the integrals over the gaussian basis [9]. The program was implemented on an ICL 2972 computer; optimisation was started from an assigned geometry [6] and cycled until the energy had converged to 0.00001 a.u. (1 a.u. = 2626 kJ mol^{-1}) and the bond lengths and angles to 0.001 Å and 0.01° respectively. A recent example of the power of this method using our basis for nitrogen is for S_4N_2 [10] where a crystal structure has recently been reported [11]; the two structures are nearly identical. (ii) At the end of the optimisation phase the calculations were extended to a double zeta (DZ) basis [6, 12] at the previously computed equilibrium geometry. This was to confirm that (a) no major change in either orbital ordering had occurred in the region of interest to the present photoelectron spectra, and (b) to check that the electric field gradients (c.f. [6]) (EFG) were not markedly effected by the geometry optimisation. These are discussed below (and elsewhere for the EFG), but we note that energy differences between tautomers must ideally be determined at the equilibrium geometry, and hence refer to the minimal basis calculations in the present work.

Results and Discussion

(a) *The Final Equilibrium Geometries*

The final equilibrium (computed) geometries for each tautomeric pair are shown in Fig. 2, and the total energies in Table 1. Both MB and DZ bases predict the 2H-tautomer to be more stable than the 1H- for 1,2,3-triazole, in agreement with the microwave data [5]. The ratio is predicted to be (2H/1H) 1.68 from the MB calculations, while the less rigorous value from the DZ ones is 586; the two values thus bracket the experimental estimate (~ 100). To date 4H-1,2,4-triazole has not been detected experimentally, and the present calculations suggest that the 1H-isomer is more stable than the 4H by 11.3 kJ mol^{-1} (MB), (or 21.4 kJ · mol^{-1} from the DZ calculations). These lead to equilibrium constants of 93 and 5300 respectively, the former being more rigorous. The results for the

Table 1. Total Energies in the Optimisation Process (a.u.).

	Starting Geometry		Final Geometry	
	Minimal Basis	Double Zeta Basis	Minimal Basis	Double Zeta Basis
1H-1,2,3-Triazole (4a)	— 240.0154	— 240.6370	— 240.0659	— 240.6571
2H-1,2,3-Triazole (5a)	— 240.0227	— 240.6644	— 240.0679	— 240.6631
Energy difference (2H-1H) (kJ mol^{-1})	— 19.2	— 72.0	— 1.3	— 15.9
1H-1,2,4-Triazole (6a)	— 240.0618	— 240.6909	— 240.0834	— 240.6871
4H-1,2,4-Triazole (7a)	— 240.0669	— 240.6773	— 240.0791	— 240.6789
Energy difference (4H-1H) (kJ mol^{-1})	— 13.4	+ 35.7	+ 11.3	+ 21.4
1H-Tetrazole (8a)	— 255.9109	— 256.6034	— 255.9708	— 256.6169
2H-Tetrazole (9a)	— 255.8959	— 256.6182	— 255.9697	— 256.6166
Energy difference (2H-1H) (kJ mol^{-1})	+ 39.4	— 38.9	+ 3.0	+ 0.70

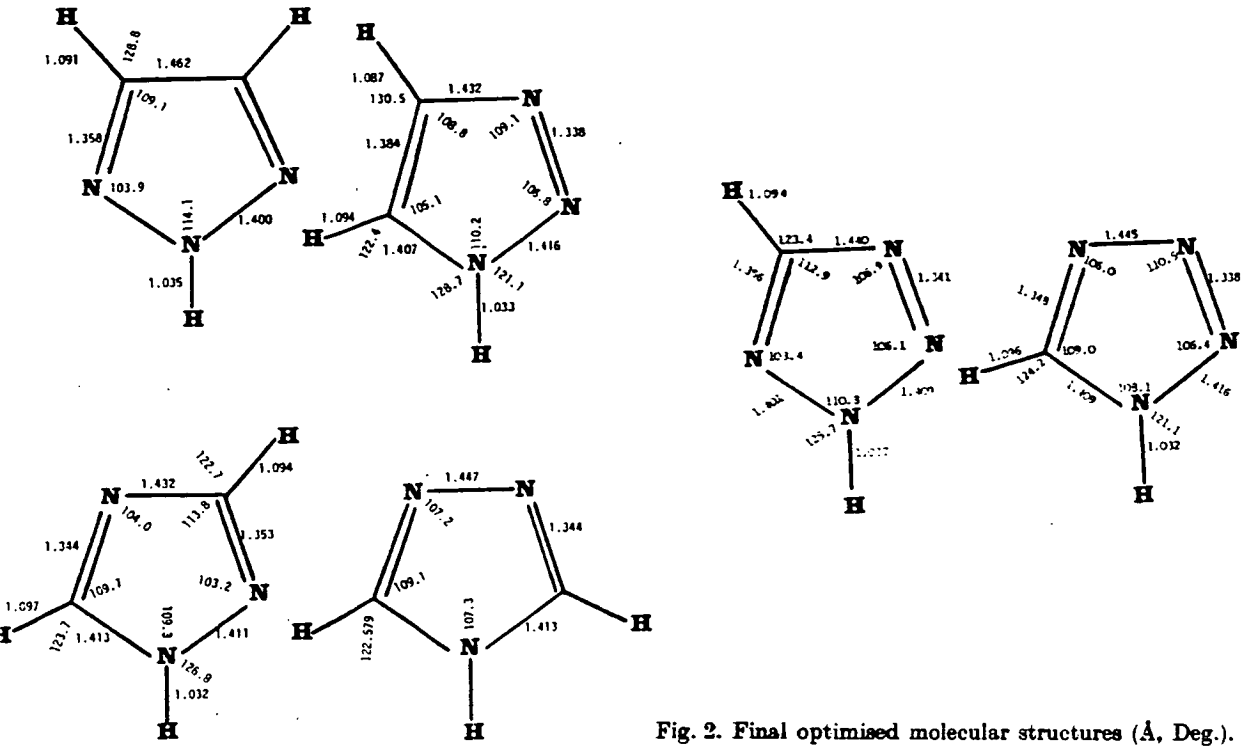

Fig. 2. Final optimised molecular structures (Å, Deg.).

tetrazoles are more nearly equal, with the 1H-isomer being preferred by 3.0 kJ mol^{-1} (MB) and 0.7 kJ mol^{-1} (DZ), leading to equilibrium constants of 3.3 and 1.3, respectively; this is in agreement with previous solution and crystal data [4], but not with the new spectral information below.

(b) *Assignment of the Dominant Tautomers from the Photoelectron Spectra*

Provided substitution of NH by NMe does not lead to a major change in spectrum, it should be possible to assign the NH-compound spectra of the mixture to a particular tautomer; this has been done previously for the pyridinone-hydroxypyridine systems (10a—d, 11a—d) [13]; previous studies of the pyroles (1a, b) and imidazoles (3a, b), where no tautomerism is possible [14] have shown the low binding region to be very similar for the NH and NMe compounds.

Replacement of an NH-delocalised bonding orbital by NMe leads to the introduction of three new valence shell orbitals of $(A_1 + E)$ symmetry, in the local C_{3v} framework. In aromatics, the E levels are split into E_σ and E_π, and are near 14 eV in toluene and related compounds [15]. The A_1 Me level has high $2s_C$ character and lies near 21 eV in such compounds. Thus all these group orbitals lie outside the present region of interest. It is convenient [1] to divide the spectra into regions A, B, C ... (low to high binding); the region of primary interest in the present work is Region A, containing most of the π- and lone pair levels [1]; it extends from about 8—10 eV for pyrrole (1a), with progressive shift to higher binding energy on aza-substitution, to 10—13 eV for tetrazole. Comparison of the spectra of 1a, b—3a, b shows there is a general shift to lower binding energy in the N-methyl compounds [14]; this is attributable in part to electron donation from the Me group, and in part from antisymmetric combinations of ring and Me group levels.

1,2,3-Triazole

It is apparent that the spectrum of the tautomeric mixture (Fig. 3) is much more similar to that of the 2-methyl- (7b) than the 1-methyl tautomer (4b); the width and placing of the IP's is such that it is not possible to say whether the minor compo-

Table 2. Orbital Energies (eV).

Pyrrole (1a)	Pyrazole (2a)		Imidazole (3a)	1H-1,2,3-triazole (4a)
− 8.211 a_2	− 9.678	a″(π)	− 9.020 a″	− 10.212 a″
− 9.579 b_1	− 10.248	a″	− 11.065 a″	− 11.782 a′(LP_N^-)
− 14.453 a_1	− 12.456 (LP_N)	a′(σ)	− 11.758 a′(LP_N)	− 11.941 a″
− 14.920 b_2	− 15.624	a′	− 15.724 a′	− 13.873 a′(LP_N^+)
− 15.630 b_1	− 16.200	a′	− 16.586 a″	− 17.297 a′
− 15.942 b_2	− 16.803	a″	− 16.646 a′	− 17.807 a′
− 16.307 a_1	− 16.904	a′	− 16.778 a′	− 18.033 a″
− 20.181 a_1	− 20.466	a′	− 20.942 a′	− 21.330 a′
− 20.979 b_2	− 22.033	a′	− 21.991 a′	− 23.612 a′
− 21.794 a_1	− 22.686	a′	− 22.879 a′	− 23.649 a′
− 26.825 b_2	− 29.113	a′	− 27.857 a′	− 30.335 a′
− 28.647 a_1	− 30.339	a′	− 32.236 a′	− 33.499 a′
− 35.576 a_1	− 38.155	a′	− 37.204 a′	− 40.557 a′

1H-1,2,4-triazole (5a)	(C_2V) 2H-1,2,3-triazole (6a)	(C_2V) 4H-1,2,4-triazole (7a)	2H-tetrazole (8a)	1H-tetrazole (9a)
− 10.728 a″	− 10.885 a_2	− 10.783 a_2	− 11.990 a″	− 11.809 a″
− 11.841 a″	− 11.181 b_1	− 11.474 b_1	− 12.720 a″	− 12.636 a′(LP_N)
− 12.173 a′(LP_N^-)	− 12.868 b_2(LP_N^-)	− 12.394 a_1(LP_N^+)	− 12.880 a′(LP_N)	− 13.077 a″
− 13.616 a′(LP_N^+)	− 13.741 a_1(LP_N^+)	− 12.558 b_2(LP_N^-)	− 13.545 a′(LP_N)	− 13.319 a′(LP_N)
− 16.687 a′	− 17.035 b_2	− 17.001 a_1	− 15.686 a′(LP_N)	− 15.443 a′(LP_N)
− 17.651 a″	− 17.323 a_1	− 17.310 b_1	− 18.366 a′	− 19.185 a″
− 18.072 a′	− 17.491 b_1	− 17.645 b_2	− 19.025 a″	− 19.458 a′
− 21.364 a′	− 20.335 a_1	− 21.762 a_1	− 21.460 a′	− 21.945 a′
− 22.654 a′	− 22.719 b_2	− 22.997 a_1	− 24.082 a′	− 24.929 a′
− 24.159 a′	− 23.437 a_1	− 23.677 b_2	− 25.585 a′	− 25.404 a′
− 31.081 a′	− 30.320 a_1	− 30.867 b_2	− 33.39 a′	− 33.568 a′
− 33.479 a′	− 32.911 b_2	− 32.968 a_1	− 34.98 a′	− 35.273 a′
− 39.392 a′	− 39.413 a_1	− 38.242 a_1	− 42.239 a′	− 42.497 a′

1-methyl-1,2,4-triazole (5b)	2-methyl-1,2,3-triazole (6b)	4-methyl-1,2,4-triazole (7b)	2-methyltetrazole (8b)	1-methyltetrazole (9b)
− 10.390 a″	− 10.281 a″	− 10.604 a″	− 11.718 a″	− 11.585 a″
− 11.281 a″	− 11.027 a″	− 10.878 a″	− 12.007 a″	− 12.322 a″
− 11.928 a′(LP_N^-)	− 12.724 a′(LP_N^-)	− 12.190 a′(LP_N^+)	− 12.572 a′(LP_N)	− 12.344 a′(LP_N)
− 13.346 a′(LP_N^+)	− 13.603 a′(LP_N^+)	− 12.320 a′(LP_N^-)	− 13.309 a′(LP_N)	− 13.074 a′(LP_N)
− 15.813 a″	− 15.441 a′	− 15.698 a″	− 15.398 a′(LP_N)	− 15.128 a′(LP_N)
− 16.008 a′	− 15.480 a″	− 16.370 a′	− 16.329 a′	− 16.835 a″
− 16.594 a′	− 16.557 a′	− 16.501 a′	− 16.506 a″	− 17.027 a′
− 17.183 a′	− 17.310 a′	− 17.782 a′	− 17.923 a′	− 18.743 a′
− 18.375 a″ Me(e)	− 18.267 a″ Me(e)	− 18.456 a″ Me(e)	− 19.415 a″ Me(e)	− 19.656 a″ Me(e)
− 20.072 a′	− 19.612 a′	− 19.810 a′	− 20.246 a′	− 20.851 a′
− 22.647 a″	− 22.125 a′	− 21.988 a′	− 23.682 a′	− 23.655 a′
− 22.844 a″	− 22.752 a′	− 23.744 a′	− 24.058 a′	− 25.210 a′
− 26.817 a′ Me(a)	− 26.372 a′ Me(a)	− 27.181 a′ Me(a)	− 28.329 a′ Me(a)	− 28.394 a′ Me(a)
− 31.306 a′	− 31.211 a′	− 30.683 a′	− 33.403 a′	− 33.381 a′
− 33.463 a′	− 32.754 a′	− 33.225 a′	− 34.978 a′	− 35.516 a′
− 39.228 a′	− 39.377 a′	− 38.116 a′	− 42.009 a′	− 42.270 a′
− 307.577 a′	− 307.093 a′	− 308.093 a′	− 308.081 a′	− 308.437 a′
− 307.697 a′	− 307.122 a′	− 308.478 a′	− 308.113 a′	− 308.594 a′
− 308.321 a′	− 307.421 a″	− 308.478 a′	− 425.058 a′	− 424.806 a′
− 423.491 a′	− 425.486 a′	− 424.685 a′	− 425.661 a′	− 426.073 a′
− 425.141 a′	− 425.487 a′	− 424.696 a′	− 426.837 a′	− 426.506 a′
− 426.149 a′	− 426.651 a′	− 425.786 a′	− 427.514 a′	− 426.999 a′

Table 2. (continued).

-methylpyrrole[a] (1b)	1-methylpyrrole[b] (1b)	1-methylpyrazole (2b)	1-methylimidazole (3b)	1-methyl-1,2,3-triazole (4b)
– 8.106 a″	– 8.099 a′	– 9.559 a″	– 8.858 a″	– 10.031 a″
– 9.158 a″	– 9.152 a′	– 9.796 a″	– 10.529 a″	– 11.329 a″
– 14.286 a″	– 14.306 a′	– 12.377 a′(LP_N)	– 11.550 a′(LP_N)	– 11.533 a′(LP_N^-)
– 14.360 a′	– 14.324 a″	– 14.184 a″	– 15.159 a″	– 13.683 a′(LP_N^+)
– 14.402 a′	– 14.406 a″	– 15.057 a′	– 15.345 a′	– 16.031 a″
– 15.504 a′	– 15.497 a″	– 15.662 a′	– 15.871 a′	– 16.103 a′
– 15.517 a′	– 15.522 a″	– 16.125 a′	– 16.071 a′	– 17.129 a′
– 16.469 a′	– 16.469 a″	– 16.695 a′	– 17.018 a′	– 17.655 a′
– 17.318 a″ Me(e)	– 17.319 a′ Me(e)	– 17.465 a″ Me(e)	– 17.879 a″ Me(e)	– 18.788 a″ Me(e)
– 19.378 a′	– 19.377 a″	– 19.785 a′	– 19.735 a′	– 20.298 a′
– 20.429 a′	– 20 424 a″	– 21.138 a′	– 21.445 a′	– 22.274 a′
– 21.103 a′	– 21.100 a″	– 22.209 a′	– 22.092 a′	– 23.622 a′
– 25.558 a′ Me(a)	– 25.559 a″	– 25.744 a′ Me(a)	– 26.548 a′ Me(a)	– 27.611 a′
– 26.767 a′	– 26.762 a″	– 29.243 a′	– 27.978 a′	– 30.166 a′
– 29.353 a′	– 29.351 a″	– 30.766 a′	– 32.486 a′	– 33.901 a′
– 35.664 a′	– 35.661 a″	– 38.166 a′	– 37.147 a′	– 40.419 a′
– 305.257 a′	– 305.243 a″	– 305.829 a′	– 306.255 a′	– 306.687 a′
– 305.286 a′	– 305.284 a″	– 306.552 a′	– 306.872 a′	– 307.216 a′
– 306.428 a′	– 306.376 a″	– 307.296 a′	– 307.643 a′	– 307.974 a′
– 306.428 a′	– 306.463 a″	– 307.560 a′	– 307.676 a′	– 424.531 a′
– 307.224 a′	– 307.234 a″	– 424.434 a′	– 423.307 a′	– 425.766 a′
– 424.698 a′	– 424.694 a″	– 425.744 a′	– 425.281 a′	– 426.359 a′

[a] All methyl "H's" out of plane of molecule. [b] All methyl "H's'$_2$ in plane of molecule.

ient is present in small amounts or below the detection limit for the technique (say 0.1%). The dominance of the 2H-tautomer is, however, consistent with recent microwave studies [5] and the computed relative energies of the present study.

,2,4-Triazole

The spectrum of the 4-methyl isomer (8b) Fig. 4 s markedly different in the low binding Region A when compared with either the 1-methyl compound 5b) or the tautomeric mixture; we conclude that he latter is almost entirely in the 1H-form (5a) in he vapour phase, and thus is the same in solution nd solid state measurements made to date. This is onsistent with the high difference in computed nergy between 5a and 8a.

Tetrazole

The assignment for tetrazole shows the 2H-automer (9a) to be dominant; the almost complete bsence of the 1H-form (6a) can be assumed from he absence of a broad band near 12.8 eV which ccurs in the 1-Me spectrum. The presence of narked vibrational structure on the tautomer pectrum and that of the 2-methyl compound (9b) s very evident (Figure 5).

Conclusions

The present results confirm the earlier suggestions that the most stable tautomer for 1,2,3-triazole in the gas phase is the 2H-one (4a), and that photoelectron spectroscopy can be used to differentiate between tautomers in cases of this type. 1,2,4-Triazole appears to be in the 1H-form under all conditions so far investigated, and the calculations suggest that this is likely to be true for most circumstances. In contrast, the energy difference between the tautomers of tetrazole is clearly small, and either tautomer can be anticipated, depending upon conditions. The 2H-tautomer is dominant in the gas phase at low pressures. It seems probably that the assumption of particular tautomeric structures for the vapour phase based upon solution or crystal data is likely to be hazardous, since further examples in the hydroxypyridine-pyridinone (10—11) systems have led to be the same conclusion [13]. Relative energies based upon arbitrary choices of geometry seem particularly suspect, and the failure of the present ab initio minimal calculations for tetrazole make the use of even more restricted basis sets, such as in semiempirical calculations even less reliable.

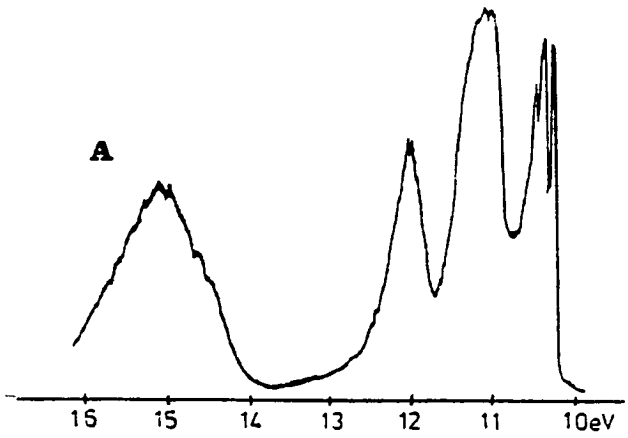

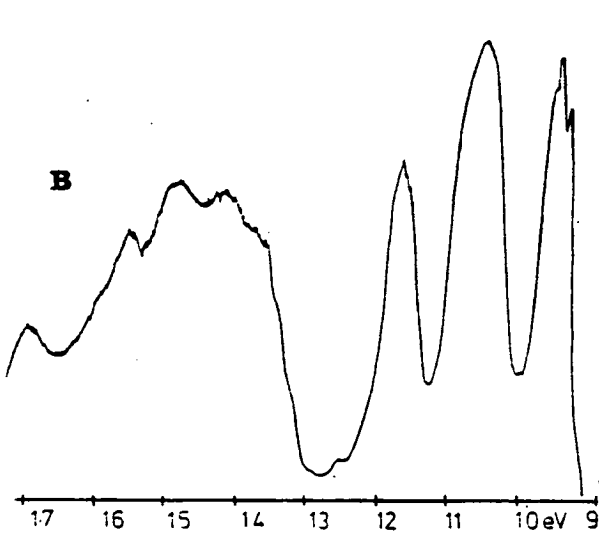

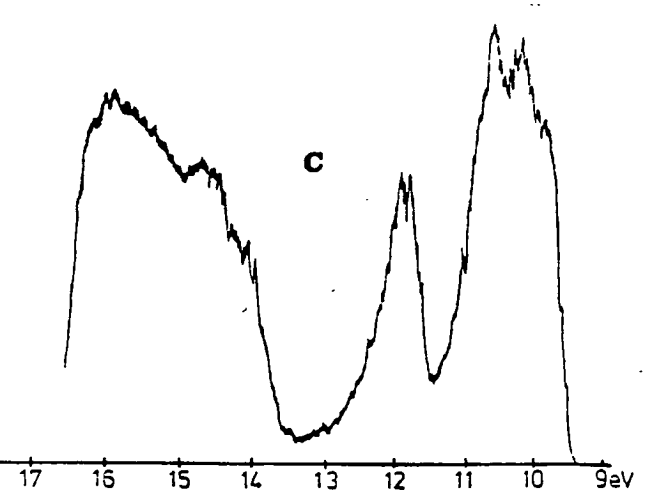

Fig. 3. Photoelectron spectra (HeI) of 1,2,3-Triazole (A) and its 1- and 2-Methyl compounds (C & B, respectively).

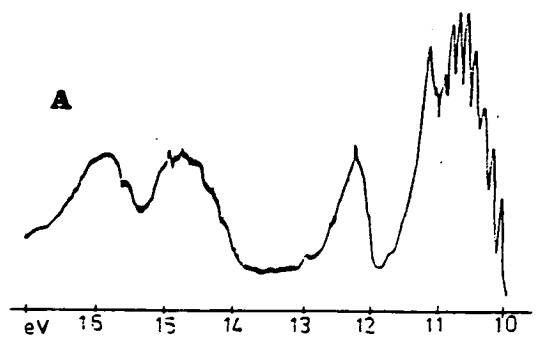

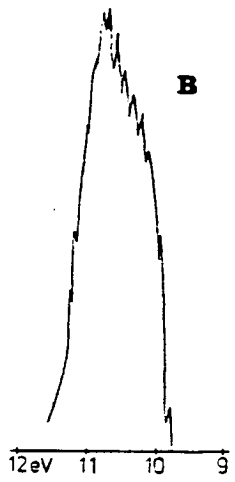

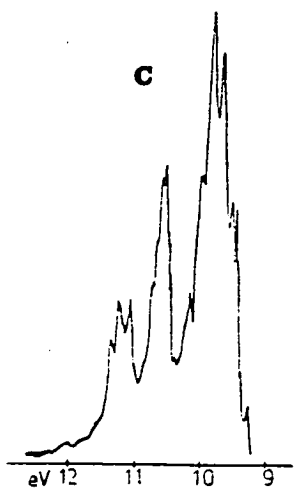

Fig. 4. Photoelectron spectra (HeI) of 1,2,4-Triazole (A) and its 1- and 4-Methyl compounds (B and C, respectively).

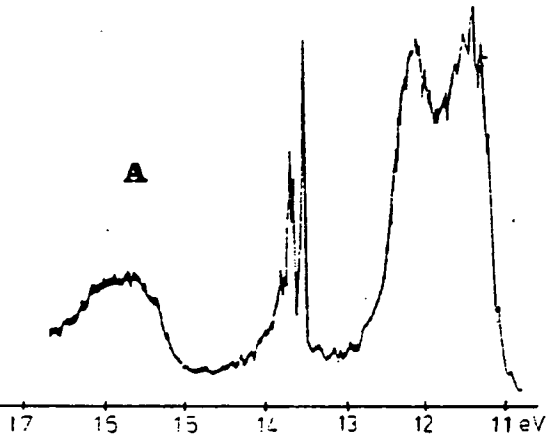

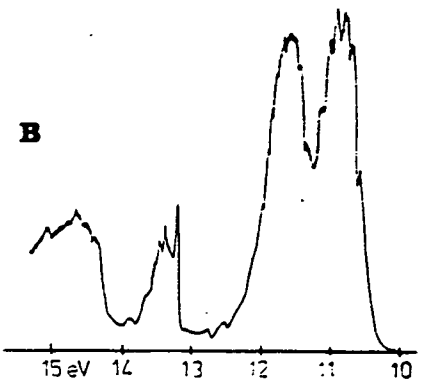

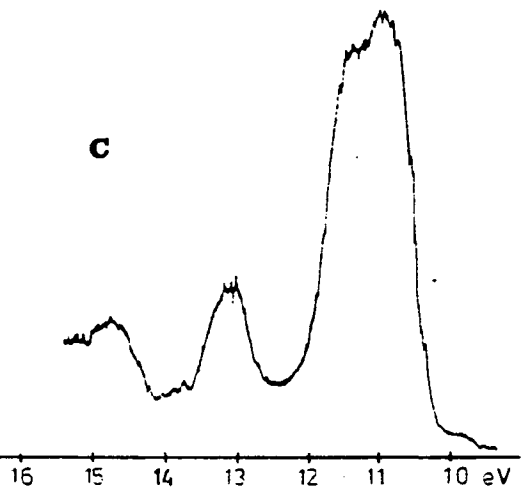

Fig. 5. Photoelectron spectra (HeI) of Tetrazole (A) and its 1- and 2-Methyl compounds (C and B, respectively).

Appendix

The present double zeta calculations yielded the orbital energies shown below. In this present paper we are primarily concerned with the gas-phase tautomers rather than assignment of the photoelectron spectra. We will be continuing this latter topic in a further paper involving configuration interaction calculations for the ionised states of **1**—**9**; since however Koopmans' theorem is widely utilised in this field, the orbital energies give a provisional assignment for the lower IP's, and are included. Very few differences in the calculated order (by symmetry and nature of orbital) occur between the present and our previous work [1], except that the inner-most π-level is often more shifted to lower binding energy relative to some σ-levels on going from MB to DZ.

[1] M. H. Palmer, S. Cradock, and R. H. Findlay, Tetrahedron **29**, 2173 (1973).
[2] T. L. Gilchrist and G. E. Gynerin, Adv. in Heterocyclic Chemistry **16**, 33 (1974); Ed. A. R. Katritzky and A. J. Boulton, Academic Press, London.
[3] L. T. Creagh and P. Truitt, J. Org. Chem. **30**, 1892 (1968).
[4] (a) M. F. Kaufman, F. M. Ernsberger, and W. S. McEwan, J. Amer. Chem. Soc. **78**, (1956); (b) M. Witanowski, L. Stefaniak, H. Januszewski, Z. Grabowski, and G. A. Webb, Tetrahedron **28**, 637 (1972); G. A. Webb, M. Witanowski, and L. Stefaniak, J. Magnetic Resonance **36**, 232 (1979).
[5] C. J. Nielsen, L. Nygaard, and G. O. Sorensen, IVth European Microwave Spectrosc. Conference, Tübingen 1977; L. Nygaard, Personal communication.
[6] M. H. Palmer, I. Simpson, and R. H. Findlay, Z. Naturforsch. **36a**, 34 (1981).
[7] M. H. Palmer and J. D. Nisbet, J. Molecular Structure **67**, 65 (1980).
[8] M. Dupuis, J. Rys, and H. F. King, J. Comp. Phys. **21**, 1, 144 (1976).
[9] M. Dupuis, J. Rys, and H. F. King, J. Chem. Phys. **65**, 111 (1976); program distributed by Q.C.P.E., Indiana University, Q.C.P.E. Bulletin **13**, 403 (1981).
[10] M. H. Palmer, J. R. Wheeler, R. H. Findlay, N. P. C. Westwood, and W. M. Lau, J. Molecular Structure, "THEOCHEM", **85**, 193 (1981).
[11] T. Chivers, P. W. Codding, and R. T. Oakley, Chem. Comm. 584 (1981).
[12] T. Dunning, J. Chem. Phys. **53**, 2823 (1970).
[13] M. J. Cook, S. El-Abbady, A. R. Katritzky, C. Guimon, and G. Pfister-Guillouzo, J.C.S. Perkin II, 1652 (1977).
[14] L. Klasinc, B. Ruščić, F. Kajfež, and V. Šunjić, Int. J. Quantum Chem. Quant. Biol. Symp. **5**, 367 (1978); A. D. Baker, D. Betteridge, N. R. Kemp, and R. E. Kirby, Anal. Chem. **42**, 1064 (1970).
[15] M. H. Palmer, W. Moyes, and M. Spiers, J. Molec. Struct. **49**, 105 (1978); ibid. **53**, 235 (1979); ibid. **55**, 243 (1979).

Bibliography

AND 65: J. B. Anderson and J. B. Fenn, Physics of Fluids, 8, 780 (1965)

AND 65: J. B. Anderson, R. P. Andres and J. B. Fenn, Adv. Chem. Phys. 10, 275 (1966)

ANL 67: K. G. Anlauf, P. J. Kuntz, D. M. Maylotte, P. D. Pacey and J. C. Polanyi, Faraday Disc. Chem. Soc., 44, 183 (1967)

APP 75: E. H. Appelman and M. A. A. Clyne, JCS Faraday I, 71, 2072 (1975)

BAS 71: N. Basco and F. G. M. Hathorn, Chem. Phys. Letts. 8, 291 (1971)

BAT 61: D. R. Bates, Ed.(1961), Quantum Theory, 1, Elements, Academic Press, London

BEN 72: A. Ben-Shaul, R. D. Levine and R. B. Bernstein, J. Chem. Phys. 57, 5427 (1972).

BER 62: H. C. Berg and D. Kleppner, Rev.Sci.Instr., 33, 248 (1962)

BER 79: Atom molecule collision theory: A guide for the experimentalist, Ed. R. B. Bernstein, Plenum, New York (1979).

BIR 75: J. W. Birks, S. D. Gabelnick and H. S. Johnston, J. Mol. Spectrosc. 57, 23 (1975)

BLA 63: N. C. Blais and D. L. Bunker, J. Chem. Phys., 39, 315, (1963)

BLA 64: N. C. Blais and D. L. Bunker, J. Chem. Phys., 41, 2377 (1964)

BLA 70: N. C. Blais and J. B. Cross, J. Chem. Phys., 55, 3580 (1970)

BLA 81: G. W. Black, PhD. thesis, Edinburgh University 1981.

BRU 73: P. Brumer and M. Karplus, Faraday Disc. Chem.Soc., 55, 80 (1973).

BUN 71: D. L. Bunker, Methods in Computational Physics, Vol.10, 287 (1971)

CAM 78: I. M. Campbell and D. L. Baulch, Spec. Per. Report to the Chem. Soc.: Gas Kinetics and Energy transfer Vol. 3, p 42 (1978)

CAR 73: C. F. Carter, M. R. Levy, K. B. Woodall and R. Grice, Faraday Disc. Chem. Soc., 55, 381 (1973)

CLO 78: P. N. Clough, J. Geddes and G. M. O'Neil, J. Chem. Phys., 69, 3128 (1978)

CLY 76: M. A. A. Clyne and I. S. McDermid, JCS Faraday II 72, 2242, (1976)

CLY 78: M. A. A. Clyne and I. S. McDermid, JCS Faraday II 74, 1644, (1978)

COT 72: F. A. Cotton and G. Wilkinson, Advanced Inorganic Chemistry, 3rd Edition, Wiley, New York (1972)

COX 72: J. A. Coxon, Spec. Per. Reports to the Chem. Soc. : Molecular Spectroscopy, Vol. 1, p 177, (1973)

CRU 73: H. W. Cruse, P. J. Dagdigian and R. N. Zare, Faraday Disc. Chem. Soc., 55, 277 (1973)

DAG 74: P. J. Dagdigian, H. W. Cruse, A. Schultz and R. Zare, J. Chem. Phys. 61, 4456, (1974).

DIN 73: A. M. G. Ding, L. J. Kirsch, D. S. Perry, J. C. Polanyi and J. L. Schreiber, Faraday, Disc. Chem. Soc., 55, 252 (1973)

DIN 75: U. Dinur, R. Kosloff, R. D. Levine and M. J. Berry, Chem. Phys. Letts, 34, 199 (1975).

DIX 73: D. A. Dixon, D. D. Parrish and D. R. Herschbach, Faraday Disc. Chem. Soc., 55, 385 (1973)

DON 80: R. J. Donovan et al., Chem. Phys. Lett, 69, 472 (1980)

DUF 79: J. W. Duff and P. Brumer, J. Chem. Phys., 71 2693 (1979)

FAR 75: J. M. Farrar and Y. T. Lee, J. Chem. Phys. 63, 3639 (1975)

FAI 76: M. B. Faist, J. Chem. Phys., 65, 5427, (1976)

FAI 78: M. B. Faist, J. T. Muckermann and F. E. Schubert, J. Chem. Phys., 69, 4087 (1978)

FAI 79: J. T. Muckermann and M. B. Faist, J. Phys. Chem., 83, 79 (1979)

FEH 65: F. C. Fehsenfeld, K. M. Everson and H. P. Broida, Rev.Sci. Instr. 36, 294 (1965)

FER 80: D. P. Fernie, PhD. Thesis, Edinburgh University 1980

FIS 67: G. A. Fisk, J. D. McDonald and D. R. Herschbach, Faraday Soc. Disc., 44, 228 (1967)

FIT 79: D. E. Fitz and P. Brumer, J. Chem. Phys., 70, 5527 (1979)

FLE 82: I. W. Fletcher and J. C. Whitehead, J. Chem. Soc. Faraday Trans. II, 78, 1127 (1982).

FLU 73: M. A. D. Fluendy and K. P. Lawley, Chemical Applications of Molecular Beam Scattering, Chapman and Hall, London (1973).

FLU 76: M. A. D. Fluendy, I. H. Kerr, K. P. Lawley and D. R. MacDonald, Chem.Phys.Letts., 13, 452, (1976).

FOO 75: R. Foon and M. Kaufman, Prog. Reaction Kinetics, 8, 81 (1975).

GEA 71: C. W. Gear, Numerical Initial Value Problems in O.D.E.s', Prentice Hall, New York (1971).

GIO 58: G. Gioumousis and D. P. Stevenson, J. Chem. Phys., 29, 294 (1958).

GIO 60: J. A. Giordmaine and T. C. Wang, J. Appl. Phys. 31, 463 (1960)

GLE 80: R. M. Glen, Ph.D. Thesis, Edinburgh University, 1980.

GOL 50: H. Goldstein, Classical Mechanics, Addison Wesley, Reading Mass (1950)

GOR 79: P. A. Gorry and R. Grice, J. Phys. E, 12, 857 (1979)

GRI 75: R. Grice, Advan.Chem.Phys., 30, 247 (1975).

GRI 81: R. Grice, Spec. Per. Reports to the Chem. Soc.: Gas Kinetics and Energy transfer Vol.4, Chapt. 1, (1981)

HAM 64: J. M. Hamersley and D. C. Hanscombe, Monte Carlo Methods, Methuen, London (1964).

HAN 72: T. W. Hansch, App. Optics, 11, 895 (1972)

HEN 65: A. Henglein and G. A. Muccini, J. Chem. Phys., 43, 1048, (1965)

HER 51: G. Herzberg Spectra of polyatomic molecules, Van Nostrand, Reinholt (1951)

HIA 72: R. Hialt and S. W. Benson, Int. J. Chem. Kinetics, 4, 479 (1972).

HOL 77: L. Holmlid and K. Rynefors, Chem. Phys., 19, 261, (1977).

HUT 78: I. Hutchinson, Carneigie Trust vacation scholarship report (1978).

JOH 66: J. C. Johnson, A. T. Stairs and S. L. Pritchard, J. App. Phys. 37, 1551 (1966)

KAH 80: C. C. Kahler and Y. T. Lee, J. Chem. Phys. 73, 5122 (1980).

KAR 64: M. Karplus and L. M. Raff, J. Chem. Phys., 41, 1267, (1964).

KIN 77: J. L. Kinsey, Ann.Rev. Phys. Chem., 28, 349 (1977)

KOL 72: C. E. Kolbe and M. Kaufman, J. Phys. Chem. 76, 947 (1972)

KUN 66: P. J. Kuntz, E. M. Nemeth, J. C. Polanyi, S. D. Rosner and C. E. Young, J. Chem. Phys., 44, 1168 (1966).

KUN 70: P. J. Kuntz, Trans. Faraday. Soc., 66, 2980, (1970)

KUN 76: P. J. Kuntz, Modern Theoretical Chemistry, Vol.2, Part B, Chapt. 2. Ed. W. H. Miller, Plenum, N.Y.(1976)

LEE 68: Y. T. Lee, P. R. LeBreton, J. D. McDonald and D. R. Herschbach, J. Chem. Phys., 49, 2447 (1968)

LEE 69: Y. T. Lee, P. R. LeBreton, J. D. McDonald and D. R. Herschbach, J. Chem. Phys. 51, 455, (1969)

LEE 77: J. J. Valentini, Y. T. Lee and D. R. Auerbach, J. Chem. Phys., 67, 4866 (1977)

LER 70: R. J. LeRoy, J. Chem.Phys., 52, 2683, (1970).

LEV 72: R. D. Levine and R. B. Bernstein, Molecular Reaction Dynamics, Oxford University Press, New York, (1972)

LEV 75: R. D. Levine and R. B. Bernstein, Adv. At. Mol. Phys. 11, 216 (1975).

LEV 79: R. D. Levine and J. L. Kinsey, Atom-Molecule Collision Theory - a Guide for the experimentalist, R. B. Bernstein Ed., Plenum Press, New York. (1979).

LIG 67: J. C. Light, Faraday Disc. Chem. Soc., 44, 14, (1967)

LIU 77: K. Liu and J. M. Parson, J. Chem. Phys. 67, 1814 (1977)

LOE 71: H. J. Loesch and D. Beck, Ber. Bunsenges, Phys. Chem. 75, 736 (1971).

LON 29: F. London, Z. Elektrochem., 35, 552, (1929).

LOS 79: J. Los and A. W. Kleyn, Ion Pair Formation in Alkali Halide Vapours, P. Davidovitz and D. McFaddon Ed.s, A. P., New York (1979).

MAG 40: J. L. Magee, J. Chem. Phys., 8, 687 (1940)

MIL 67: W. B. Miller, S. A. Safron, D. R. Herschbach, Faraday Disc. Chem. Soc., 44, 108, (1967).

MIL 69: D. R. Miller and D. F. Patch, Rev. Sci. Instr. 40, 1566 (1969).

MIL 73: W. B. Miller, S. A. Safron and D. R. Herschbach, J. Chem. Phys., 56, 3581, (1973).

MOO 58: C. E. Moore, Atomic Energy Level Tables, Nat.Bur. Stand. Cir., p.467 (1958).

MUC 73: J. T. Muckermann, QCPE 229, Indiana University (1973)

MUC 79: J. T. Muckermann and D. G. Truhlar, Atom - Molecule Collision Theory: A Guide for the Experimentalist, Ed. R. B. Bernstein, Plenum, New York (1979).

MUR 78: J. N. Murrell, Spec. Per. Reports to the Chem Sec.: Gas Kinetics and Energy Transfer, Vo.3, p.200 (1978)

NAG 78: NAG-Version 7, Numerical Algorithms Group, 7 Banbury Road, Oxford.

PAR 72: J. M. Parson and Y. T. Lee, J. Chem. Phys. 56, 4658 (1972)

PAR 73: C. A. Parr, J. C. Polanyi and W. H. Wong, J. Chem. Phys., 58, 5(1973)

PAT 74: M. D. Pattengill and J. C. Polanyi,Chem.Phys.,3,1(1974)

PEY 68: S. D. Peyerimhoff and R. J. Buenker, J. Chem. Phys., 49, 2473 (1968).

POL 72: J. C. Polanyi and Woodall, J. Chem. Phys. 57, 1574 (1972)

POL 74: J. C. Polanyi and S. L. Schreiber, Physical Chemistry an Advanced Treatise,Ed.s H.Eyring, D. Henderson and W. Jost, A.P., New York, Vol.VIA, p.383 (1974).

POL 77: J. C. Polanyi and W. J. Skrlac, Chem.Phys., 23, 167 (1977)

POL 79: J. C. Polanyi, J. L. Schreiber and W. J. Skrlac, Faraday Disc.Chem.Soc. 67,66 (1979)

POP 80: D. Poppe, Chem. Phys. 45, 382, (1980).

POR 76: R. N. Porter and L. M. Raff, Modern Theoretical Chemistry, Vol.2, Part B, Chpt. 1, Ed. W. H. Miller, Plenum New York (1976).

PRO 78: E. S. Prochaska, L. Andrews, A. Smyrl and G. Mamantor, Inorg.Chem., 17 975 (1978)

PRU 76: J. G. Pruett and R. N. Zare, J. Chem. Phys. 64, 1774 (1976)

RAD 75: D. St. A. G. Radlein, J. C. Whitehead and R. Grice, Mol. Phys. 29, 1823 (1975)

RAF 66: L. M. Raff, J. Chem. Phys., 44, 1202, (1966)

RAL 60: A. Ralson and H. S. Wilf, Mathematical Methods for Digital Computers, Vol. 1., Chapt. 8, Wiley New York (1960)

SAF 72: S. A. Safron, N. D. Weinstein, D. R. Herschbach and J. C. Tully, Chem. Phys. Letts. 12, 564, (1972)

SAN 77: J. Santamaria and D. L. Bunker, Chem. Phys. 23, 243, (1977)

SAT 55: S. Sato, J. Chem. Phys, 23, 2465 (1955).

SCH 72: A. Schultz, H. W. Cruse and R. N. Zare, J. Chem. Phys. 57, 1354 (1972)

SIB 80: S. J. Sibener, R. J. Buss and Y. T. Lee, Rev.Sci. Instr. 51, 167 (1980)

SMI 75: I. W. M. Smith, J. Chem. Soc. Faraday Trans II, 71, 1970, (1975)

STE 79: L. Stein, J. Wanner, H. Figger, and H. Walther, Springer Series in Chemical Physics Vol. 6; Laser Induced Processes in Molecules, Springer Verlag, Berlin, (1979), P.232.

STE 80: L. Stein, J. Wanner and H. Walther, J. Chem. Phys. 72, 1128 (1980).

SUN 77: T. P. Sung and D. W. Setser, Chem. Phys. Letts., 48, 413 (1977).

TRI 80: T. Trickl, and J. Wanner, Poster Session, 6th Int. Symposium on Gas Kinetics, Southampton, July 1980.

TRI 81: T. Trickl, and J. Wanner, J. Chem Phys. 74, 6508 (1981)

TUL 71: J. C. Tully and R. K. Preston, J. Chem. Phys, 55, 562 (1971).

TUL 76: J. C. Tully, Modern Theoretical Chemistry, Vol.2, Part B, Chapt. 4, Ed. W. H. Miller, Plenum N.Y.(1976).

TUL 81: J. C. Tully, Adv. in Chem. Phys., Vol.42, p.63. Ed. K. P. Lawley.

UNG 76: S. R. Ungemach and H. F. Schaefer III, J. Am. Chem. Soc., 98, 1658 (1976)

VAL 77: J. J. Valentini, M. J. Coggiola and Y. T. Lee, Rev. Sci. Instr. 48, 58 (1977).

WAL 53: A. D. Walsh, J. Chem. Soc., p.2288, (1953).

WHI 75: J. C. Whitehead, Mole. Phys., 29, 177, (1975).

WHI 76: J. C. Whitehead, Mole. Phys., 31, 549, (1976)

WON 73: Y. C. Wong and Y. T. Lee, Faraday Disc. Chem. Soc., 55, 383, (1973).